ABSTRACT

Title of Document: A PARTICLE EROSION MODEL OF MONOCRYSTALLINE SILICON FOR HIGH HEAT FLUX MICROCHANNEL HEAT EXCHANGERS

David William Squiller
Doctor of Philosophy
2017

Directed by: Professor Patrick McCluskey
Department of Mechanical Engineering

As package-level heat generation pushes past 1 kW/cm^3 in various military, aerospace, and commercial applications, new thermal management technologies are needed to maximize efficiency and permit advanced power electronic devices to operate closer to their inherent electrical limit. In an effort to align with the size, weight and performance optimization of high temperature electronics, cooling channels embedded directly into the backside of the chip or substrate significantly reduce thermal resistances by minimizing the number of thermal interfaces and distance the heat must travel. One implementation of embedded cooling considers microfluidic jets that directly cool the backside of the substrate. However, as fluid velocities exceed 20 m/s the potential for particle erosion becomes a significant reliability threat. While numerous particle erosion models exist, seldom are the velocities, particle sizes, materials and testing times in alignment with those present

in embedded cooling systems. This research fills the above-stated gaps and culminates in a calibrated particle-based erosion model for single crystal silicon. In this type of model the mass of material removed due to a single impacting particle of known velocity and impact angle is calculated. Including this model in commercial computational fluid dynamics (CFD) codes, such as ANSYS FLUENT, can enable erosion predictions in a variety of different microfluidic geometries.

First, a CFD model was constructed of a quarter-symmetry impinging jet. Lagrangian particle tracking was used to identify localized particle impact characteristics such as impact velocity, impact angle and the percentage of entrained particle that reach the surface. Next, a slurry erosion jet-impingement test apparatus was constructed to gain insight into the primary material removal mechanisms of silicon under slurry flow conditions. A series of 14 different experiments were performed to identify the effect of jet velocity, particle size, particulate concentration, fluid viscosity and time on maximum erosion depth and volume of material removed. Combining the experimental erosion efforts with the localized particle impact characteristics from the CFD model enabled the previously developed Huang et al. cutting erosion model to be extended to new parameter and application ranges. The model was validated by performing CFD erosion simulations that matched with the experimental test cases in order to compare one-dimensional erosion rates. An impact dampening coefficient was additionally proposed to account for slight deviations between the CFD erosion predictions and experimental erosion rates. The product of this research will ultimately enable high fidelity erosion predictions specifically in mission-critical military, commercial and aerospace applications.

A PARTICLE EROSION MODEL OF MONOCRYSTALLINE SILICON FOR HIGH HEAT FLUX MICROCHANNEL HEAT EXCHANGERS

By

David William Squiller

Dissertation submitted to the Faculty of the Graduate School of the
University of Maryland, College Park, in partial fulfillment
of the requirements for the degree of
Doctor of Philosophy
2017

Advisory Committee:
Professor Patrick McCluskey, Chair
Professor Michael Ohadi
Professor Aris Christou
Professor Bao Yang
Professor Isabel Lloyd

Table of Contents

List of Figures

List of Tables

1 INTRODUCTION

As package-level heat generation pushes past 1 kW/cm^3 in various military, aerospace and commercial applications, new thermal management technologies are needed to maximize efficiency and to permit advanced power electronic devices to operate closer to their inherent electrical limits [1]. In order to continue the trend of optimizing the size, weight and performance of advanced electronic systems, new technologies must emerge which tackle the thermal management bottleneck imposed on current power electronic packages.

1.1 Fundamentals of Power Electronics and Thermal Management

Despite aggressive cooling strategies such as integrating state-of-the-art materials and complex junction-to-ambient thermal paths, the limitations imposed by conventional "remote cooling" strategies impede significant progress to be made in the realm of high powered electronic cooling [2]. In one fashion or another, conventional power electronic modules and components rely on thermal conduction and heat spreading to transfer generated heat to locations away from the source. This creates a remote cooling scheme where the cooling action takes place somewhat removed from the source. The inherent limitation to this type of cooling method lies in the junction-to-ambient thermal resistance which restricts heat from being adequately removed. There exist a number of ways to reduce this thermal resistance such as using higher conducting materials, more efficient thermal pastes, optimizing heat sink design, and to decrease the overall distance the heat must travel before it can

be removed. A schematic of a typical power electronic package is shown in Figure 1-1.

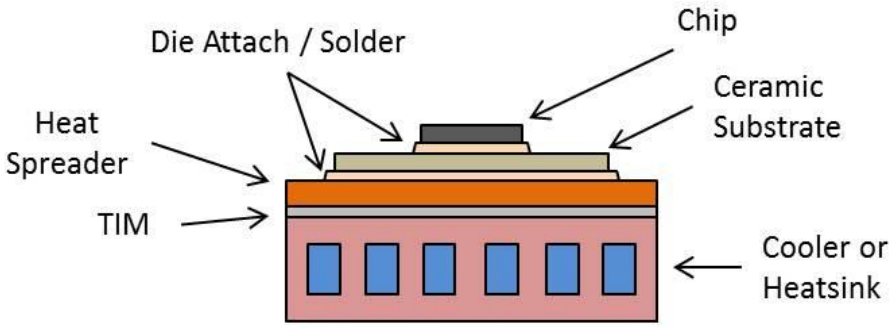

Figure 1-1 Schematic of power electronic package

As heat is generated from the chip, it conducts away from the source through the metallized ceramic substrate. Typically Aluminum Nitride is chosen for high power density applications due to its high thermal conductivity and CTE close to that of Si or SiC which reduces thermomechanical stresses. The substrate is attached to a heat spreader which consists of a thermally conductive material such as Cu, Cu-W, Mo-Cu and various alloys of such materials [3]. Exotic new materials such as silver-diamond and copper-diamond composites have been developed to significantly improve thermal management and can replace conventional heat spreader materials [4]. In most packages the heat spreader will be attached to the heat sink or cooler using a thermal interface material (TIM) such as conductive greases or films [5]. While the schematic above references a liquid-cooled power electronic package, the heat sink can also be air cooled as one would see in a personal computer. In an effort to minimize junction-to-ambient thermal resistance by reducing the number of material interfaces, the heat spreader can often times be integrated into the cooler by fabricating the cooler out of similar thermally conductive materials. In addition,

eliminating the substrate is made possible by directly attaching the chip to the cooler [6] [7]. This can only be done however if the CTE mismatch between the bonded materials is small enough such that cracking and attach failure will not occur.

1.1.1 High Temperature Considerations

The primary concern arising from insufficient cooling is reliability [8]. Increased heat fluxes can adversely affect device performance and lead to a number of degradation mechanisms at both the chip and package level including passivation cracking, electromigration, chip or substrate cracking, wirebond lift-off and die attach failure [9]. The temperature limit for most silicon chips is around 150-175°C [8]. Above these temperatures the increased leakage current across the p-n junction typically renders the device inoperable resulting in permanent failure. In the past 20 years wide bandgap (WBG) semiconductor devices such as Silicon Carbide (SiC) and Gallium Nitride (GaN) have enabled increased power densities and heat fluxes by allowing devices to operate reliably at temperatures significantly greater than 150°C. For example, a SiC transistor was shown to reliably operate at 500°C for 6000 hours [10] and a SiC based electronics and ceramic package was shown to operate at 300°C for 1000 hours for a geothermal wellbore monitoring application [11]. Aside from being able to operate at higher temperatures than silicon, additional benefits of WBGs are as follows [12]:

- Lower on-state resistances yielding lower conduction losses. Overall this leads to increased efficiency for systems containing WBG semiconductors.

- Higher breakdown voltages due to their higher dielectric breakdown field. SiC diodes are commercially available with breakdown voltages upwards of 10 kV [13].
- Increased thermal conductivity enabling heat to be more efficiently transported away from the source.
- Lower switching losses enable WBG devices to operate at frequencies much greater than that of Si (> 20 kHz).

Table 1-1 Material properties for a variety of WBG Semiconductors [12]

	Si	GaAs	6H-SiC	4H-SiC	GaN	Diamond
Bandgap (eV)	1.12	1.43	3.03	3.26	3.45	5.45
Dielectric constant	11.9	13.1	9.66	10.1	9	5.5
Electric breakdown field (kV/cm)	300	400	2500	2200	2000	10000
Electron mobility (cm^2/V-s)	1500	8500	500	1000	1250	2200
Hole mobility (cm^2/V-s)	600	400	101	115	850	850
Thermal conductivity (W/m-K)	150	46	490	490	130	2200

1.1.2 GaN High Electron-Mobility Transistors

While SiC devices are typically used for high voltage power conversion applications due to their substantial electric breakdown field and low conduction losses, GaN devices are most often used in applications involving radio frequency (RF) transmission or very high switching speeds. High electron mobility transistors (HEMTs) are best suited for applications requiring high gain and low noise at high frequencies used in microwave satellite communications, radar, imaging, remote sensing and radio astronomy. MOSFETs and other Field Effect Transistors (FETs) operate based on the principle of doping the semiconductor to create alternating n-type and p-type regions, shown in Figure 1-2. If a positive voltage is applied to the gate, a positive electrical field is built up which attracts electrons in the p-type layer and repels holes. These electrons form an n-channel which carries electrons from source to drain. Raising the potential on the gate increases the electric field allowing a larger current to flow throw the p-type region.

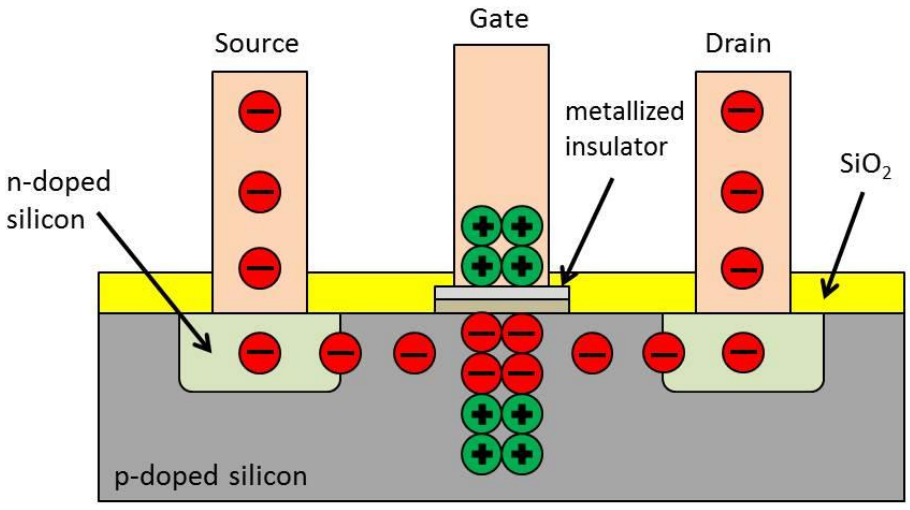

Figure 1-2 Field effect transistor with positive voltage applied to gate

HEMT operation relies on a completely different mechanism based on the concept of a heterojunction which forms when two different materials, such as AlGaN/GaN, with different bandgaps are interfaced. Similar to FET operation, electrons move from the source to the drain when a bias is applied to the gate. However, the electrons traverse the structure at the interface between the two materials in a thin electron film known as the 2-Dimensional Electron Gas (2DEG). As a result of the electrons moving through un-doped crystalline materials, they move freely without collision and have significantly higher mobility compared to those in FETs. This is a primary reason why HEMTs are suitable for applications involving extremely high switching speeds. A schematic of an AlGaN/GaN HEMT is shown in Figure 1-3.

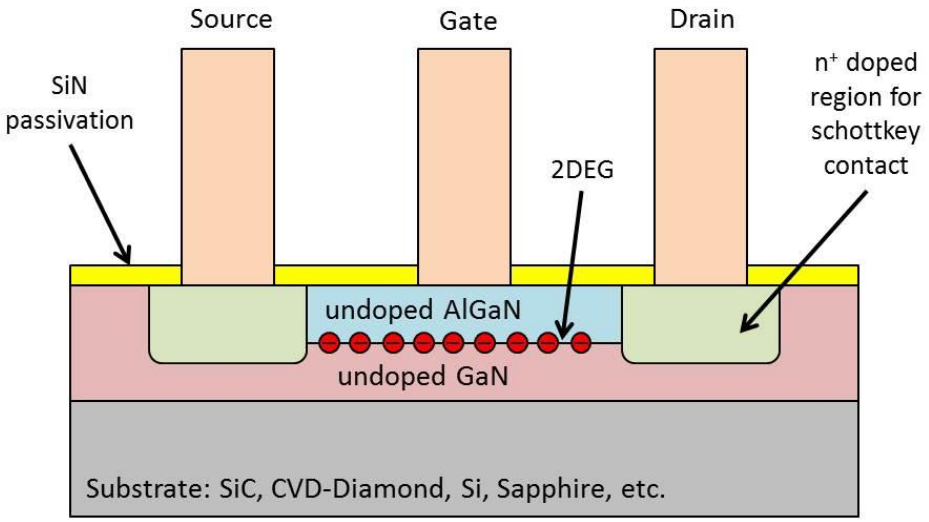

Figure 1-3 AlGaN/GaN HEMT structure

Compared to SiC, GaN has a significantly lower thermal conductivity which imposes challenges for the thermal management of these devices. However, the development of SiC and Diamond substrates from which the GaN is grown or transferred to has permitted further advancement for this technology [14]. Although

Diamond and SiC substrates enable heat to be removed from the source efficiently, their high-price and fabrication complexities may yield them unsuitable for large scale commercial applications. While these substrates have very niche applications fitting for defense and military electronics [6] [14] [15], GaN-on-Si technology has been shown to be low-cost solution for increasing the flexibility of GaN power devices [16].

1.2 The Embedded Cooling Paradigm Shift

In an effort to align with the size, weight and performance optimization of high temperature and high powered electronics, cooling channels embedded directly into the backside of the substrate significantly reduce the junction-to-ambient thermal resistance by reducing the number of thermal interfaces and overall distance the heat must travel. Compared to other "remote cooling" type approaches, embedded cooling can enable chips to operate at higher power levels while maintaining the same junction temperature. Over 30 years ago, Tuckerman and Pease [17] etched 300 micron deep channels into the backside of a silicon wafer and demonstrated a cooling capacity of 790 W/cm^2. Although this pioneering effort demonstrated a novel technique for electronic cooling, fabrication efforts posed many challenges and pressure drops were very high. With the development of Deep Reactive Ion Etching (DRIE) fabrication became simplified and facilitated further research in the area of Si microchannel design [18].

1.2.1 Manifolded Microchannel Heat Exchangers

Pressure drop and overall cooling power improved drastically through the development of manifolded microchannel coolers [19] [20] [21]. Additionally, properly designed manifolds enable greater temperature uniformity across the chip which in turn enhances mechanical reliability by lowering the risk of cracking caused by in-plane temperature gradients [20]. One implementation of a manifolded microchannel cooler consists of a series of inlet and outlet manifold channels positioned perpendicularly to microchannels etched into the backside of a substrate [22]. A diagram of this is shown in Figure 1-4.

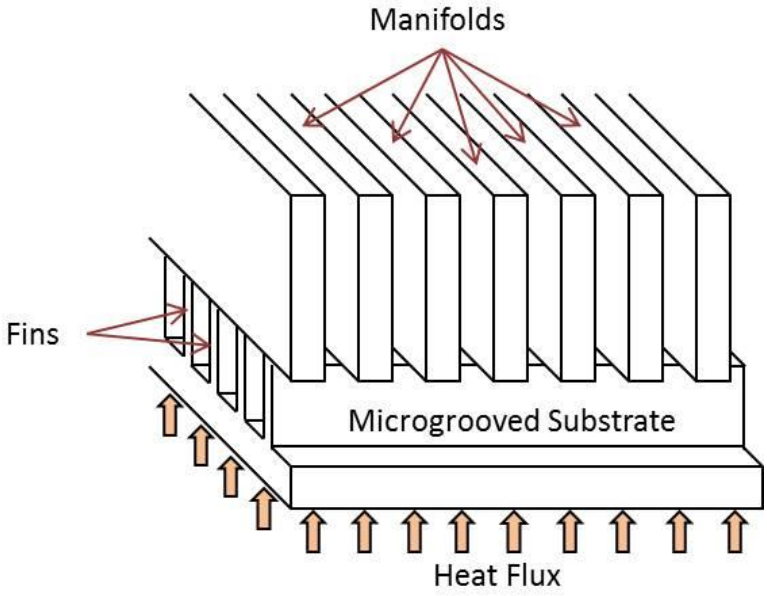

Figure 1-4 Force Fed Microchannel Heat Exchanger, as described in [22]

This type of system splits the flow up into two stages, in which fluid enters and exits through the larger channels of the manifold and is forced into the smaller channels of the microgrooved substrate. Shown in Figure 1-5, cooler fluid enters in

alternating manifold channels and subsequently exits in the same fashion at a higher temperature.

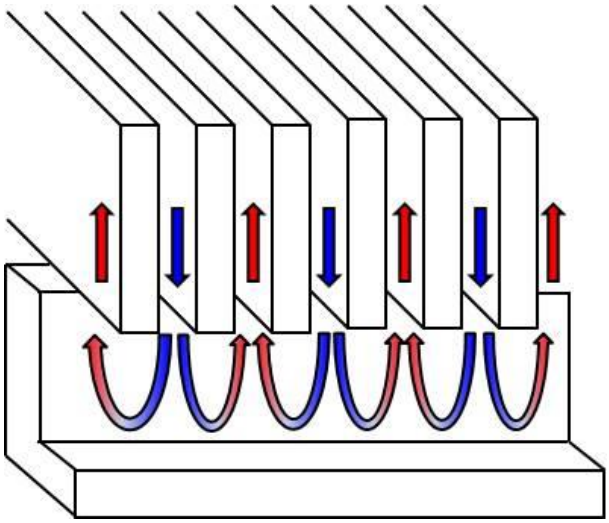

Figure 1-5 Operation of manifolded microchannel cooler

1.2.2 Pin-fin Array

Aside from etching microchannels into the backside of a chip or substrate, micropins or blunt fins can also be selectively etched to enhance heat transfer by increasing surface area. This type of approach was demonstrated to successfully cool power densities greater than 300 W/cm^2 and is suggested to be able to cool chips with power densities greater than 400 W/cm^2 [23]. A variety of shapes can be used for the fins, including circular [24] and hydrofoil [25] shapes, however the general premise of this design is to maximize the area over which heat transfer can occur.

1.2.3 Jet-Impingement Cooling

Another implementation of embedded cooling considers microfluidic impingement jets that directly cool the backside of a substrate [26] [27] [28]. One advantage to this type of design over the manifold or pin-fin designs is that it requires

minimum modifications to the substrate, if any at all. While the manifold design requires channels to be etched into the backside of the substrate, jet impingement cooling would not. The primary issue with etching the backside of the substrate lies in the fact that it must be done very carefully as to not disrupt the electrical design of the device or introduce crystalline defects that may propagate up to the active layer.

With jet impingement cooling however, the major reliability challenge lies in the potential for erosion. For a jet impingement configuration with velocities greater than 5 m/s, particle erosion must be considered [29]. While there exists numerous particle erosion studies in literature for a wide variety of materials (discussed thoroughly in Chapter 2), seldom are the velocities, particle sizes, materials and testing times in alignment with those that may be present in embedded cooling systems. While jet-impingement cooling offers a feasible technique for embedded cooling, it would be very difficult to predict with any level of certainty whether or not a specific jet-impingement configuration would induce catastrophic erosion damage.

1.3 Reliability Concerns of Embedded Cooling Systems

Reliability can be defined as "the ability of a product or system to perform as intended (i.e., without failure and within specified performance limits) for a specified time in its life cycle conditions" [30] . In any system there may be specific processes at work – mechanical, thermal, electrical or chemical in nature - which cause the system performance to degrade or catastrophically fail in time. In an effort to design a reliable product, it is imperative to understand the potential threats which may compromise normal operation. This approach, wherein the designer considers the

physics of the specific degradation or failure mechanisms at play, is referred to as a "physics-of-failure" methodology [31].

The primary function of an embedded cooling system is to maintain the chip or device temperature below a certain critical temperature, above which the electrical performance will suffer. As such, the degradation mechanisms of the cooling system pertain to the processes that hinder or reduce the ability to dissipate heat from the chip. Any process that occurs throughout the lifetime of the cooler that alters the geometry or internal features, which were precisely chosen by system designers to dissipate a definitive amount of heat, can be characterized as the fundamental degradation mechanisms. The three most prominent and likely to occur in embedded cooling systems are particle erosion, corrosion and clogging.

1.3.1 Particle Erosion

Particle erosion occurs when a particle entrained in the fluid stream impinges on a surface resulting in wear and the subsequent removal of material. In the pin fin or microchannel type implementations of embedded cooling, erosion may result in the alteration of pin or channel geometries lending to a change in the heat dissipation ability. Additionally, in the jet impingement scenario where the backside of the chip is cooled by high-velocity fluid jets, the substrate material may erode away leading to direct contact between the fluid and the active electronics on the topside of the die. As the concentration of particles build up in the fluid stream, this mechanism may intensify in a snowball-like effect as more and more particle impingements occur. Although filters are typically required for these types of systems, they can be quite

bulky especially if a small pressure drop across the system is critical. Furthermore, micrometer and sub-micrometer sized particles may still get through the filter.

1.3.2 Corrosion and Dissolution

The chemical process known as corrosion occurs when the working fluid interacts unfavorably with the cooler material. Corrosion often refers to the build-up of an oxide or thin film layer at the interface between the fluid and the surface. Depending on the material, this can lead to poor thermal transport by increasing the junction-to-ambient thermal resistance for two reasons: the additional thermal interface between the oxide and the bulk material and the typically lower thermal conductivity of the oxide compared to the bulk material (i.e. silicon has a thermal conductivity of 156 W/m-K at room temperature [32] while silicon dioxide has a thermal conductivity of around 1.4 W/m-K [33]).

A similar chemical interaction that may occur between fluid and surface is dissolution. This process refers to the uniform wear across all fluid-surface interfaces where the substrate material reacts with the fluid and dissolves. Although single crystal silicon is relatively inert, a thorough reliability analysis should still consider this mechanism as corrosion or dissolution rates on the order of 1 micron per year would be drastic over the 10 or 20 year life cycle of the device.

1.3.3 Erosion-Corrosion

While particle erosion and corrosion are independent mechanisms the combined effect, known simply as erosion-corrosion, can impose a synergistic effect

on the wear-rate depending on the materials [34] [35] [36]. This process is shown in Figure 1-6.

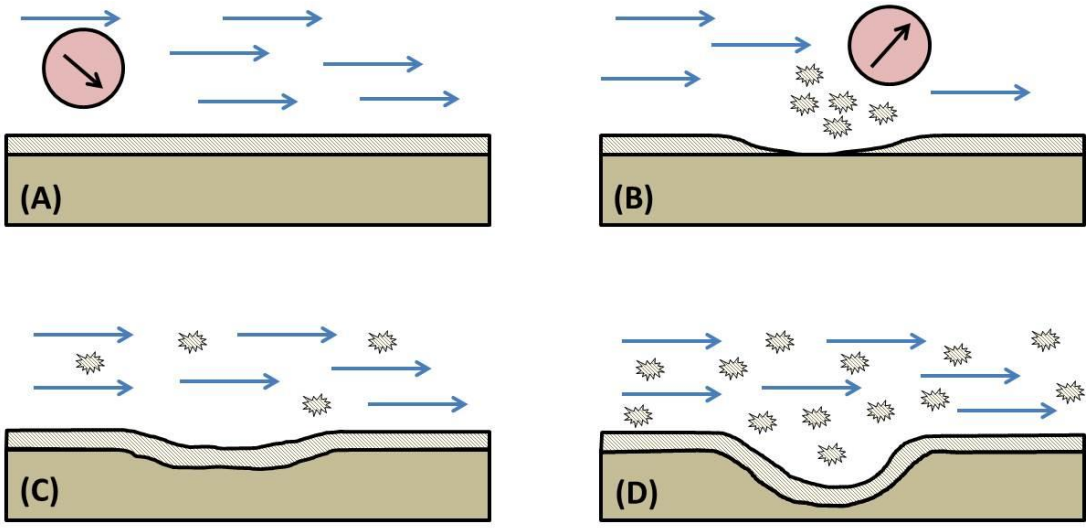

Figure 1-6 Diagram showing erosion-corrosion phenomenon

First, an oxide is formed due to the chemical interaction between the working fluid and the substrate material (A). Next, a particle entrained in the fluid stream impinges on the oxide layer removing small fragments of material into the coolant loop (B). As fresh substrate is exposed, corrosion continues by transforming this unprotected region into another oxide layer (C). This process perpetuates as more and more oxide particles become entrained in the fluid stream (D). It should also be noted that the erosion-corrosion process is highly material and chemically dependent. In some instances the oxide layer may in fact protect the substrate material from impinging particles while in other instances the oxide layer may be more susceptible to erosion than the pure substrate

1.3.4 Clogging and Fouling

The continuous deposition and subsequent build-up of particles on a clean surface is referred to as fouling and can eventually lead to a complete blockage of the fluid cross-section. Channels or fluid paths can be clogged entirely, where no fluid can enter, or they can be partially clogged which results in a significant increase in pressure. With respect to heat transfer, fouling can increase the junction-to-ambient thermal resistance in a similar fashion as corrosion would; the fouled layer both introduces an additional thermal boundary resistance and may be of a lower thermal conductivity than the bulk substrate. Furthermore, fully or partially clogged channels can decrease the cooling uniformity of the chip which may permit certain regions of the active layer to exceed the maximum allowable chip temperature. The four basic mechanism of particulate clogging and fouling are depicted in Figure 1-7, where each of these processes are a result of various particle-particle, particle-particle fluid, and particle-surface interactions [37].

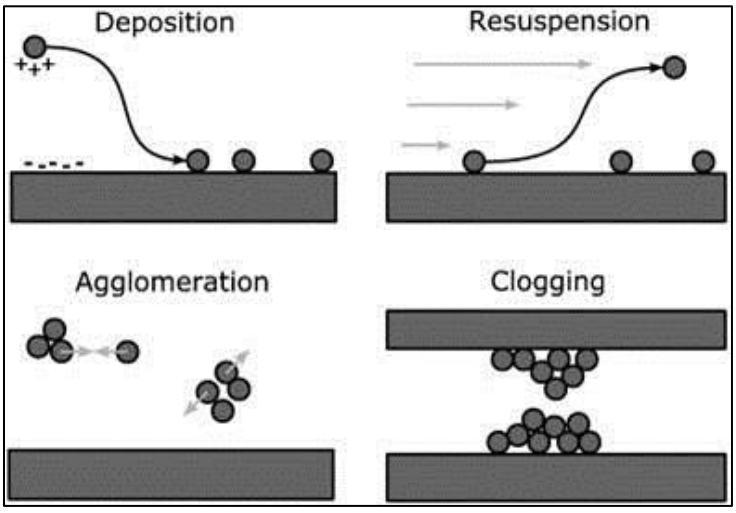

Figure 1-7 Four main mechanisms of clogging/fouling. Image taken from [37]

1.4 Dissertation Outline

This dissertation is divided into eight essential chapters. The present chapter introduces the reader to the concept of embedded cooling and discusses the potential degradation mechanisms associated with failure. Chapter 2 surveys much of the related particle erosion research and methodologies. Topics discussed pertain to particle erosion of brittle materials, two theories surrounding brittle erosion, slurry erosion and related modeling, and the concept of the brittle-to-ductile transition. Based on the gaps in literature and need for further research, Chapter 3 explicitly outlines the problem statement, scope of work and discrete objectives of this dissertation.

Chapter 4 describes the computational fluid dynamics (CFD) simulations performed which investigate how various slurry erosion parameters such as nominal jet velocity, particle size and fluid viscosity affect particle impact characteristics. Through running a series of simulations that correlate directly to the experimental efforts discussed in Chapter 6, the impact parameters extracted will facilitate the calibration of a particle erosion model within a new set of operating parameters.

Chapter 5 describes the design and construction of a slurry erosion test apparatus. Aspects pertaining to pump calibration, materials, creation of the testing slurry, cleaning procedures and sample holder fabrication will be discussed. Additionally, limitations surrounding the test setup will also be disclosed.

The primary experimental efforts are described in Chapter 6, which outline the 14 slurry erosion experiments. A stylus profilometer was used to capture the two-dimension erosion contours which were then processed in MATLAB to approximate

the total volume of material removed. To perform this task and algorithm was developed which uses a numerical volume of revolutions type approach to approximate the total volume of material removed. Furthermore, this chapter presents the results of these experiments in two principle erosion metrics: a mass loss rate in units of milligrams-per-year and a one-dimensional erosion rate in units of micrometers-per-year.

Chapter 7 discusses the development and calibration of a particle erosion model based on the slurry erosion experiments and CFD simulation efforts. First, the data from the previous chapter is converted to the conventional erosion ratio metric, in units of milligrams-per-milligram, and represents the mass of material removed per mass of impacting particles. In the simplifying case of a single particle of known mass, this ratio defines the amount of mass removed per single impacting particle. Both the calibration process and the results of the validation testing are described. Furthermore, an impact dampening factor is proposed and validated. This factor serves as a possible explanation as to why CFD erosion simulations tend to over-predict experimental results. While there are numerous findings of this research, one of the major products of this dissertation is the calibrated and validation erosion model.

A concluding section, Chapter 8, will summarize the efforts and findings described throughout each chapter of this work. Technical and academic contributions will be explicitly listed. Lastly, potential areas of future work will be described based on the work performed in this study,

2 LITERATURE REVIEW

This chapter will introduce the fundamental concepts pertaining to particle erosion and wear of brittle materials. A number of studies will be reviewed along with associated models. In addition, a series of related topics will be discussed to thoroughly describe the mechanisms associated with the degradation of such materials.

2.1 Early Erosion Studies of Sheldon and Finnie

Materials can typically be classified as either ductile or brittle. While this is an oversimplification as materials can exhibit both ductile and brittle behaviors under different conditions, these terms will be used to describe the nominal behavior under most conditions. With respect to material removal, nominally ductile materials undergo large plastic strains which precede fracture and the subsequent ejection of material. Nominally brittle materials undergo no plastic deformation and material is removed by the propagation and intersection of cracks surrounding an impact or defect site.

It should additionally be mentioned that many of the particle erosion models presented in this chapter assume a continuum mechanics approach wherein the crystallographic structure of the material is not inherently considered in the model. Rather, the material is treated in a bulk fashion and the models reflect how much mass of material is removed per particle impact. One caveat to this is with regard to the mechanisms taking place, such as in the cases of grains or grain boundaries influencing the type of wear. That being said, the final erosion model reflects the

amount of material removed and typically does not consider grains, grain boundaries, or crystallographic structure in the analytical or empirical formulation.

One of the first efforts to study particle erosion was conducted in 1960 by Finnie [38]. The effects of particle impact velocity and impingement angle were studied by measuring the weight loss of 1020 steel, aluminum and copper samples. It was found that for these materials maximum material removal occurred at impact angles around 20°. This observation can be explained by the cutting action an impacting particle has on the target surface, as depicted in Figure 2-1. It can be seen that plastic deformation is a primary mechanism leading to the eventual loss of material.

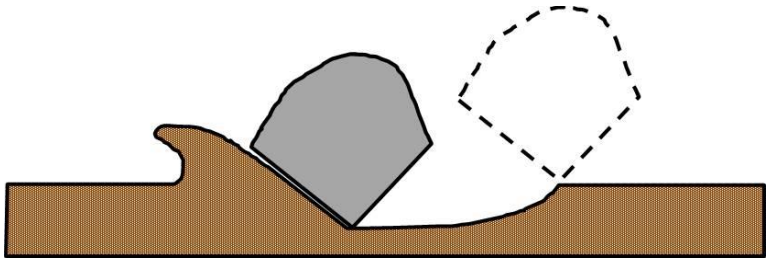

Figure 2-1 Schematic of cutting action from impacting particle on ductile material

It was also found that for ductile materials target weight loss 'W' was proportional to velocity squared, $W \sim V^2$, of the impacting particles. It was predicted that at lower velocities (38 m/s was the minimum velocity tested) particles would tend to produce only elastic stresses upon impact lending to a deviation in the $W \sim V^2$ prediction.

In the same study [38], Finnie attempted to study the erosive nature of brittle materials but found that weight loss measurements conducted in the same fashion as the ductile materials would not suffice. Impacting spherical steel shot against glass resulted in the formation of cone-cracks, shown in Figure 2-2, but no material loss.

As the number of particle impacts increased, the cone shaped cracks began to intersect resulting in eventual material loss. Once a first layer of material was removed it became difficult to observe the formation of individual fracture surfaces. As such, the diameter of the crack-ring was used to assess how velocity and impact angle would affect the propensity for erosion.

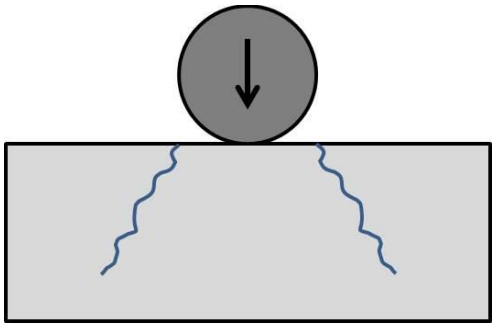

Figure 2-2 Cone-cracks resulting from spherical particle impact on brittle materials

Assuming the glass would remain perfectly elastic until fracture, Hertzian analysis was conducted to show that the magnitude of the maximum radial stress was a function of density, velocity, Poisson's ratio and modulus of elasticity of the impacting sphere as well as the Poisson's ratio and modulus of elasticity of the target surface. This analysis predicted that the diameter of the crack was proportional to $V^{0.4}$ but if it was assumed that the shear stress due to oblique impact was neglected, the diameter of the crack would be proportional to $(V\sin\alpha)^{0.4}$, where α is the impact angle. This suggested that the maximum diameter of the cone-crack is formed when a particle is impacting the target surface at a normal incidence. Figure 2-3a shows the relationship between the size of crack ring formed from 0.58 mm impacting steel shot and the angle of incidence, revealing a close match between experimental results and theory. For a comparison, Figure 2-3b shows the variation of volume removal for

aluminum, copper and 1020 steel (all ductile materials) showing that maximum erosion occurs at an impact angle of around 20°.

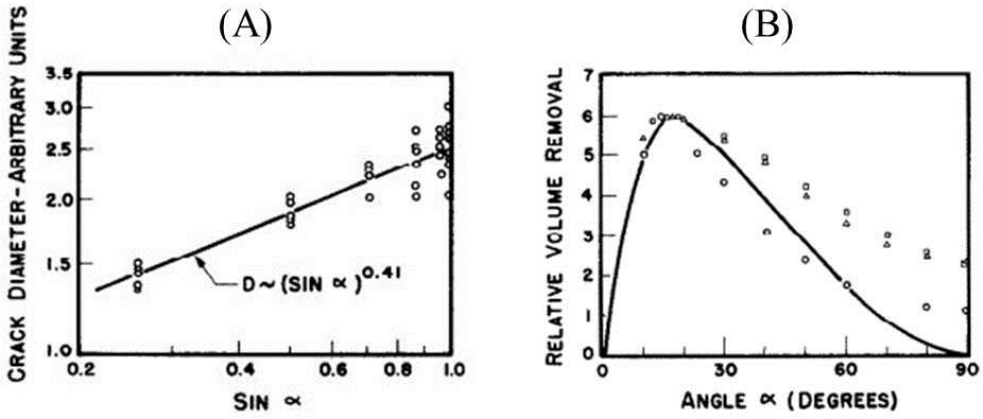

Figure 2-3 Crack diameter vs. angle of incidence for 0.58mm impacting steel shot on glass (A) on left and variation of erosion vs. impact angle for ductile materials (B) on right [38]

Although information surrounding the mechanisms brittle erosion was acquired, the following conclusions were drawn from this initial study: "there is no very simple parameter which combines the effects of velocity and angle in producing material removal." It was also concluded that "if a prediction of erosion is required there appears to be no satisfactory approach except that of testing under the specific conditions of interest."

One of the first successful attempts quantify the erosive nature of brittle materials was conducted in 1966 by Sheldon and Finnie [39]. For a variety of brittle materials including glass, MgO, graphite, hardened steel and Al_2O_3, they showed that the volume of material removed, *W*, by a normal impacting particle could be related by the following:

$$W = kR^{f_1(m_w,s)}V^{f_2(m_w,s)} \tag{2-1}$$

where k is a material constant, R is the particle radius and V is the particle impact velocity. The exponents f_1 and f_2 can be considered the radius and velocity exponents respectively and are functions of the flaw parameter of the Weibull fracture strength distribution, m_w, and the shape of the particle, s, for angular or spherical particles. The particle diameters ranged from 22 – 335 μm for angular SiC and 282 – 940 μm for steel shot, while the velocities ranged from 38 – 183 m/s. Table 2-1 summarizes the experimentally derived radius and velocity exponents obtained for different materials.

Table 2-1 Summary of experimental results showing radius and velocity exponents [39]

Material	Experimental Values			
	Steel Shot		SiC Grit	
	Radius Exponent	Velocity Exponent	Radius Exponent	Velocity Exponent
Glass	5.12	4.37	4.25	3.0
MgO	3.39	2.73	3.95	2.74
Graphite	3.14	2.67	3.78	2.69
Hardened Steel	n/a	n/a	3.58	2.53
Al_2O_3	n/a	n/a	3.86	2.62

Overall the experimental data matched well with their derived model showing that particle size and shape, velocity, and target material parameters could be systematically correlated to a metric of erosion.

In a parallel study, Sheldon and Finnie [40] studied the ductile behavior that nominally brittle materials sometimes exhibit during erosion under specific impact conditions. Using the same testing apparatus and methodology as their previous study [39], the effect of impact angle was investigated in the erosion of glass using 9μm, 21μm and 127μm angular SiC particles. The results can be summarized in Figure 2-4.

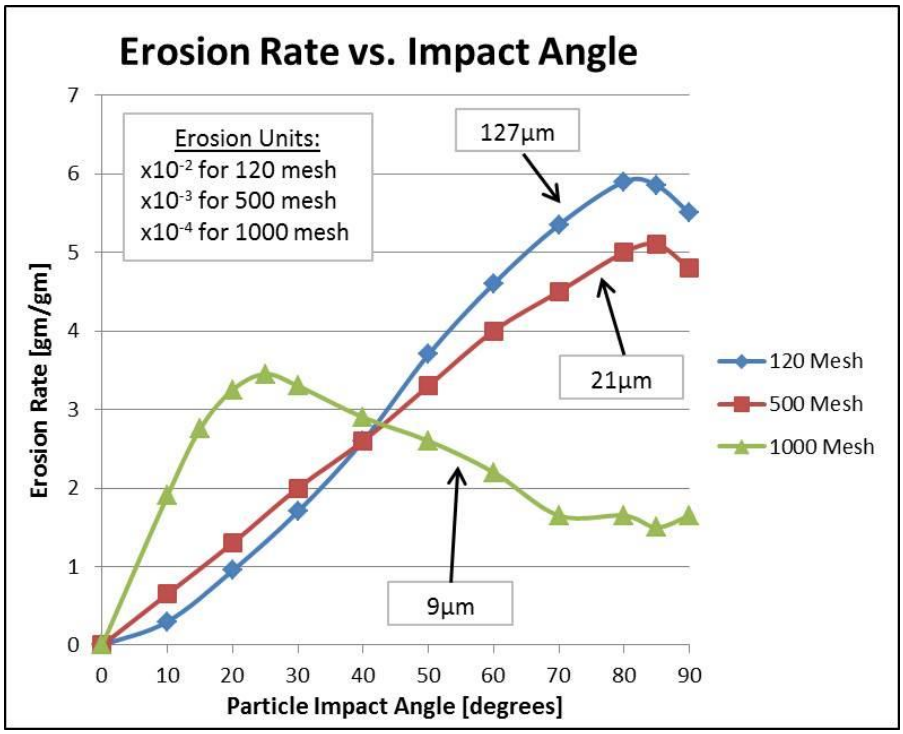

Figure 2-4 Erosion of glass as a function of impact angle by angular SiC particles at 152 m/s [40]

For the larger 127µm particles, the effect of impact angle is characteristic of nominally brittle materials, as shown previously in Figure 2-3a. However, as the particle size decreases to 9µm the graph shifts and reveals material behavior similar to that of nominally ductile materials where the impact angle leading to the greatest erosion is approximately 20°. It was also shown that even at 305 m/s, the glass still produced this characteristic curve. Although glass exhibited this brittle-to-ductile transition at small particle sizes, when high density Alumina was tested it behaved in a nominally brittle fashion.

The occurrence of plastic deformation is suggested to be the primary mechanism justifying these results as previous studies involving micro-indentation, scratching, and abrasion also produced ductile behavior in nominally brittle materials. For example, Klemm and Smekal [41] [42] showed that silicate glass, quartz and

Corundum crystals could be scratched without inducing fracture if the scratch width was very small, on the order of 1μm. It was also shown that plastically displaced material would pile up on the sides of the scratches without inducing any fracture [43].

In another study Hockey [44] examined the room-temperature abrasion and micro-indentation of single crystal and polycrystalline Al_2O_3. Transmission Electron Microscopy (TEM) showed regions of high-density dislocations in the near-surface regions after mechanical polishing with 0.25μm diamond abrasives. It was also shown that plastic deformation by both slip and mechanical twinning mechanisms occurred near the region of a Vickers hardness micro-indenter. It was suggested that the occurrence of plastic deformation was a result of the local stress fields that evolved under irregularly shaped abrasive and small tipped indenters.

2.2 Micro-Indentation Studies of Brittle Materials

The primary conclusion that can be drawn from early erosion work is that under certain small-scale conditions nominally brittle materials can behave in a ductile manner by exhibiting modes of plastic deformation. If the impact area between a particle and target surface is large, for example rounded steel shot impacting a glass plate, the interaction would be completely elastic up until the initiation of fracture at some dominant flaw resulting from a critical loading. This results in the characteristic Hertzian cone-crack shown previously in Figure 2-2.

2.2.1 Crack Propagation of Median/Radial and Lateral Cracks

In the mid 1970's, indentation testing began to centralize as the method through which certain material properties of brittle materials could be characterized [45]. By loading a target material with a spherical, conical or pyramidal indenter the material property of hardness, or a materials resistance to permanent deformation, could be studied. In addition, the following mechanism was substantiated to describe the phenomenon of chipping fracture in brittle materials: Upon *loading* a material with a sharp indenter, plastic flow initiates in the zone immediately surrounding the impact site [46]. This results in a region of irreversible plastic deformation from which median/radial cracks initiate and spread radially outward. The locations of these cracks are often times defined by the indenter geometry, i.e. the corners of a pyramidal indenter, or the preferential cleavage planes of the material. The formation of median/radial cracks is shown in Figure 2-5 and the region of plastic flow is indicated by the dashed lines.

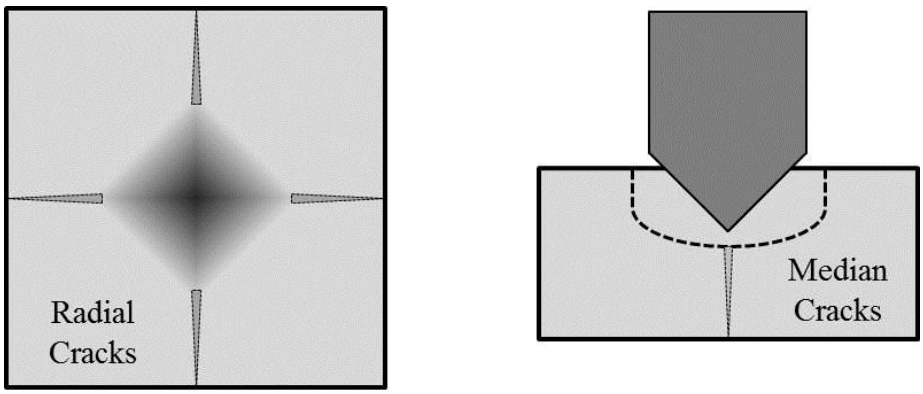

Figure 2-5 Median/Radial crack system upon indenter loading

Upon *unloading* the indenter, the median/radial cracks close and lateral cracks initiate from the bottom of the indentation zone and extend outwards towards the

surface. This phenomenon is depicted in Figure 2-6. Upon reaching the surface, material is removed in a fashion characteristic of brittle chipping.

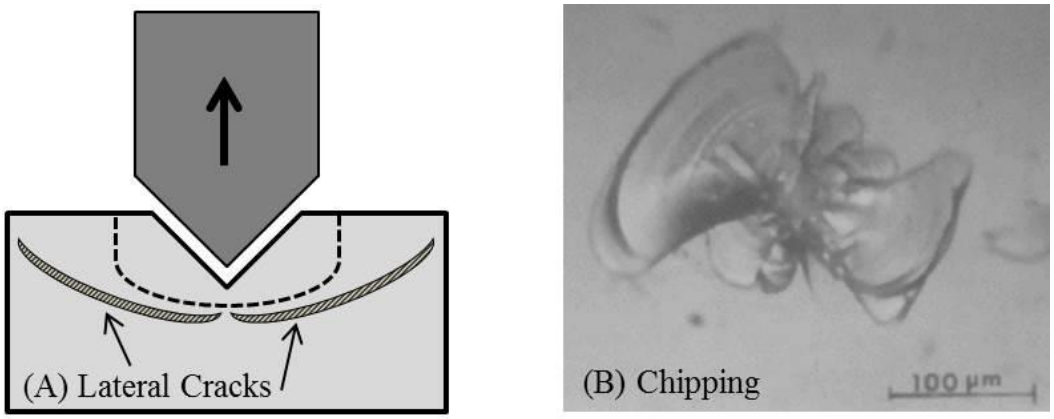

Figure 2-6 Lateral cracks form upon indenter removal (A). Upon reaching the surface chipping occurs (B). Image taken from [47].

Since the lateral crack system initiates upon *unloading*, it becomes clear that the conditions under which these cracks form originate from a residual stress field associated with the irreversible deformation zone [46]. As such, it can be suggested that material hardness, or resistance to plastic deformation, plays an important role in determining the extent of crack propagation.

From this observation a number of studies began to examine the characteristics of these two crack systems surrounding various loading conditions. Hockey and Lawn [48] used TEM to exam geometrical features of the micro-crack patterns formed upon indenting sapphire and carborundum. They found that the crystallographic structure plays a significant role in the crack evolution - that silicon carbide has a greater tendency to cleave along the basal plane while sapphire tends to cleave nearly parallel to the (0001) plane. Although both materials are single crystal, the idea of anisotropic micro-fracture suggests further investigations are necessary.

In studying the damage and fracture modes developed during plastic indentation, Evans and Wilshaw [49] showed that lateral crack extension depend on the radius of the indenter and the hardness-to-fracture toughness ratio of the target material. Extending their observations to abrasive wear by assuming the radius of the plastic deformation region can be related to the force on the particle, they obtained the following relation for the volume removed by *N* abrasive particles:

$$W \propto \frac{1}{K_c^{\frac{3}{4}} H^{\frac{1}{2}}} \sum_{i=1}^{i=N} P_i l_i \tag{2-2}$$

where P_i is the vertical force on a particle, l_i is sliding distance, *Kc* is the fracture toughness and *H* is the hardness.

Assuming that the pressure induced by an impacting particle can be replaced by a functional dependence on particle impact velocity, the volume of material removed was derived in a similar fashion for *N* impacting particles:

$$W \propto \frac{N R^4 G^{\frac{4}{5}} V^{\frac{12}{5}} \rho_p^{\frac{6}{5}}}{K_D^{\frac{3}{2}} H_D^{\frac{1}{2}}} \tag{2-3}$$

where *G* is the shear modulus of the target, ρ_{part} is the particle density, and K_D and H_D are the dynamic fracture toughness and dynamic hardness of the target respectively. It is further noted that this relation is predicted to hold true only for low velocity impacts due to the fact that the force-velocity dependence cannot be described by a single function over the entire velocity range [49]. At higher velocities the force-velocity function cannot be expressed in terms of simple material and projectile properties as these properties cannot be modeled in a static fashion. One example of

this is that the velocity exponent is expected to decrease as the velocity or hardness decreases [49]. This theory would eventually become the foundation for the dynamic particle impact theory [50] discussed in a later section.

Additionally Swain and Lawn [51] studied localized cracking of Westerly granite and silicate glass by indentation of sharp and blunt indenters. By measuring crack length as a function of indenter load, they produced explicit relations which identify the role of basic material properties such as fracture surface energy and hardness to crack propagation.

2.2.2 Threshold Conditions for Crack Initiation

While the discussion to this point has focused on how the median/radial and lateral crack systems evolve and ultimately result in material removal under quasi-static indentation conditions, this subsection will briefly discuss conditions of crack initiation. Lawn and Evans [52] proposed a model which provides a relationship between the size of a critical flaw located directly below the indenter and the load necessary to make the flaw extend into median cracks. The model proposes three distinct regions of stability pertaining to flaw size at a constant load: (1) small flaws which can never fully expand into median cracks, (2) intermediate flaws which expand spontaneously into median cracks and (3) large flaws which describe the initiation of median cracks as a continuous event as opposed to an abrupt event – it is in this region where Griffith-based fracture mechanics takes over. In the context of micro-indentation, this study concluded that materials most resistant to cracking would be those of high fracture toughness, K_c, and low hardness, H.

In another study, Perrott [53] proposed a similar model which assumes that the maximum stress within the plastic zone occurs at the surface of the target material near the indenter corners as opposed to underneath the indenter. As such, this model proposes the initiation of radial cracks at the surface as opposed to median cracks under the indenter.

In an effort to compare both models, Lankford and Davidson [54] used Scanning Electron Microscopy (SEM) and acoustic emission techniques to assess the threshold indentation loads leading to crack initiation for a variety of materials including crystalline NaCl, Si and Ge and polycrystalline Al_2O_3 and SiC. In all the materials studied it was found that the first cracks to form, thus the cracks associated with threshold events, were the radial surface cracks. While Perrott's model was correct with respect to the crack system associated with threshold events, Lawn and Evan's model perfectly predicted the ordering of materials with respect to indenter load and crack size, although the threshold load was more than an order of magnitude in error. By considering the indentation and stress field analysis conducted by Perrott, it was found that an adjustment could be made to the threshold loads in Lawn and Evan's model leading to more accurate predictions.

2.2.3 Unifying Models of Lawn, Evans and Marshall

By combing theories of crack initiation and propagation, Lawn and Marshall [55] proposed the ratio H/K_c as an index of brittleness, where hardness is the resistance to deformation and fracture toughness is the resistance to fracture. Brittleness essentially describes the relative susceptibility to both these mechanisms and provides a convenient explanation for the empirically discovered brittle-to-ductile

transition. In their analysis, a variety of materials were ranked according to their index of brittleness, shown in Table 2-2. The term P^* represents the maximum load a material can sustain without the onset of fracture assuming a material dependent critical flaw size.

Table 2-2 Hardness, Toughness and Brittleness [55]

Material	**Comments**	**H (GPa)**	**Kc (MPa-m$^{1/2}$)**	**H/Kc (μm$^{-1/2}$)**	**P* (N)**
Fe	Medium Strength Steel	5	50	0.1	800000
NaCl	Monocrystalline	0.24	0.4	0.6	30
ZnSe	Vapor Deposited	1.1	0.9	1.2	8
WC	Co-bonded	19	13	1.4	70
ZnS	Vapor Deposited	1.9	1.0	2	2
Si_3N_4	Hot Pressed	16	5	3	2
Al_2O_3	MgO-doped	12	4	3	2
SiC	Hot Pressed	19	4	5	0.6
MgF_2	Hot Pressed	5.8	0.9	6	0.05
MgO	Hot Pressed	9.2	1.2	8	0.04
SiO_2	Glass	6.2	0.7	9	0.02
B_4C	Hot Pressed	77	6	13	0.05
Si	Single Crystal	10	0.6	17	0.002

According to this analysis and based upon specific loads or environments, optimal materials can be selected for a variety of engineering applications. For example, in abrasive environments such as those with high concentrations of small particle where the nominal load P is less than P^*, materials exhibiting high hardness would be most appropriate as the damage mode would primarily be deformation based. Consequently, materials with high fracture toughness would be most appropriate in environments where the load P is greater than P^*, such as those with high energy impacts. In environments where $P \approx P^*$, the metric of brittleness should be minimized in order to prevent crack initiation once deformation takes place. A

prime example of this is the use of ZnSe [55] to promote optical integrity in infrared windows where preventing crack initiation if of great importance. Of course, in the selection of engineering materials care must be taken to choose materials that are also chemically, thermally, electrically and optically suited for the specific application.

Compiling over a decade of research in indentation mechanics, Lawn, Evans and Marshall developed a universal theory for describing the evolution of both the median/radial [56] and lateral crack systems [57]. Regarding the growth of median/radial cracks, their analysis assumes the stress field below the indenter can be resolved into elastic and residual components. The reversible elastic component is largely responsible for the downward growth of median cracks during the loading cycle, and the plastic residual component is largely responsible for the growth of radial cracks during the unloading cycle. They established a model for predicting crack propagation mechanics, specifically relating crack length and the plastically deformed indenter contact area to known material properties such as H, K_c and the elastic modulus E. Assuming the load is sufficient enough to induce cracking, i.e. the radial crack length c^R is larger than the plastically deformed indenter contact length a, the following relation was made using soda-lime glass as a calibration material:

$$\left(\frac{K_c}{Ha^{\frac{1}{2}}}\right)\left(\frac{H}{E}\right)^{\frac{1}{2}} = 0.28\left(\frac{c^R}{a}\right)^{-\frac{3}{2}} \tag{2-4}$$

Figure 2-7 demonstrates its capability in predicting the crack growth characteristics for a variety of materials.

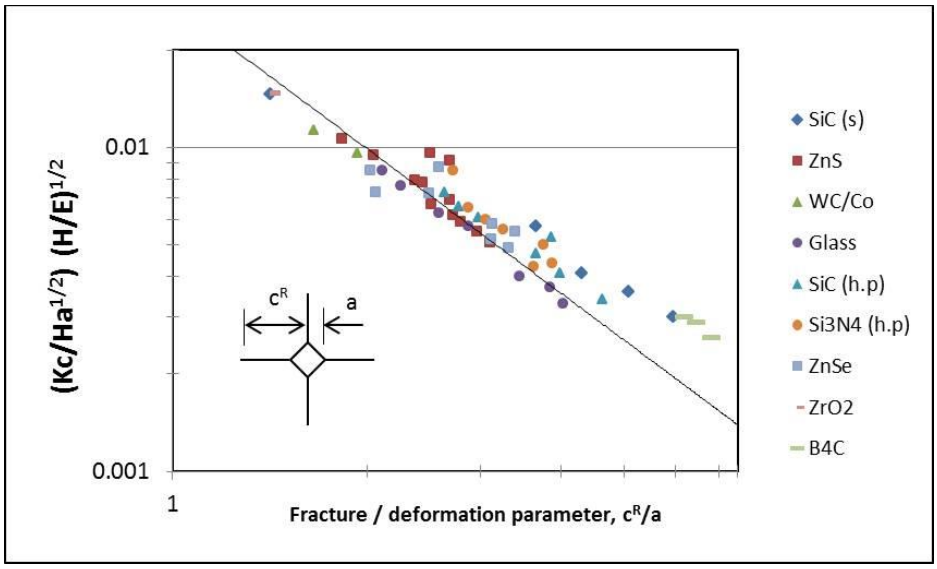

Figure 2-7 Universal plot relating material properties to fracture and deformation parameters in a variety of engineering materials [56]

Concerning the lateral crack system, a similar analysis demonstrated the relation between load and crack parameters to material properties. An interesting consequence of lateral cracking is the role it plays in material removal if the contact pressure is significantly larger than the threshold pressure to induce cracking. It was shown that the volume of material removed could be predicted by [57]:

$$W \propto \left(\frac{\left(\frac{E}{H}\right)^{\frac{5}{4}}}{K_c H^{\frac{1}{6}}} \right) U_k^{\frac{7}{6}} \qquad (2\text{-}5)$$

where U_k is the incident kinetic energy of the particle. In both crack propagation models, specific attention is drawn to the modulus-to-hardness *E/H* ratio which serves as a metric to determine the effects of the elastic and residual components in the stress field. According to the equation above, decreasing this ratio has a direct effect in reducing the volume of material removed due to impacts causing lateral cracking.

Consequently, in ceramics with higher values of *E/H* there is the tendency for material to pile up around the indenter similar to the behavior of ductile materials [56] [58].

2.3 Elastic-Plastic Particle Damage Theories

In parallel with research surrounding crack evolution in brittle materials, two elastic-plastic theories emerged and would become the basis for subsequent erosion modeling. Termed the "Quasi-Static" and "Dynamic Impact" theories, both are based on the concept that lateral crack growth results from residual stresses induced by particle impact events. In short, the volume of material removed can be predicted by the size and depth of the lateral crack formed beneath an impact site.

2.3.1 Quasi-Static Particle Impact Theory

The quasi-static theory originated from studies involving indentation mechanics but was later defined more explicitly by Wiederhorn and Lawn [59]. This theory stems from the idea that particle impact damage can be closely correlated to plastic indentation physics and subsequent fracture associated with indentation experiments. The "quasi-static" model assumes that the kinetic energy of an impacting particle is completely dissipated into plastic flow [59]. While this would represent a condition where no rebound occurs, this assumption serves as an upper bound in predicting the impulse load. Additionally, the "quasi-static" condition assumes that the contact velocity is relatively slow compared to the sonic velocities of the particle or the target materials.

Ruff and Wiederhorn [60] derived an erosion model based on the quasi-static theory by assuming that the radial and lateral crack sizes are proportional to one another and that the maximum penetration depth of the particle is proportional to the depth of the lateral crack. The following relation was formed which describes the factors affecting the volume of material removed for a single impacting particle at normal incidence.

$$W \propto \frac{V^{\frac{22}{9}} R^{\frac{11}{3}} \rho_p^{\frac{11}{9}} H^{\frac{1}{9}}}{K_C^{\frac{4}{3}}} \tag{2-6}$$

The velocity exponent, n = 2.44, compares well with the n = 2.4 value determined by Evans and Wilshaw [49] in Equation 2-3 and that of the n = 2.24 value determined by Marshall, Lawn and Evans [57] in Equation 2-5. Additionally the radius exponent, m = 3.67, compares well with the m = 4 value also determined by Evans and Wilshaw [49]. Lastly, these values compare well with those determined by Sheldon and Finnie [39] denoted in Table 2-1.

Hockey, Wiederhorn and Johnson [61] examined the quasi-static approach by demonstrating the correlation between quasi-static indention and sharp particle impact in both single particle impact tests and multiple particle erosion tests. Figure 2-8 compares the damage caused by an impacting particle and a Vickers diamond pyramidal indenter.

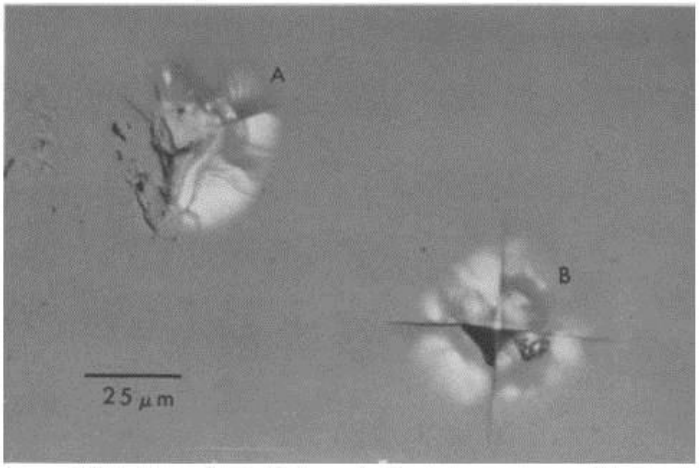

Figure 2-8 Comparison of surface damage in SiC caused by normal impingement of 150um SiC particle at 90 m/s (A) and quasi-static indentation of Vickers diamond pyramid, 400g load (B).

It can be seen that both fracture patterns contain median and radial cracks in association with geometrical indenter/particle features along with lateral cracks resulting in material loss. In an effort to expand the single particle impact model to a multiple particle erosion model, erosion tests of alumina and silicon nitride were conducted to identify the dependence of material removal on temperature, impingement angle and velocity. Tests were conducted on each material from 25ºC to 1000°C, impingement angles from 15° to 90º and velocities from ~ 35 to 125 m/s. SiC particles with a nominal size of 150μm were used.

When tested at normal incidence, the erosion rate was found to be relatively independent to temperature. However a significant effect on temperature was found for oblique incidences, 15º and 30º from the target plane. The velocity exponent showed a strong dependence on temperature, increasing for all materials from 25ºC to 1000ºC. When tested at a 15º impact angle, the velocity exponent increased from 1.7 to 2.7 for hot-pressed silicon nitride, from 2 to 2.6 for hot-pressed alumina and from 2.1 to 2.6 for sintered alumina [61]. Although the velocity exponent was found to

increase with temperature at oblique angles, a consistent relationship could not be established relating this exponent to other experimental variables.

To account for oblique impact angles, Equation 2-6 was modified by assuming that lateral crack extension is only determined by the normal component of the impact velocity [61]. As such, the following relation was proposed:

$$W \propto (V sin\alpha)^n \tag{2-7}$$

The dependence on erosion rate with impingement angle, shown in Figure 2-9, indicates that two modes of material removal are present.

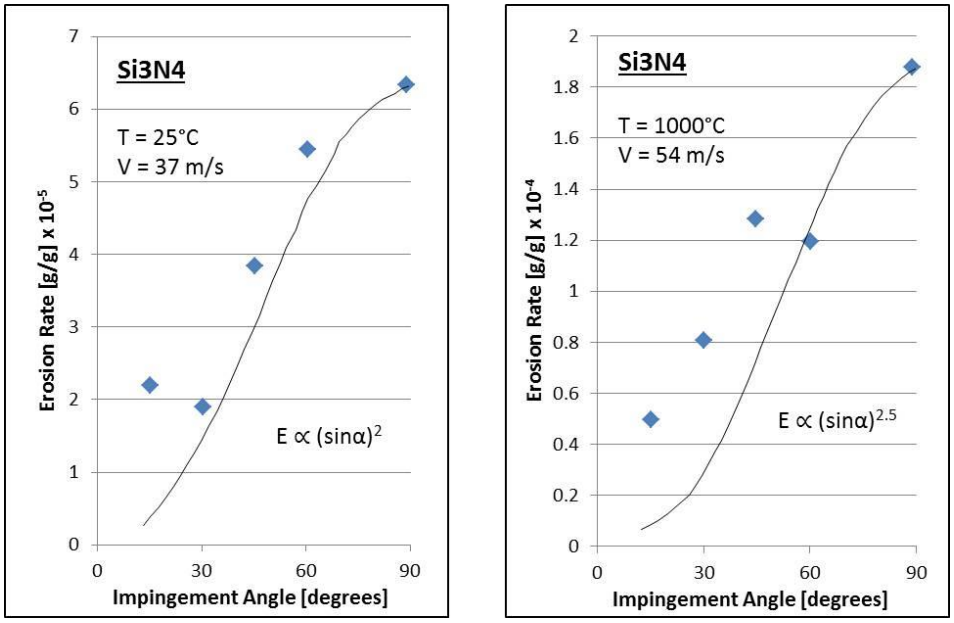

Figure 2-9 Dependence of erosion rate on impingement angle at 25ºC and 1000ºC [[61]

Previous studies, such as those conducted by Sheldon and Finnie [39] [40] and as indicated in Figure 2-3, indicate that maximum erosion occurs at a 90º impingement angle for brittle materials and around a 20º angle for ductile materials. For the room temperature case it can be seen that above an impact angle of approximately 30º the theoretical curve matches the data quite well, while for the

1000ºC case the curve matches the data for impact angle above 60º. These deviations at low impact angles suggest that ductile wear mechanisms become more pronounced [61]. Additionally the more pronounced deviations at 1000ºC suggest that the role of plastic flow in erosion becomes increasingly more important [61].

2.3.2 Dynamic Impact Theory

In parallel with the quasi-static theory, the dynamic impact theory was originally developed by Evans and Wilshaw [50] but more explicitly defined by Evans, Gulden and Rosenblatt [62]. While similar in nature, the fundamental difference between the two theories is their assumed dependence of impact load on the material and kinetic parameters most affecting erosion [63]. While the quasi-static theory assumes that the kinetic energy of an impacting particle completely transforms into work creating plastic flow, and can thus be modeled assuming static material properties, the dynamic theory predicts that substantial changes in material response may occur due to impact. Under impact conditions, the stress fields are expected to be more complex due to the potential introduction of shock waves and elastic and plastic waves that interact with rapidly moving cracks [62].

This idea is based off of earlier work by Tabor [64] who conducted static and dynamic hardness tests on soft metals. He found that the force required to induce plastic flow in metals via indentation is greater the faster the indentation test is performed. Essentially the pressure required to produce plastic deformation in a dynamic manner, such as that involved in a particle impact, would be much greater when compared to the pressure involved in a quasi-static indentation test. The other consideration regarding dynamic indentation as it differs from quasi-static indentation

is that particle rebound is assumed to occur. As such, the contact time between a particle and target surface becomes a critical factor as well.

Based on these principles, Evans, Gulden and Rosenblatt [62] derived a model that relates the volume of material removed by a single particle to various impact and material properties:

$$W \propto \frac{V^{\frac{19}{6}} R^{\frac{11}{3}} \rho_p^{\frac{1}{4}}}{K_c^{\frac{4}{3}} H^{\frac{1}{4}}} \tag{2-8}$$

This model varies slightly from that derived assuming the quasi-static condition, Equation 2-6, in the velocity exponent n = 3.17 vs. n = 2.44 and the relationship to hardness. The quasi-static theory predicts that as the target hardness increases, the erosion rate will increase slightly, however the dynamic impact theory predicts a slight inverse relationship between erosion rate and hardness.

To test their theory a series of erosion experiments were conducted on four ceramic materials by impacting 115μm quartz particles under normal incidence at velocities between 98 – 180 m/s [62]. Figure 2-10 shows the results of the experiments, where the volume of material removed was displayed as a function of the quantity $K^{4/3}H^{1/4}$.

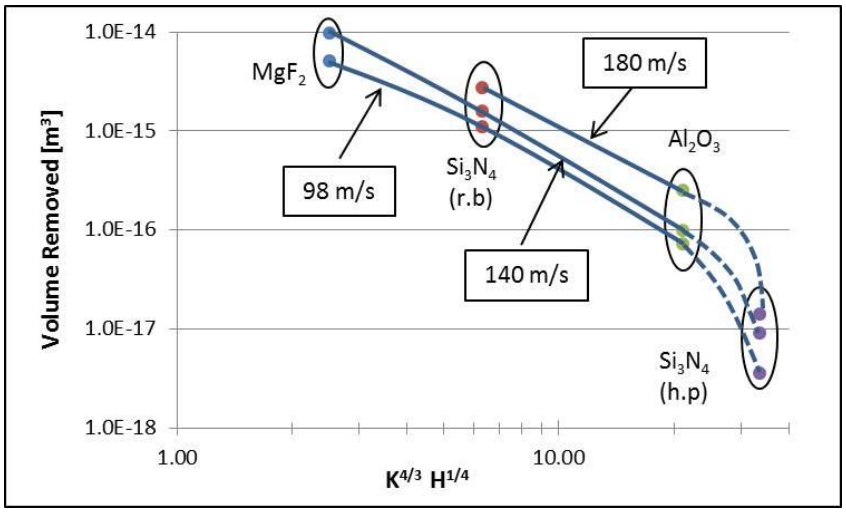

Figure 2-10 Volume of material removed a function of material properties [62]

It is evident that the erosion rates directly correlate with the $K^{4/3}H^{1/4}$ quantity. However, this dependence is non-linear suggesting that the erosion rate may also have a functional dependence on other parameters unaccounted for in this analysis.

2.3.3 Comparison of Quasi-Static vs. Dynamic Impact Theories

In order to assess the validity of both particle impact theories, Wiederhorn and Hockey [63] conducted a systematic investigation to assess the effect of particle velocity, material hardness and fracture toughness on erosion rate. In their experiments they tested nine ceramics from a wide range of material and microstructural properties, at temperatures between 25ºC and 1000ºC and velocities between 37 and 94 m/s. The particles used in this study were 150um SiC abrasives as the hardness of the particles was thought to simulate the non-yielding particle properties in which the two theories were derived from.

Table 2-3 shows the velocity exponents obtained in these experiments over a range of temperatures. The results are similar to those found previously [61] in that the velocity exponent tends to increase with temperature. It can also be seen that the

exponents for the room temperature condition tend to align closer the 2.4 exponent predicted by the quasi-static model than the 3.2 exponent predicted by the dynamic impact theory.

Table 2-3 Velocity exponents at normal incidence for 25ºC, 500ºC and 1000ºC [63]

	25ºC	**500ºC**	**1000ºC**
MgO, polycrystalline	2.2	-	-
Soda-lime – silica glass	2.5 (0.12)	3.5 (0.2)	-
Vitreous silica	2.9	3.0	-
Sapphire	2.3 (0.1)	2.4 (0.25)	3.3 (0.03)
Sintered Al_2O_3, 30μm	2.3 (0.003)	2.8 (0.09)	2.7 (0.15)
Hot-pressed Al_2O_3, 3-4μm	2.3 (0.03)	2.1 (0.04)	2.3 (0.11)
Silicon	2.9 (0.03)	3.8	3.4
Hot-pressed SiC	1.8 (0.16)	-	-
Hot-pressed SiN	2.1 (0.08)	2.5 (0.03)	2.4 (0.20)
*Standard error shown in (parenthesis)			

Figure 2-11 compares erosion data and the material properties H and K_c to the erosion rates predicted by the quasi-static and dynamic theories. This data was taken for and impact velocity of 63 m/s at room temperature.

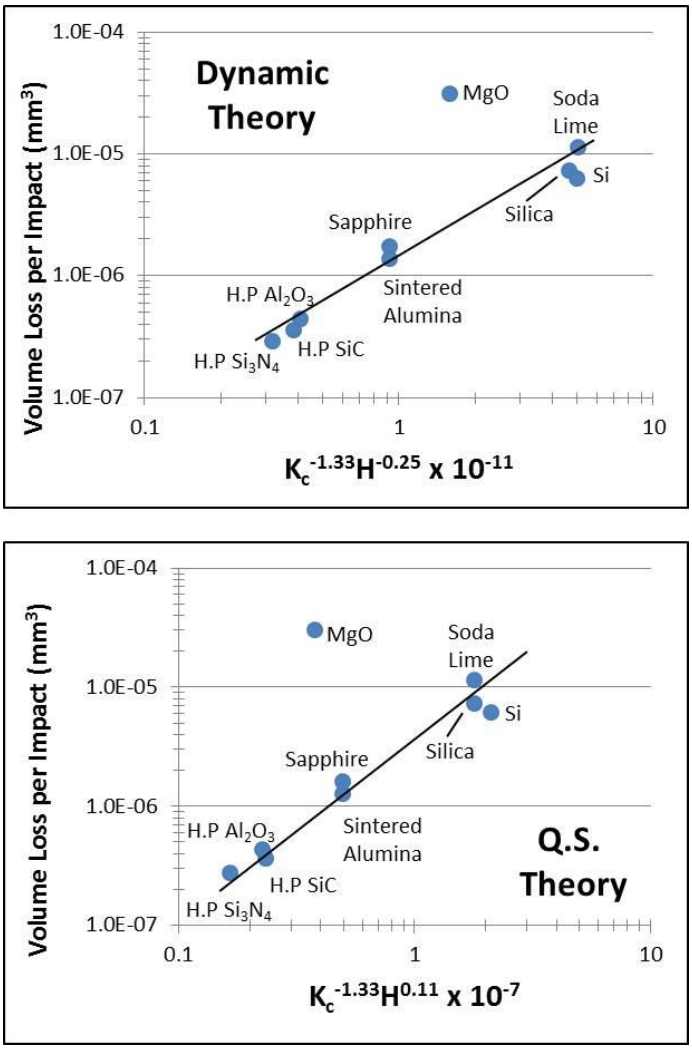

Figure 2-11 Comparison of erosion data with the dynamic (a) and quasi-static (b) theories [63]

Excluding the results for MgO, both theories predicted the effect of K_c and H on the erosion rate. However, the slopes of both lines are greater than one suggesting that the K_c and H exponents may not be the most accurate. Using the results found these experiments the quasi-static and dynamic models were calibrated to form the new relation [63]:

$$W \propto V^{2.8} R^{3.9} \rho_p^{1.4} K_c^{-1.9} H^{0.48} \tag{2-9}$$

The most pronounced difference between this equation and previous erosion models is the dependence on hardness and fracture toughness. One observation from this study was that not every particle impact resulted in material removal. In the case of glass, every particle impact site was seen to result in crack formation. However for the case of sapphire and SiN, many impact sites left plastic impressions while a small percentage of impact sites resulted in fracture. While it is predicted that this percentage has a dependence on K_c, it can also be suggested that the dependence of erosion rate on this property is not accounted for correctly in any of the models.

In Equation 2-9 the erosion rate is predicted to increase as the hardness increases, shown by the positive exponent. The balance of two opposing phenomena, maximum load during impact and maximum penetration depth, ultimately determines whether the hardness exponent is positive or negative. In the formulation for determining impact load, the load resulting from an impact increases as hardness increases. A decreased hardness would result in a decreased impact load due to the occurrence of plastic flow that would absorb some of the impact energy. Since the maximum load is proportional to the amount of chipping, the relation between hardness and erosion rate suggests a positive correlation.

Consequently, hardness also determines the maximum penetration depth. A decreased hardness leads to an increased penetration depth leading to an increase in erosion rate. In the quasi-static approach the maximum penetration depth is assumed critical whereas the dynamic impact theory suggests that the impact load dominates. The results from this study predict a hardness exponent of 0.48 suggesting that the dynamic impact model may be more appropriate under certain circumstance.

While both theories qualitatively predict erosion in a correct fashion, neither theory is quantitatively accurate based on the data collected in this study. Each theory is composed of a number of simplifying assumptions, many of which break down for certain materials under certain conditions. This study ultimately showed that microstructure plays a critical role in accurately modeling erosion – a factor that neither study fully considers.

2.4 Particle Erosion of Brittle Materials

Many prior attempts to assess the accuracy of the quasi-static and dynamic particle impact theories have relied largely on commercial ceramics with a wide variety of microstructural differences.

2.4.1 Single Crystal Silicon

To assess the validity of these two theories using a homogenous single-phase material in the absence of microstructural effects, Routbort, Scattergood and Kay [65] conducted erosion experiments of single crystal silicon with the (111) plane being impacted. The velocities ranged from 32 – 134 m/s, particle sizes from 23 – 270μm and impact angles from 10 - 90º. Angular Al_2O_3 particles were used for all tests. The effect of velocity and impingement angle can be seen in Figure 2-12.

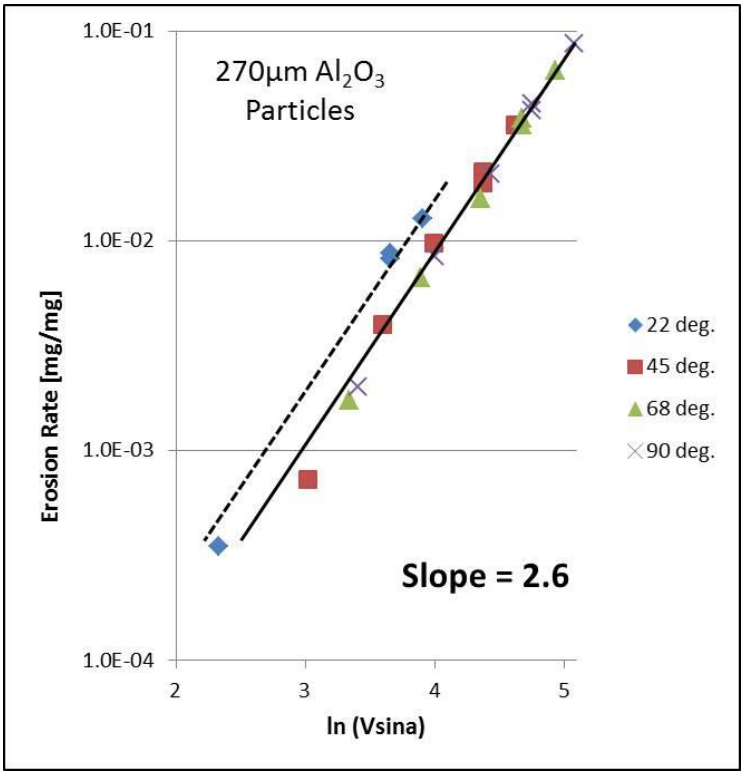

Figure 2-12 Steady state erosion rate as a function of Vsinα [65]

The data is in good agreement with the quasi-static theory, assuming the oblique angle adjustment proposed by Hockey [61], $W \propto (V\sin\alpha)^n$ where n = 2.6 for impingements angle above 45º. However at low impingement angles the model under predicts the erosion rate. This is thought to occur due to the fact that the erosion model only accounts for the normal component of the velocity vector thus neglecting the cutting and scribing processes that tend to occur at low impingement angles.

Additionally, the concepts of threshold particle sizes and velocities are considered. This idea is based off previous work by Routbort, Scattergood and Turner [66] who studied particle erosion of reaction bonded SiC. They discovered that at the smallest particle size, 23µm, the erosion rate became anomalously low indicating either a microstructural effect or a true threshold effect. In the case of Silicon the

same threshold effects were observed and are suggested to follow the following relation D_oV_o = 2200x10^{-6}, where D_o and V_o are the threshold particle diameter and velocity respectively. Considering these effects, they formulated a new model:

$$ER = k(Vsin\alpha - V_o)^{2.6}(D - D_o)^{0.6} \quad (2\text{-}10)$$

where *ER* is the erosion ratio (presented as the mass of material removed to the mass of impacting particles) and *k* is a material constant. The particle size exponent *m* = 0.6 varies significantly from those presented in the quasi-static or dynamic theories, *m* = 11/3 or 3.67 due to the way the erosion metric is presented. In previously studies the erosion metric is given as the volume of material removed, *W* in units of [length]^3, due to a single impacting particle. This study presents the erosion metric as a change in weight-loss per dose of impacting particles ΔW in units of grams/gram. The erosion formulation from previous studies:

$$W\,[length]^3 \propto (R\,[length])^{\frac{11}{3}} \quad (2\text{-}11)$$

can be converted to the erosion metric of the present study by normalizing each side of the above equation by the units [length]^3:

$$\frac{W[length]^3}{[length]^3} \propto \frac{(R\,[length])^{\frac{11}{3}}}{[length]^3} \quad (2\text{-}12)$$

which gives the dimensionless erosion ratio *ER*:

$$ER\,[dimensionless] \propto (R\,[length])^{\frac{2}{3}} \quad (2\text{-}13)$$

In light of this conversion, it can be seen that the particle size exponent *m* = 0.6 determined in this study matches well to the predicted *m* = 2/3 or 0.67 predicted

by both the quasi-static and dynamic impact theories. Figure 2-13 shows that their experimental data matches quite well with their erosion model if threshold effects are considered for impact angles above 45º.

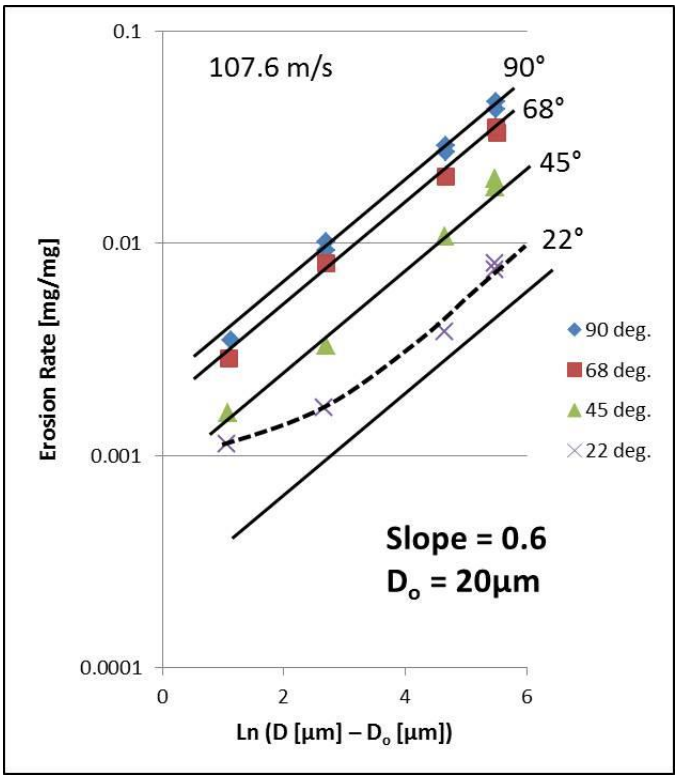

Figure 2-13 Erosion Rate as a function of D - Do for different impact angles [65]

The divergence between the model and experimental data for an impact angle of 22º lies in the fact that the model only considers the effect of the normal component of the velocity vector. This would neglect cutting and other ductile erosion mechanisms that may be present at smaller impact angles.

2.4.1.1 Velocity Exponent as a Function of Particle Size

One observation in previous studies is that the velocity and size exponents are not constant values through the entire range of experiments. This suggests that there may be some hidden dependencies of these values not captured by either the quasi-

static or dynamic theories. Scattergood and Routbort [67] conducted a series of experiments in an attempt to thoroughly investigate the velocity and size exponents on the erosion rate of single crystal silicon. The most pronounced observation they found, shown in Figure 2-14, is that the velocity exponent systematically decreases as the particle size is increased.

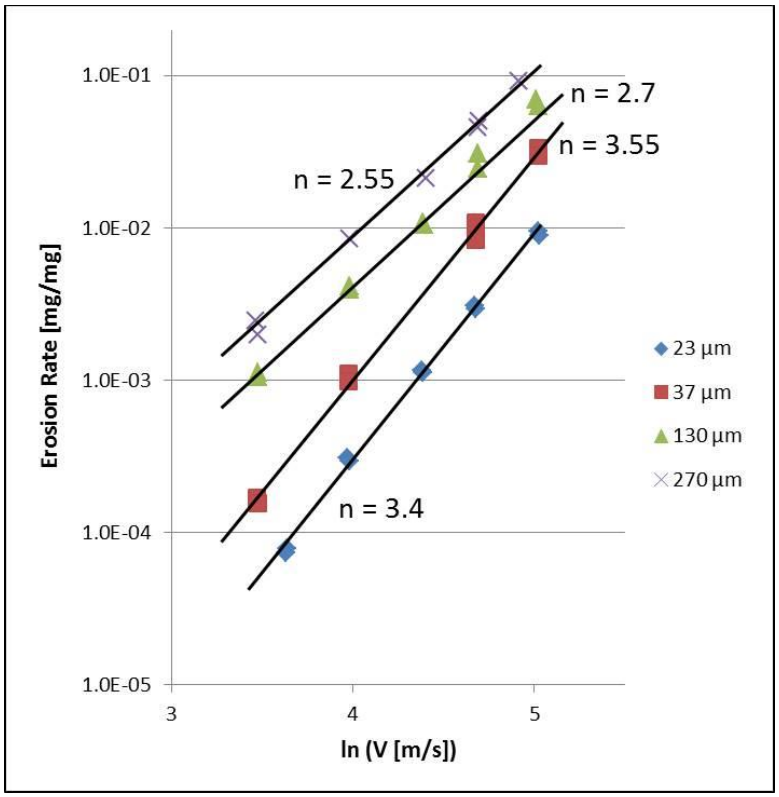

Figure 2-14 Erosion rate as a function of velocity for different particle sizes [67]

The largest particles in the study, 270µm, produced a velocity exponent of n = 2.55 while the smallest particles in the study, 23µm, produced a velocity exponent of n = 3.4. From these results it can be suggested that the larger particles tend to follow more closely to the quasi-static theory, which predicts n = 2.4, whereas the smaller particles tend to follow the dynamic theory, which predicts n = 3.2. This observation

is not just limited to silicon, but has been found previously in erosion studies of reaction-bonded SiC [66] and hot-pressed SiC [68].

Another observation was that the particle size exponent changed as the particle size changed. For particle sizes above 130μm, the erosion rate could be accurately modeled assuming the typical $m = 0.6$ found in previous studies. However for particles below 37μm, the erosion model would better fit the data assuming a size exponent of approximately $m \approx 1.8$. In addition to this observation, the tests conducted at small particle sizes indicated a constant velocity exponent even at low velocities. This invalidates the $D_o V_o = 2200 \text{x} 10^{-6}$ velocity threshold prediction previously made [65].

In a follow-up study Scattergood and Routbort [69] performed similar tests with angular SiC and rounded SiO_2 particles and compared the results to those previously conducted with Al_2O_3 particles [65]. The results of these experiments, shown in Table 2-4, aligned with those found in previous tests; that the velocity exponent is dependent on particle size.

Table 2-4 Velocity exponent as a function of erodent material and size [69]

Erodent Material	Velocity Exponent 40um Particles	Velocity Exponent 270um Particles
Al_2O_3	3.55 ± 0.1	2.55 ± 0.1
SiC	3.18 ± 0.1	2.65 ± 0.09
SiO_2	3.44 ± 0.07	2.48 ± 0.09

While some variation exists between erodent materials, it can be suggested that the particle size effect on the velocity exponent is material and shape independent. One explanation that may account for this is localized heating due to

particle impact [69]. This anomaly was also found by Yust and Crouse [70] who observed via SEM images localized melting in the case of 240μm SiC particles impacting mullite ceramic at 24 m/s with an impact angle of 20º.

In an analysis by Shewmon [71] it was postulated that localized heating of the target surface increases as particle size increases. Larger particles would thus better facilitate the development of a plastically deformed region surrounding the impact site. As the quasi-static theory suggests that the kinetic energy of an impacting particle is converted into work creating plastic flow, this would explain why larger particles tend to follow along the quasi-static theory more closely than smaller particles. Since smaller amounts of localized heating would occur for small particles, the dynamic model would conversely fit better. It was also calculated that the threshold particle sizes above which localized heating becomes important in the erosion of silicon is 46μm for Al_2O_3 particles and 41μm for SiC particles [69].

2.4.2 Sapphire and Zinc Sulphide

Telling and Field [72] studied the degradation of Sapphire (single crystal Al_2O_3) and Zinc Sulphide by weight loss measurements and optical transmission tests. They impinged 25 - 700μm quartz particles at velocities between 25 – 200 m/s. The erosion rate results for zinc sulphide and sapphire are shown in Figure 2-15.

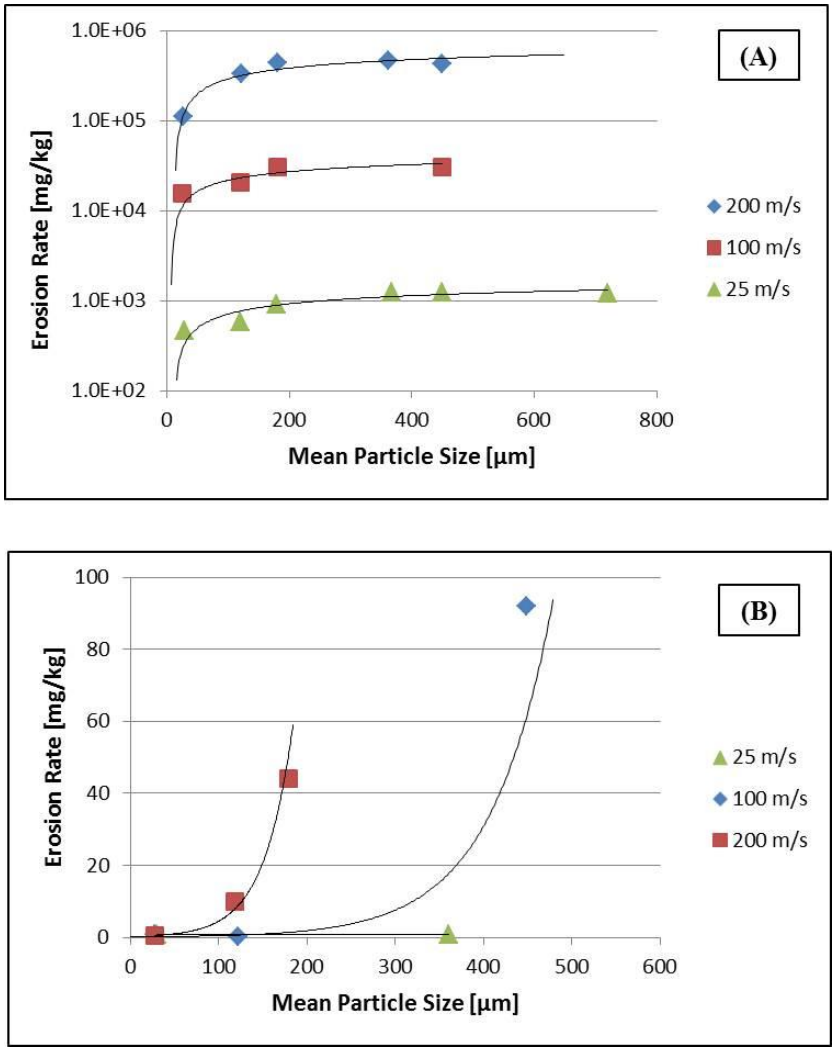

Figure 2-15 Effect of particle size and velocity on the particle erosion of Zinc Sulphide (A) and Sapphire (B), taken from [72]

It can be seen that the erosion rate is relatively independent of particle size for Zinc Sulphide yet largely dependent for sapphire within the parameter ranges studied. The difference in the erosion behavior can be attributed to the presence of threshold particle sizes under which no material loss occurs. The erosion rate curve of sapphire appears to be in a "tail-off" region where the erosion rate significantly increases as the particle size increases. It is expected that if larger particle sizes were tested for sapphire, the curve would level out as it did for the Zinc Sulphide tests.

From these curves it is clear that sapphire is significantly more erosion resistant than zinc sulphide and that the following threshold particle sizes exist:

Table 2-5 Threshold particle sizes for Zinc Sulphide and Sapphire at given impact velocities [72]

	Threshold Particle Size (μm)	
Velocity (m/s)	Zinc Sulphide	Sapphire
25	< 50	> 400
100	< 20	~ 250
200	~ 0	~ 100

Interestingly, optical transmission measurements of the samples subjected to erosive conditions indicate a decrease in optical transmission without any mass loss. This suggests the presence of surface damage without chipping, such as events associated with plastic deformation.

In their analysis, Telling and Field [72] also derived threshold velocity and particle size relations assuming Auerbach's Law [73] which states that the critical load to form a Hertzian cone crack is proportional to the size of the indenter radius. For a given particle radius, and particulate and target material properties, the following relationship exists:

$$V_{threshold} = A^{\frac{5}{6}} \left(\frac{3}{4}k\right)^{\frac{1}{3}} \left(\frac{5}{3}\pi\rho\right)^{-\frac{1}{2}} R^{-\frac{5}{6}} \tag{2-14}$$

where ρ is the particle density and k is a material constant which is a function of the Poisson's ratio, v, and Young's modulus, E, of both the target and particulate:

$$k = \frac{1 - v_{target}^2}{E_{target}} + \frac{1 - v_{particle}^2}{E_{particle}} \tag{2-15}$$

A is Auerbach's constant defined by Mouginot and Maugis [74]:

$$A = 6.7x10^3 k_b \gamma \tag{2-16}$$

where γ is the free surface energy of the target and k_b is also a material constant:

$$k_b = 1 + \frac{(1 - \nu_{target}^2)E_{particle}}{(1 - \nu_{particle}^2)E_{target}} \tag{2-17}$$

This analytical relationship can be applied to the silicon-alumina target-particulate system found in the works of Routbort and Scattergood [65]. Using the experimentally derived threshold relation where D_oV_o = 2200x10^{-9} and assuming the free surface energy of silicon to be 1.24 J/m^2 [75] a comparison can be made between analytical predictions and experimental findings:

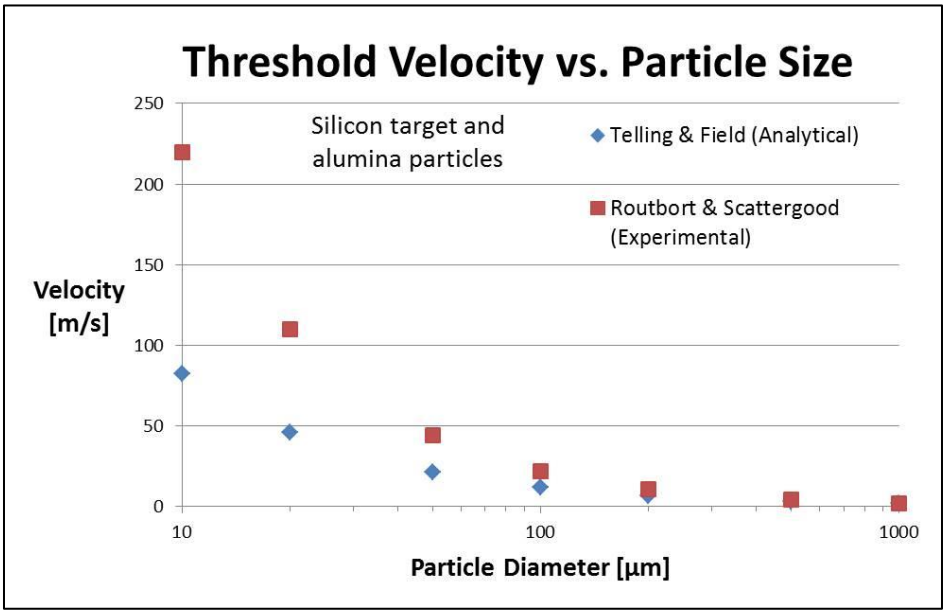

Figure 2-16 Threshold velocity vs. particle size to induce cracking - silicon target and alumina particles

It can be seen in Figure 2-16 that above a particle diameter of approximately 100µm, the experimental and analytical findings match well. However, below 100µm

the two results diverge. This can be primarily attributed to two reasons. First, at particle sizes above 100μm and at the velocities used in the Routbort and Scattergood studies, the mechanism of erosion is primarily fracture, chipping and cracking. However below 100μm, the contribution of ductile erosion mechanisms and plastic deformation take on more prominent roles. The analysis by Telling and Field does not consider the effects of ductile erosion mechanisms. Secondly, the divergence between experimental and analytical threshold conditions can also be attributed to the fact that the analytical model assumes a perfectly uniform particle size whereas the experimental study used alumina particles with some (unspecified) particle size distribution. While the mean particle size may be under the analytical threshold, a percentage of particles may be above it. As such, the experimental threshold particle velocity at a given particle size should be lower than the analytical which assumes uniform particle size.

2.5 Slurry Erosion of Brittle Materials

The discussion up to this point has assumed air to be the medium through which particles travel through. Erosion experiments are typically conducted by "sandblasting" target materials with a known quantity of particulates and measuring the resultant weight loss that occurs. In the case where erodent particles are entrained in a fluid, factors such as impact angle and impact velocity can be significantly skewed due to the strong particle-fluid interactions that occur.

The Stokes number, defined in Equation 2-18, represents how strongly the trajectory of an entrained particle is coupled to the fluid flow in the presence of an obstacle.

$$St = \frac{\rho d^2 U}{18 l_o \mu_f} \tag{2-18}$$

where ρ is the particle density, d is the particle diameter, U is the velocity of the fluid far away from the obstacle, l_o is the characteristic dimension of the obstacle and μ_f is the viscosity of the fluid. Particles with very high stokes numbers >> 1 are highly inertial and respond slow to changes in fluid velocity whereas particles with very low Stokes number << 1 are strongly coupled to the flow conditions [76]. Additionally the presence of chemical or physical interactions between the fluid and wall may exist, requiring a decoupling procedure to separate out which variables contribute to overall material loss.

This section will discuss a number of factors affecting erosion specific to slurry conditions along with implications pertaining to nanofluid erosion and abrasive waterjet machining.

2.5.1 Observations from Slurry Pot Erosion Experiments

In a number of studies Clark, Lynn, Wong and co-workers [77] [78] [79] [80] [81] examined the effects of particle size, velocity and fluid viscosity on the erosion characteristics for ductile and brittle material. In all experiments they used a slurry pot erosion tester which operates by rotating a stainless steel shaft via electric motor through a slurry in a confined vessel. Cylindrical samples are attached to shaft such that the rotational speed of the shaft can be correlated to the nominal velocity the sample move through the fluid. This type of testing apparatus is shown in Figure 2-17 and more details regarding design, construction and modifications can be found elsewhere in literature [82] [83] [84].

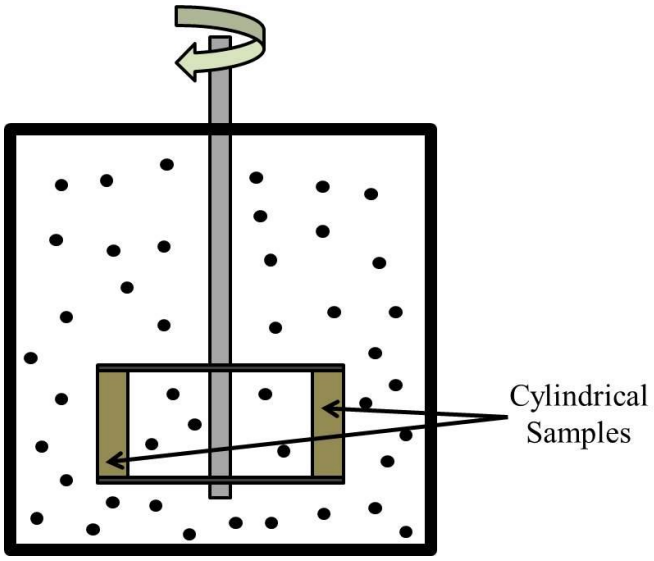

Figure 2-17 Schematic of slurry pot erosion testing apparatus

Clark [77] conducted short-term erosion tests on polished copper samples with dilute suspensions of water/glycerin and glass beads ranging in sizes from 75 - 750μm. Two nominal speeds were used in the tests, 9.35 and 18.7 m/s. A collision efficiency metric was determined by counting the number of impact sites per square millimeter and dividing this by the number of particles estimated to be in the volume of a 1 mm^2 swept zone assuming a homogenous slurry. An average impact velocity was also determined by measuring the crater diameter formed during impact and comparing it to microhardness indentation tests. In this manner it was assumed that all kinetic energy was transferred into work creating plastic flow in the copper samples.

It was discovered that fluid viscosity, particle size and nominal flow velocity directly influence the collision efficiency and actual impact velocity. Figure 2-18 shows the results of the 18.7 m/s tests.

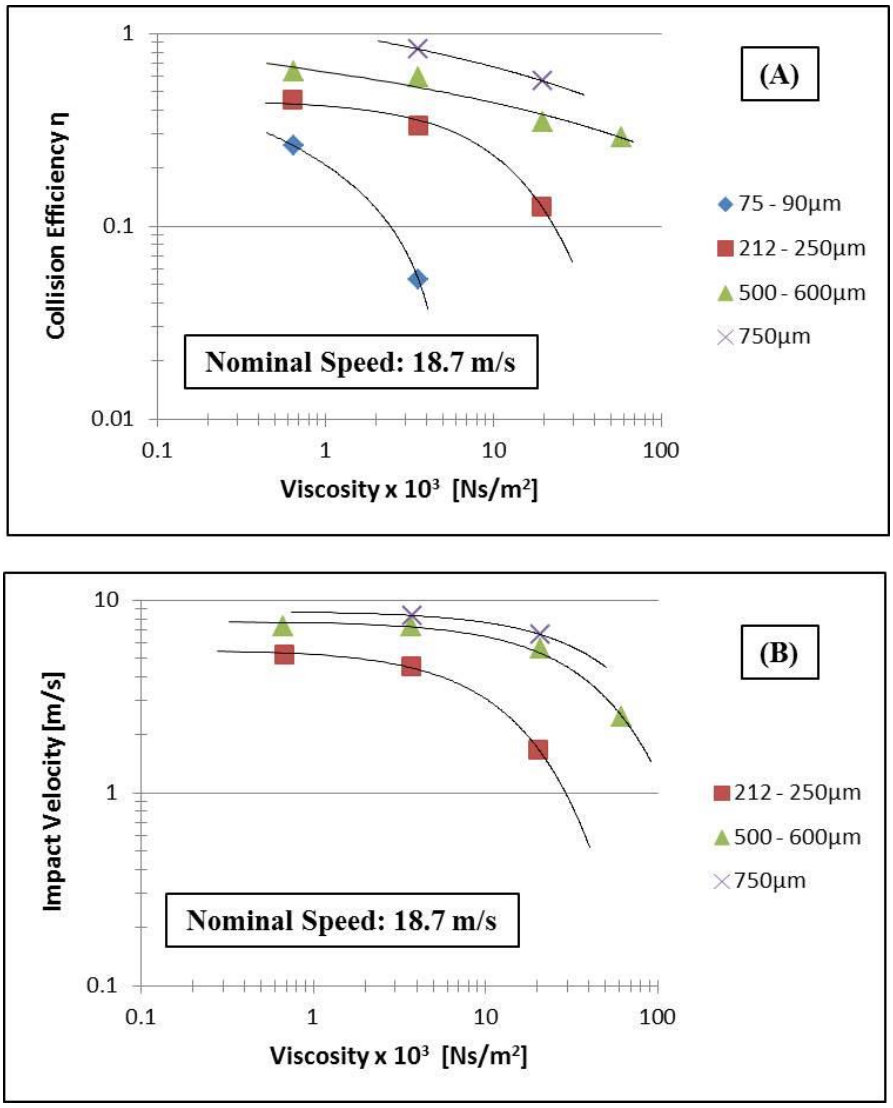

Figure 2-18 Collision efficiency (A) and impact velocity (B) as a function of particle size and fluid viscosity [77]

Referring to Equation 2-9, it can be seen that increasing the particle size and decreasing the fluid viscosity result in a higher particle Stokes number meaning they are less responsive to changes in the flow field. As the sample is swept through the slurry, more particles would tend to impact the specimen as their motion is less affected by the displaced fluid. The decrease in impact velocity with increasing fluid viscosity and decreasing particle size is suggested to be a function of a boundary layer

effect. In order for a particle to impact the surface it must penetrate a boundary layer of slow moving fluid and as the particle travels through this layer a significant deceleration is suggested to occur.

Using the same type of slurry pot erosion testing apparatus Lathabai and Pender [85] investigated the effects of varying the particle size distribution and particle concentration on the erosion of a variety of ceramics. One observation they found was that increasing the particle concentration from 5% to 20% a significant increase in material loss was measured. However increasing the particle loading from 20% to 30% resulted in much less of an increase and even a decrease in material loss for certain materials. This implies that at higher particle concentrations particle-particle interactions become more prevalent and in some cases may inhibit particles from striking the target surface.

Upon SEM inspection of the surface it was found that microstructure played a critical role in the erosion mechanism. Inspection of fine and course grained alumina samples both indicated that the wear mechanism was primarily grain ejection and grain boundary microfracture. In the case of the Si_3N_4-SiC composite, preferential phase erosion was observed causing the grains of the SiC phase to protrude as the Si_3N_4 phase was removed. 3Y-TZP showed the least amount of erosion. Inspection of the surface morphology indicated the presence of significant plastic deformation wear scars but no signs of lateral fracture. The biggest conclusion from this study was that microstructure plays a critical role in the erosion mechanisms of ceramics.

2.5.1.1 Particle Size Effect

Lynn, Wong and Clark [86] investigated the particle size effect in slurry erosion by conducting erosion experiments on P110 steel using 20 – 500μm SiC particles in oil. They found the same qualitative results regarding collision efficiency and impact velocity however their experimental and calculated erosion rates diverged at small particle sizes, shown in Figure 2-19. They defined their erosion model assuming it to be proportional to the particle impact energy, collision efficiency and the relative number of particles in the path of the specimen in units of area per unit time.

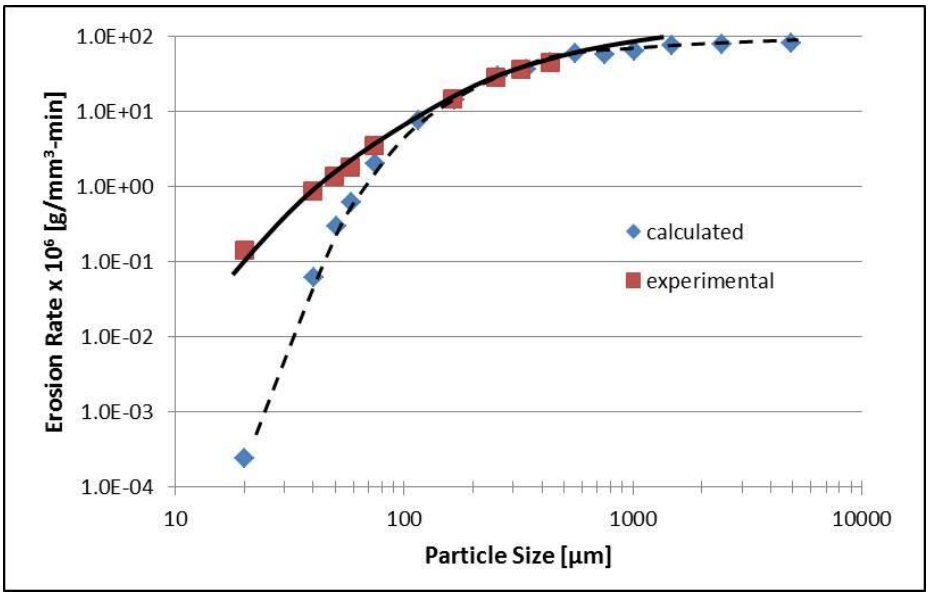

Figure 2-19 Erosion rate as a function of particle size [86]

It can be seen that their model aligns well with erosion data for particles above 100μm. However smaller particles tend to produce higher than expected erosion rates. The discrepancy between experimental and calculated erosion rates is thought to originate from the fact that their model assumes particle impact to be the only mechanism involved in material removal. This finding suggests that direct particle

impact may take on a smaller role and other material removal mechanisms may become prominent.

In a later study Clark and Hartwich [81] re-examined the particle size effect by conducting experiments on Pyrex glass and Aluminum using 14 - 780μm SiC particles in oil. For Pyrex glass, the peak wear rate for particle sizes between 390 - 780μm was found to be proportional to D^4, as was suggested by the quasi-static and dynamic theories. No measurable damage was observed for particle sizes under 196μm however damage was observed for particle sizes between 196 - 275μm. Under the experimental conditions used in this study, specifically a nominal velocity of 18.7 m/s, they estimated the threshold particle size under which no damage should occur was between 300 - 425μm. The reason damage was observed in the 196 - 275μm was thought to be a function of the particle size distribution in each batch of particles. In each batch of erodent, there exists a spread of particle sizes with the mean particle size presented as the nominal size. Although the mean particle size in each batch was below the theoretically determined thresholds, the portion of particles above this threshold is thought to cause the observed damage.

For the aluminum samples erosion was found at all particle sizes even though direct impact was expected to cease for small particles. It is suggested the primary wear mechanism taking place at these small particle sizes was a byproduct of the boundary layer directly above the surface of the sample. This layer is referred to as the "squeeze film" and is thought to inhibit direct particle impact but also prevents particles from rebounding back into bulk fluid flow. As such, small particles are thought to accumulate in this fluid layer and are swept away by tangential flow –

rolling, bouncing, and scratching along the surface as the go. The resulting wear mechanism arising from this condition can best be described as wet-abrasion.

A later study by Gandi and Borse [87] was conducted to determine the effect of a distribution of particle sizes and the effect of small particles in nominally larger particulate slurry. They found that when the absolute particle size range is within approximately 40% of the mean particle size, such as in the scenario of filtering the particle through low and high pass sieves, the mean particle size can be used to represent the nominal particle size. However when a large spread of particle sizes is present in the slurry, a more appropriate metric would be the weighted mass particle size. They also found that the addition of fine particles <75μm reduced the amount of erosive wear. Similar to the previous work by Clark et al. [81], it was suggested that the presence of small particles slightly increases fluid viscosity, increases particle-particle collisions and decreases the impact velocity of larger particles due the formation of a thin layer of small particles trapped in the squeeze film.

2.5.1.2 Influence of the Squeeze Film

Clark and Burmesiter [80] analytically derived solutions that describe the fluid motion in the squeeze film between an impacting particle and a wall. They found the ratio between the impact velocity V_i and the normal velocity determined by potential flow analysis V_N to be a function of the particle Reynolds number described below in Equation 2-19.

$$Re_p = \frac{D_p V_N \rho_l}{\mu_l} \tag{2-19}$$

where ρ_l is the liquid density and μ is the liquid viscosity. Through this analysis they determined a critical Reynolds number, Re_c, below which impact would cease to exist. The relationship describing this critical particle Reynolds number is described in Equation 2-20.

$$Re_c\left(\frac{\rho_p}{\rho_l}+\frac{1}{2}\right)=80 \tag{2-20}$$

Another finding was that the squeeze film should also retard the particle's velocity on the rebound as well as the approach. For example, if the rebound is considered elastic the particle Reynolds number upon entering the squeeze film must be twice that of the critical Reynolds number in order escape the squeeze film [80]. In the case of a ductile material with a coefficient of restitution of 0.1, the particle Reynolds number upon entering the squeeze film must be 10x that of the critical Reynolds number in order to exit the squeeze film.

This analysis suggests that particles may tend to congregate near the surface forming an abrasive bed. Not only would this alter the experimental particle concentration of the slurry, as the squeeze film would contain a denser particle count, but the abrasive bed may act as a shield for incoming particles [79]. This may introduce an additional factor reducing the collision efficiency.

2.5.2 Jet Impingement Studies of Ceramics

Fang et al. [88] studied the erosion behavior of four ceramics using a slurry jet impingement apparatus. The particulate used was 600 - 850μm silica sand in concentrations between 3 – 7.5% by weight. The nominal impingement velocity was set at 7.3 m/s and the impingement angle was varied from 15 - 90º. Of all the

materials tested Al_2O_3 was found to be most susceptible to erosion, even more than aluminum metal which was also tested. PSZ had the lowest erosion rate, about 100 times less than that of Al_2O_3. For all materials tested, the erosion rate was found to be constant with time.

For Sialon and PSZ the effect on particle concentration was negligible, however for SiC an increased particle concentration led to an increased erosion rate. For Al_2O3 the opposite was found where an increased particle concentration led to a decreased erosion rate. Additionally the effect on impact angle was not uniform for all materials. Al_2O3 showed a typical brittle response peaking in erosion rate around 90º while SiC showed a larger than expected jump between erosion at 60º and 90º. For Sialon and PSZ the erosion rate was relatively unaffected by impact angles between 30º and 90º suggesting that these materials undergo different wear mechanism. The fundamental justification for the wide range of erosion observation originates from the microstructural differences. Similar to the results found by Lathabai and Pender [85], the significantly high erosion rates of alumina compared to the other tested materials was due to the mechanism of grain ejection and grain dislodgement. While other materials showed signs of both brittle and ductile material removal mechanisms, it was thought that grain ejection would disrupt the development of plastic flow.

In an effort to examine more closely the effects of microstructure on erosion, Zhang et al. [89] conducted air and slurry jet impingement experiments on three types of alumina ceramics. Slightly rounded 200 - 600μm garnet particles were used as abrasives. At low impact angles, material removal was characterized by ploughing

and subsequent spalling while at normal incidence grain ejection was the primary mechanism of wear. In the case of airborne tests, localized melting of the target and splashing of the garnet was observed generated by adiabatic heating caused by impact. This localized heating phenomenon was not observed in slurry tests.

Regarding microstructure, lower velocity exponents were found for the samples that contained a higher presence of intergranular glass phase. The glass phase is thought to enable a higher absorption of impact energy. This belief was based on a prior test that showed alumina with a 4% wt. intergranular phase exhibited an increase in erosion resistance at increased temperatures [90]. It has also been suggested that the presence of an intergranular glass phase can reduce stresses at the grain boundaries, accommodate the non-uniform deformation behavior and reduce residual stress at the grain boundaries [89] [91]. Comparing two samples of different grain sizes but the same weight percentage of alumina, it was found that the samples with larger grain sizes were more susceptible to erosion. This originates from the fact that the main wear mechanism is grain boundary fracture resulting in grain ejection.

Lastly it was found that when the slurry and dry erosion data were extrapolated to similar conditions, the slurry erosion was shown to be much more severe. It is suggested that the fluid plays a critical role in crack propagation, thus facilitating the erosion process.

2.5.3 Abrasive Slurry Jet Machining

Abrasive Slurry Jet Machining (ASJM) is used specifically to etch channels and holes in brittle materials where other conventional machining methods may not be appropriate. Machining occurs by impinging a high velocity slurry jet onto a

substrate that is either stationary, in the case of micro-hole formation, or is moving in the case of channel formation. Typically the abrasive particles are small, on the order to tens of micrometers or less, and the impinging jet is often less than a millimeter in diameter. As such, the erosion modeling and characteristics involved in this process have similar characteristics to those that would be involved in embedded cooling systems.

2.5.3.1 Mechanisms of Microhole and Microchannel Formation

Wang et al. [92] studied the mechanisms of microhole formation in soda-lime glass using a 200μm jet, alumina particle sizes between 10 – 17μm with concentration of 2.5% and 5% by mass at nominal jet pressures of 1, 2 and 3 MPa. These pressures approximately translate to nominal fluid velocities of 44, 63 and 77 m/s respectively. Scanning the cross-sectional profiles using a stylus profilometer it was found that the holes were characterized by a "W" shape, shown in Figure 2-20, where the outer diameter of the etched region is nearly four times the diameter of the nozzle.

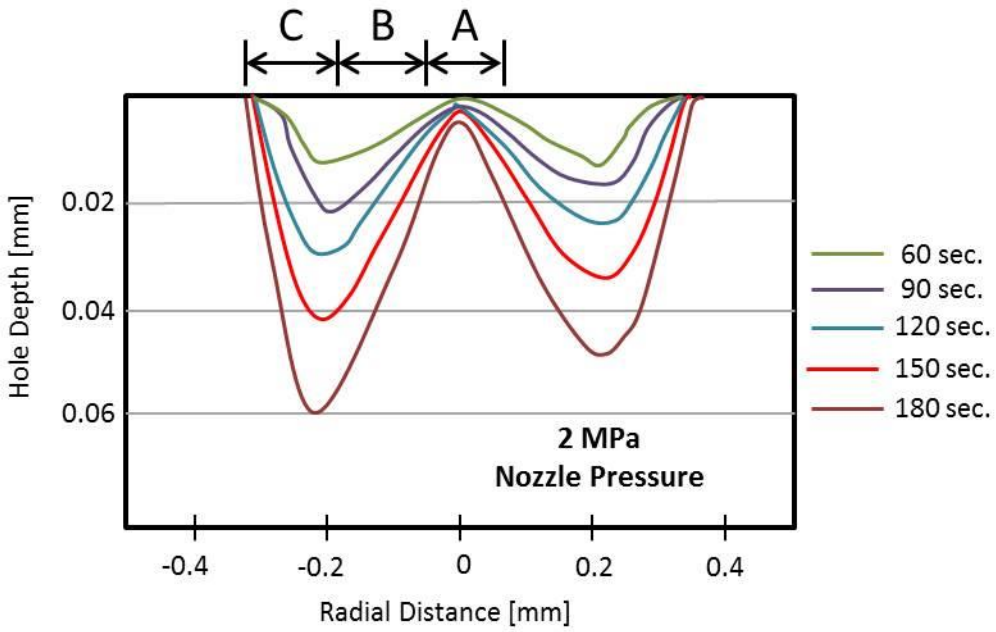

Figure 2-20 Microhole profile, 13um particles, 2.5% concentration [92]

The morphology of the microhole can be divided into three primary regions: the jet impact zone (A), the viscous flow erosion zone (B) and the turbulent flow erosion zone (C). The jet impact zone is located directly under the nozzle and, according to Figure 2-20 little erosion occurs in the region. This is due to the stronger coupling between the particles and fluid preventing direct impact from occurring directly below the impinging jet. As a result the particles are swept to the side and impinge the surface at shallower angles. If the jet pressures are high enough however, the particles directly impinge on the surface below the jet causing erosion in this region [93] [94].

Depending on the impact angle, the primary mechanisms of material removal may be brittle in nature, such as in the case of direct normal impacts, or ductile as in the case of shallow impacts causing a cutting acting. The erosive wear in the viscous flow region was found, through surface examination, smoother than that of the jet-

impact or turbulent regions. It is suggested that this is a result of the squeeze film that forms on the surface acting to lubricate and reduce friction between the particles and surface. The surface characteristics indicate that the mode of material removal is primarily ductile in the viscous flow region.

The turbulent zone forms as the erosion depth increases and causes a sudden change in fluid direction. This region is suggested to be the cause of the substantially large hole-width due to particles continuously recirculating thus increasing the number of impacts. Interestingly, it was also found that that as the test parameters changed, i.e. increasing particle size velocity or particle concentration, the overall width of the hole changed.

In a similar study, Dadkhahipour et al. [95] studied the mechanisms of microchannel formation using a high pressure slurry jet (100 – 200 MPa, approximately 450 – 630 m/s) by traversing the nozzle across a glass substrate. They also investigated the effects of standoff distance, traverse speed and impact angle. Given the high pressures of the slurry jet, the cross-sectional profile appeared more along the lines of a "U" shape rather than the "W" shaped profile found in lower pressure systems. Increasing the nozzle traverse speed reduces substrate exposure time to the abrasive jet, thus reducing the number of particle impacts.

Overall, they found the material removal rate to be relatively independent of nozzle impact angle and standoff distance when compared to the effects of pressure and traverse speed. Conversely the resulting wall inclination angle, defined as the angle between the side of the channel and the non-eroded surface, was largely

affected by the standoff distance and water pressure, slightly dependent on jet impact angle and relatively independent of nozzle traverse speed.

Using a test rig designed for lower velocities, Pang et al. [96] investigated the effects of water pressure, nozzle traverse speed, particle concentration and stand-off distance on channel depth, width and inclination angle in glass. Alumina particles with a nominal size of 25μm were used, the water pressure varied between 8 – 14 MPa (approximately 126 – 167 m/s), the standoff distance was varied between 3 – 6 mm, particle concentrations varied between 15% and 30% and the nozzle traverse speed varied between 0.15 – 0.3 mm/s. Figure 2-21 shows the effects of pressure and particle concentration on channel width, depth and wall inclination angle where the traverse speed is 15 mm/s and standoff height is 3 mm.

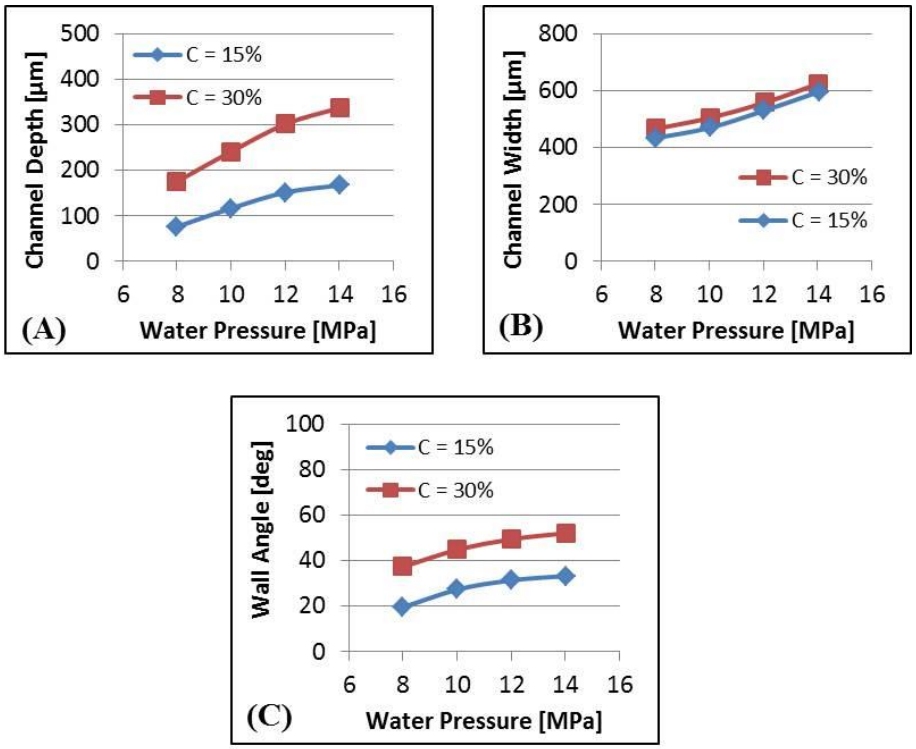

Figure 2-21 Effect of water pressure and particulate concentration on channel depth (A), channel width (B) and wall inclination angle (C) taken from [96]

Regarding channel depth, it was found that increasing pressure and concentration increased this parameter. In alignment with previous studies [95] , reducing the nozzle traverse speed increased the channel depth while changing the standoff distance of the nozzle had little effect. With reference to channel width, water pressure was the major factor influencing this dimension. Within the ranges used in this study, stand-off distance, traverse speed, and particle concentration had little effect. Upon hitting the surface, the flow diverges generating the secondary viscous flow resulting in shallow angle particle impacts. At increased velocities those impacts would take place farther away from the jet centerline due to the increased velocity of the parallel flow. Since the stand-off distance, traverse speed and concentration have little effect on the amount of jet-divergence, it follows that they would have little effect on the channel width.

It was found that the wall inclination angle was mostly associated with an increased in channel depth, i.e. the parameters that resulted in an increased channel depth also resulted to an increased wall angle. This is largely due to the fact that a turbulent region at the bottom of the channel forms as the fluid abruptly changes direction. This drives the motion of both impacting and accumulated particles to induce wear at the bottom of the channel.

Nouraei et al. [97] compared the formation of microhole and microchannel geometries created by ASJM to those created by Abrasive Jet Machining (AJM). ASJM originated from AJM, often times referred to as “powder-blasting”, and uses high speed air as the medium to bring the particles to the surface. The erosive wear is typically controlled through the use of masks due to the spread of particle trajectories

as they leave the nozzle. Ghobeity et al. conducted a number of studies on AJM such as creating predictive surface evolution models [98] and an analytical model to deal with the particle size distribution of abrasives [99].

In the work of Nouraei et al. [97] lower pressures between 1 – 4 MPa and lower particulate concentrations between 0.25 – 1% by mass were used. As in other experiments the effects of the nozzle traverse speed, standoff distance and jet impact angle were also investigated. Similar to the analysis conducted by Clark [78], who found that the impact velocity of particles entrained in the fluid was different than the nominal fluid velocity due to the presence of a squeeze film, the difference between the particle and fluid velocities at the centerline of the jet near the impact wall was found. Shown in Figure 2-22, it can be seen that for a slurry jet exiting the nozzle at approximately 62 m/s, a 25µm spherical alumina particle decelerates to approximately 28 m/s upon impact.

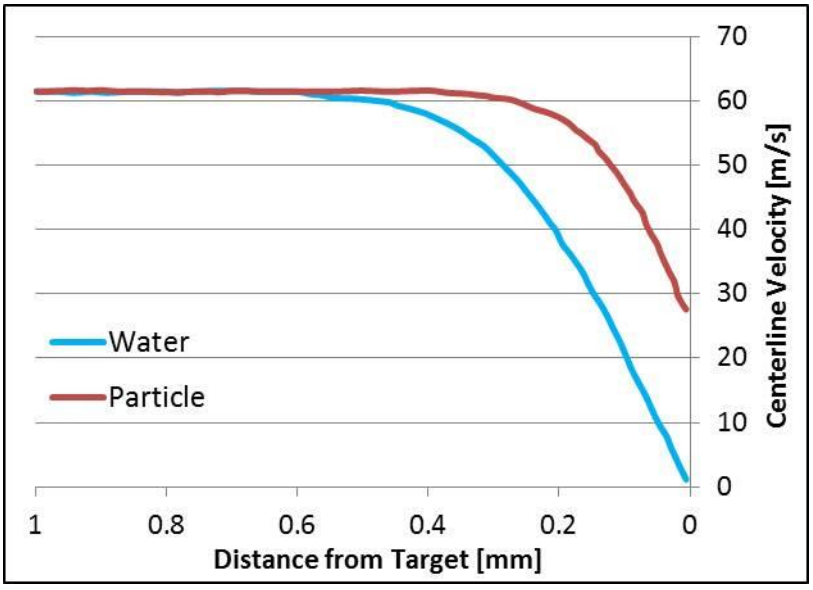

Figure 2-22 Centerline velocity of a 25µm Al_2O_3 particle decelerating near the wall [97]

Examination of the glass surface showed signs of both brittle and ductile wear mechanisms. Wensink and Elwenspoek [100] found that the brittle-to-ductile transition for borosilicate glass was occurs at an impact kinetic energy of 17 nJ. This translates to an impact velocity of 32 m/s for a 25µm alumina particle. Although the nominal particle size was 25µm, Ghobeity et al. [99] found that for these same particles approximately 27% were larger than 25µm, and would thus decrease the brittle-to-ductile impact energy. While the majority of the particles would induce ductile modes wear on the glass surface, a small percentage of particles would have enough kinetic energy to cause fracture.

Figure 2-23 compares the normalized profiles of holes machined using ASJM and AJM. For both profiles the dimensions were normalized by dividing by the diameter of the hole formed. The ASJM profile was conducted by Nouraei [97] using a 254µm nozzle, 25µm alumina particles, 0.25% mass concentration, 20mm standoff while the AJM profile was created by Ghobeity [101], 760µm nozzle, 2.83 g/min of 25µm alumina particles, 200kPa and a 20mm standoff distance.

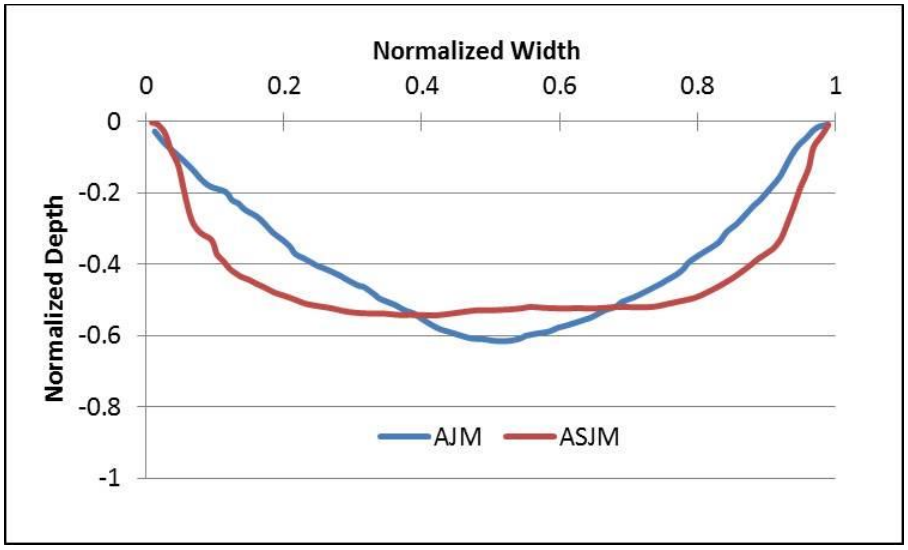

Figure 2-23 Comparison of normalized profile of ASJM and AJM [97]

It can clearly be seen that the ASJM shape more closely resembles a “U” while the AJM shape appears to be a “V”. The difference in shape is largely attributed to the non-uniform particle flux and velocity distribution across the air-jet. It was found by Li et al. [102] and Dehnadfar et al. [103] that radial distance from the centerline of the jet largely determines the air and particle velocities. Compared to AJM, the velocity profile and thus inherently the particle flux in ASJM are relatively uniform across the jet. This is due to the fact that the slurry jet has a low drag force acting on it from the surrounding air. In summary the velocity profile across the jet is non-uniform in AJM systems, however the trajectories of the particles are not influenced by objects creating changes to the air streamlines. While the velocity profile is relatively uniform across the jet in ASJM systems, changes in the fluid flow field caused by obstacles can largely influence the trajectories of the particles given low enough Stokes numbers.

2.5.3.2 Erosion Modeling in ASJM

Pang et al. [104] developed predictive models for the material removal rate (MRR), channel height, width and wall inclination angle for the ASJM micro-channeling process in amorphous glass. A schematic of the channel cross-section with specific geometries is shown in Figure 2-24.

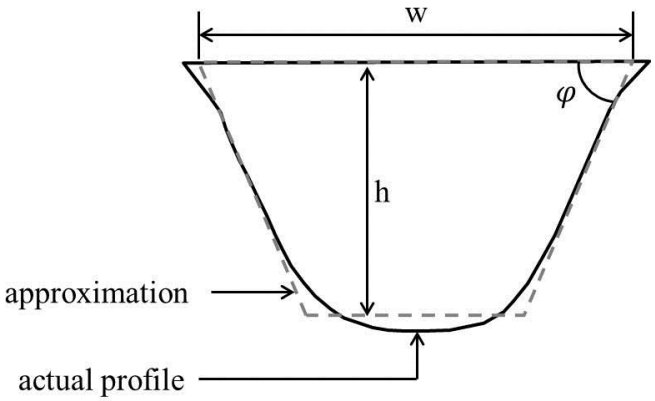

Figure 2-24 Schematic of ASJM channel cross-section

A total of 90 tests were performed over the following operating conditions: water pressure between 8 – 14 MPa (126 – 167 m/s), nozzle traverse speed between 0.15 – 0.3 mm/s, alumina particle concentration between 15 – 30% by mass and nozzle standoff distance between 3 – 6mm. For all tests alumina particles with a mean particle size of 25μm were used. Additionally, due to the high velocity slurry used in these tests, a "U" shaped channel geometry was formed as opposed to the "W" shape found in lower velocity slurry jets [92].

The derived model that relates the MRR to various operating parameters is as follows:

$$MRR = k\left(\frac{P}{\rho_s}\right)^{1.83} C_p^{1.78}\left(\frac{v_n\sqrt{\rho_s}}{\sqrt{P}}\right)^{-0.78} \tag{2-21}$$

where k is a material constant found to be $1.99\text{x}10^{-22}$, P is jet pressure, v_n is the nozzle traverse speed, C_p is the particle concentration and ρ_s is the slurry density calculated by:

$$\rho_s = \frac{\rho_p\rho_f}{\rho_p + C_p(\rho_f - \rho_p)} \tag{2-22}$$

where ρ_p is the particle density and ρ_f is the fluid density. Overall, the model correlated well with experimental results according to Figure 2-25.

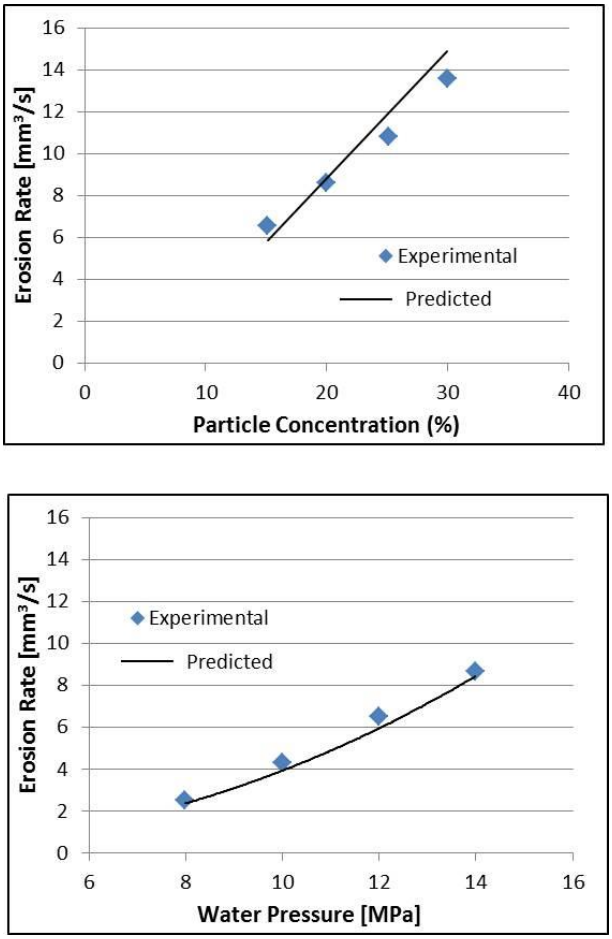

Figure 2-25 Predicted vs. experimental results [104]

The most prominent factor affecting MRR was the jet pressure which is intuitive due to the fact that pressure is proportional to velocity-squared according to Bernoulli's principle. As such, the MRR was found to be proportional to $V^{3.66}$, i.e. the nominal jet velocity exponent is 3.66. This value is within the ballpark of previously found velocity exponents for brittle erosion assuming the dynamic impact theory holds true. One drawback to this model is that it assumes a non-zero value for the nozzle traverse speed. In the case of jet-impingement cooling, the nozzle would be

stationary. While this model shows good correlations to experimental results, the highly empirical nature suggests that this model may only be applicable within the specific parameter ranges used in this study. As such, the applicability to other scenarios is unknown.

Jafar et al. [105] used a combined CFD-experimental approach to investigate how various operating parameters, such as pressure and jet angle, influenced the erosion rate of channels etched into borosilicate glass. CFD was used to determine the impact angle and impact velocity of individual alumina particles in order to calculate the normal component of the particle's kinetic energy upon impact. The normal component was used for analysis because surface examination revealed that brittle fracture was the primary mode of material removal.

The erosion model was based on the fact that particles will only cause damage in glass if the normal component of the kinetic energy is above the threshold impact energy, U_{th}, determined by Slikkerveer [106]:

$$U_{th} = 23{,}225\ \frac{E^{\frac{3}{2}} K_C^6}{H^{\frac{13}{2}}} \tag{2-23}$$

While the threshold value for borosilicate glass was calculated to be 39 nJ using this formulation, Wensink and Elwenspoek [100] experimentally found this value to be 19 nJ for Pyrex glass. As such, 19 nJ was used in this study as the threshold kinetic energy.

To predict the volume of material removed due to an impacting particle, two different models for the erosion rates were assessed. The first model, ER_1, assumes that the lateral crack formed from a particle impact originates at the base of the plastic

zone, aligning with the theory developed by Marshall, Lawn and Evans [57]. The second erosion model, ER_2, is based on previous work by Jafar et al. [107] who showed that the depth of the chip removed can be better approximated by the indentation depth of the particle as opposed to the depth of the plastic zone. The erosion models are defined as follows:

$$ER_1 = \frac{\pi}{6}\frac{\rho_t b(b^2 + 3c_L^2)^2}{m_p} \tag{2-24}$$

$$ER_2 = \frac{\pi}{6}\frac{\rho_t a(a^2 + 3c_L^2)^2}{m_p} \tag{2-25}$$

where m_p is the mass of particle, ρ_t is the density of the glass and a and b are the depths of the indentation zone and plastic zone respectively, defined as [106]:

$$a = \left(\frac{3U}{2\pi H}\right)^{\frac{1}{3}} \tag{2-26}$$

$$b \cong 0.63a\left(\frac{E}{H}\right)^{\frac{1}{2}} \tag{2-27}$$

The size of the lateral crack, C_L, was derived by Marshal et al. [57] as:

$$c_L = \left(\frac{\zeta_L}{\sqrt{A}}(\cot(\psi))^{\frac{5}{6}}\frac{E^{\frac{3}{4}}}{HK_C}\right)^{\frac{1}{2}}\left(1 - \left(\frac{F_0}{F}\right)^{\frac{1}{4}}\right)^{\frac{1}{2}} \tag{2-28}$$

$$F = (18H\tan^2(\psi)^{\frac{1}{3}}U^{\frac{2}{3}} \quad (2\text{-}29)$$

$$F_0 = \frac{\zeta_0}{A^2}\cot(\psi)^{-\frac{2}{3}}\left(\frac{EK_c^4}{H^4}\right) \quad (1\text{-}30)$$

where F and F_0 are the indentation force and the threshold load for cracking respectively, ζ_L is a constant found to be 0.025, A is a geometrical constant equal to 0.75, ψ is the indenter angle assumed to be 74º and ζ_0 was experimentally determined to be 1200 [57].

Particle sizes between 5 - 45μm were considered due to the fact that a known particle size distribution exists for a batch of nominally sized 25μm alumina particles. To deal with the particle size distribution, an effective kinetic energy was used in the modeling efforts and defined to be the weighted average normal kinetic energy of the particles above the threshold kinetic energy. Using this assumption, the impact kinetic energy of the particle, U in the Equation 2-26, is essentially an effective average impact kinetic energy of the particle size distribution.

A comparison of the predicted erosion rate, defined as the ratio of the mass of material removed to the mass of impacting particles, is shown in Figure 2-26. The experimental conditions were composed of 25μm alumina particles (with known particle size distribution ranging from 5 - 45μm), jet pressures between 2.1 – 6.1 MPa (approximately 65 – 110 m/s), 0.25% by mass particle concentration and a normal jet impingement.

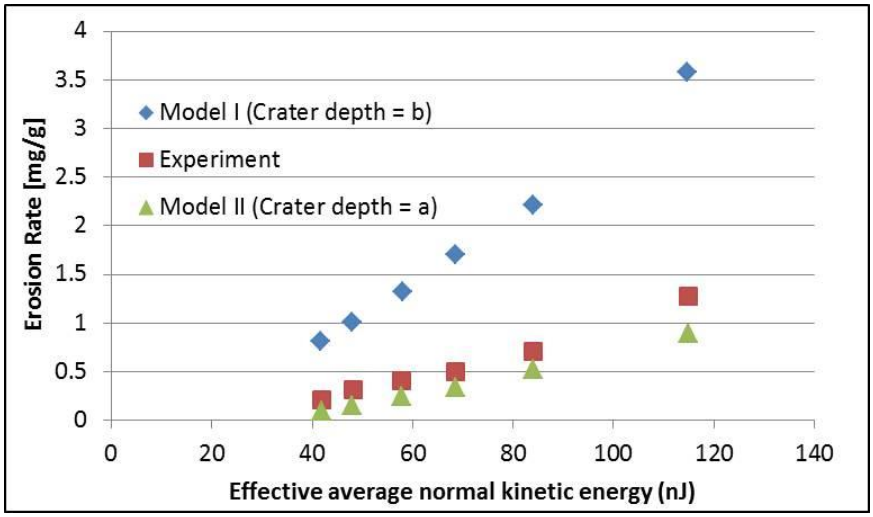

Figure 2-26 Erosion rate of borosilicate glass as a function of effective average normal impact kinetic energy [105]

It can be seen that ER_2 (Model II), which assumes that the depth of the chip removed can best be approximated by the indentation depth of the particle, matches the experimental data quite well. While Model II better predicted the erosion rate compared to Model I, it was still found to under predict the erosion rate by an average of 41%. It was found that increasing the crater depth *a* by 22% to match the experimental results in another study [107] reduced the average error down to 12%.

2.5.4 Nanofluid Erosion

While the majority of particle erosion and slurry erosion studies assume particle sizes on the order of tens to hundreds of micrometers, erosion studies involving nanofluids may offer additional insight regarding the potential for erosion in microchannel and embedded cooling loops due to the small particles used. The primary parallelism lies in the fact that electronic cooling loops typically have filters that prevent larger particles from entering the region where erosion protection is critical. Nanofluids typically have high concentrations of particles that are on the

order of tens of nanometers in size. They are prepared in such a way to prevent particle agglomeration, meaning they would be extremely challenging to filter out using conventional filtering techniques. While the number of erosion studies involving nanofluids is limited, the information presented here may provide insight regarding the phenomenon of fine-scale erosion.

Routbort, Singh and co-workers [108] studied the effects of nanofluids on heavy vehicle cooling systems, specifically the potential for erosion on select materials. The erosion of Aluminum 3003 was assessed using a suspension of copper nanoparticles in 50/50 water/ethylene glycol and trichloroethylene at 50ºC. Through mass loss measurements, the erosion rate was determined for impingements velocities between 1 – 10 m/s and impact angles from 30 - 90º. The only test that showed any measureable erosion between 200 – 300 hours of testing was the test of 9.6 m/s at normal incidence resulting in a mass loss rate of $3.5x10^{-6}$ grams/hour, or approximately 165 μm/year. CuO/ethylene glycol and SiC/water nanofluids were also tested [109] and yielded no measureable erosion, although surface pitting and corrosion was observed upon closer inspection of the surface.

In conducting these experiments it was found that significant wear of the pump occurred, specifically in the gears. In a test running > 700 hours using a 2% by volume SiC nanofluid at 8 m/s and an impact angle of 30º, erosion of the target material was not observed, however pump wear was [110] [108]. While these studies may provide valuable insight regarding the potential for erosion in radiator applications, velocities of less than 10 m/s are about half that of those present in embedded cooling systems.

In a similar study Nguyen et al. [111] studied the jet impingement slurry erosion of aluminum at 19 m/s using a SiC-water nanofluid (36nm particles, 5% by volume concentration). After 180 hours of testing a total of 14 mg mass loss was recorded, while the control sample showed no change in mass loss. Surface examinations revealed rounded microstructures and pits not present on the pre-eroded samples. While it was concluded that nanofluids can lead to significant wear over time, the specific mechanism of material removal was not assessed.

Molina et al. [112] conducted erosion experiments on aluminum and copper samples using an alumina-water/ethylene glycol nanofluid (2% volume concentration, 10nm particle size before agglomeration) at 10.7 m/s normal impact. Tests times ranged from 3 to 112 hours. Mass loss and surface roughness measurements were taken periodically throughout the experiments to monitor surface evolution.

For aluminum a slight 5mg mass gain was observed over the first 28 hours followed by no measureable change. This was likely due to the formation of a protective oxide layer that formed on the surface. Additionally, roughness measurements indicated that surface modification takes place over the course of the first 28 hours in the form scratch removal and slight removal of loose surface fragments. After 28 hours slight pitting was observed specifically near the original polishing lines, suggesting the presence of a mild abrasion mechanism.

No measureable weight change was measured for copper, however mild surface modifications were observed throughout the test. Similar to aluminum, mild pitting was observed for both the reference fluid and nanofluid, suggesting a slight chemical component affecting material removal.

The literature reviewed in this section focused solely on the erosion potential of aluminum and copper. While it was generally observed that weight loss measurements yielded no appreciable change, the effects on surface roughness were noteworthy.

2.6 Brittle-to-Ductile Transition

The phenomenon where a nominally brittle material exhibits ductile wear properties under certain impact conditions, specifically as the particle size is reduced, was first observed by Sheldon and Finnie [40]. In studying the particle erosion of soda-lime glass at 152 m/s they found that as the particle size decreased from 127μm to approximately 9μm, the angle of peak erosion changed from that of normal incidence to approximately 20º. This corresponds to a shift in wear mechanism from fracture dominated wear at 90º impingement angles to plastic dominated wear at shallow impingement angles.

Sparks and Hutchings [113] studied the erosive behavior of silicate glass ceramic using rounded and angular silica particles at impingement velocities between 28 – 69 m/s. All particles were sieved through high and low pass filters such that the size of all particles used was between 125μm to 150μm. At a 30º impact angle there was found to be a sharp jump in the erosion rate for rounded particles above a velocity of approximately 50 m/s, shown in Figure 2-27.

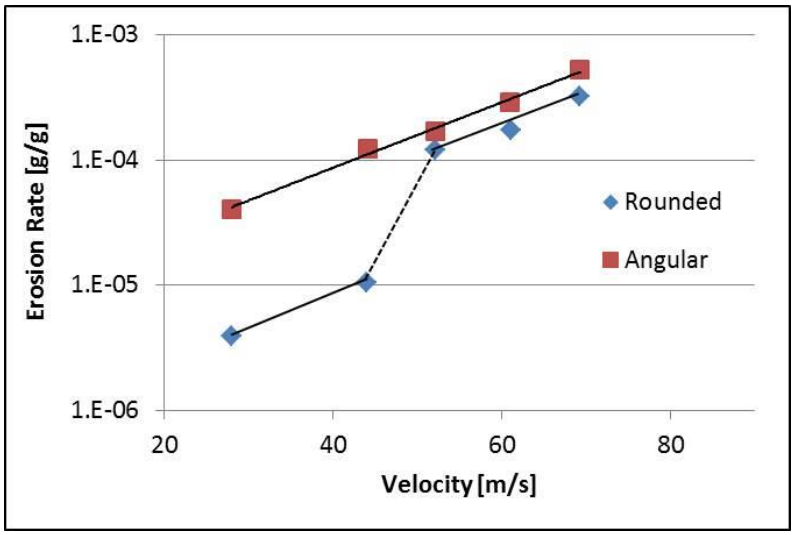

Figure 2-27 Erosion rate vs velocity of angular and rounded particles at 30º impact [113]

At 50 m/s and above, the erosion rate for the angular particles was approximately 1.5 times that of the rounded particles; however below this transition the erosion rate for angular particles was approximately 10 times that of the rounded particles. Surface examinations revealed that this transition point marked a transition in the mechanism of material removal for rounded particles. Above this transition material was removed in the form of flaky fragments approximately 30 - 50μm across and 1μm thick. It was observed that these flakes formed as a result of multiple impacts, each of which produces lateral fractures but no material removal. Below this transition material is removed via small fragments arising from accumulated plastic strain and fatigue. At the impact sites, localized regions of plastic deformation were found without the presence of lateral fracture. A similar transition was also observed by altering the impact angle.

2.6.1 Transitional Wear Maps

Hutchings [114] developed wear maps to illustrate how altering the particle size and impact velocity shift the wear mechanisms away from fracture dominated to those dominated by plastic flow. These maps consider the effects of both rounded and angular particles and assess whether the potential fractures takes the form of Hertzian or lateral cracking.

The transition map depicting the onset of Hertzian cracking from either elastic or plastic collisions was developed by plotting two equations and assessing their intersection point. The first equation was derived by Wiederhorn and Lawn [115] and showed that the critical impact velocity above which Hertzian fracture will occur, V_H, can be related to the diameter of the impacting sphere:

$$V_H \propto \frac{K_c^{\frac{5}{3}}}{E^{\frac{7}{6}}} \rho^{-\frac{1}{2}} d^{-\frac{5}{6}} \tag{2-31}$$

where E is an effective elastic constant and depends on the Young's modulus and poisons ratio of both the impacting particle and target surface. This equation can alternatively be written to relate the critical dimeter of the impacting sphere, d_H, to the impact velocity:

$$d_H \propto \frac{K_C^2}{E^{\frac{7}{5}}} \rho^{-\frac{3}{5}} V^{-\frac{6}{5}} \tag{2-32}$$

The second equation used to create the transitional wear map for Hertzian fracture relates the critical velocity necessary to initiate plastic flow, V_P, to various material parameters. This formulation additionally assumes that the mean contact pressure is independent of the diameter of the sphere [116].

$$V_P \propto \frac{\rho^{-\frac{1}{2}} H^{\frac{5}{2}}}{E^2} \tag{2-33}$$

Plotting Equations 2-32 and 2-33, as shown in Figure 2-28, a number of regions can be discerned which indicate the primary wear mechanisms associated with the impact conditions.

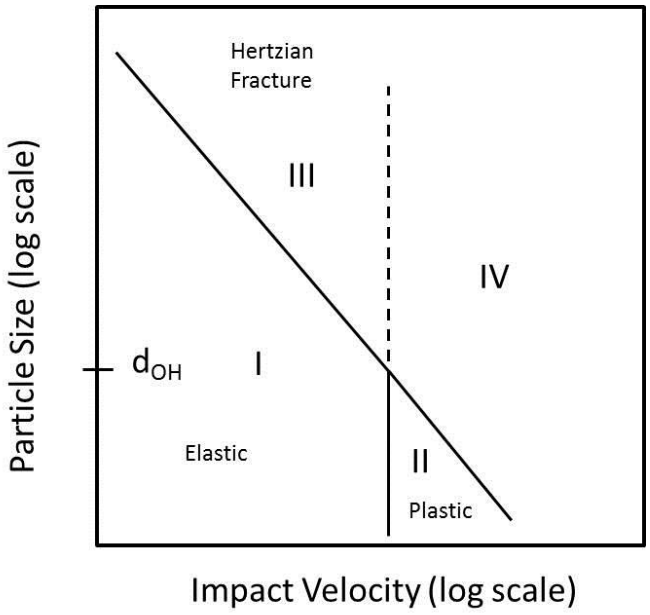

Figure 2-28 Schematic showing transitional wear map associated with Hertzian fracture [114]

In region I at low velocities and small particle sizes, the impact is purely elastic and any wear in this region can be associated with fatigue processes, i.e. many impacts would be required to induce cracking. Increasing the velocity at small particle sizes transitions the system to region II, where ductile wear mechanisms begin dominate the erosion process. At large particle sizes and low velocities, region III, Hertzian cone cracks will form. If the system enters region IV the assumptions presented in the previous equations will no longer be valid, however it is predicted that both Hertzian fracture and plastic deformation mechanisms will be present.

The same analysis was conducted to illustrate the transition from elastic/ plastic impact conditions to the onset of lateral fracture for spherical and angular particles. For angular particles, the critical particle size above which lateral fracture will occur is given by [114]:

$$d_L \propto \left(\frac{K_C}{H}\right)^2 \frac{E^{\frac{1}{2}}}{H^{\frac{1}{6}}} \rho^{-\frac{1}{3}} V^{-\frac{2}{3}} \tag{2-34}$$

Additionally, the critical particle size for spherical particles is given by:

$$d_L \propto \left(\frac{K_C}{H}\right)^2 \frac{E^{\frac{1}{2}}}{H^{\frac{1}{4}}} \rho^{-\frac{1}{4}} V^{-\frac{1}{2}} \tag{2-35}$$

These equations are plotted in Figure 2-29 indicating the various wear regimes.

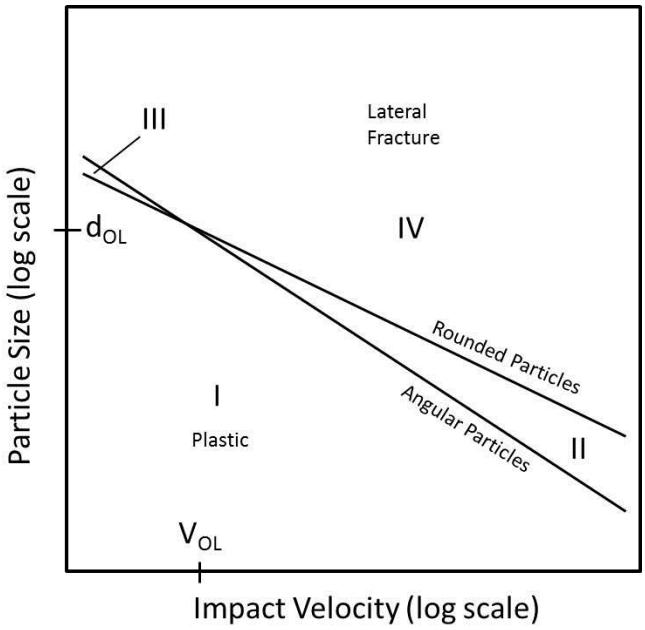

Figure 2-29 Schematic showing transitional wear map associated with lateral cracking [114]

In region I, both rounded and angular particles impacting the surface will cause plastic indentation without lateral fracture. In this region material will be removed

primarily by plastic processes, although brittle mechanisms may occur due to cyclic fatigue arising from multiple impacts. According to the assumptions inherent in the defining equations, all particles are expected to cause plastic flow due to the notion that an indenter, whether perfectly sharp or with a slight radius of curvature, will cause a stress singularity. In region IV lateral fracture will occur for all particles regardless of shape, and the erosion mechanisms will be dominantly brittle. In region II, angular particles will cause lateral fracture while rounded particles will just result in plastic flow. Region III represents the region where rounded particles will cause fracture but rounded particles will not. It is not clear if this region has physical significance as it is suggested that key assumptions in the equations may break down at these low velocities. Although ideal angular particles will cause plastic flow at all velocities, in reality the velocity may not be high enough to induce plastic deformation resulting in an elastic collision.

2.6.2 Glass and Silicon

Wensink and Elwenspoek [100] examined the transition from brittle to ductile wear processes for Pyrex, sodalime glass and single crystal <100> silicon. In their experiments, sharp alumina particles from 3 – 29.2μm were air-blasted onto the various substrates at velocities up to 200 m/s. Weight loss measurements were conducted post-erosion to determine the erosion rate in grams of material lost divided by the grams of particulate used. An erosion classification value was defined, E_{CV}, which is the ratio of the erosion rate at 45º impingement to that of the erosion rate at normal incidence. Additionally, the erosion rate at 90º was fitted to be proportional to the kinetic energy of the impacting particle:

$$ER \propto U_{kin}^{p} \tag{2-36}$$

where p is the kinetic energy exponent and is half that of the typically defined velocity exponent. Figure 2-30 shows the results for silicon where E_{CV} and the erosion rate are plotted against the kinetic energy.

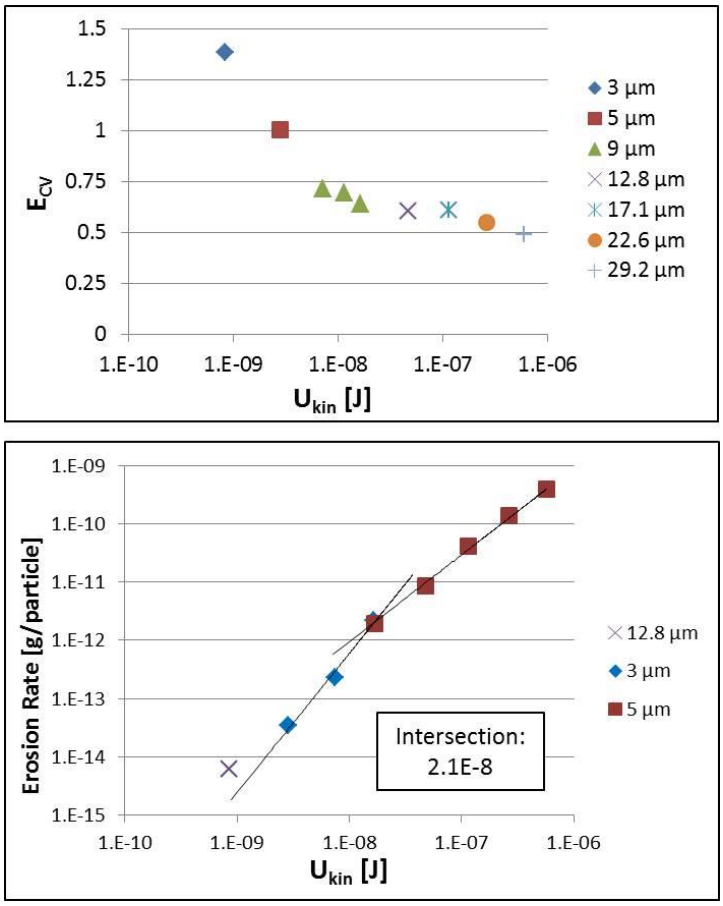

Figure 2-30 ECV and erosion rate of silicon as a function of kinetic energy [100]

Regarding the erosion rate plot, two regimes can be seen. One regime is considered the low energy regime and is mostly comprised of ductile erosion mechanisms while the other high energy regime consists mostly of the brittle wear mechanisms. The intersection of these two lines is considered the brittle-to-ductile

transition point. For the three materials studied, the kinetic energy exponents for both regimes are shown in Table 2-6.

Table 2-6 Kinetic energy exponents for high and low energy regimes [100]

	High Energy Regime	Low Energy Regime
Pyrex	1.42	2.35
Silicon	1.53	2.35
Sodalime Glass	1.38	3.2

This transition was found to be relatively gradual due to the many variances between individual impacts such as particle size, shape, velocity and angle. However, at low enough kinetic energies it is expected that the velocity exponent should converge to that of a typical ductile material, between 2.2 and 2.4 [117].

The E_{CV} graph can be divided into three primary stages with respect to the impact kinetic energy. Transitioning from the high energy region to low energy region, the E_{CV} initially rises. It is suggested that at lower kinetic energies the contribution of tangential forces, such as those present in 45º impacts, contribute more to lateral crack propagation. In the second stage, the E_{CV} decreases slightly to a minimum as the tangential impact force plays less of a role in enhancing lateral crack propagation. In the third stage the E_{CV} rises as the number of ductile impacts occurring at normal incidence increases. An $E_{CV} > 1$ indicates a shift in the erosion rate vs. impact angle curve from nominally brittle to nominally ductile behavior.

Using the analysis conducted by Slikkerveer et al. [106], the theoretical threshold energies for lateral crack propagation were calculated. These values are compared to the experimentally determined ones in Table 2-7.

Table 2-7 Analytical and experimental threshold impact energy [100]

	Analytical (nJ)	Experimental (nJ)
Pyrex	30	17
Silicon	32	21
Sodalime Glass	37	24

The difference between the analytical and experimental values is thought to originate from the material properties used in the analytical calculation. According to Equation 2-23, the fracture toughness is raised to the power of 6 while the hardness is raised to the power of 6.5. Any slight deviation in material properties would yield a larger change in the calculated threshold energy.

2.7 Concluding Remarks

This chapter presented a widespread literature review surrounding different areas of brittle wear and erosion relevant to microfluidic cooling. A number of related topics were presented including the early erosion studies of Sheldon and Finnie, elastic-plastic indentation theories, particle erosion of ceramics, slurry erosion and the concept of the brittle-to-ductile transition. Although fundamentally separate, each of these topics relate in their own fashion to the study presented here. A couple key points can be summarized as follows:

- Quasi-static and dynamic impact model analytically correlate micro-indentation physics to particle impact conditions.
- The quasi-static model predicts a velocity exponent of n = 2.4 while the dynamic impact model predicts a velocity exponent of n = 3.2. Both models predict a particle size exponent of 3.67.

- Units through which the erosion rate metrics are presented vary from author to author. Typically, the erosion rate is described as a volume loss rate (ex: mm^3/hour), a mass loss rate (ex: mg/hour) or an erosion ratio in units of mg/mg defined as the ratio of material removed per mass of impacting particle. Erosion models are often formulated such that the mass of material removed can be calculated for a single impacting particle.
- Routbort and Scattergood showed that the velocity exponent changes depending on particle size. Small particles (40μm) tend to follow the dynamic impact theory while large particles (270μm) tend to follow the quasi-static model.
- Fluid plays a large role in particle impact conditions. Fluid velocity does not equate to particle impact velocity. The Stokes number can be used to determine how closely coupled a particle trajectory is to a fluid streamline.
- The squeeze-film may facilitate erosion by introducing an additional 'wet-abrasion' mechanism. This has only been observed in ductile materials.
- Brittle-to-ductile transition occurs as the impact kinetic energy of particles is decreased. At low velocities and particle sizes, brittle erosion transitions into ductile wear.
- ASJM offers qualitative insight into the type of erosion resulting from jet-impingement cooling. Characteristic 'W' erosion contour will likely be observed.

As discussed in the Chapter 1, a common theme surrounding previously conducted erosion studies is that the particle sizes, velocities and materials used are

vastly different than those present in microchannel or embedded cooling systems. It is unknown if these models can be extrapolated down to the particle sizes or velocities of interest given that they were calibrated for vastly different parameter ranges. Additionally, the brittle-to-ductile transition suggests that a shift in wear mechanism may occur at the conditions present in microchannel and embedded coolers. Although unknown, it is unlikely that erosion from this alternative mechanism can be modeled using the same predictive equations as the brittle erosion mechanism. It will be the purpose of this study to fill this research gap and conduct erosion studies using conditions most likely found in microchannel and embedded cooling systems.

3 PROBLEM STATEMENT AND OBJECTIVES

This brief chapter recounts the fundamental problem statement and explicitly states the goals of this research. Of the various embedded cooling architectures described in the introduction and literature review chapters, jet-impingement cooling provides excellent cooling capabilities, however the major drawback is the potential for particle erosion and wear of the substrate. As jet velocities reach and exceed 20 m/s, this mechanism becomes a significant reliability threat due to the fact that the substrate separating the active electronics from the impinging jet can be on the order of 50-100μm thick. While jet-impingement cooling may be most susceptible to erosion, other types of liquid cooling techniques may be at risk especially over long term operation.

In the design phase of an embedded or microchannel cooling system, an erosion prediction is vital to ensure that catastrophic damage does not occur over the expected lifetime of the device. Even more important is to identify safe operating regions where, even though erosion may be present, significant damage will not occur. This erosion prediction is typically conducted using CFD simulations and tracking particle impingements using Lagrangian methodologies. An erosion equation determines how much material is removed per impinging particle. Commercial CFD codes such as ANSYS FLUENT and CFX have built in erosion equations and/or predefined constants in their user manuals that can be used. Other times erosion equations taken from the open literature are hooked into the CFD code using custom scripts.

While numerous particle erosion models exist, seldom are the velocities, particle sizes, materials and testing times in alignment with those that would exist in

embedded cooling systems. In addition, the models from literature are typically calibrated using air as the transportation medium which ignores potential surface-particle interaction effects caused by fluids. Furthermore, as discussed in the Chapter 2, at very low particle sizes and velocities there exists a fundamental shift in wear mechanism that takes place in nominally brittle materials. The accuracy of the established brittle erosion models is unknown given this shift in wear mechanism. This same principle applies to the erosion correlations built into the commercial CFD codes - they were derived for ductile materials such as copper, steel and aluminum. While many of these models may provide a sound first order approximation as to the qualitative extent of erosion, it is unknown how well they can be applied to the specific conditions present in microchannel coolers.

Given the need for high accuracy erosion predictions, this research aims to fill the gap in erosion models currently available in literature. Nominal jet velocities will be kept in the range of 20 – 40 m/s, considering both realistic and accelerated velocities. Particle sizes will be kept below 20μm enabling the consideration of many different filtering levels. Silicon was chosen as the material of interest due to its wide use in power electronic substrates, specifically in the current and future implementations of GaN-on-Si power devices.

The primary objective of this research is to develop a particle erosion model, calibrated for silicon, within the parameter ranges relevant to those in microchannel and embedded cooling systems. However, this objective can be broken down into six fundamental segments:

1) Develop a jet-impingement CFD model in ANSYS FLUENT to obtain localized particle impact characteristics. Along with this task comes the development of user-defined functions to amend the abilities inherently present in the software. Simulations will be performed that correspond directly to the slurry erosion experiments.
2) Design and construct a slurry erosion jet-impingement test apparatus to perform erosion experiments on single crystal silicon.
3) Formulate and execute a series of tests to investigate the effects of jet velocity, particle size, concentration, fluid viscosity and time.
4) Gain insight into the wear mechanisms of single crystal silicon under microchannel cooler operating conditions, namely particle sizes less than 20μm and jet velocities less than 40 m/s.
5) Combine localized particle impact data from the CFD simulations with experimental erosion data to extend the Huang cutting erosion model to new parameter ranges and new materials. This involves developing the process and calibrating new particle size and velocity exponents, along with a new material/system constant.
6) Perform validation simulations in FLUENT to compare measured 1-D erosion rates from experiments to the predicted 1-D erosion rates of the simulations. While the model will be developed using the erosion ratio metric, the output of the validation simulations will be in units of micrometers-per-year. As such, a different erosion metric will be used to validate the model compared the one used to calibrate the model. Lastly, an impact dampening coefficient will be proposed

to provide potential explanations for slight inconsistencies between experiments and the CFD predictions.

4 COMPUTATIONAL FLUID DYNAMICS

4.1 Introduction

CFD is a widely used erosion prediction tool commonly used in applications surrounding oilfield pipelines, valves and other devices involving slurry transport. The process through which this prediction method is applied can be divided into three essential parts, described in Figure 4-1. First, the flow field is generated using a commercial or custom built CFD code which solves the Navier-Stokes equations. Second, particles are coupled to the flow field using Lagrangian techniques. Lastly an erosion equation is applied as a boundary condition upon particle impact. When a particle impacts a surface, the erosion equation determines how much subsequent material is removed based on the incoming particle's velocity, size, impact angle and material.

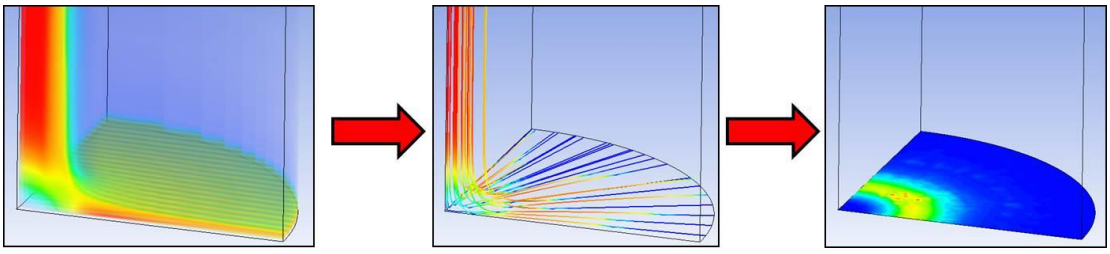

Figure 4-1 Three steps involved in erosion prediction using CFD

The purpose of the CFD simulation effort described in this chapter is to obtain localized particle impact information, specifically particle velocity, particle impact angle and the percentage of entrained particles that result in impact. The literature review section describes in detail the effects of the squeeze film that forms in a directly above the surface. Due to this phenomenon, impact velocities vary and in some cases considerably from the nominal jet velocity of the fluid. In the case of air

where the carrier medium has negligible viscosity, the particle impact velocity can be taken as the same velocity at which the particles exit the jet. As the viscosity of the fluid increases, particles become more strongly coupled to the fluid motion and therefore this viscous effect becomes more pronounced. This has a significant effect on where the particles impact the surface, the speed and angle at which they impact, and how many entrained particles actually reach the surface. In the case of air it can be assumed that all particles reach the surface, however as the fluid viscosity increases a smaller percentage of particles reach the surface as many become entrained in the bulk flow.

This chapter will be outlined as follows. First, a general description of CFD theory will be given along with an explanation of the flow and particle-specific models implemented in ANSYS FLUENT. Next, the quarter-symmetry jet-impingement geometry will be introduced. Meshing strategies, convergence criteria and mesh independence will be discussed. The flow field solutions for seven different simulations will be presented which satisfy the first step in conducting a CFD-based particle erosion prediction. In order to capture particle impact characteristics, a series of user-defined functions (UDFs) were written, of which the details will be given. Lastly, the results will be presented including the effect of jet-velocity, particle size, particle concentration and fluid viscosity. The chapter will conclude by addressing the relevance to high heat flux embedded cooling systems.

4.2 Theory and Models

Computational fluid dynamics is a numerical technique used to analyze and solve problems involving fluid flow. Fundamentally, CFD operates by discretizing

the flow field geometry into a finite number of control volumes. The basic equations of fluid motion are solved in an iterative fashion until a defined convergence criteria is met. As a result, approximate values of each flow variable are solved for at each control volume throughout the domain enabling a clear representation of the behavior of the flow. One assumption specific to the CFD approach is that the flow is treated as a continuum implying that molecular and atomic forces can be ignored. In addition, the models presented in this section are described in a manner compatible with ANSYS FLUENT. More detailed information surrounding each model can be found in the ANSYS Documentation [118].

4.2.1 Fundamental Transport Equations

For all types of flow, the conservation equations for mass and momentum are solved. For flows involving heat transfer or compressibility, the energy equation is solved in conjunction. The equation describing conservation of mass is as follows:

$$\frac{\partial \rho}{\partial t} + \nabla \cdot (\rho \vec{\boldsymbol{v}}) = S_m \tag{3-1}$$

where ρ is the density, $\boldsymbol{v}$ is the velocity field and the source S_m represents the mass added to the continuous phase from secondary phases or user-defined sources. For the simulations used in this work, the flow is considered incompressible and mass is not added to or taken away from the system. Therefore the continuity equation simplifies to:

$$\nabla \cdot \vec{\boldsymbol{v}} = 0 \tag{3-2}$$

Given the 3D nature of the simulations, the expanded form of the divergence of the velocity field is given as:

$$\frac{\partial v_x}{\partial x} + \frac{\partial v_y}{\partial y} + \frac{\partial v_z}{\partial z} = 0 \tag{3-4}$$

The momentum equations of fluid flow, also referred to as the Navier-Stokes equations, solve for the velocity field at every point in space and time within the region of interest. Once solved, the velocity field can be analyzed to determine other quantities of interest such as the pressure fields. While FLUENT has the ability to solve for compressible flows, the form of the Navier-Stokes equation assuming incompressible flow is shown below:

$$\frac{\partial \vec{\boldsymbol{v}}}{\partial t} + (\vec{\boldsymbol{v}} \cdot \nabla)\vec{\boldsymbol{v}} - \nu \nabla^2 \vec{\boldsymbol{v}} = -\nabla p + \vec{\boldsymbol{g}} \tag{3-5}$$

where p is the pressure, $\boldsymbol{g}$ is the gravity vector, and ν is the kinematic viscosity. In addition, other force terms can be applied to the right hand side of the equation such as in cases where forces are applied from secondary dispersed phases. When considering the three Cartesian directions (X, Y, Z), the momentum equation needs to be solved for each direction, giving a total of four partial differential equations (including the conservation of mass) that need to be solved simultaneously. The simulations in this work are assumed to be isothermal, and as such the energy equation is not solved.

4.2.2 Multiphase Volume-of-Fluid (VOF) model

The VOF model enables the simulation to track two or more immiscible fluids by solving a single set of conservation transport equations and tracking the volume fraction of each fluid throughout the domain. While this model is ideal for applications involving jet-breakup, a few limitations apply:

- Pressure-based solver must be used.
- Void regions cannot exist. Each control volume must be filled with either a single fluid or combination thereof.
- Special memory allocations must be made when tracking particles in parallel using the Discrete Phase Model (DPM) discussed later.

Interface tracking between each of the phases is conducted by solving the continuity equation for the volume fraction of one or more phases. For the ith phase, the continuity equation takes on the following form:

$$\frac{1}{\rho_i}\left[\frac{\partial}{\partial t}(\alpha_i\rho_i) + \nabla\cdot(\alpha_i\rho_i\vec{v}) = S_{UD} + \sum_{p=1}^{n}(\dot{m}_{pq} - \dot{m}_{qp})\right] \quad (3\text{-}6)$$

where α represent the volume fraction of the ith phase in the control volume, m represents the mass transfer between phases q and p, and S_{UD} is zero by default but user-defined mass source terms can be added. The implicit solver formulation was used with 'sharp' type interface modeling.

4.2.3 SST k-ω Turbulence Model

To account for turbulence, a Reynolds averaging approach is used, referred to as solving the Reynolds-Averaged Navier-Stokes (RANS) equations. This is conducted by decomposing the velocity field into mean and fluctuating components such that:

$$u_i = \bar{u}_i + u_i' \quad (3\text{-}7)$$

where $\bar{u}_i$ and u_i' are the mean and fluctuating components respectively. When substituting this formulation into the instantaneous form of the Navier-Stokes

equations, the Reynolds-Averaged Navier-Stokes equations are derived and shown below in tensor format:

$$\frac{\partial \overline{\boldsymbol{u_i}}}{\partial t} + \overline{u_i}\frac{\partial \overline{\boldsymbol{u_i}}}{\partial x} + \overline{u_j}\frac{\partial \overline{\boldsymbol{u_i}}}{\partial y} + \overline{u_k}\frac{\partial \overline{\boldsymbol{u_i}}}{\partial z} = F_i - \frac{1}{\rho}\frac{\partial \bar{p}}{dx_i} + \nu\left(\frac{\partial^2 \overline{\boldsymbol{u_i}}}{\partial x^2} + \frac{\partial^2 \overline{\boldsymbol{u_i}}}{\partial y^2} + \frac{\partial^2 \overline{\boldsymbol{u}}_i}{\partial z^2}\right) - \frac{\partial\left(\overline{u_i{}' u_j{}'}\right)}{\partial x_j} \quad (3\text{-}8)$$

However, an additional term appears on the right-hand side of the equation and represents the effect of turbulence. In order to close the equation, these Reynold stresses must be modeled. The SST *k-ω* turbulence model was chosen as it has been shown to yield excellent accuracy for impinging jet problems [119] and is capable of handling a wide class of flows such as adverse pressure gradients, airfoils and transient shockwaves. Standard values and constants were assumed or the implementation of this model in FLUENT, including the Low-Re number correction factor.

4.2.4 Discrete Phase Model (DPM)

In order to track a large number of discrete particles throughout the flow field, Lagrangian particle tracking is implemented through the Euler-Lagrange approach. The dispersed phase is solved for by tracking the motion of the discrete particles through the calculated continuous flow field. The particles can also exchange mass, momentum and energy with the continuous phase. One assumption with this approach is that particle-particle interactions are neglected making it appropriate for flow fields containing low-volume fractions of particles even if relative mass loading of the dispersed phase is high.

FLUENT solves for the trajectory of a discrete particle by integrating the force balance on the particle assuming a Lagrangian reference frame. Equating the inertia of the particle with the forces acting on it, the force balance equation can be written as follows:

$$\frac{d\overrightarrow{\boldsymbol{u_p}}}{dt} = \frac{\vec{\boldsymbol{u}} - \overrightarrow{\boldsymbol{u_p}}}{\tau_r} + \frac{\vec{\boldsymbol{g}}(\rho_p - \rho)}{\rho_p} + \vec{\boldsymbol{F}} \tag{3-9}$$

where τ represents the particle relaxation time [118] [120] as part of the drag force term. The buoyancy force is considered as well as additional force terms, combined into the force vector $\boldsymbol{F}$ that may be acting on the particle such as lift, virtual mass, thermophoretic and Brownian forces.

FLUENT also has the ability to account for the stochastic nature of particle trajectories in turbulent flow fields. To predict the dispersion of particles due to turbulence, the Discrete Random Walk (DRW) is implemented which calculates the particle's velocity by considering the mean and fluctuating velocity components of which the latter is a function of a normally distributed random number and the localized kinetic energy of turbulence. Implementation of this model assumed standard constants. However, one limitation with this model is that it has been shown to give non-physical results in non-homogenous diffusion-dominated flows or in wall-impacting cases where particle sizes enter the sub-micrometer range. These limitations likely exist due to the fact that particle trajectories at these particle sizes are dominated by forces other than hydrodynamic ones such as Van Der Waals attractive forces and electric repulsive forces.

Additionally, two different types of particle-fluid coupling options are available. One-way coupling assumes that the fluid phase can transfer energy (heat, momentum or mass) to the discrete phase but the discrete phase cannot transfer energy to the fluid phase. Two-way coupling assumes that both the fluid and discrete phases can exchange energy between one-another. Although one-way coupling is computationally less expensive than two-way coupling, erosion predictions in FLUENT can only be conducted if two-way coupling is implemented.

4.2.5 Solver Theory

In this work the pressure-based solver was used which operates by solving a pressure or pressure correction equation obtained through manipulating the continuity and momentum transport equations. The solution generates the pressure field from which other flow quantities can be derived. The other solver available is the density-based solver which calculates the density field from the continuity equation and the pressure field from the equation of state. The density-based solver is mainly used for high speed compressible flow containing large density gradients. While both approaches use the finite-volume approach, they each linearize and discretize the fundamental transport equations in different manners.

Spatial discretization for momentum and turbulent quantities are achieved using the Second-Order Upwind Scheme. The First-Order Upwind Schemes assumes that the cell-face quantities are identical to the cell-center quantities; however the Second-Order scheme uses a multidimensional linear reconstruction approach which considers the cell-center value and the gradient in the upstream cell. While

computationally more expensive, the Second-Order scheme can enable higher accuracy numerical simulations.

Gradient discretization was achieved using the Least Squares Cell-Based approach and pressure-velocity coupling was performed using the Pressure Implicit with Splitting Operators (PISO) algorithm. This approach, compared to the SIMPLE or SIMPLEC algorithms can provide a higher degree of the approximate coupling between the corrections for velocity and pressure.

In some cases, solution steering was implemented to achieve convergence quickly. This was performed by manually adjusting the under-relaxation factors (URFs). If the URFs are too low the solution will take a very long time to converge, however if the URFs are too high the solution will not reach convergence as oscillations will begin to occur. By starting the simulation with high URFs and decreasing them as the solution proceeds, convergence can be reached in a timely fashion.

The sections previously described should provide a reasonable introduction to the theory and models implemented and available in FLUENT. A more thorough description can be found in the ANSYS Workbench Documentation [118].

4.3 Geometry and Meshing

4.3.1 Dimensions of Jet and Flow Field

A quarter-symmetry 3D jet-impingement geometry, shown in Figure 4-2, was developed using ANSYS DesignModeler.

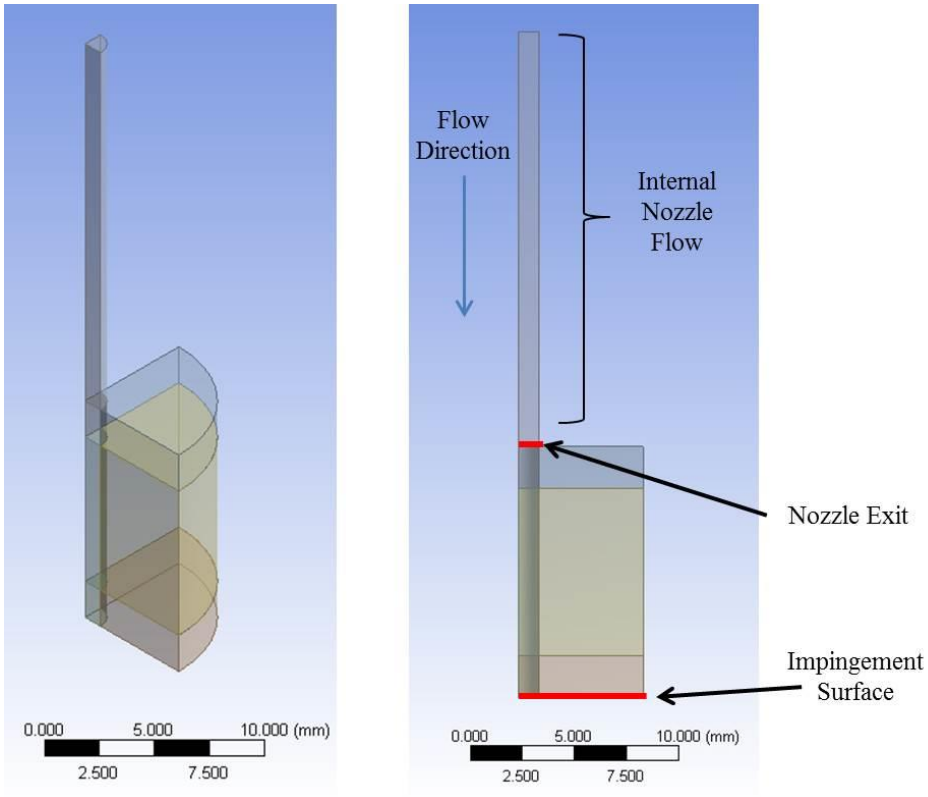

Figure 4-2 Overview of quarter-symmetry jet-impingement geometry

A 1.98mm diameter nozzle was chosen and the distance between the nozzle exit and the impingement surface was set at 12mm. In the image above it can be seen that the flow field is divided up into various segments. This aids in the meshing process, to be discussed later in this chapter. The specific dimensions of the simulation model are shown more explicitly in Figure 4-3.

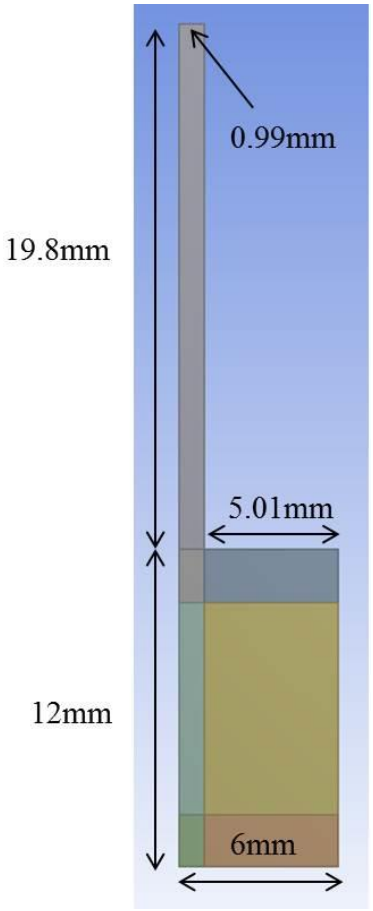

Figure 4-3 Dimensions of jet-impingement simulation

The fluid will travel a length 10x the nozzle diameter before exiting in order for the flow to fully develop. To capture all relevant information pertaining to the jet impact, a radius of 6mm was chosen. Information greater than 6mm away from the nozzle center was found not to affect the localized flow field near the impingement region. As such, the far-field was truncated to reduce computational efforts.

4.3.2 Boundary Conditions

Figure 4-4 shows the boundary conditions chosen to set up this model.

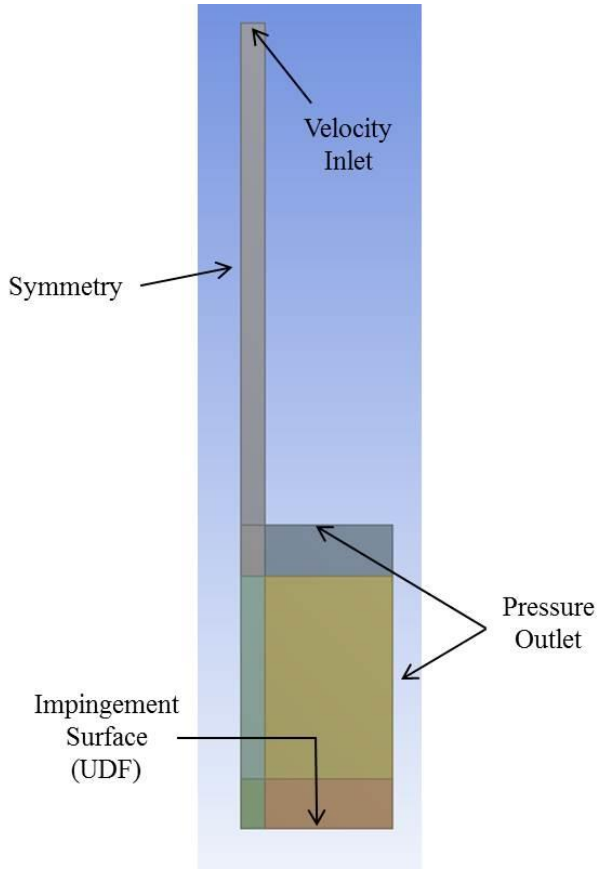

Figure 4-4 Boundary conditions for jet-impingement model

The velocity inlet condition assumes a constant velocity across the domain entrance. As stated previously, a length 10x the nozzle diameter was chosen in order for the flow to reach a fully developed state before exiting the nozzle. A pressure outlet boundary condition was chosen to represent the far-field flow boundary. At these locations, a value of 0 Pa was chosen to represent the relative pressure compared to the high pressure impingement region directly below the nozzle. The impingement surface boundary condition was represented by a custom written user-defined function, more of which will be explained later in this chapter. In short, the UDF was written to optimize the particle impact data collection process.

The symmetry condition was chosen to minimize computational effort by assuming the flow field is pseudo-axisymmetric about the nozzle center. One alternative to the 3D flow simulation was to perform a 2D axisymmetric simulation. Although this would significantly reduce computational effort, much of the information pertaining to localized particle impact parameters would be lost due to the reduction of impingement area.

4.3.3 Meshing

In order to discretize the flow domain, ANSYS' built in meshing program was used. As stated earlier, the flow domain was divided up into seven parts, each of which was meshed separately using the 'MultiZone' method. This facilitated better control over localized and global meshing parameters such as element sizing and bias type. Additionally prism-type mesh elements were used, shown in Figure 4-5, which allowed for a smoother mesh construction compared to hex-elements.

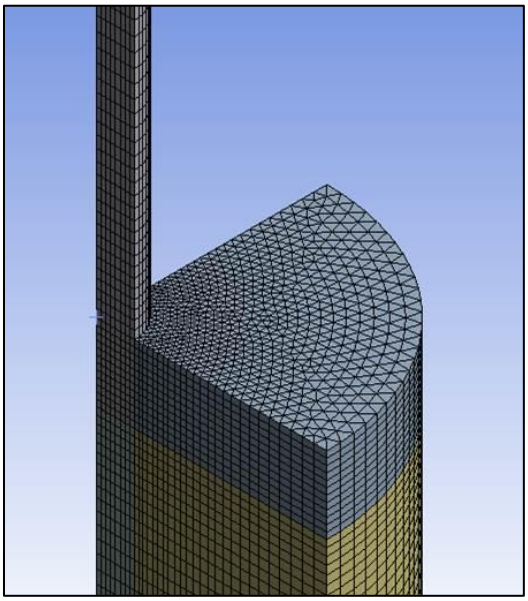

Figure 4-5 Mesh constructed using prism elements

Mesh size was controlled by explicitly defining how many elements were to fit on each line or curve of the mesh. This enabled a systematic method through which the number of total elements can be changed. For example, in Figure 4-6, the lines labeled ‘A’ and ‘B’ were both defined to contain 25 elements. As can be seen, the mesh density of line ‘B’ changes across the length while the mesh density of line ‘A’ stays uniform across the length. This was conducted by defining line ‘B’ to exhibit a density bias. In this example a bias of 3 was defined which states the size of the right most element is 3x the size of the right most element. By altering these different parameters, total meshing control of the domain can be obtained.

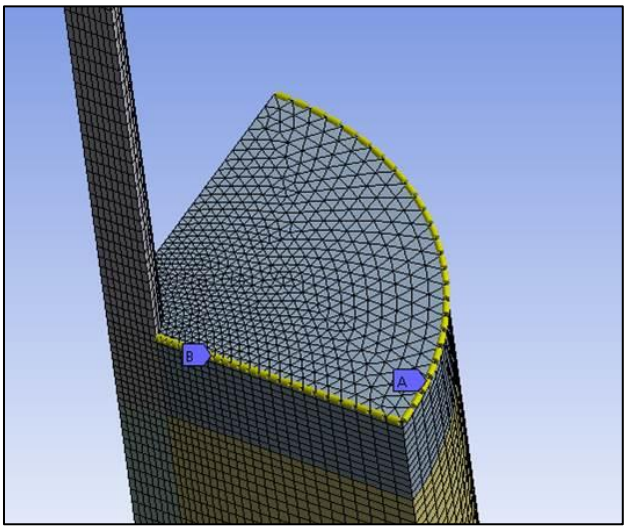

Figure 4-6 Mesh size control

Establishing an appropriate mesh density is vital when conducting CFD simulations for two primary reasons. If the grid is too coarse, small-scale details of the flow field may be neglected. Furthermore, if the grid is too dense the computational effort becomes exorbitant. The above example shows a relatively course mesh however an appropriately sized mesh for the simulation is correctly identified through a mesh independency study. This is conducted by running

simulations using different mesh sizes and monitoring the flow solution. A solution is said to be ‘mesh-independent’ when the monitored variables maintain their value as the mesh is increased further.

4.3.4 Convergence Criteria

Prior to discussing the mesh independency study, convergence criteria will be identified. As a simulation transpires, the flow field changes and values are updated each iteration. Eventually the changes that occur between iterations become smaller and smaller to the point when these changes become negligible. When this occurs the simulation is said to be converged. However, explicit convergence criteria cannot be universally defined across every type of CFD simulation although certain guidelines can be commonly applied. As such, the criteria used to identify convergence in these particular simulations will be stated.

During the simulations, four different monitors were used to check for convergence: the maximum velocity, a volume integral of the velocity field, a volume integral of the phase volume fraction and residuals. The maximum velocity monitor tracks the absolute magnitude of the velocity anywhere in the flow field while the volume integrals are computed by summing the product of the cell volume and the selected variable across the entire flow field. Essentially, the volume integrals provide a metric by considering every element in the flow field. Residuals were used as a secondary means of identifying convergence due to the fact that certain mesh densities yielded oscillating solutions even though the other monitoring points suggested convergence.

Convergence was achieved when the three volume monitoring points reached a steady value, shown in Figure 4-7, and when all residuals dropped below 10^{-3}. In cases of high mesh density, such as the simulations containing greater than 500K elements, the residuals dropped below 10^{-4} well before the other monitoring points achieved convergence. In the coarser meshes however, solution oscillations prevented the continuity residual from dropping to this point. While the coarser meshed simulations were conducted as part of the mesh independency study, difficulty in achieving convergence further justified the need for a finer mesh.

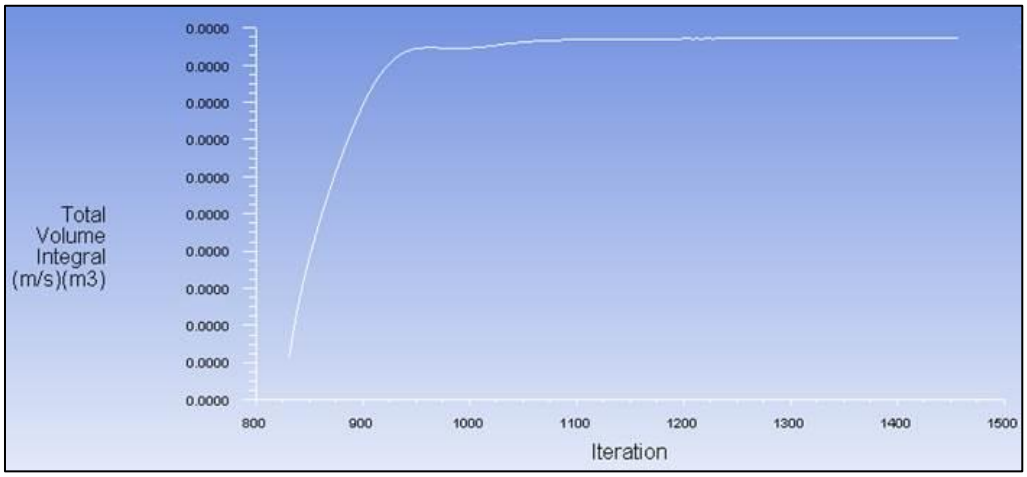

Figure 4-7 Convergence achieved by monitoring volume integrals

4.3.5 Mesh Independency Study

The process for identifying mesh independency was conducted by running the same simulation, including all boundary conditions, at different mesh densities and monitoring the outputs. The outputs used to track the effect of mesh density were maximum velocity and the volume integrals of the velocity field and phase volume fraction. A total of seven different mesh densities were used as part of this study with

the resulting total number of elements ranging from approximately 24,700 to 2,050,000. For all simulations, 20 m/s was assumed to be the inlet velocity.

Figure 4-8 shows the results of the mesh independency study indicating the chosen mesh of 936,950 elements to perform further studies with.

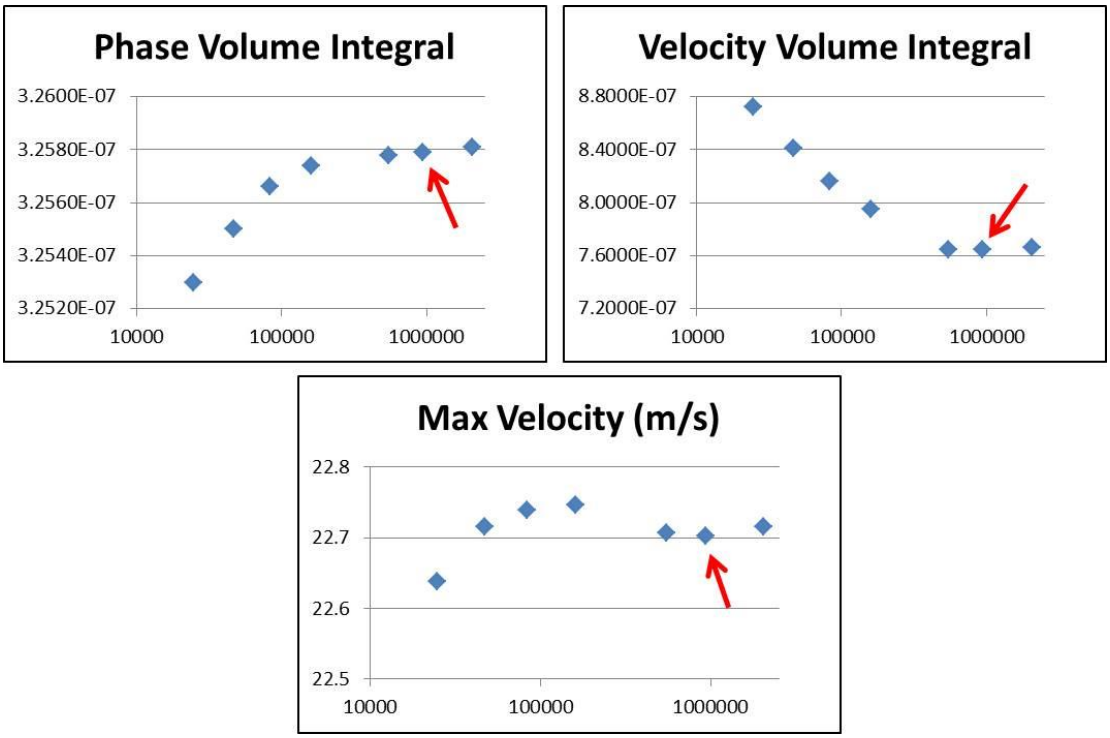

Figure 4-8 Results of mesh independency study indicating chosen mesh

In some instances higher mesh density does not always equate to higher accuracy simulations. For example, if simulations were performed using higher density meshes than those performed in this independency study, there would likely be a divergence of the monitored quantities. As such this type of study is necessary in order to identify how coarse a mesh needs to be as opposed to simply choosing a very dense mesh.

4.4 Flow Field Solutions

Using the 936,950 element mesh found from the independency test, a series of flow simulations were conducted at different inlet velocities and fluid viscosities, the latter of which was implemented by assuming different ratios of Propylene Glycol / Water (PGW) solutions. For the simulations in which velocity was altered, pure water was assumed to be the fluid. Table 4-1 lists the physical properties of the fluids used in the simulations, taken at 34ºC. Preliminary simulations were run assuming material properties taken at room temperature (23ºC) however experimental tests, discussed in later chapters, revealed that heating of water occurs due to the mechanical action of the pump and motor. As such, the simulations were revised and run assuming material properties taken at the same temperature of the experimental tests, 34ºC. The properties of different ratios of PG solutions were determined by using a simple volume-fraction approach.

Table 4-1 Material properties of fluids used, 34ºC

Fluid	Density (kg/m^3)	Viscosity (kg/m-s)
Water	994.4	0.0007337
10% PG	997.6	0.003277
25% PG	1002.3	0.007093
50% PG	1010.2	0.013452
100% PG	1025.9	0.02617

Seven different simulations were conducted, shown in Table 4-2, to study the effects of inlet velocity and fluid viscosity on the flow field. In the process of conducting these simulations, the solution from one simulation served as the initial

conditions for another. This significantly reduced computation time and enabled the solutions to converge using less manual solution steering.

Table 4-2 CFD simulations conducted

Simulation #	Velocity (m/s)	Fluid	Reynold's Number
1	20	Water	53700
2	25	Water	67100
3	30	Water	80500
4	40	Water	107000
5	40	10% PG	24100
6	40	25% PG	11200
7	40	50% PG	5950

For the purposes of simplicity and brevity, the flow solutions from simulations 1, 4 and 7 according to Table 4-2 will be discussed. In order to depict differences and similarities between flow fields, the quantity contours will be shown across the symmetry plane.

As stated previously, the VOF model enables two immiscible phases to be included. Contours of the air volume fractions for each of the three simulations are compared in Figure 4-9 where blue corresponds to the fluid phase and red corresponds to air phase.

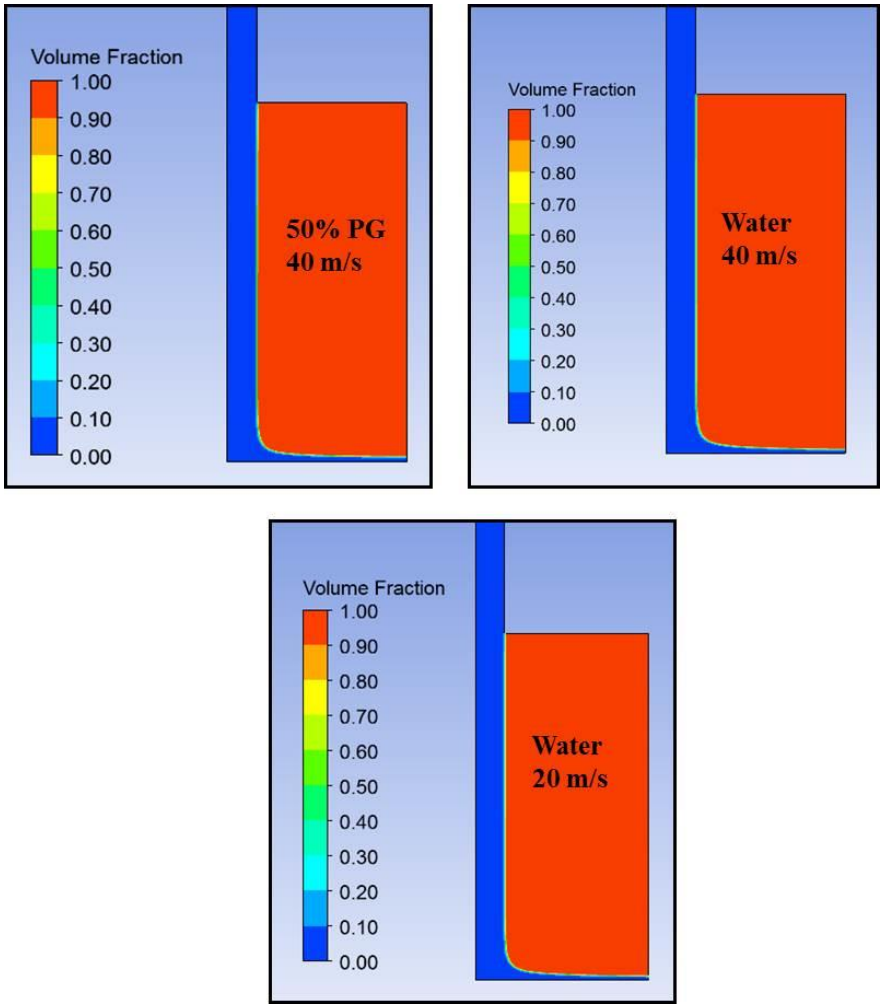

Figure 4-9 Contours of air volume fraction for different flow field solutions

The first observation is that the flow fields are nearly identical and essentially indistinguishable. At the relatively low velocities of these simulations, drastic qualitative changes should not occur.

Figure 4-10 compares the velocity field of the 20 m/s and 40 m/s inlet jet velocity simulations where fluid is assumed to be water.

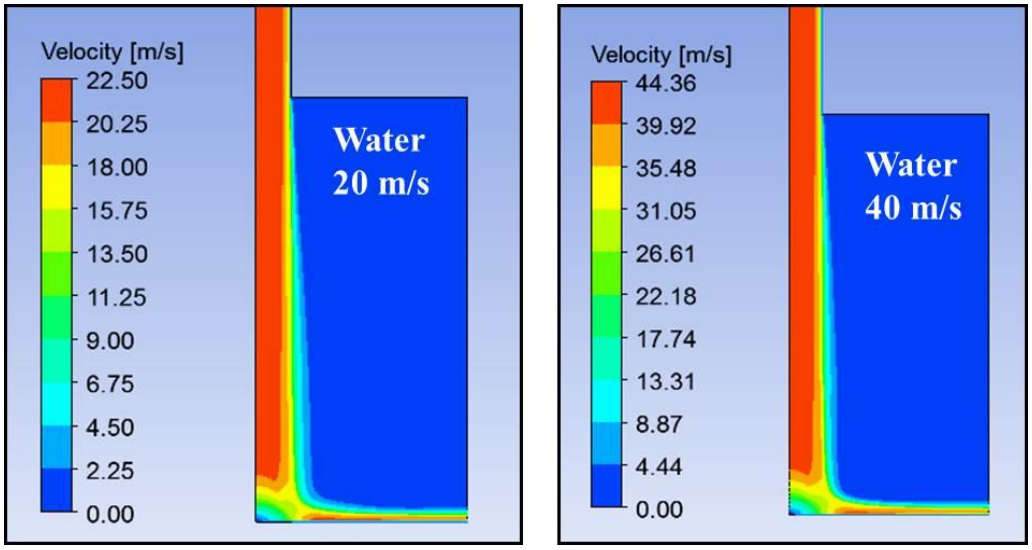

Figure 4-10 Velocity fields of 20 m/s and 40 m/s jet velocity, taken at 34ºC.

In both simulations the maximum velocity of the flow field is larger than the inlet jet velocity, however with respect to all qualitative observations both solutions appear identical. Comparing the velocity fields of both water and 50% PG, shown in Figure 4-11, both qualitative and quantitative differences exist.

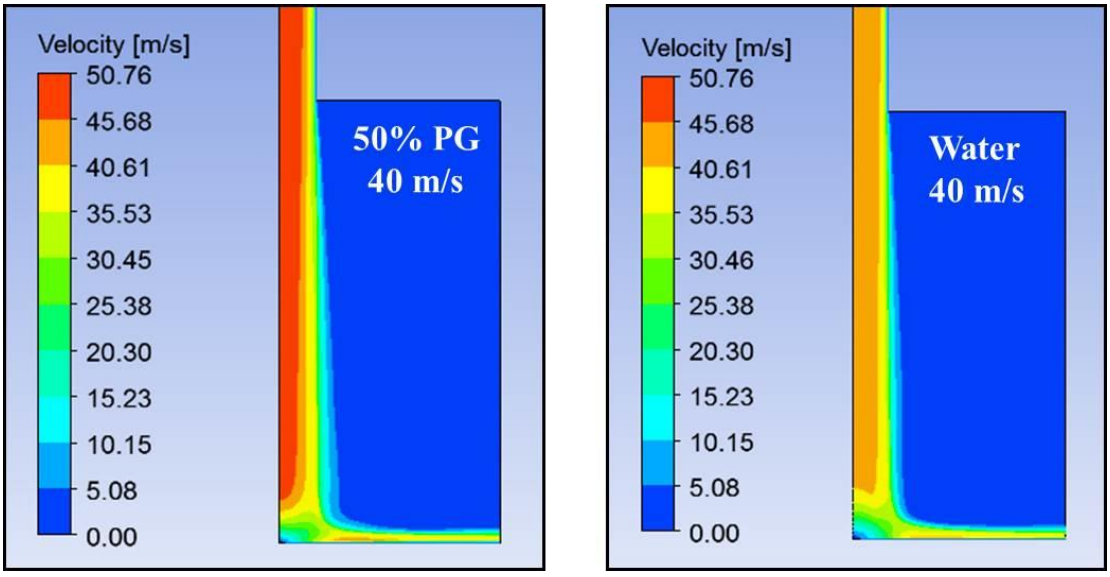

Figure 4-11 Velocity field of Water and 50% PG at 40 m/s jet velocity, taken at 34ºC

First, the maximum velocity is larger in the 50% PG fluid compared to pure water. According to Figure 4-12 as the percentage of PG in the solution is increased, the resulting Reynolds number of the jet decreases and the flow transitions from a turbulent flow regime to a laminar flow regime. As this transition begins the velocity profile becomes fuller, as depicted in Figure 4-12. In addition, the localized velocities of the flow field are affected by the fluid properties which will ultimately affect the particle impact parameters.

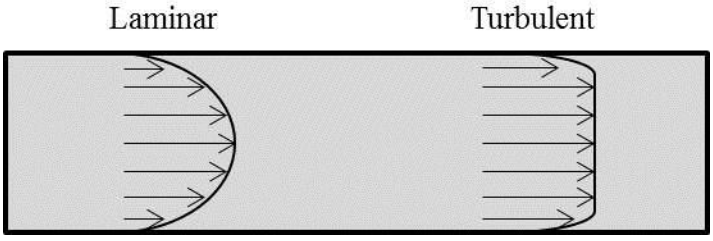

Figure 4-12 Laminar and turbulent velocity profile in tube

One interesting prediction concerning erosion can be made from qualitatively analyzing the flow field solutions. For example, by assessing the 40 m/s water solution shown in Figure 4-13, one can identify the region near the surface that contains a local maximum velocity.

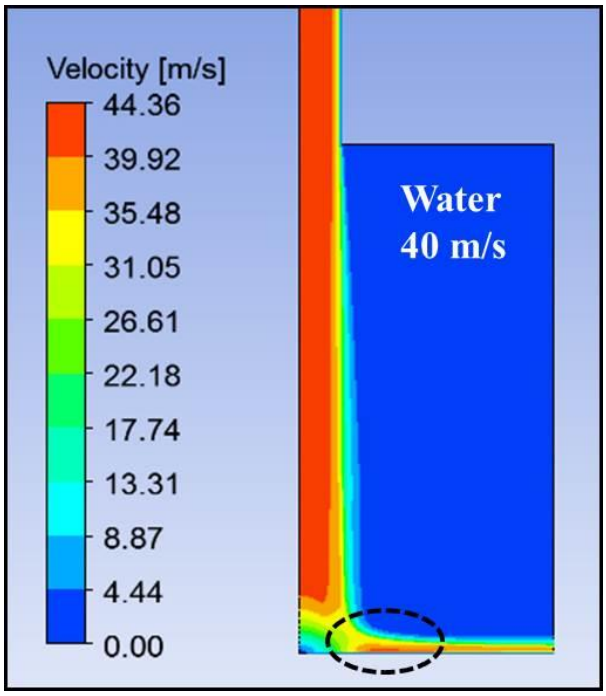

Figure 4-13 Region of high velocity near surface suggests location of maximum erosion

It can be predicted that this location would correlate to the region of maximum erosion. On the other hand, the stagnation region can be clearly identified as the region directly under the impinging jet where the velocity of the fluid approaches zero and it can be predicted that this region would contain minimal impacts. One caveat to this would be in the case of larger particles where the momentum of the particle would be too large to follow along the fluid streamline resulting in a direct impact in the stagnation region. This prediction would also fall in line with the work of Wang et. al. [92] who studied the mechanisms of micro-hole formation due to an abrasive-laden impinging jet.

4.5 Implementation of Particle Tracking using Discrete Phase Modeling

The main purpose of developing the abovementioned CFD simulations is to enable localized particle impact information to be gathered. As discussed in the literature review section the main parameters influencing the amount of material removed for a single particle impact are impact velocity, impact angle and particle size. While particle size can be experimentally controlled, impact velocity and impact angle can be determined via simulation efforts.

While FLUENT can easily track particle motion through the flow field, there is no built-in way to obtain, store and analyze particle impact information. As such, two User-Defined Functions (UDFs) were written to aid in this process and an additional UDF was written to hook in custom erosion models. This section will discuss how FLUENT's discrete phase model was implemented and how the UDFs operate to gather relevant data.

4.5.1 Injection Parameters

FLUENT enables the user to explicitly define properties of the discrete phase including start positions, velocities, size or size distribution of the particles, concentration loading, etc. The injection parameters serve as the initial conditions for the discrete phase and, once released, FLUENT calculates the trajectories of the particles throughout the fluid phase. The particles were chosen to be inert, alumina (Al_2O_3) particles with a uniform diameter distribution. Table 4-3 lists the following point-properties used for this injection.

Table 4-3 Point properties for particle injection

X-Position (m)	0
Y-Position (m)	0.0198
Z-Position (m)	0
Diameter (m)	Depends on particle size
Azim. Start Angle (deg.)	270
Azim. Stop Angle (deg.)	360
X-Axis	0
Y-Axis	1
Z-Axis	0
Velocity Magnitude (m/s)	0
Cone Angle (deg.)	0
Radius (m)	0.00099
Total Flow Rate (kg/s)	Depends on particle concentration

4.5.2 Particle Track Independency Study

Steady state simulations in FLUENT solve for particle tracks (also referred to as streams) as opposed to trajectories of individual particles. In this manner the number of particle tracks and a total particle mass flow rate are defined. However, due to the stochastic nature of particle motion in turbulent flow fields and in conjunction with the DRW model, enough particle tracks must be specified in order to establish particle-track independency. This was determined in a similar fashion as the number of mesh elements required. Essentially, a series of simulations were run (30 m/s water with 10μm alumina particles) using a generic erosion model and the maximum erosion rate along the impingement surface was tracked. Through the study, the results of which are shown in Figure 4-14, it was found that 320,000 particle tracks were necessary to yield a particle-track independent erosion simulation.

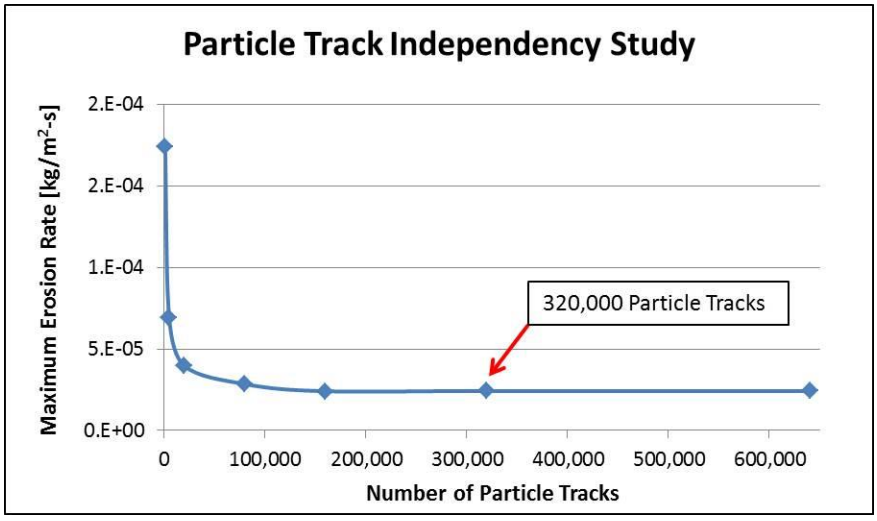

Figure 4-14 Results of particle track independency study

4.5.3 Development of User Defined Functions

A user-defined function is a custom script written in C that can be loaded into FLUENT to enhance and/or customize standard features. More information on the capabilities, limitations and implementation strategies can be found in the ANSYS Help Documentation [118]. In this work three UDFs were written and they all incorporate the DEFINE_DPM macro. This section will simply describe the purpose and function for each UDF, however the complete code will be included in Appendix C.

4.5.3.1 DPM Erosion Model

FLUENT enables user-defined erosion models to be hooked into the software using the DEFINE_DPM_EROSION macro. These types of UDFs calculated the mass of material removed for a single particle or particle track impact given the impact velocity, impact angle and particle or particle track mass flow rate.

Generically, the erosion rate for a given cell face on the impingement surface can be defined as:

$$ER = \sum \frac{\dot{m}_p f(D) f(\alpha) f(V)}{A_{cell}} \tag{3-10}$$

where m_p is the particle mass flowrate of a given particle track and *f(D)*, *f(α)* and *f(V)* are all functions of the particle size, impact angle and impact velocity respectively. In addition, the summation is taken across all particles or particle tracks that impact the unit cell. In FLUENT the erosion rate is calculated as an erosion flux in units of kg/m^2-s. In order to convert this unit into a one-dimension erosion rate, such as m/s or μm/year, the erosion flux should be divided by the density of the substrate material.

4.5.3.2 DPM Boundary Condition

Through the DEFINE_DPM_BC macro, user-specified boundary conditions can be applied which execute every time a particle is found to impact the specified surface. This UDF was written to gather and store pertinent information specifically relating to particle impact characteristics such as impact velocity, impact angle, impact position and the number of times a specific particle track hits the surface. Each of these values were stored in a user-defined storage array associated with each particle track using the P_USER_REAL(p,i) macro where 'p' refers to the tracked particle and 'i' refers to the index of the array.

The index i = 0 was used to count the number of impacts for a specific particle track, therefore each time the UDF was called (each time the particle track results in an impact) the value stored at the i = 0 location would increment by 1. Indexes i = 1 through i = 10 were used to store the impact velocity for the first ten impacts.

Likewise, indexes i = 11 through i = 20 were used to store the impact angle for the first ten impacts. Tracking up to ten particle impacts was deemed appropriate as the contribution to erosion from more than ten impacts per particle was assumed to be negligible compared to the effect of the first couple impacts.

These simulations consider all geometries with reference to the standard XYZ Cartesian coordinate system. When storing the impact velocity, the magnitude of the velocity must be taken because some particle velocities are negative with respect to the positive XYZ directions. Likewise, the impact angle is determined by considering the impact velocity vector and the cell face normal direction vector and is defined as the angle between the impingement surface and the impacting particle track.

One concern regarding the DEFINE_DPM_BC macro is that the rebound conditions of a particle must be explicitly defined, meaning the rebound angle and the rebound velocity need to be calculated within the UDF. This enables the user to also define coefficients of restitution for both the normal and tangential directions. For this work it was assumed that these coefficients were both one, primarily due to the assumption that the fluid flow largely dictates the particle motion. Even if a slight amount of kinetic energy was removed from the particle this would likely be negligible considering how closely coupled the particle motion is to the fluid motion. In cases where the medium is gaseous or if the particles are quite large, then it may be wise to introduce more accurate coefficients of restitution.

Preliminary CFD simulations suggest that the majority of erosion is due to the first few impacts per particle track as the impact angle and velocity decrease once the particles are swept away in the tangentially moving fluid. Additionally, Mansouri et

al. [121] showed that tracking six impacts per particle track slightly under predicted erosion rates with 25μm particles by a factor of 0.87 while tracking up to 30 impacts per particle over predicted erosion rates by a factor of 2.74. For this work it was assumed that ten impacts per particle track would be sufficient to capture the overwhelming majority of erosion-pertinent impacts.

4.5.3.3 DPM Sampling Output

While the DEFINE_DPM_BC macro gathers and stores particle impact data, the DEFINE_DPM_OUTPUT macro outputs the stored data into a *.dpm file which can be converted to a *.dat or a *.txt file for post-processing. In FLUENT, the sampling can be taken at any boundary through which the particles pass through, and for this work that boundary was taken to be the outlet of the simulation. In this UDF once each particle passes through the outlet boundary all the velocity, impact angle and position variables are printed to the sampling output. This file is then imported into a MATLAB code for post-processing.

4.6 Particle Impact Results

This section shows the results of the simulations previously discussed to depict how altering the jet velocity, particle size, fluid viscosity and particulate concentration effect particle impact characteristics. For the purposes of data presentation, averages of the 320,000 particle tracks will be given for each impact for each of the impact characteristics. The impact ratio is defined as the ratio of the number of impacts to the total number of particle tracks.

In order to better relate the results of these simulations to the experimental work discussed in later chapters, the particle sizes used in these simulations were the average particle sizes measured from a particle size distribution analysis. Samples of nominally sized 2.5μm, 5μm, 10μm and 20μm alumina particles were acquired from Inframat Advanced Materials and sent out for independent particle size distribution analysis using a CILAS laser particle size analyzer. A comparison of the manufacturer specified average particle size and the independently measured average particle size used in the simulations are shown in Table 4-4. The raw data from these tests are included in Appendix B.

Table 4-4 Comparison of manufacturer specified and measured average particle sizes

Manufacturer (μm)	Measured and used in simulations (μm)
2.5	2.59
5	5.53
10	8.95
20	16.5

The 20μm particles were not measured using the particle size analyzer, but were rather approximated using SEM. An image of the 20μm particles are shown in Figure 4-15.

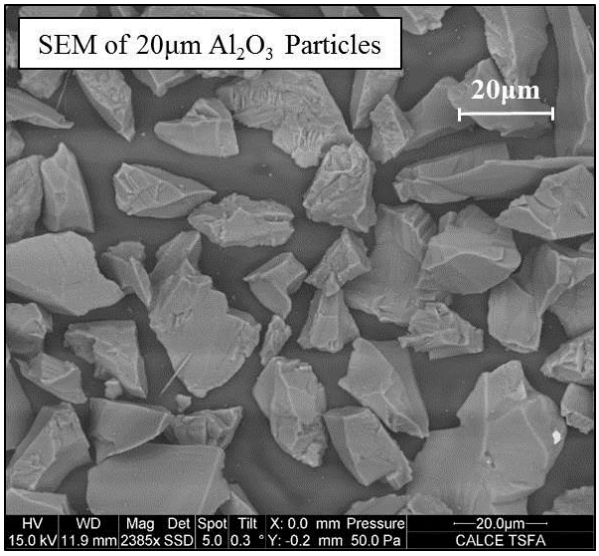

Figure 4-15 SEM image of 20µm particles

4.6.1 Effect of Jet Velocity

Figure 4-16 shows how changing the nominal jet velocity affects the impact velocity of the particles. One interesting observation is that, on average, the first impact has a lower velocity than the second impact for the 30 m/s and 40 m/s cases. This can be explained by the fact that as the particle approaches the surface the squeeze film slows the particle down resulting in a primary impact significantly below the nominal jet velocity. Upon rebound after the particle impacts the surface, the tangentially moving fluid sweeps the particle away and results in a second impact at a higher velocity in a direction more in line with the surrounding fluid.

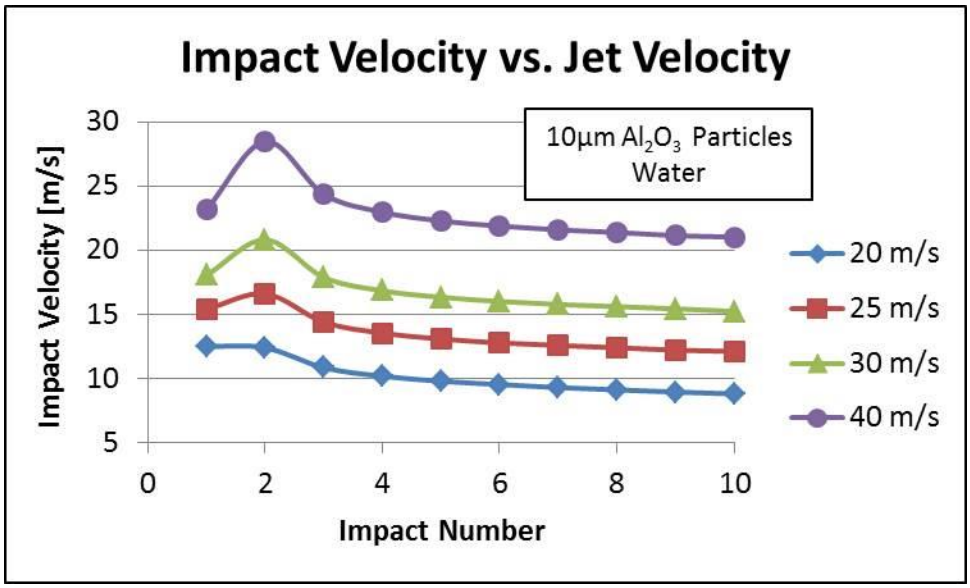

Figure 4-16 Particle impact velocity as a function of nominal jet velocity

After the first few impacts occur, the average impact velocity steadies out and slightly decreases as the impacts continue to occur. For the 20 m/s and 25 m/s cases the impact velocity does not increase on the secondary impact because the particles are more closely coupled to the fluid streamlines. As such, the squeeze film plays less of a role in slowing the particle down right before impact.

Figure 4-17 shows the particle impact angle as a function of different jet velocities. All impacts in each simulation occur at shallow angles. The first few impacts occur at larger angles because the fluid is changing directions from a normal impacting jet to tangentially moving fluid. However after the first few impacts the data suggests that the particles roll, bounce and scratch along the surface. This is evident from the shallow angle impacts occurring at relatively constant velocities for each jet velocity.

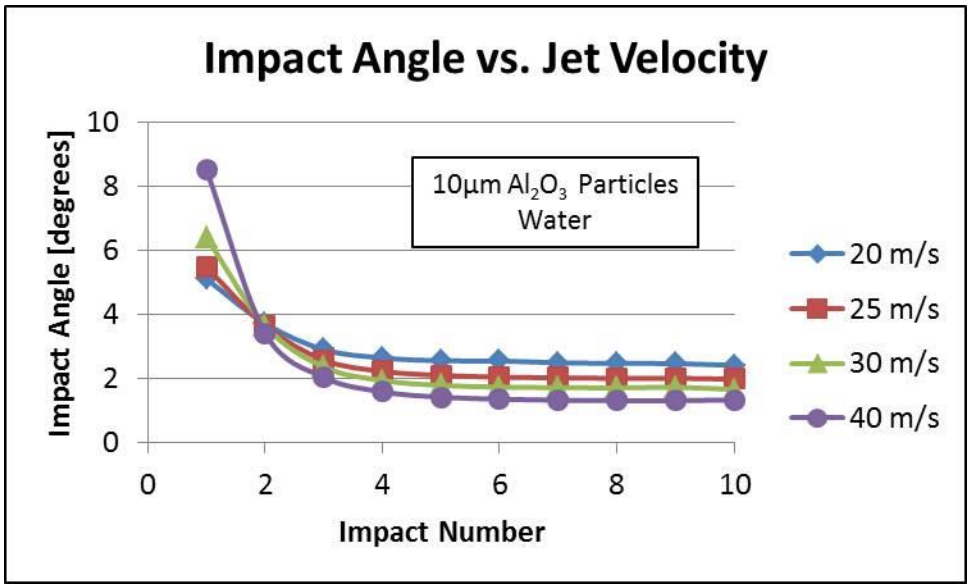

Figure 4-17 Particle impact angle as a function of nominal jet velocity

While it can be seen that the impact angle of the first impact for the 40 m/s jet is slightly higher than the rest of the jets, the shapes of the trends are relatively uniform. This suggests that the impact angle of the particles is not largely affected by jet velocity assuming all other properties are the same. For impacts 4 through 10, the impact angles within the 40 m/s case are less than that of the 20 m/s case. This can be attributed to the fact that particles exhibiting a larger impact would be swept away in the bulk fluid rather than being stuck in the slower moving squeeze film. This phenomenon can be seen in Figure 4-18 which shows why particles wouldn't likely impact the surface at higher impact angles in the tangentially moving fluid.

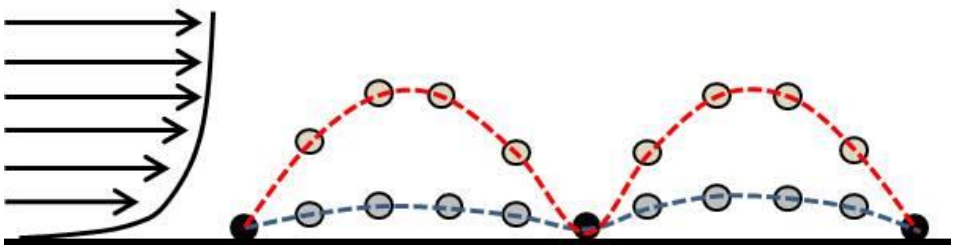

Figure 4-18 Comparison of high and low impact angles

The effects of the particle impact ratio can be seen in Figure 4-19. The first observation is that the general shapes of the trends are not significantly affected by jet velocity. Higher velocity jets do slightly result in a larger percentage of entrained particles that reach the surface, approximately 93% for the 40 m/s jet and 82% for the 20 m/s jet. High velocities result in a looser coupling between the particle trajectories and fluid streamlines and therefore makes it easier for the particles to diverge from the fluid streamline and impact the surface.

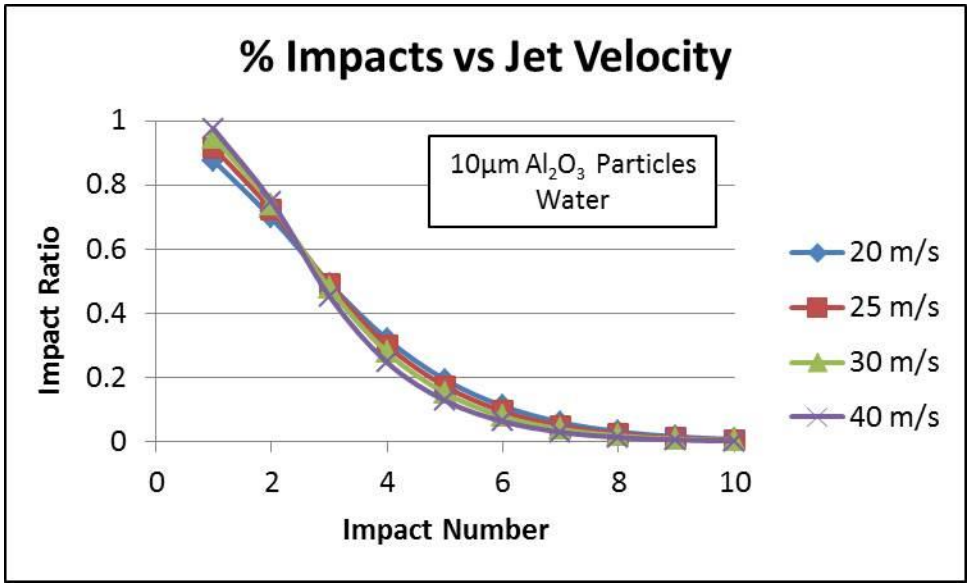

Figure 4-19 Particle impact ratio as a function of jet velocity

For subsequent impacts at all jet velocities, the number of particle tracks resulting in impacts uniformly decrease. This can be explained in a similar manner using Figure 4-18 where more and more particles are carried out of the squeeze film and swept away in the bulk moving fluid.

4.6.2 Effect of Particle Size

As described above, Figure 4-20 reinforces the notion that secondary and subsequent impacts play an import role in jet-impingement erosion scenarios.

Comparing the impact velocities for 10µm and 20µm particles, it can be seen that the 10µm particles result in a higher first impact velocity and a lower secondary impact velocity. This can be explained by also considering the results in Figure 4-21 which show the effect of particle size on impact angle.

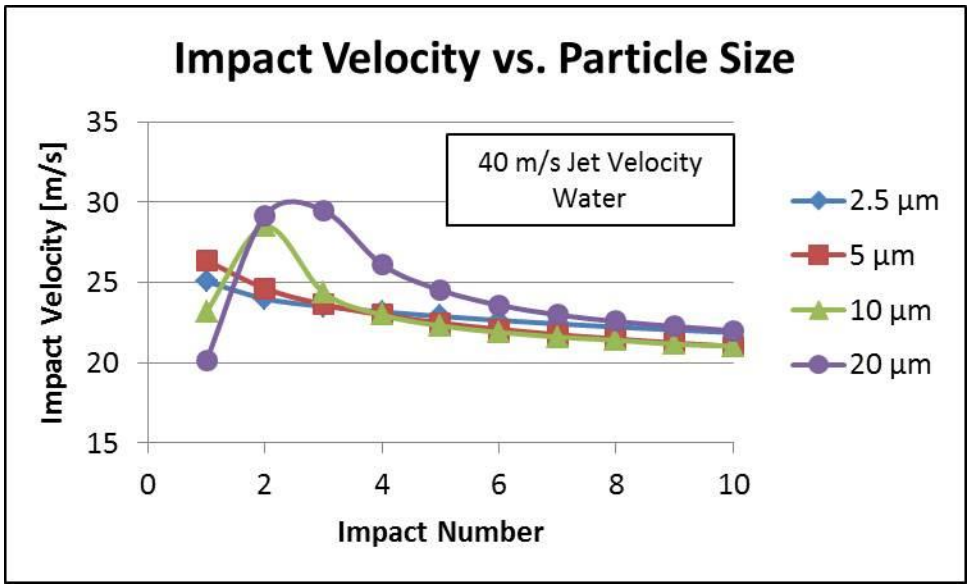

Figure 4-20 Particle impact velocity as a function of particle size

The first impact in the 20µm particle size case hits the surface at a relatively high angle compared to the other particle sizes. As such, the squeeze film has a greater effect on slowing the larger particles down. This can be further justified with the idea that larger particles have a greater surface area, and although FLUENT treats the particles as a point, an effective drag force is calculated and influences the trajectories of the particles. Additionally, at shallower impact angles the particle trajectories are more in line with the tangentially moving fluid and thus require less energy to change direction.

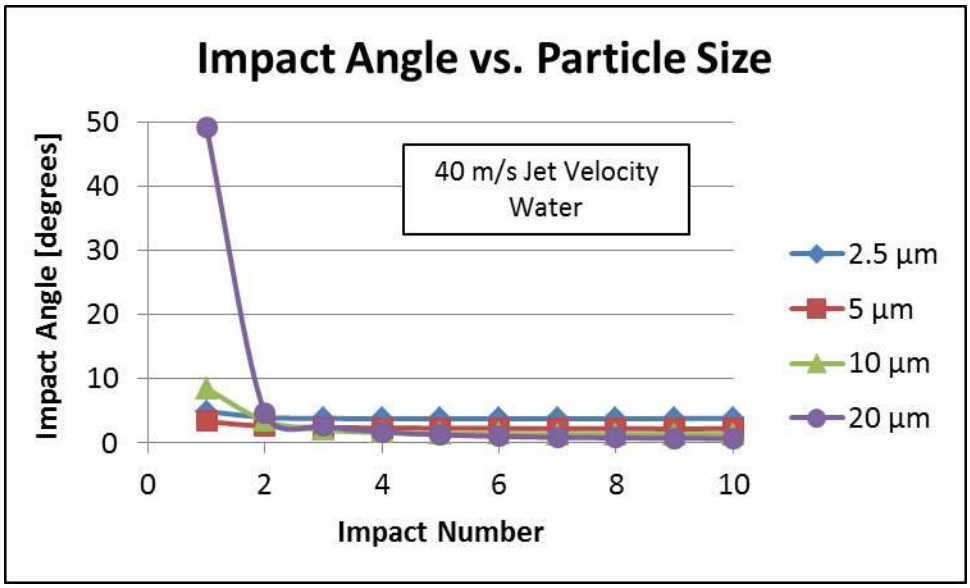

Figure 4-21 Particle impact angle as a function of particle size

It can also be seen that subsequent impacts still take place at shallow impact angles regardless of particle size. From this data, it can be seen that particle size greatly influences the impact angle of the first impact but has negligible effect on additional impacts.

Compared to the effect of jet velocity, particle size has a greater effect on the percentage of entrained particles that reach the surface as shown in Figure 4-22. For the 20µm particles, the data suggests that 100% of entrained particles reach the surface. As the particle size decreases, it can be seen that fewer particles reach the surface. In addition, it can be seen that subsequent impacts have fewer impacts associated with them for all particle sizes.

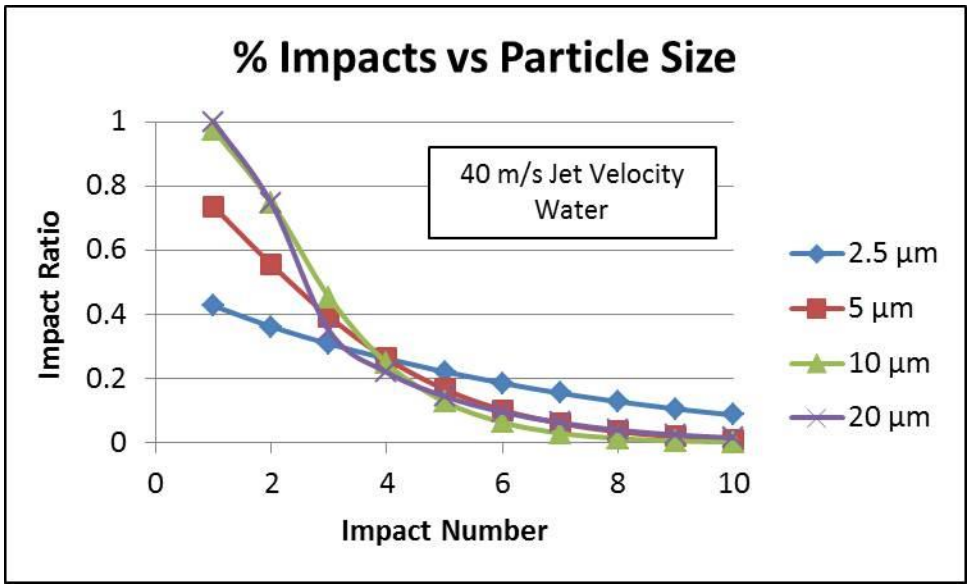

Figure 4-22 Particle impact ratio as a function of particle size

Looking at the curve for the 2.5µm particles, impacts 6 through 10 have a larger percentage of impacts compared to the curves from other particle sizes. This can be explained by the fact that smaller particles have a greater tendency to stay entrained in the squeeze film compared to larger particles. As suggested by Clark and Hartwich [81], the squeeze film not only slows down incoming particles but also acts to prevent particles from rebounding into the free stream fluid flow.

4.6.3 Effect of Fluid Viscosity

Figure 4-23 shows that particle impact velocity decreases as fluid viscosity increases for the same relative jet velocity and particulate loading. As previously discussed, this is due to the stronger coupling between particle trajectories and fluid streamlines.

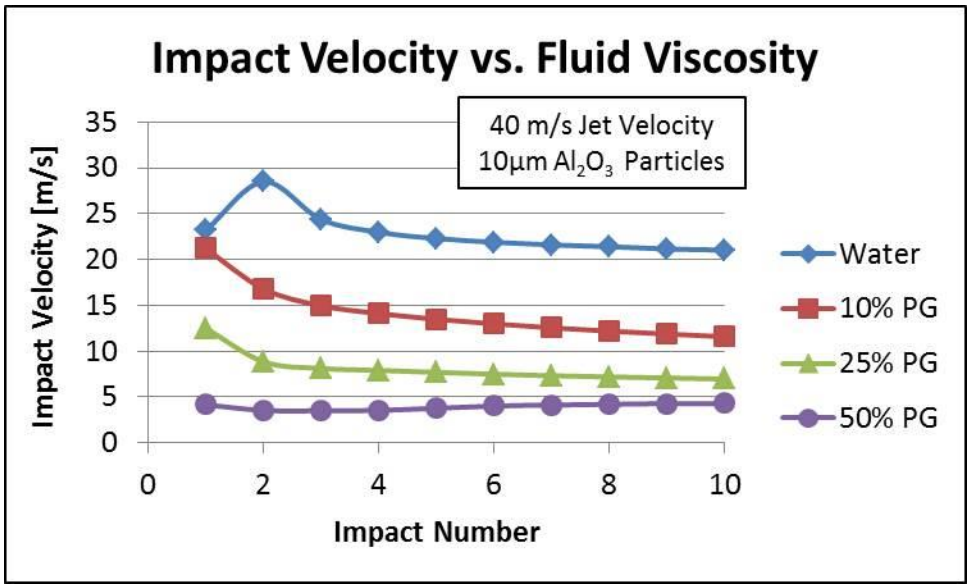

Figure 4-23 Particle impact velocity as a function of fluid viscosity

For the 50% PG solution cases, the impact velocity is significantly below that of the nominal fluid velocity suggesting that particles are trapped in the squeeze film and are not easily swept away by the tangentially moving flow. This would also suggest more of an abrasion wear mechanism as predicted by Clark et al. [81] where particles accumulate in the slower moving viscous film directly above the surface.

The relationship between particle impact angle and fluid viscosity is shown in Figure 4-24. The results seem somewhat counter-intuitive as a stronger coupling between particle and fluid would suggest a lower angle of impact for impingement scenarios. In order to justify the CFD results, the percentage of entrained particles that reach the surface must also be considered, shown in Figure 4-25.

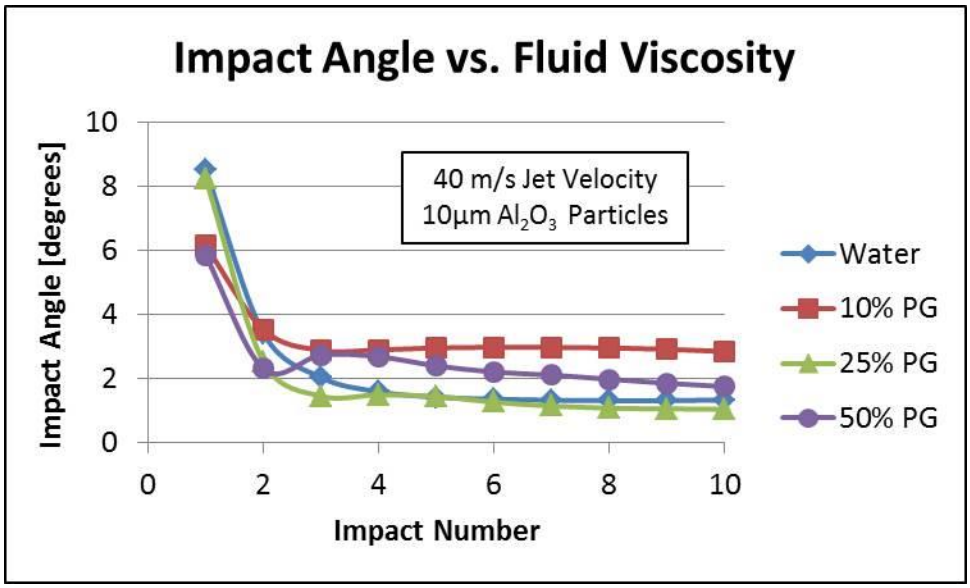

Figure 4-24 Particle impact angle as a function of fluid viscosity

The reason the first impact has a higher impact angle for more viscous fluids is likely due to the fact that in order for an impact to occur it must approach the surface at a higher angle. On average, particles approaching the surface at lower angles of impacts would likely get swept away by the bulk fluid. Because of this only higher particle impact angles are considered in the average for which each one of the data points represent. In addition, the stochastic nature of the particle trajectories due to the DRW model may account for some of the discrepancies, keeping in mind that the range of impact data in Figure 4-24 is only a few degrees.

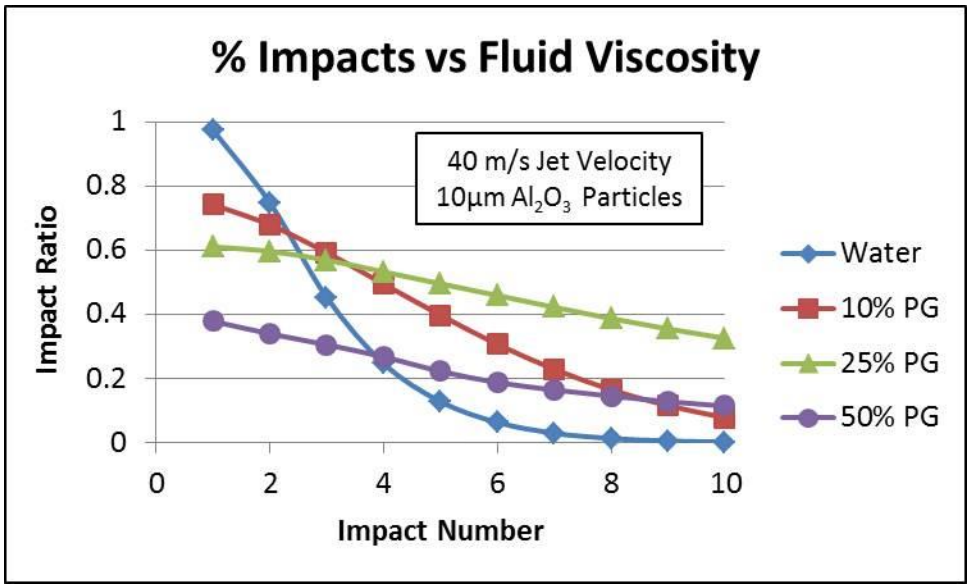

Figure 4-25 Particle impact ratio as a function of fluid viscosity

As the fluid becomes more viscous, fewer particle tracks have enough momentum to divert from the fluid streamlines which result in a surface impact. Reflecting on how fluid viscosity affects particle impact characteristics, it can be predicted that more viscous fluids can significantly reduce erosion. In the case of high heat flux cooling loops, of which 50% PG/W is a common fluid, entrained particles would impact the surface at low velocities compared to less viscous fluids like water.

4.6.4 Effect of Particulate Concentration

In the simulations presented here the particulate concentration of the slurry is defined as a particle mass flow rate. For example, in the case of the a 40 m/s jet flowing through a 1.98 mm nozzle the mass flowrate is calculated:

$$\left(40\frac{m}{s}\right)\left(\frac{\pi}{4}*0.00198^2\right)\left(998.2\frac{kg}{m^3}\right)=0.12294\frac{kg}{s} \quad (3\text{-}11)$$

However, considering the quarter symmetry geometry this value must be divided by a factor of four to give: $3.0735x10^{-2}$ kg/s. In the case where particle concentration is assumed to be 0.1% by mass, this would yield a particle mass flow rate of:

$$\left(3.0735x10^{-2}\frac{kg}{s}\right)(0.001) = 3.0735x10^{-5}\frac{kg}{s} \quad (3\text{-}12)$$

This value is the total particulate mass flowrate of all particle tracks. Therefore to calculate the mass flowrate of an individual particle track this value would be divided by the number of particle tracks in the simulation. In theory, doubling the particulate concentration should yield twice as much mass removed because twice as many particles per unit time would be traversing through a given particle stream. In addition, the major assumption when implementing Lagrangian particle tracking is that particles are non-interacting, therefore the interaction of particle tracks should not be considered.

4.7 Conclusion

This chapter outlines the development and results of a series of 3D quarter-symmetry jet-impingement simulations constructed using ANSYS FLUENT 16.1. The main purpose of these simulations was to obtain particle impact data, specifically particle impact velocities, impact angles and the percentage of entrained particles that reach the surface.

First, a brief overview of CFD theory was presented and the main models used in the simulations were discussed. Multi-phase modeling is handled using the VOF model which tracks the boundary between the fluid and surrounding air. Turbulence

is modeled using the SST k-ω turbulence model assuming standard values and constants. The DRW model is included in the Lagrangian particle tracking calculation as this enables the stochastic nature of particle trajectories in turbulent flow fields to be considered.

Next, a thorough description of the geometry, boundary conditions, meshing properties and convergence criteria was given. Through the mesh independency study it was found that independency was achieved at slightly less than 1 million elements. A series of seven different flow field simulations were conducted at different fluid velocities and viscosities assuming different mixtures of propylene glycol / water solutions.

A series of UDFs were written to gather and store particle impact characteristics as FLUENT does not have this inherent capability. Through a particle-track independency study using a generic erosion model, it was found that 320,000 particle tracks needed to be simulated in order to produce track-independent erosion results. For each of the 320,000 particle tracks, up to ten impacts were considered. The UDFs were written so that an output data file could be imported into MATLAB for post-processing.

The results of these simulations were presented in a series of graphs that show how nominal jet velocity, particle size and fluid viscosity affect localized impact characteristics. To summarize a few points:

- Particle impact velocity is less than the nominal jet velocity due to the dampening action of the squeeze film.

- In some cases the velocity magnitude of the second impact is larger than the first due to the tangentially moving fluid and dampening action of the squeeze film.
- Increasing fluid viscosity magnified the effect of the squeeze film and further reduces impact velocity.
- Impact angles for particles less than 10μm are small, typically less than 6º.
- Impact angles of subsequent impacts after the first suggest that particles are rolling, bouncing and scratching along the surface
- The 20μm particles yielded significantly higher impact angles on the first impact, approximately 45º, due to the weaker coupling between particle trajectory and fluid streamline.
- In the simulations with lower jet velocities, smaller particle sizes, and higher fluid viscosities, a smaller percentage of entrained particle tracks resulted in impact.
- Due to the assumptions inherent in steady-state particle tracking in CFD, concentration affects the mass flow rate of individual particle tracks. As such, the mass of material removed is expected to vary linearly with concentration.

5 DESIGN OF SLURRY EROSION TEST APPARATUS

This chapter will discuss the design and development of the jet-impingement slurry erosion test apparatus.

5.1 Overview

Multiples types of erosion test setups exist, each of which enable the erosion of different materials to be studied under a variety of conditions. Some examples of these test setups include “sandblasting” rigs, such as those used by Sheldon and Finnie [39] [40], Wiederhorn and Hockey [63], Telling and Field [72], as well as many others. With these types of test setups the velocity of particles can be determined directly from the air pressure. In addition, the impingement angle of all the particles in the stream is assumed to be relatively constant.

In the case of particles entrained in a fluid, one method of studying erosion is through the use of a slurry pot erosion rig, as was employed by Clark and co-workers [77] [79] [78]. While this type of test rig allows for the effect of different fluids to be considered, the major limitation is with regards to discerning the particle impact velocity.

A final method used to study slurry erosion of various materials is the jet-impingement apparatus, as will be discussed in this chapter. With regards to electronics cooling, jet-impingement type architectures are quite prevalent [29] and enable highly localized cooling of hot spots as well as bulk cooling of cold plates. Due to the wide range of applicability and ease of parameter control, this type of slurry erosion test rig was constructed to study the erosion potential of silicon and. An

overview of the jet-impingement test rig used in this research is shown in Figure 5-1, with a schematic shown in Figure 5-2.

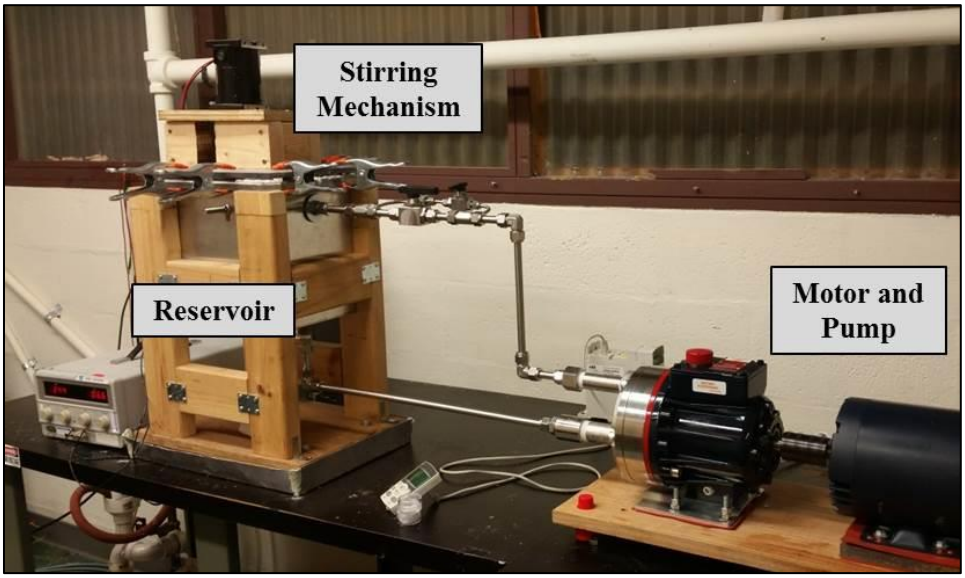

Figure 5-1 Overview of slurry erosion test apparatus

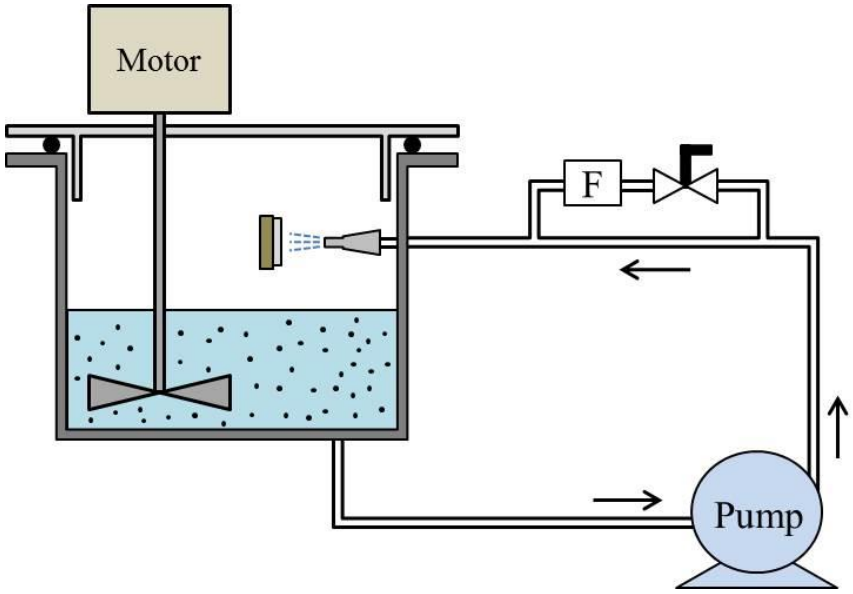

Figure 5-2 Schematic of test rig

The primary subsystems consist of the motor and pump, reservoir and plumbing, stirring mechanism, and sample holder. Each of these subsections will be discussed in detail throughout this chapter.

5.2 Reservoir, Plumbing and Sealing

The reservoir was constructed of 316 Stainless Steel, had dimensions of approximately 11” x 8” x 10.5” (LxWxH) and was purchased by Stainless Steel Fabricators, Inc. A drain was fabricated in the bottom of the reservoir, shown in Figure 5-3 by welding a half coupling in place. This facilitates the transition from reservoir to the compression fitting based plumbing network. Additionally, the nozzle enters the front of the reservoir through a bulkhead fitting also shown in Figure 5-3.

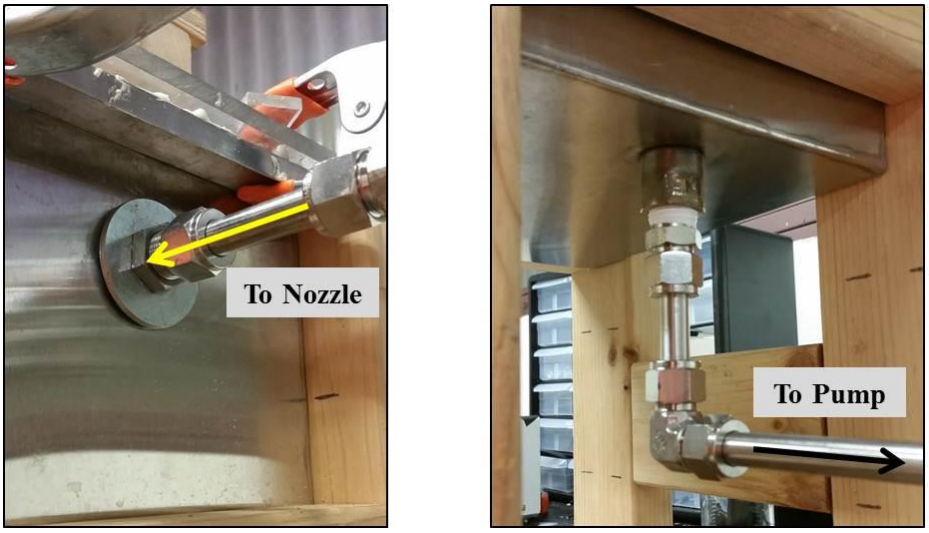

Figure 5-3 Bulkhead fitting leading to nozzle (left) and drain welded to reservoir (right).

The cover was made of 3/8” thick acrylic. Vertical side walls were attached to the underside of the cover to minimize direct splashing of the slurry near the O-ring. The O-ring was made of Viton Fluoroelastomer to ensure that the test setup chemically compatible with a variety of glycol based fluids that may be tested. Additionally the O-ring was looped around the flanges and was attached using superglue and Gorilla Glue®. A schematic cross section of the reservoir, O-Ring and cover is shown in Figure 5-4.

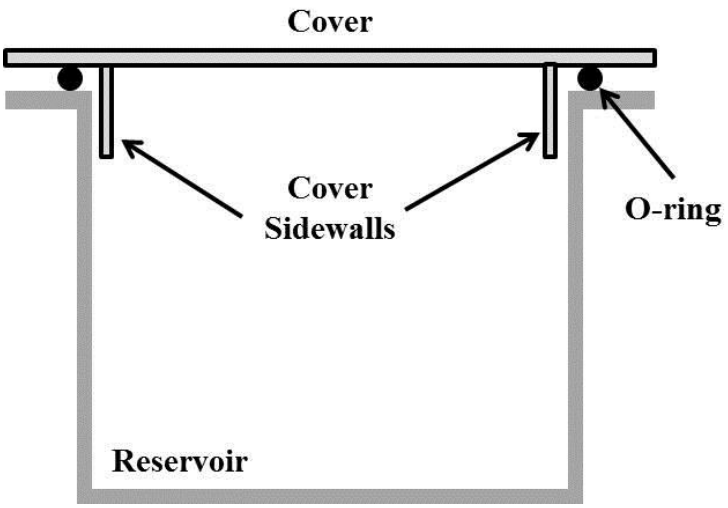

Figure 5-4 Schematic cross-section of reservoir, cover and O-ring.

A number of spring clamps hold the cover to the reservoir, compressing the O-ring. The test setup was originally designed using a glass cover; however sealing the reservoir proved challenging and issues with cracking the glass were common.

A small hole was drilled in the back of the reservoir towards the top to prevent the buildup of pressure. Preliminary testing indicated a temperature rise of the fluid caused by the motor and pump. A consequence of this was increased pressure in the reservoir making sealing difficult. The pinhole prevented pressure buildup, solved the leakage issue and did not pose any problem with fluid or slurry escaping through the opening.

The plumbing was constructed entirely out of 316 Stainless Steel including all tubing, pipes, couplings, valves, hardware and adapters. A particulate filter was placed in parallel with the main fluid path, shown in Figure 5-5. This facilitated with the cleaning and draining process associated with running tests with different sized particulates. It was not placed in series with the main fluid path because even a filter

with pore sizes significantly larger than the abrasive sizes would clog immediately. The filter did aid in the cleaning procedure between tests.

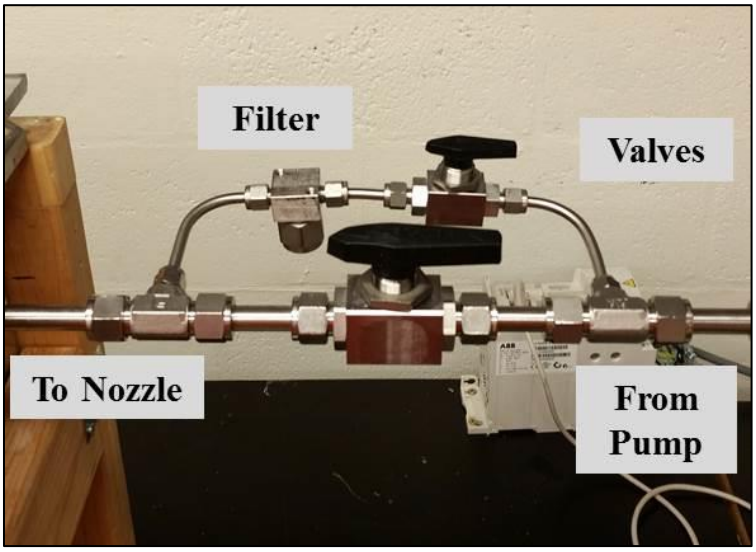

Figure 5-5 Valve system with filter in parallel to main fluid line

5.3 Stirring Mechanism

The test setup was originally designed to use a magnetic stirrer in order to keep the particles suspended in the fluid. Preliminary testing revealed that particles in the reservoir settled to the bottom after approximately 24 – 48 hours of testing. To combat this occurrence, a more powerful stirring mechanism was constructed, shown in Figure 5-6.

Figure 5-6 Stirring mechanism - motor, shaft, propeller

A motor drives the propeller, connected by a shaft and coupling. The motor is mounted to a supportive wooden box which is also attached to the reservoir cover via epoxy. The length of the shaft was designed such that approximately 3 inches of space lie between the bottom of the reservoir and the propeller. Additionally, the propeller pushes water down towards the bottom of the reservoir to induce a significant turbulent effect throughout the entire volume of slurry. Testing of this stirring mechanism further revealed that particle settling in the reservoir did not occur. Vibration was found not to be an issue as well.

5.4 Pump and Motor

The pump used in this test setup was a Hydracell D10 model slurry pump, with specific part number D10EKSTHFHHA. This pump is a positive displacement diaphragm pump and is specifically designed to handle abrasive slurries and corrosive and viscous fluids. The D10 model can deliver up to 8.0 GPM and has a maximum outlet pressure of 1000 psi. The speed of the pump, thus the flowrate, is controlled by

a three-phase induction motor. The motor is driven by a 3HP 460V variable frequency ABB motor drive. These instruments are all shown in Figure 5-7.

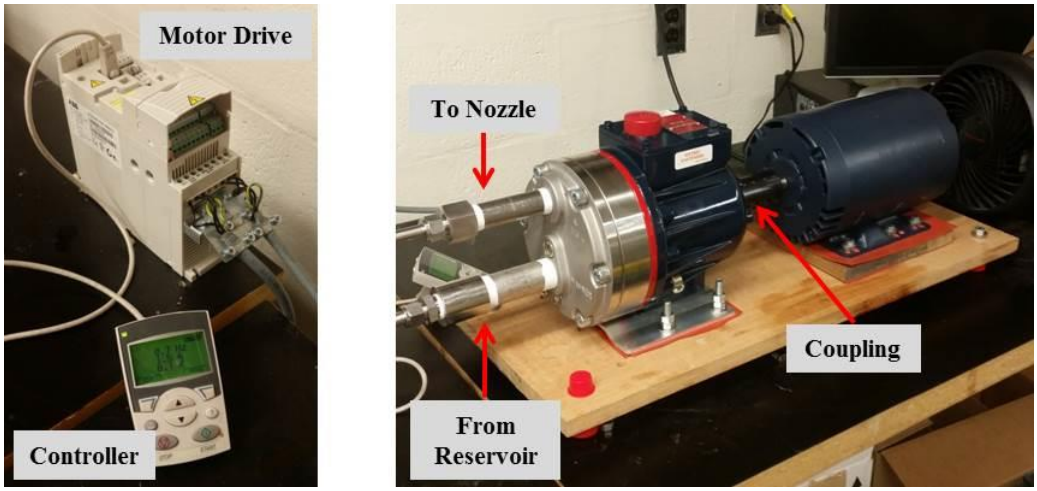

Figure 5-7 Motor drive, pump and motor

The pump and motor subsystem are mounted to a wooden board which has rubber vibration-dampening feet. While the motor can induce significant vibration when operated at higher speeds, the speeds at which these tests take place do not pose issues with vibration.

5.4.1 Pump Calibration

The pump documentation outlines a flow rate vs revolutions chart at pressures between 100 – 1000 psi, shown in Figure 5-8.

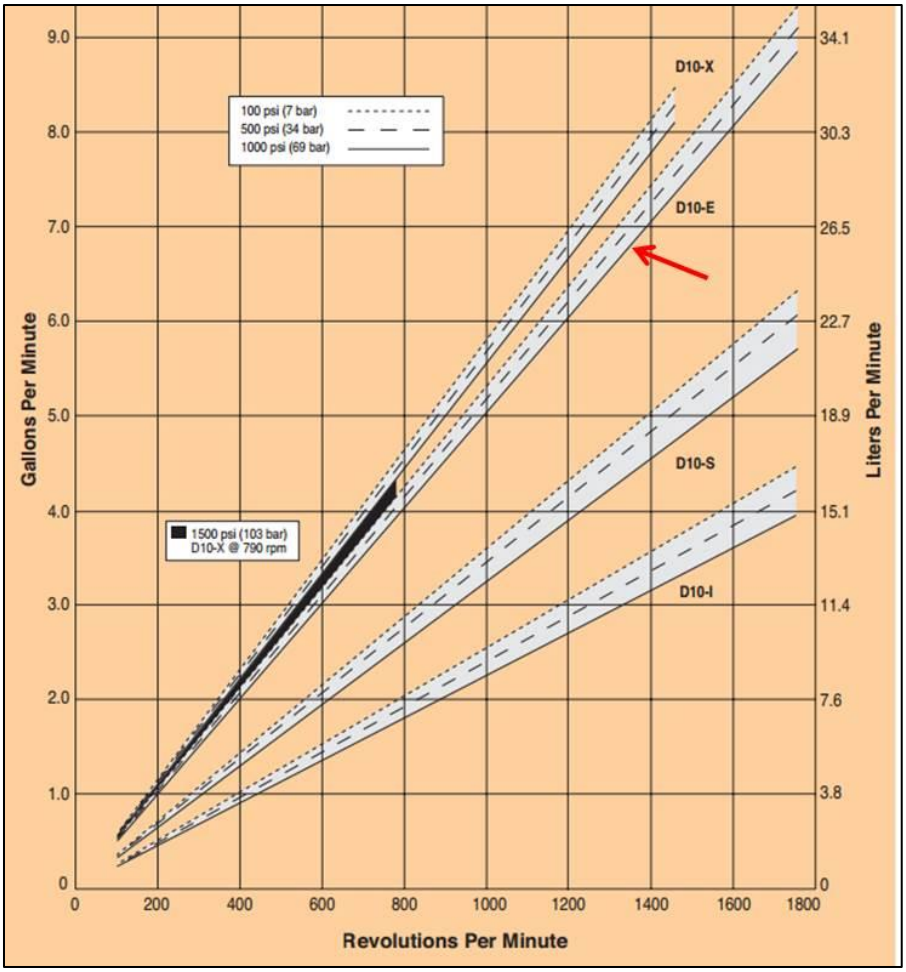

Figure 5-8 Flowrate vs. pump speed for D10-E pump, from manufacturer [122]

Given that the slurries will contain very fine abrasive particles, direct flowrate measurement were not included in the test setup. Of the various techniques that can measure flow rate, each one posed potential issues. Turbine flow meters rely on a propeller that spins by the force imposed from the moving fluid. The rotational speed is thus proportional to the velocity of the fluid. However, the propeller would eventually wear due to the fine particles entrained in the flow. While slight wear is not an issue for most of the test apparatus, slight wear of this propeller would significantly alter the flowrate calibration. Ultrasonic flow meters were also

considered, however these are typically the most expensive flow measuring techniques.

The technique ultimately chosen to calibrate the pump was to weigh the amount of fluid displaced by the pump over a known period of time. A hose was connected to the plumbing and led to a ~30 gallon trash can. After each test the fluid was weighed and a mass flow rate was calculated. This test was repeated for pump speeds ranging from 3 – 12 Hz. Approximately 12 gallons of fluid were used for each test. The results of the pump calibration are shown in Figure 5-9.

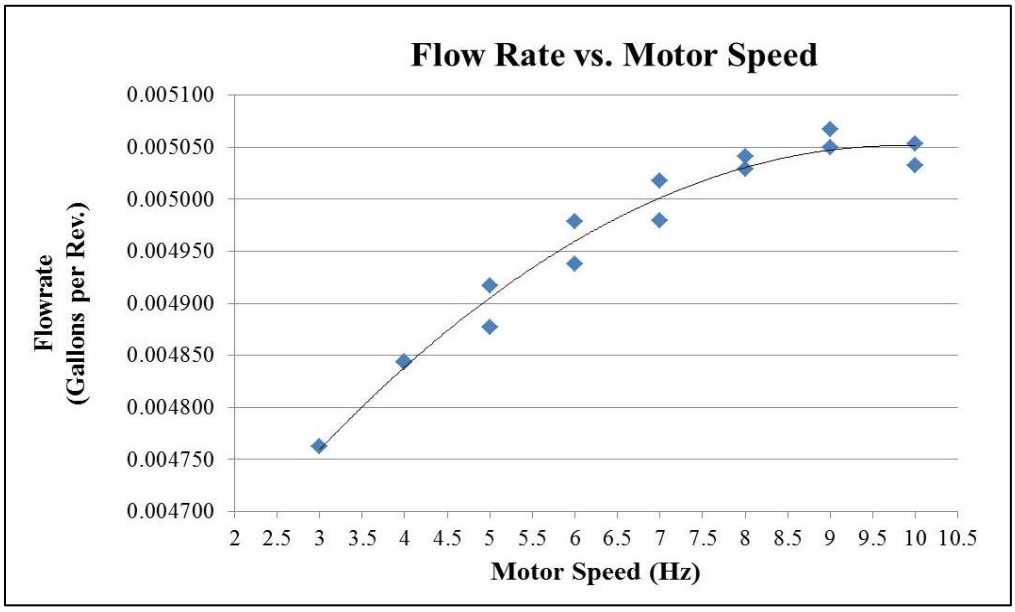

Figure 5-9 Pump calibration raw data

The calibration data varies slightly from the manufacturer data at frequencies below ~ 9 Hz. This is largely due to the fact that this pump is not necessarily designed to run at the low frequencies required by this application. Therefore the flowrate for each test will be determined by the calibration data as opposed to the manufacturer data.

5.5 Nozzle and Nominal Jet Velocity

The nozzle orifice size is the prime factor determining the nominal jet velocity. While there are a number of different types of commercially available nozzles, a 1.98mm nozzle purchased from Jetstream® and shown in Figure 5-10 was chosen. It consists of a tungsten carbide liner which interfaces with the slurry and is enveloped by a stainless steel shell. Additionally, the ¼ NPT fitting enabled easy installment to the test setup.

Figure 5-10 Nozzle used in the test setup. Image taken from [123]

Due to the non-uniform pump flowrate at various motor speeds, a nominal jet velocity – motor speed relation was constructed. Given that the controller determines the motor speed in Hz (as opposed to RPM), a jet velocity vs. Hz graph was constructed for easy determination of the nominal jet velocity. This relation is shown in Figure 5-11. When describing jet velocity, the term 'nominal' is used due to localized fluctuations within the jet that may occur. Additionally, this quantity is defined as the flowrate divided by the nozzle orifice.

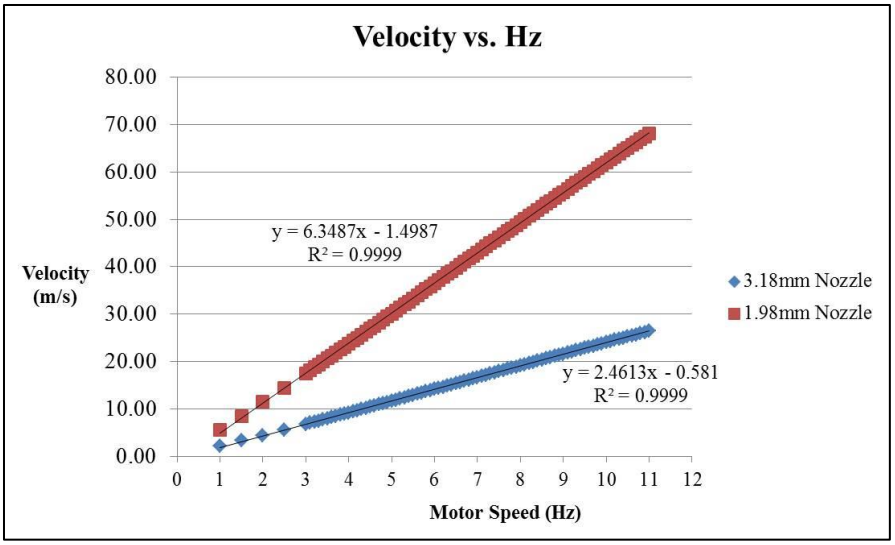

Figure 5-11 Nominal velocity of jet as a function of nozzle size and motor speed

5.6 Sample Holder and Fabrication of Test Samples

A sample holder was placed within the reservoir and was positioned such that approximately 1cm of space lies between the surface of the sample and the nozzle exit. The sample holder, shown in Figure 5-12, was fabricated from 316 stainless steel and was welded to a stainless steel 'allthread' rod that spans the width of the reservoir. This configuration allows the sample holder to be rotated, changing the jet impingement angle. Additionally, four set screws hold the sample in the holder.

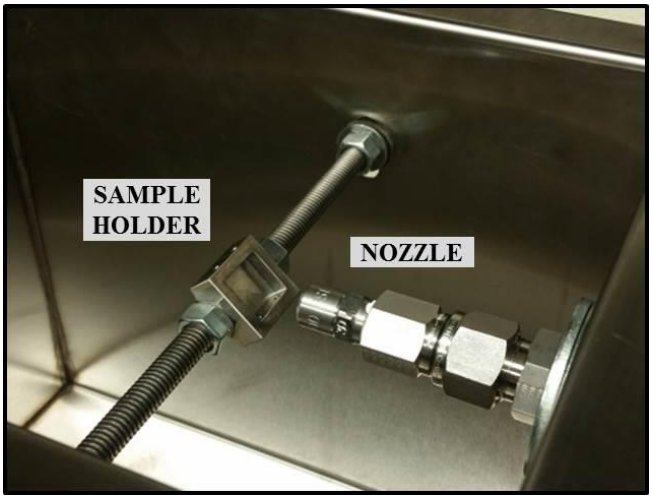

Figure 5-12 Nozzle and Sample Holder

The samples were fabricated by soldering 12x12mm Si chips to a 14x14x5mm Kovar coupon. Originally copper was used as the sample substrate however preliminary studies indicated relatively large global warpages due to the CTE mismatch between copper and Si. Kovar has a significantly better matched CTE reducing, but not completely eliminating, the initial warpages induced from soldering.

In order to solder the Si sample chips to the Kovar coupon, the backside of the chip was metallized using the stack depicted in Figure 5-13.

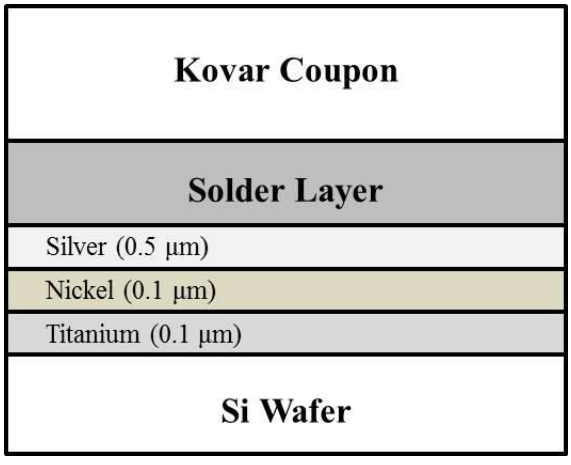

Figure 5-13 Metallization stack used for soldering chip to substrate

The Kovar coupon was prepared for soldering by grinding down and polishing the surface using SiC grit paper to remove any surface oxides. After the chip was soldered to the Kovar substrate using a standard Tin-based solder, the surface was cleaned with acetone, methanol and isopropyl alcohol with Q-tips.

5.7 Creation of Testing Slurry

The testing slurries were created by measuring out the appropriate amount of abrasive and mixing it with a small amount of water (or whichever solution was being used) in a 500mL glass jar. In addition a polyacrylic acid dispersant was added, Dispex AA 4140 NS manufactured by BASF, to appropriately disperse the abrasives within the fluid. The mass of dispersant added was equal to the mass of abrasive used. The solution was then sonicated for 20 minutes to further ensure agglomerates were broken up. This mixture was then added to the test setup with the remaining two gallons of fluid for testing.

5.8 Cleaning Procedure

In order to ensure that unwanted particles from previous tests are removed from the test loop, a robust cleaning and flushing procedure was followed. First, the dirty fluid was drained from the system at the filter port and two gallons of water were flushed through the loop. All parts of the reservoir, O-ring stirrer and cover were wiped down to remove all visible remnants of particulate fouling and build-up.

Next, one gallon of water was added to reservoir and a “dummy” sample was placed in the sample holder. The system was then run for 10-20 minutes at a high flowrate (10 Hz). Upon examination the water usually appeared murky, signifying

that particles were picked up from places in the fluid loop other than the reservoir. The water was then drained and fresh water was added. This process was repeated approximately 4-6 times or until the water appeared visibly clear and without contaminants. Although this process may not remove every particle, the extremely sparse particles that may be left in the solution are assumed to affect the erosion negligibly compared to the relatively large concentration of other sized particles. In addition, more stringent cleaning process occurred when smaller particles would be used in tests after large particles.

5.9 Limitations

While this setup enables the slurry erosion phenomena to be studied, a number of limitations exist. These limitations are inherent in this type of slurry erosion test apparatus and should be taken into account during the post-erosion analysis and in any future studies involving jet-impingement slurry erosion.

The primary limitation of the test setup lies in the fact that a filter is not used in the main fluid loop. Although a small filter in the secondary parallel loop exists which aids in cleaning the test setup, a primary filter is not used during the experiments. The reasoning behind this is that a filter, regardless of the size, would inevitably clog. For example, in the case of a 25μm filter and 1μm abrasive particles, the filter may do its job for a period of time, trapping unwanted particles larger than 25μm that develop during the test. However, at some point a small percentage of the filter would get clogged from these larger particles. In a “snow-ball” like effect, the smaller 1 micron particles would get trapped also in the filter. Not only would this perpetuate the clogging process of the filter but it would significantly change the pre-

defined particulate concentration of the slurry. Although continuous cleaning of the filter could be used, preliminary studies showed that this may not be necessary. It was found in the first couple experiments that the vast majority of the observed wear was in fact due to the particulate abrasives even with larger particles existing in the fluid loop. Particles generated in the test setup most often originated from the rubber seals and gaskets or the acrylic cover. Despite the size of these particles, their impact on erosion was trivial due to their soft nature.

It should be mentioned however that further inspection of the surface did reveal a few locations of discrete chipping likely caused by the impact of higher energy particles. However, the relative number of these discrete impacts is small and considered negligible compared to the amount of wear caused by the abrasive particles.

Another challenge the test setup imposes is that the temperature of the slurry heats up during the experiments. This is caused by the mechanical action of the pump. To deal with any significant heating, a fan was setup to continuously blow air over the motor and pump. This minimized the overall temperature change of the fluid and kept the bulk fluid temperature at approximately 34°C.

Lastly, the final limitation with the test setup is that the pump occasionally produces random pulsations. These most often occur at frequencies below 2 Hz, but occur periodically throughout all testing ranges. The main effect arising from this is that a pulsating jet will exit the nozzle as opposed to a smooth fluid stream. Pulsation dampeners are typically installed in systems like these, however it was predicted that the inclusion of one of these dampeners may cause more harm than good. One type of

pulsation dampener utilizes a rubber diaphragm to smooth out the flow rate fluctuations. This may be a viable solution if the fluid had no abrasive particles in it due to the fact that they may eventually wear away the rubber. Another type of pulsation dampener operates by significantly increasing the volume of the fluid loop, operating much like a "fluid-capacitor". While this design may also work if the fluid had no particles, over time the particles may settle out in the sub-reservoir and significantly reduce the predefined particulate concentration of the slurry.

While these factors impose certain challenges and limitations regarding the operation and test procedure, they are acknowledged and will be taken into considering during the post-erosion analysis and model development.

6 EXPERIMENTAL EROSION TESTING OF SILICON

6.1 Introduction

This section discusses the procedures involved in testing and measuring the Silicon erosion samples. First, the Design of Experiments (DOE) is presented which covers the range of experiments performed. The parameters investigated are nominally jet velocity, particle size, particulate concentration, fluid viscosity and time. Next, the method in which the stylus profilometer was used to approximate the total amount of volume loss will be discussed including the numerical analysis performed in MATLAB. Additionally, the procedure for factoring in initial warpage will be described.

Two principle erosion metrics are described in this chapter, a mass loss rate in units of milligrams per year and a one-dimensional erosion rate in units of micrometers per year. The mass loss rates found in this chapter will be used to formulate the erosion ratio metrics while the one-dimensional erosion rates will serve as the metric through which the final erosion model will be validated against.

6.2 Design of Experiments

Prior to introducing the DOE, the meaning behind the various Test IDs will be briefly discussed. Figure 6-1 represents how the various Test IDs were constructed.

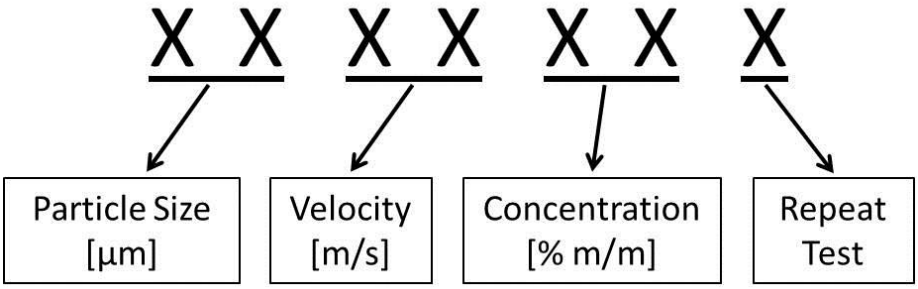

Figure 6-1 Explanation of Test IDs

The first two digits represent the particle size in micrometers and the next two digits represent the nominal jet velocity in meters per second. In most instances the concentration is represented by two digits however one of the test points requires three digits namely the 0.025% concentration tests. As an example a concentration of 0.1% means that 7.57 grams of particles are added to 7570 grams of fluid. For reference 7570 grams of water equates to approximately 2 gallons which is the working volume of the test setup.

Most of the test points utilize repeat tests therefore this final digit is represented by letters B, C, D where the 'A' test is assumed in the first test. Additionally, water is assumed to be main working fluid for all tests unless the Test ID is explicitly PG10 or PG25. The transient tests are also explicitly noted with a 'TR' reference. As an example, the Test ID of 104010D represents the test point of 10µm particles, 40 m/s jet, 0.10% concentration, Water as the fluid and the fourth test conducted at that test point.

Table 6-1 shows the 14 different erosion test cases performed. The ranges chosen in this study were developed largely to correspond to specific proprietary systems found throughout DARPA's ICECOOL program and due to the proprietary nature of these systems, specific references cannot be provided. Depending on the application, certain systems may employ more modest or accelerated values depending on the specific microchannel or jet architectures. Although specifics vary widely from system to system, the general goal of this DOE was to conduct a series of experiments within the ballpark parameter ranges of typical systems. Depending on the type of microchannel or jet implementation, the model could then be applied to specific design and filtering restraints.

Table 6-1 Design of experiment, 14 experimental test cases

Test ID	Particle Size (µm)	Velocity (m/s)	Concentration (m/m)	Fluid
24010	2.5	40	0.10%	Water
54010	5	40	0.10%	Water
104010	10	40	0.10%	Water
204010	20	40	0.10%	Water
102010	10	20	0.10%	Water
102510	10	25	0.10%	Water
103010	10	30	0.10%	Water
1040025	10	40	0.025%	Water
104005	10	40	0.05%	Water
104020	10	40	0.2%	Water
PG10	10	40	0.10%	10% PG
PG25	10	40	0.10%	25% PG
1030TR	10	30	0.10%	Water
1040TR	10	40	0.10%	Water

Particles sizes between 2.5 - 20µm were studied and represent some of the various filtering levels commonly found in electronic cooling loops. While particles upwards of 20µm in diameter would not be commonly found in real life applications, accelerated erosion tests are necessary in order to formulate relations among the various parameters. Typical sizes of commercially available filters are 0.5µm, 1µm, 3µm, 5µm, and 10µm where these values represent the approximate pore size.

Nominal jet velocities between 20 – 40 m/s were tested. Again, these are within the range of typical values found in single phase jet-impingement systems. In single phase manifolded systems the velocities may be significantly lower than these, often

times less than 5 m/s, yet in two phase systems the velocities of entrained particles as the fluid evaporates may be around the 40 m/s value.

Dilute concentrations were chosen to represent the fact that most real applications have decent filtering systems. While the concentration test points are considered highly accelerated based on some of the typical ISO Fluid Cleanliness codes used in high performance servos and aerospace hydraulic systems, enough particles had to be used in order to obtain measureable results in a reasonable amount of time. More will be discussed on this later in the chapter.

Water is the primarily fluid used in these tests, however two other tests were conducted using a 10% and a 25% propylene glycol – water solution. These two test points were included to assess how well the developed model, calibrated in water, could be applied to other working fluids.

Lastly, two transient tests were conducted at 30 m/s and 40 m/s to assess the dependence of erosion on time.

6.3 Measurement Techniques

6.3.1 Stylus Profilometer

A stylus profilometer, also known as a line scan profilometer, generates a 2D profile by tracking the surface height across the length of the scan. A stylus is dragged horizontally across the surface and enables small surface features, on the order of tens of nanometers, to be observed. A Tencor P-20 Long Scan Profiler, shown in Figure 6-2, was used to perform these measurements.

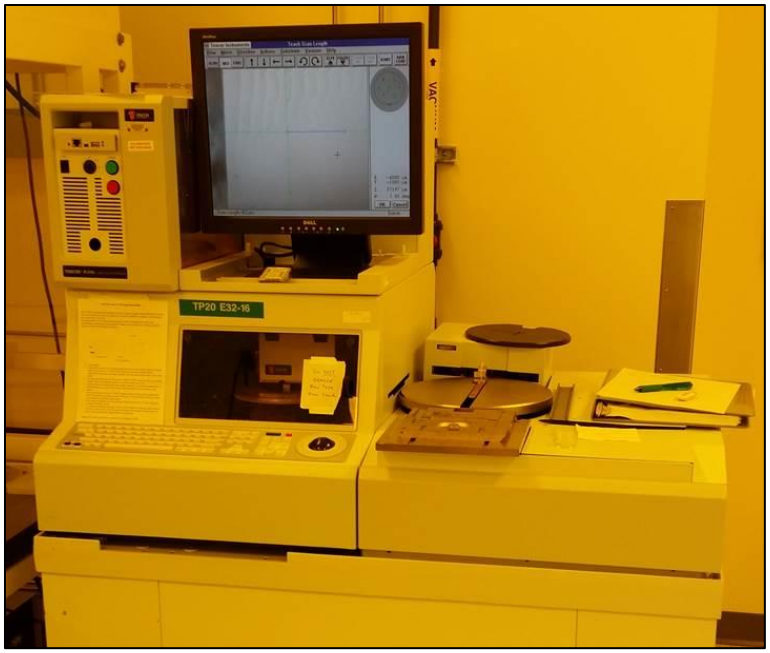

Figure 6-2 Tencor P-20 Long Scan Profiler

This profilometer has the ability to make scans on wafers up to 8 inches, making the 12mm scans on the silicon samples very easy to do. Table 6-2 lists the operating properties used for all scans.

Table 6-2 Profilometer Operating Conditions

Scan Length	11600μm
Maximum Vertical Range	130μm
Stylus Force	10mg
Range Direction	Up and Down

A scan length of 11600μm was chosen to provide a slight 200μm buffer at both of the edges to purposefully neglect any edge effects that may be present on the erosion samples. Additionally, a built in leveling function was applied in order to normalize a flat reference surface.

Assuming the jet impinges perpendicularly on the sample, the erosion scar should ideally exhibit axisymmetric properties about the stagnation region. Experimental error and uncontrollable inconsistencies prevented perfectly axisymmetric contours to be achieved. To obtain well-rounded data for each test, two profile scans were taken. One from left to right, termed the 'LR' scan, and the other from the top to the bottom termed the 'UD' scan, short for Up-Down. A schematic of the profile and the corresponding scans are shown in Figure 6-3.

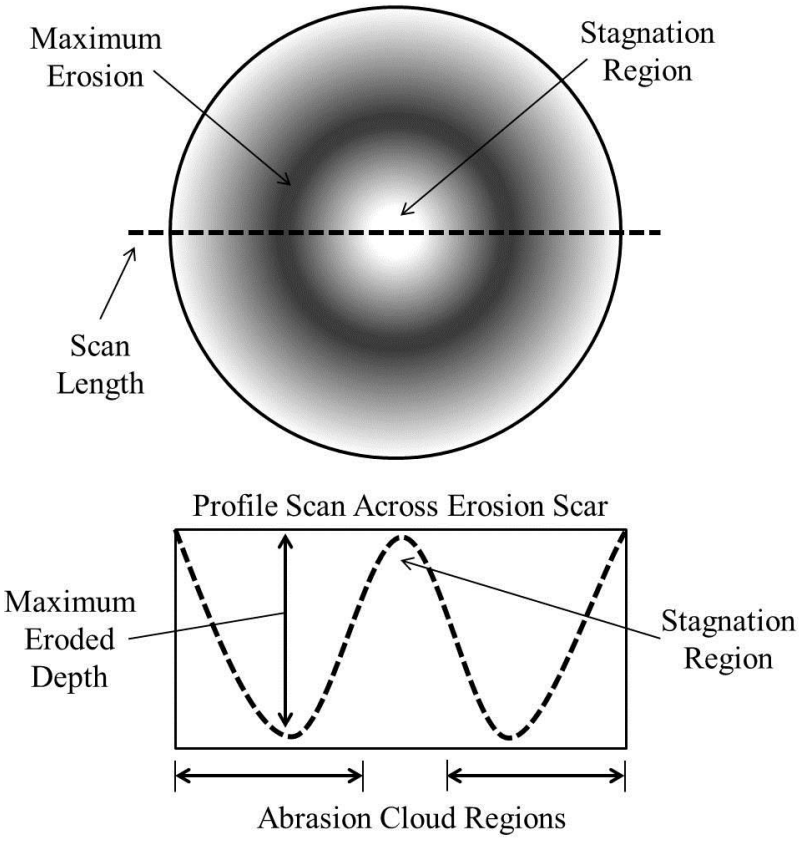

Figure 6-3 Schematic of erosion scar and stylus profilometer scans

In agreement with the findings of Wang et al. [92] the general erosion scar was found to exhibit the characteristic 'W' shape. The center, termed the stagnation region, is a region in which minimal wear occurs due to the lack of direct impacts.

The results of the CFD study described in the previous chapter indicate a high prevalence of low angle impacts which occur outside the jet-impingement region. In addition, the CFD study also indicated that particle impacts do not occur in the center of the jet region. Therefore the height of the stagnation region is assumed to serve as the reference point where no wear is assumed to occur.

6.3.2 Initial Warpage Considerations

In order to more accurately measure the quantity of eroded material, the amount of initial warpage across the Silicon sample was taken into consideration. Preliminary erosion tests were conducted by soldering the silicon samples to copper coupons. It was typically found that the initial maximum warpage height across that wafer, as measured by the stylus profilometer, was on the order of 1-2μm. This occurred due to the coefficient of thermal expansion (CTE) mismatch between the Silicon (~ 3 ppm/°K) and copper (~ 16.6 ppm/°K). While this is relatively small, the erosion depth from some of the tests was expected to be near this value. As such, Kovar coupons were chosen to replace the copper coupons for all the tests which has a CTE closer to that of Silicon, which is approximately 5.3 ppm/°K.

After soldering the silicon samples to the Kovar coupons, a profilometer measurement was taken across the sample to assess the maximum initial warpage. Only samples which had a maximum average initial warpage of less than 0.6μm were used in the erosion studies. The maximum average initial warpage was taken by averaging three measurements from the ‘LR’ direction and three measurements from the ‘UD’ direction, shown in Figure 6-4. For these measurements it was assumed that

the maximum warpage would occur at the center of the wafer and each measurement was taken 1mm apart.

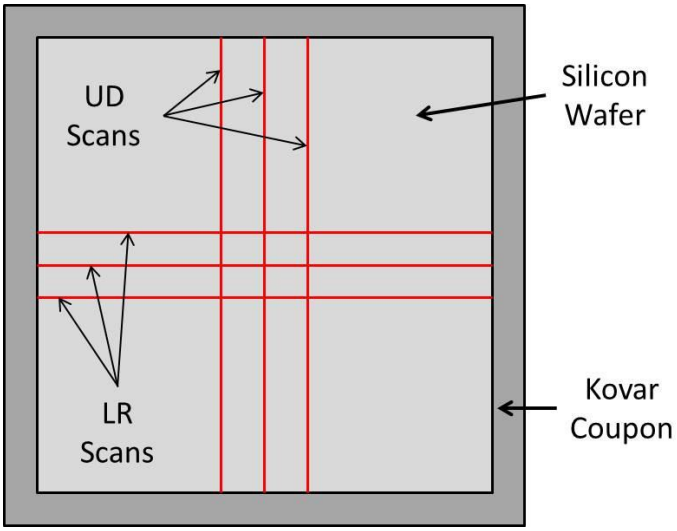

Figure 6-4 Schematic of initial warpage scans

In addition, samples with larger amounts of initial warpage were saved for tests expecting more wear while samples containing minimal initial warpage were used on tests expecting small amounts of wear.

6.3.3 Calculating Mass Loss in MATLAB

Once the erosion tests were performed, the amount of mass removed was calculated using a volume-of-revolutions type approach in MATLAB. In order to transform the two-dimensional erosion profile into a three-dimensional volume, the erosion scar was essentially rotated 180° about the stagnation point and the resulting volume between the reference plane and the scar was numerically computed. Figure 6-5 represents a simplified schematic illustrating this approach.

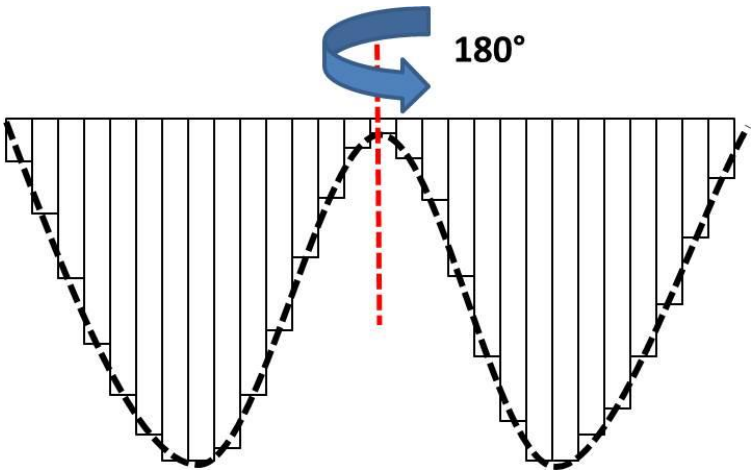

Figure 6-5 Volume-of-revolution numerical integration

Rotating the erosion scar 180° about the stagnation region enables a three-dimensional volume to be calculated. The two-dimension area was broken up into a large number of rectangles with heights corresponding to the distance between the eroded depth and the reference plane. This type of approach is also referred to as the midpoint approximation rectangular method. This procedure was repeated for both the LR and UD scans of a sample and the results were averaged together to approximate to total volume loss of the sample.

To account for the initial warpage, a similar algorithm was devised to approximate the volume associated with the initial warpage. According to Figure 6-6, the measured erosion contour does not inherently capture the initial warpage characteristics, which is shown as the grey shaded area above the erosion profile.

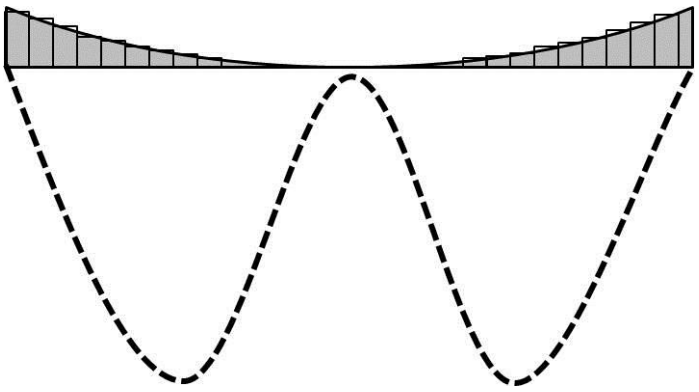

Figure 6-6 Accounting for initial warpage

The curve of the initial profile was approximated by a quadratic function corresponding to the general shape of the ‘smile’ warpage. In a similar manner as previously described, the shape was divided up into a large number of rectangles and rotated 180° about the center point. A resulting volume was then calculated. Due to the fact that the reference plane was taken at the highest point in the stagnation region, the volume computed from the initial warpage calculation was added to the volume loss from due to erosion. In the few instances where the initial warpage resulted in a ‘frown’, this process was inverted and the appropriate calculations were performed.

Due to the fact that samples with larger amounts of initial warpage were reserved for tests expecting larger amounts of erosion, the volume associated with the initial warpage was typically a small percentage of the measured erosion wear. In many cases the percentage was negligible.

6.4 Erosion Results

This section presents the results of the erosion experiments. For the purpose of brevity, data from select tests will be included in this section, however Appendix A will include all the data.

Table 6-3 summarizes the results for all erosion tests. Mass loss from the LR and the UD scans are both given separately along with the calculated initial warpage mass approximations. Typically on samples where the initial warpage was less than 0.2μm a discernable ‘frown’ or ‘smile’ did not exist. Therefore it was assumed that initial warpages of this magnitude played a negligible role in calculating total mass of material removed.

Table 6-3 Summary of Raw Erosion Results

Sample ID	Initial Warpage [µm]	Testing Time [min.]	Warpage Mass [mg]	Total Mass Loss [mg]	Mass Loss Rate [mg / yr]	Erosion Rate [µm / yr]
24010	0.19	18714	0.0000	0.0180	0.50	14.53
54010	0.40	8263	0.0173	0.0909	5.78	120.61
104010C	0.25	7200	0.0157	0.9739	71.09	594.77
103010	0.32	11650	0.0277	0.2173	9.80	87.72
102010	0.11	15749	0.0000	0.0336	1.12	20.38
104010D	0.17	6740	0.0000	1.3090	102.08	800.80
103010C	0.33	11060	0.0285	0.3892	18.49	144.22
102010B	0.23	21555	-0.0264	0.0463	1.13	15.16
102510	0.37	21297	-0.0433	0.1458	3.60	34.09
54010B	0.33	11137	0.0230	0.2149	10.14	62.91
54010C	0.40	11253	0.0116	0.0984	4.59	41.96
24010B	0.16	20390	0.0000	0.0083	0.21	4.39
204010	0.51	1316	0.0525	2.0725	827.74	13511.10
204010B	0.56	1346	0.0469	2.5797	1007.35	16477.13
104005	0.46	5636	0.0358	0.4993	46.56	338.13
104020	0.51	4033	0.0287	1.6171	210.75	1753.84
1040025	0.29	6936	0.0290	0.1024	7.76	56.90
1040025B	0.12	9894	0.0000	0.1535	8.15	56.73
104005B	0.27	5536	0.0205	0.4006	38.03	276.17
TR40-1	0.51	1540	0.0383	0.3967	135.39	1023.04
TR40-2	0.51	2843	0.0383	0.6031	111.50	873.69
TR40-3	0.51	4348	0.0383	0.7978	96.44	764.48
TR40-4	0.51	5637	0.0383	0.9124	85.07	688.08
TR30-1	0.15	2717	0.0000	0.1445	27.94	251.66
TR30-2	0.15	5449	0.0000	0.2287	22.06	188.73
TR30-3	0.15	11175	0.0000	0.3203	15.06	129.77
TR30-4	0.15	14053	0.0000	0.3629	13.57	115.94
PG10	0.65	5878	0.0448	0.4576	40.92	637.90
PG25	0.42	5675	-0.0162	0.0583	5.39	194.21

6.4.1 Effect of Velocity

Sample profile scans are presented here which show the effect of nominal jet velocity on erosion. For the following tests, 10μm nominally sized Al_2O_3 particles were used at a concentration of 0.1% in water.

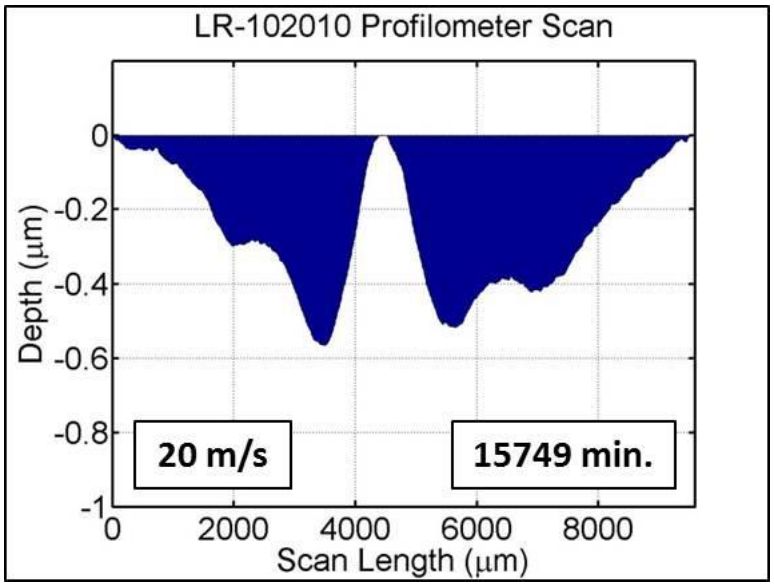

Figure 6-7 LR-102010 Profile Scan

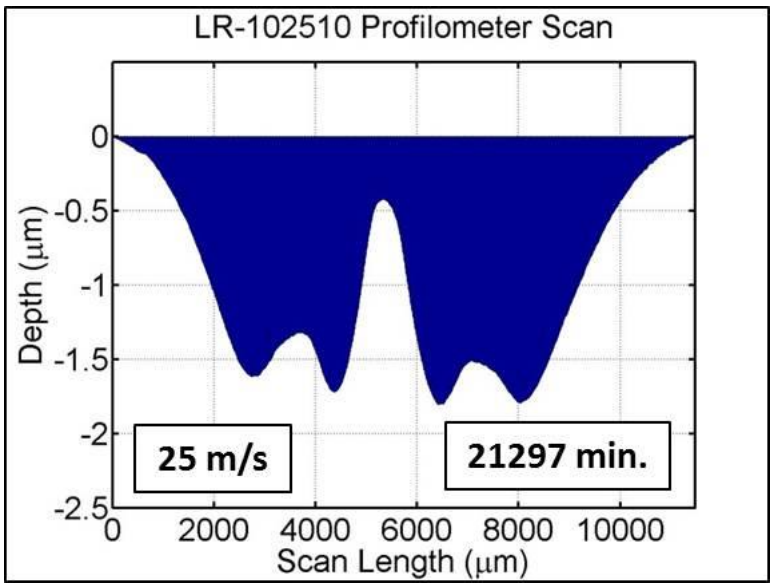

Figure 6-8 LR-102510 Profile Scan

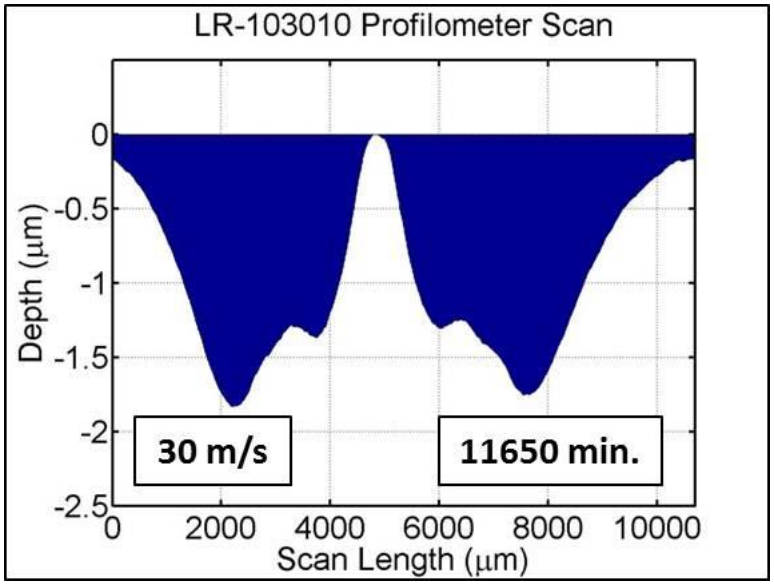

Figure 6-9 LR-103010 Profile Scan

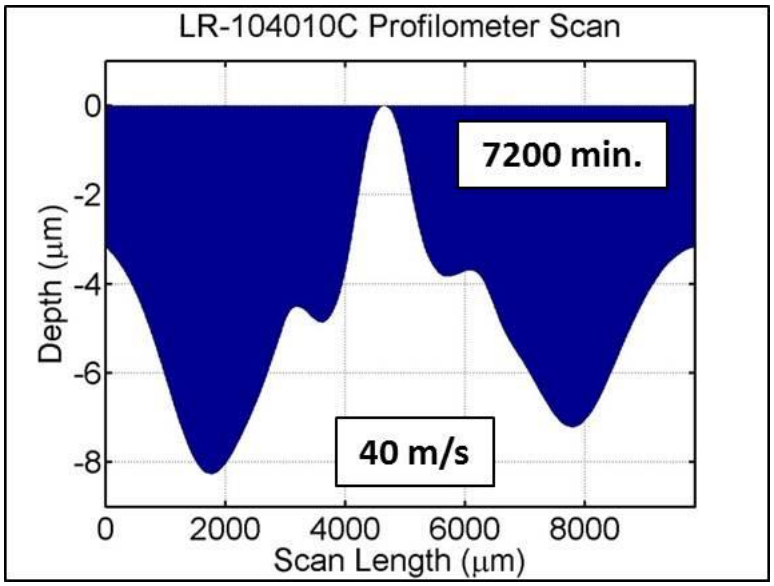

Figure 6-10 LR-104010C Profile Scan

Observing the erosion contours reveals the presence two local minima, thought to originate from the primary and secondary impacts of particles. According to the CFD analysis presented in Chapter 4, Figure 4-16 indicates that the velocity of

the first impact in the 40 m/s case is smaller than the velocity of the second impact. According to Figure 6-10 above, the depth of the local minima closest to the stagnation region for the 40 m/s case is less eroded than the minima further away from the stagnation region. It is thought that the minima closest to the stagnation region corresponds to the first impact while the minima further away corresponds to the second. Additionally as the impact number increase past two, the impact angle and the percentage of particle streams resulting in impacts significantly decreases. Discrete impact regions become indistinguishable from one-another due to the fact that material is removed in a wet abrasion mechanism. This most observable in the 40 m/s case where the edges of the profile have worn down significantly below the height of the stagnation region.

Furthermore, the relative height difference of the primary and secondary impacts correspond closely to the impact velocities determined through CFD. According to the profile scans, the primary impact depth of the 30 m/s and 40 m/s case is higher than the secondary impact depths, however in the 20 m/s and 25 m/s cases the primary impact depth surpasses that of the secondary impact depth. This is also observed in the CFD simulations where the velocity of the second impact decreases relative the first impact as the nominal jet velocity decreases.

It is also interesting to note that the distance between the primary impact sites on each side of the stagnation region stays relatively constant, approximately 2mm, throughout each of the test cases. This is most likely due to the fact that the average impact angle of the first impact stays within a few degrees across all tests. According to Figure 4-17 which shows how impact angle varies across different jet velocities,

the difference between the 40 m/s and 20 m/s case is approximately three degrees. This would not likely yield a noticeable difference in the erosion contour shapes.

The erosion results for the velocity test cases can be summarized in Figure 6-11 which shows that the erosion rate, given in milligrams per year, follows a power law with respect to nominal jet velocity.

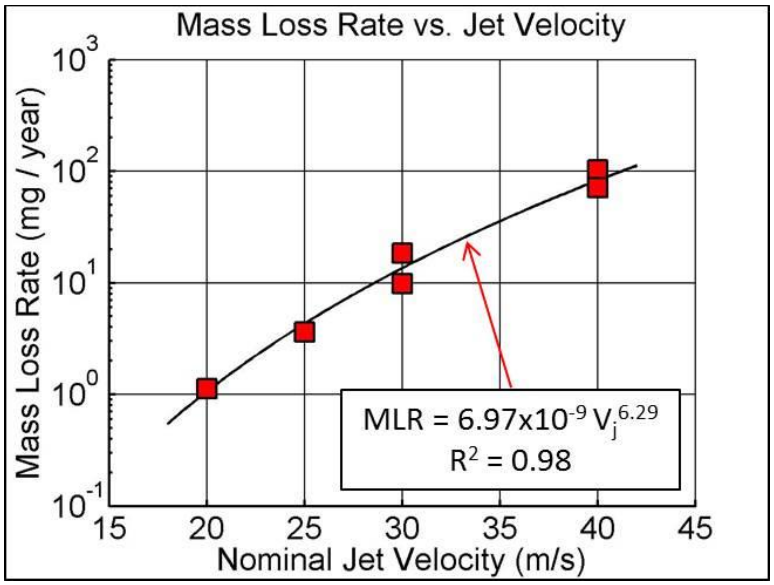

Figure 6-11 Mass Loss Rate vs. Jet Velocity

In addition, the relationship between the one-dimension erosion rate and jet velocity is shown in Figure 6-12.

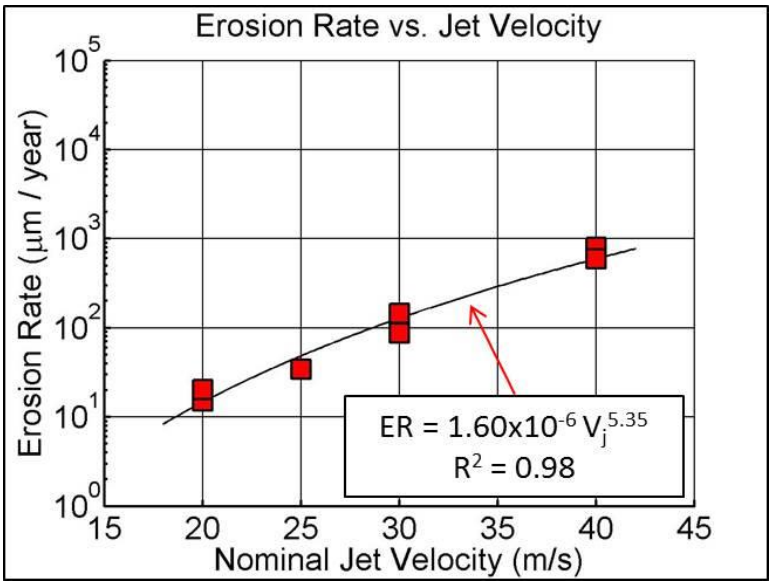

Figure 6-12 Erosion Rate vs. Jet Velocity

The one dimensional erosion rate also follows a power law with a slightly smaller exponent than the mass loss rate relation.

6.4.2 Effect of Particle Size

The following profile scans show the results of altering the average particle size. For all tests Al_2O_3 particles at a 0.1% mass loading were used. Additionally, the nominal jet velocity was 40 m/s and water was the working fluid.

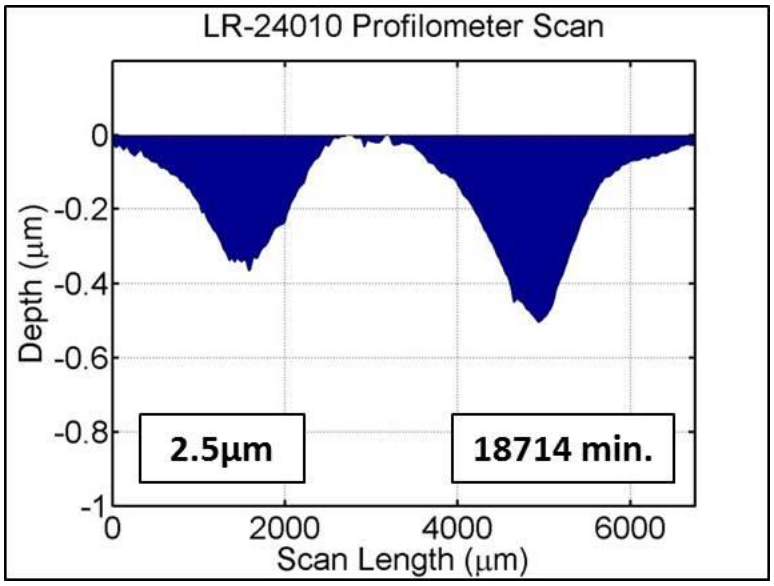

Figure 6-13 LR-24010 Profile Scan

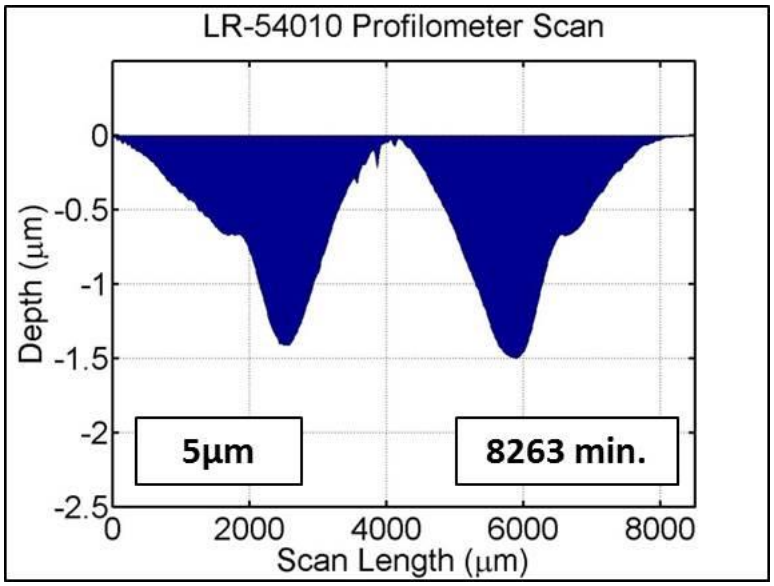

Figure 6-14 LR-54010 Profile Scan

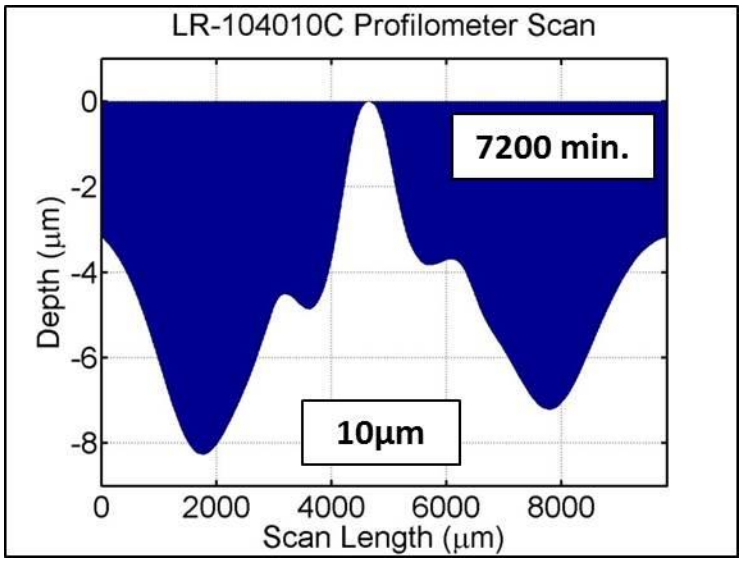

Figure 6-15 LR-104010C Profile Scan

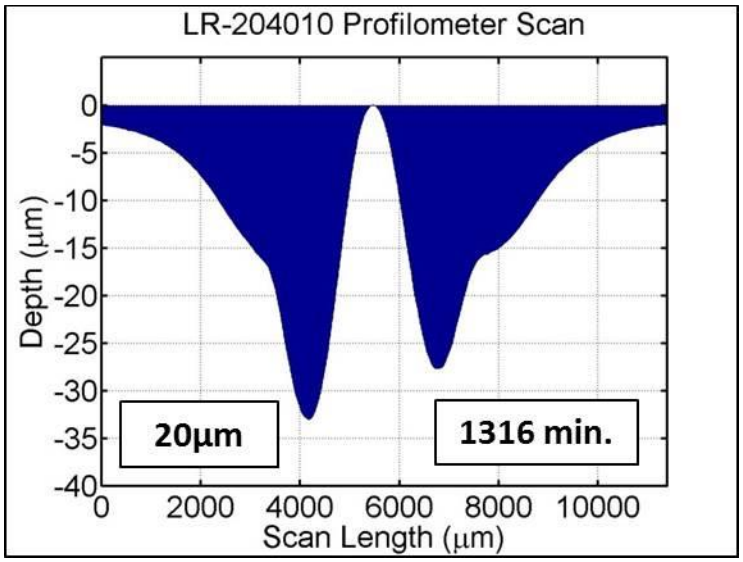

Figure 6-16 LR-204010 Profile Scan

One observation with regards to how particle size affects the erosion contour deals with the relative effect of the primary and secondary impacts. In the 20µm case the first particle impact clearly induces the maximum amount of damage. According to the CFD study, the average impact angle of the first particle impact for the 20µm case is approximately 50° whereas the impact angle of the 10µm case is

approximately 9°. This is a result of the larger particles having more momentum and being less controlled by the motion of the fluid. In addition, smaller particles would be more likely to become trapped in the squeeze film resulting in the wet abrasion mechanism. In the cases of larger particles, impact would occur but then they would likely rebound back into the bulk fluid flow above the squeeze film. This also justifies why the edges of the 10μm case are more eroded than the edges of the 20μm case.

Another observation is that the width of the stagnation region decreases with increasing particle size. As the particle size increases, the impact angle increases as a result of less fluid-particle coupling. It is thought that as the particle size increases even further, the stagnation region will fail to exist as more perpendicular impacts begin to occur. Additionally, as the particle size decreases into the sub-micrometer regime, it is thought that impingements will ceases to occur as stronger fluid-particle coupling will exist.

Interestingly, the cases with the 2.5μm and 5μm particles show that most damage is caused by the primary impacts with subsequent impacts yielding smaller amounts of damage. This is thought to be attributed to the dampening nature of the squeeze film where the fluid may protect the surface from impacts and scratches.

The mass loss rate results can be summarized in Figure 6-17 which shows that the mass loss rate follows a power law relation with the average particle size.

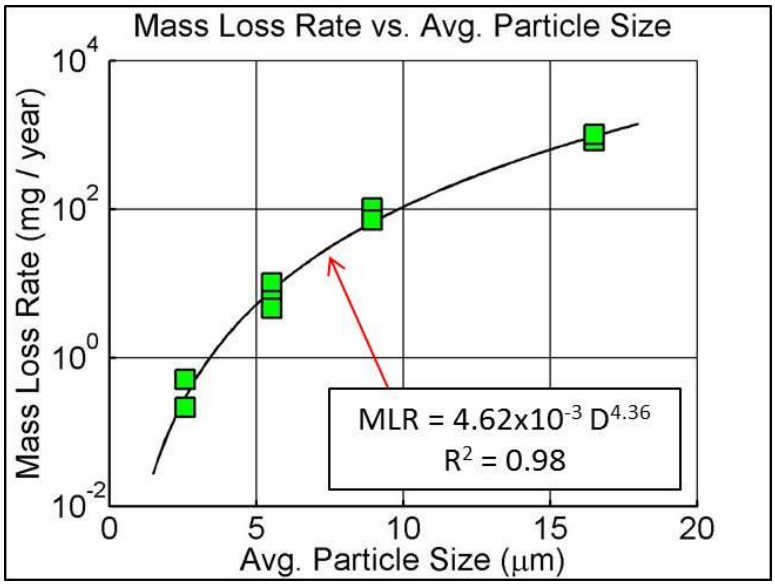

Figure 6-17 Mass Loss Rate vs. Average Particle Size

The erosion rate results can be summarized in Figure 6-18 which shows that the one-dimensional erosion rate also follows a power law relation with particle size.

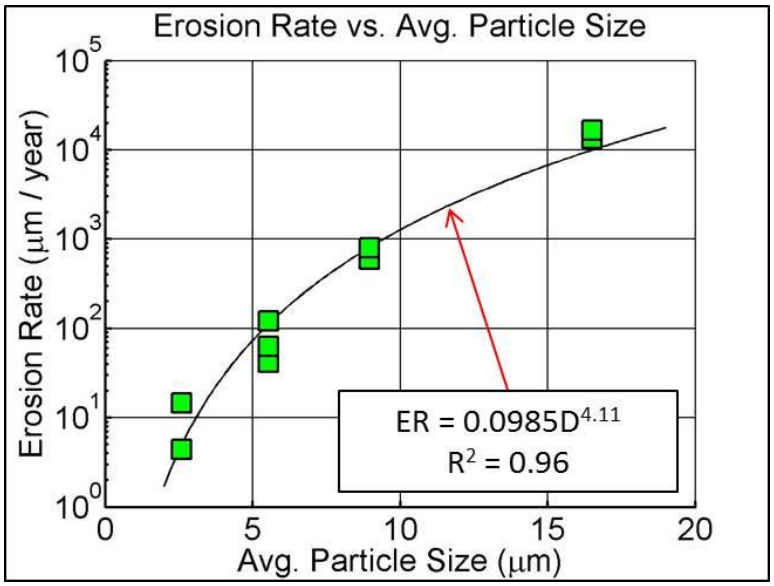

Figure 6-18 Erosion Rate vs. Avg. Particle Size

6.4.3 Effect of Concentration

The following profile scans show the result of altering the particulate loading concentration. For all tests the nominal jet velocity was 40 m/s with water as the working fluid. As stated earlier, the concentration is defined as the ratio of the mass of particles to the mass of fluid.

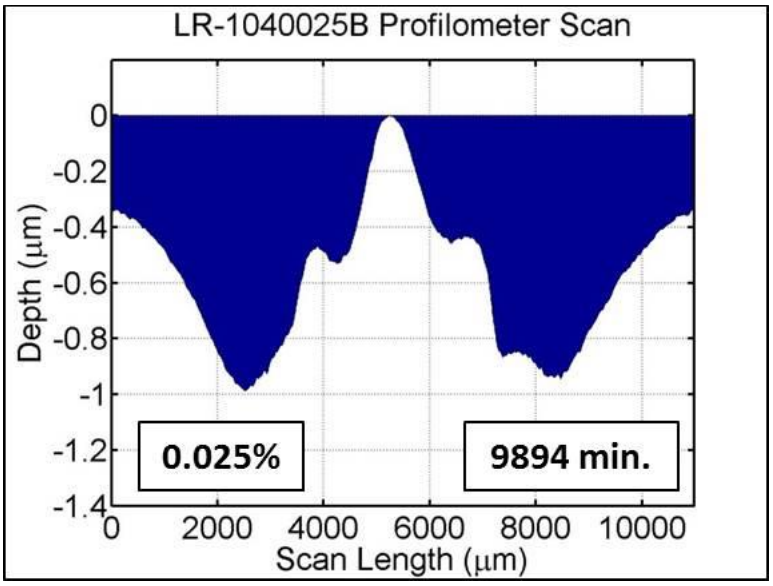

Figure 6-19 LR-1040025B Profile Scan

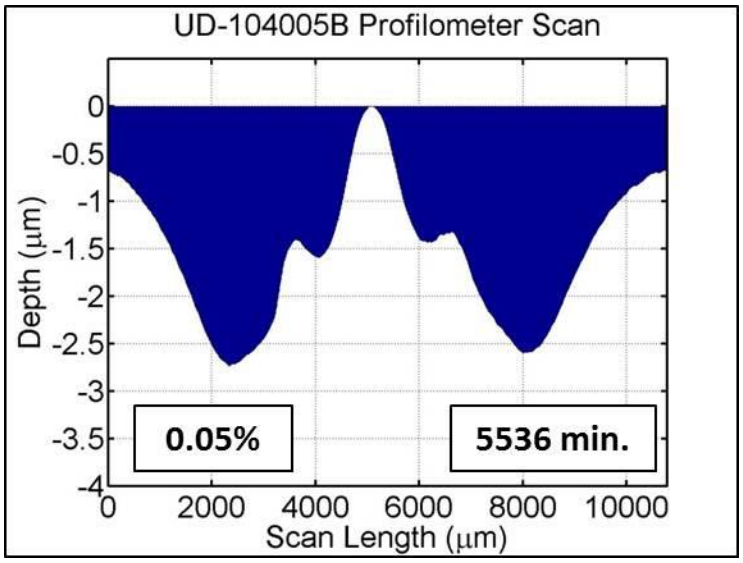

Figure 6-20 UD-104005B Profile Scan

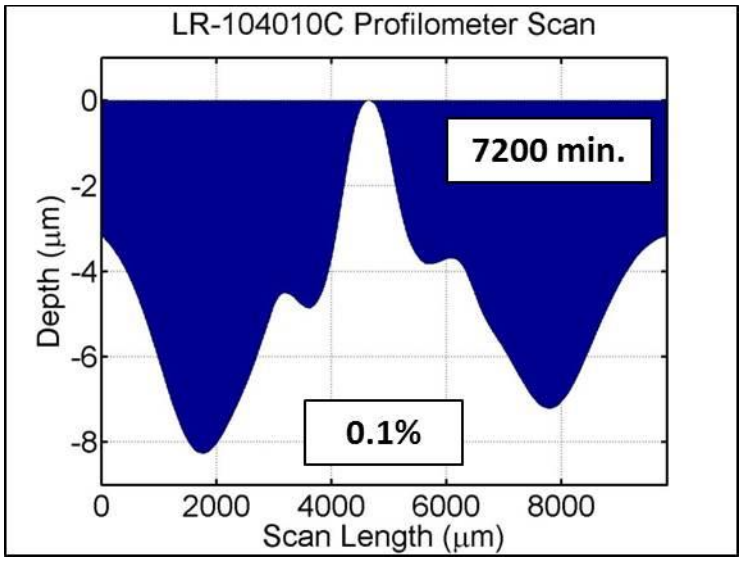

Figure 6-21 LR-104010C Profile Scan

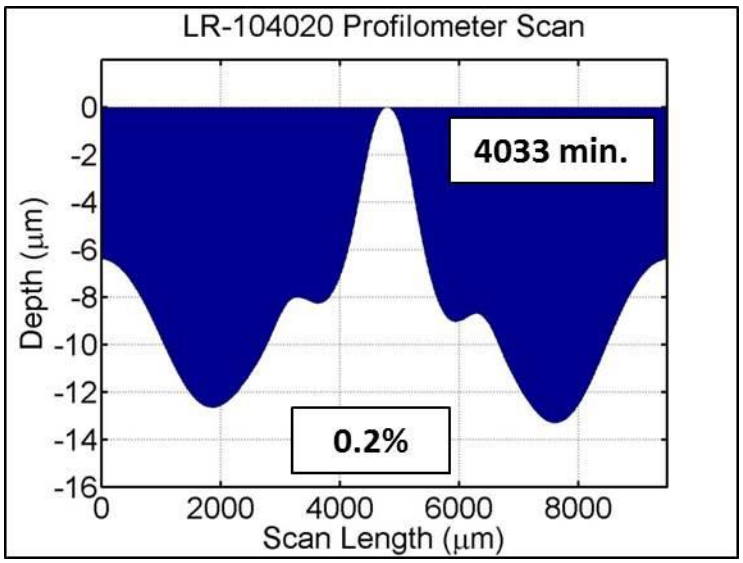

Figure 6-22 LR-104020 Profile Scan

Comparing the erosion contours from the concentration experiments, it can be seen that they all share similar qualitative attributes. All the contours exhibit similar primary and secondary impact locations, with the depth of the first impact being less than the second. Essentially the only difference between the profiles is the y-axis scale measuring depth. As described in the CFD chapter, doubling the particulate concentration should in theory double the mass loss rate as twice as many particle impingements per unit time would take place. At the low concentrations used in these experiments, particle-particle interactions can be assumed negligible, however at much higher particulate concentrations, particle-particle interactions may occur. In these scenarios, particles may agglomerate at the surface and act as a shield for incoming particles resulting in a reduction in erosion rate [85] [124].

The mass loss rate results for the concentration experiments can be summarized in Figure 6-23 which shows a linear relationship.

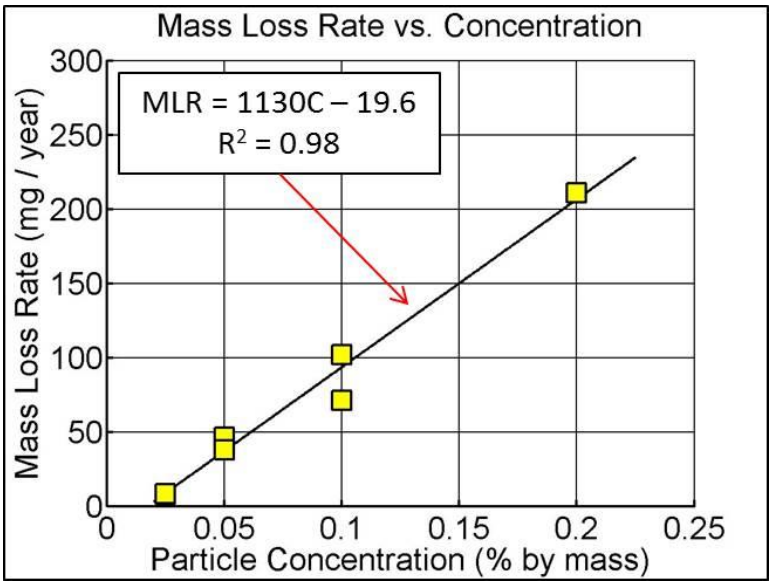

Figure 6-23 Mass Loss Rate vs. Particle Concentration

The one-dimensional erosion rates summarizing the concentration experiments are shown in Figure 6-24.

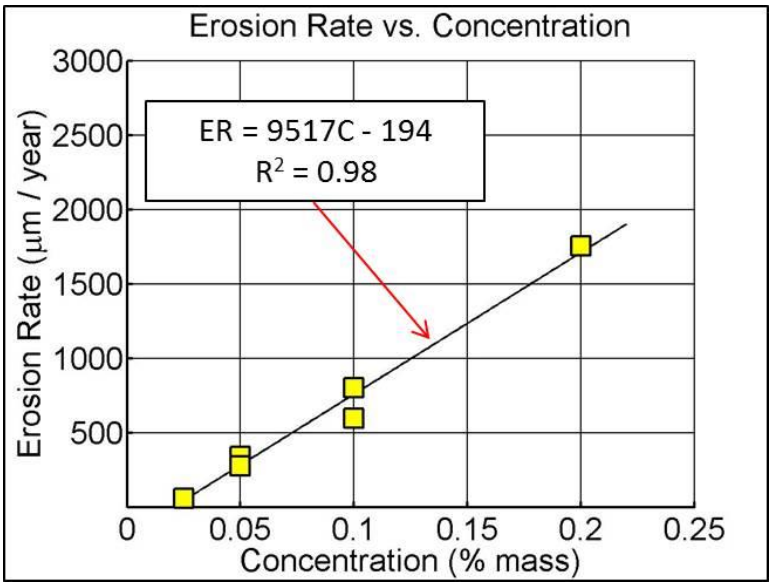

Figure 6-24 Erosion Rate vs. Particulate Concentration

Looking at the above graphs, it can be seen that the assumption where doubling the concentration doubles the mass loss rate and erosion rate is validated. The slope of the graph in Figure 6-24 is close to 1000 while the slope of the graph in

Figure 6-24 is 10,000 meaning that doubling the concentration effectively doubles the erosion metric. While the y-intercept should theoretically be zero, the negative y-intercept suggests the presence of a threshold concentration. It is thought that the negative y-intercept is a result of slight particle fouling phenomenon, where the actual concentration of the fluid impinging the surface is less than the concentration at the start of the test. Upon inspecting the test setup it was clear that particulate fouling occurred, specifically around the seals and O-ring as shown in Figure 6-25.

Figure 6-25 Particulate fouling near seals in test setup

Later sections will discuss the pertinence of this phenomenon more in depth, however from the work in this chapter it can be reasoned that of the factors contributing to erosion, concentration is least influential. The relationships between mass loss rate and erosion rate with particle size and jet velocity both follow power laws with exponents greater than four. This is compared to the linear relationship that concentration holds with these erosion metrics. As such, while a decrease in expected concentration will affect erosion results and subsequent predictions, other factors play

a more dominant role in erosion. Additionally, the fouling occurrence can be accounted for in the erosion predictions, more thoroughly described in Chapter 7.

6.4.4 Effect of Viscosity

The following profile scans show the results of the viscosity experiments. For each test case a 40 m/s nominal jet velocity was used with 10μm Al_2O_3 particles at a 0.1% concentration. Three different fluids were used: 10/90 PG/W, 25/75 PG/W and water. For each of the fluids containing propylene glycol, the solution was made by adding appropriate amounts of water to dilute the propylene glycol to the appropriate mixture proportion. For example, the 10/90 PG/W solution refers to a solution that is 10% propylene glycol by mass and 90% water by mass.

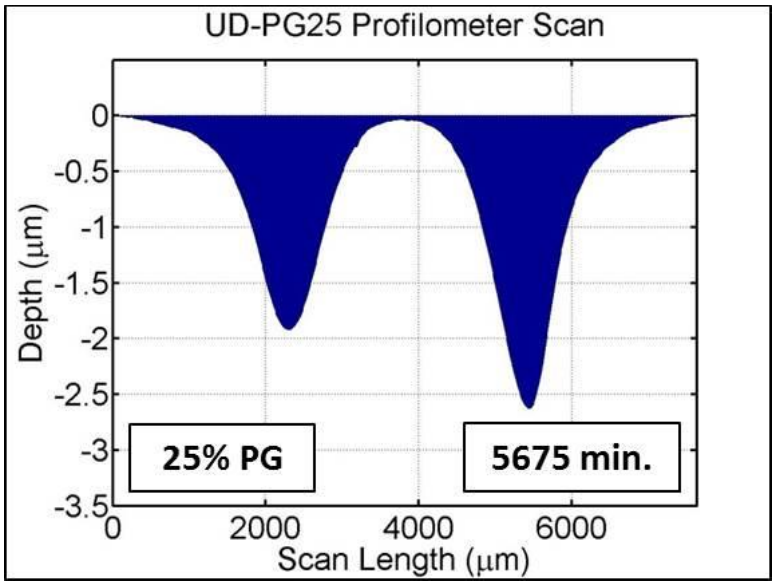

Figure 6-26 PG25 Profile Scan

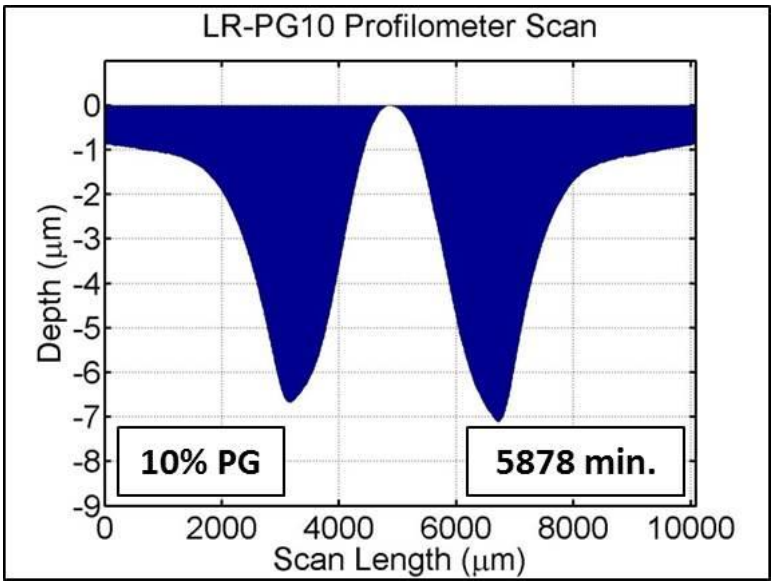

Figure 6-27 PG10 Profile Scan

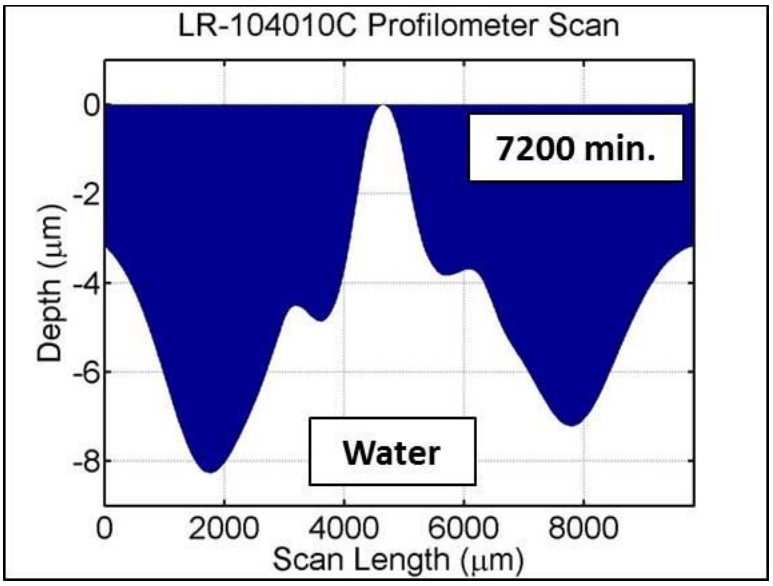

Figure 6-28 LR-104010C Profile Scan

Comparing the PG10 case to the water case , the first observation regarding the erosion contours is that distinct secondary impact sites are not observable. The viscosity of the PG10 solution is more than four times that of the water solution (0.73 cP for Water verses 3.3 cP for PG10) suggesting that stronger coupling between fluid

streamlines and particle motion exists. According to Table 4-2 the Reynold's number for both flows suggest that both are in the turbulent regime, however the PG10 solution (Re = 24100) is much less turbulent than the Water flow (Re = 107000). This may potentially reduce the random particle movement fluctuations and lead to a more precise impact location outcome.

It is also observed that the edges of the samples become less eroded with increased viscosity. As the viscosity of the fluid increases, the squeeze film may act more to protect the surface from scratches thus reducing the effect of low angle particle impacts. Comparing the PG10 and PG25 cases, it can be seen that subsequent impacts play less of a role in overall wear in the more viscous fluid.

The results of the mass loss rate experiments are shown in Figure 6-29 which suggests that the mass loss rate may follow a decreasing exponential relationship with fluid viscosity.

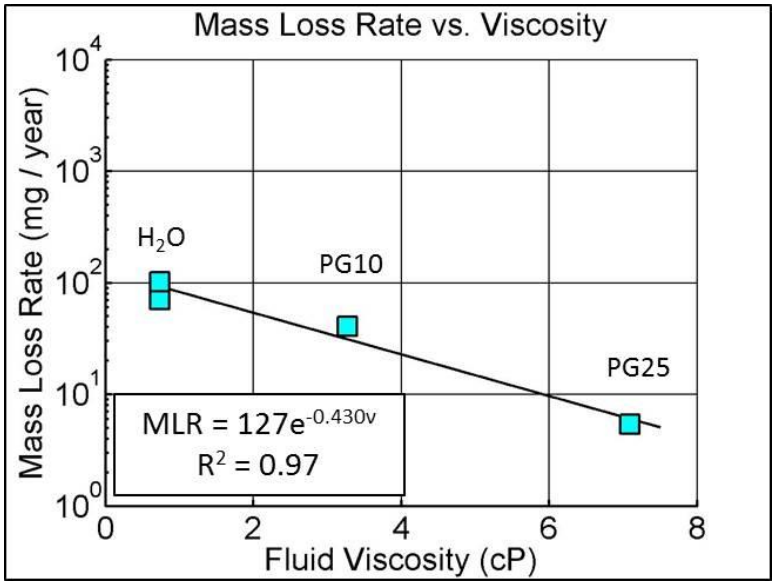

Figure 6-29 Mass Loss Rate vs. Fluid Viscosity

The relationship between the one-dimensional erosion rate and viscosity is shown in Figure 6-30.

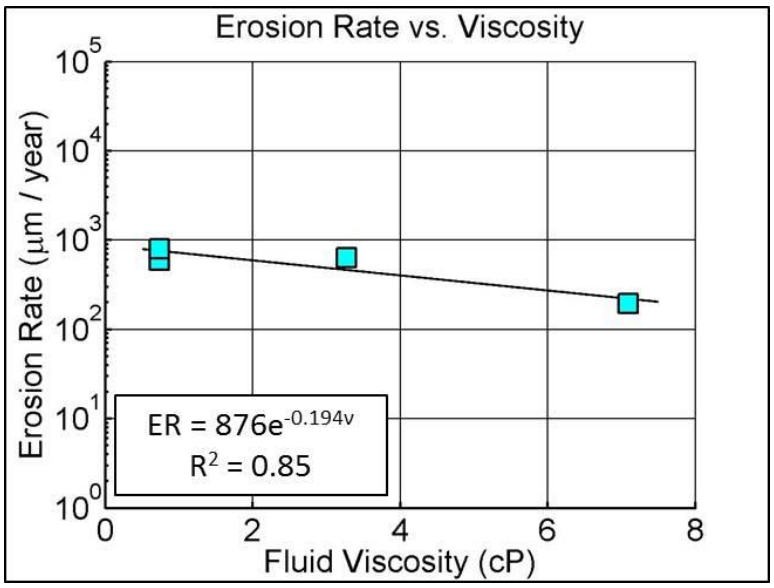

Figure 6-30 Erosion Rate vs. Fluid Viscosity

Although regression analysis suggests decreasing exponential relationships between the wear rates and viscosity, a much more thorough investigation would be necessary to confirm the exact calibration constants.

According to the graphs above, the erosion rates of the water and PG10 cases are very similar. This can be confirmed by looking at the CFD results, shown in Figure 4-23, which indicate that the impact velocities of the first particle impact are approximately 22 m/s and 23 m/s respectively for the PG10 and Water cases. This is compared to the velocity of the first impact for the PG25 case which is approximately 12.5 m/s. However, the impact velocities of subsequent impacts in the PG10 case are significantly less than those of water case. This is likely a result of the more viscous fluid (PG10) moving slower close to the surface while the less viscous fluid (water) moves quicker.

6.4.5 Effect of Testing Time

The following profile scans show the results of the 40 m/s transient test where four measurements were conducted periodically throughout the test. 10μm Al_2O_3 particles at a concentration of 0.1% in water were used as the testing slurry.

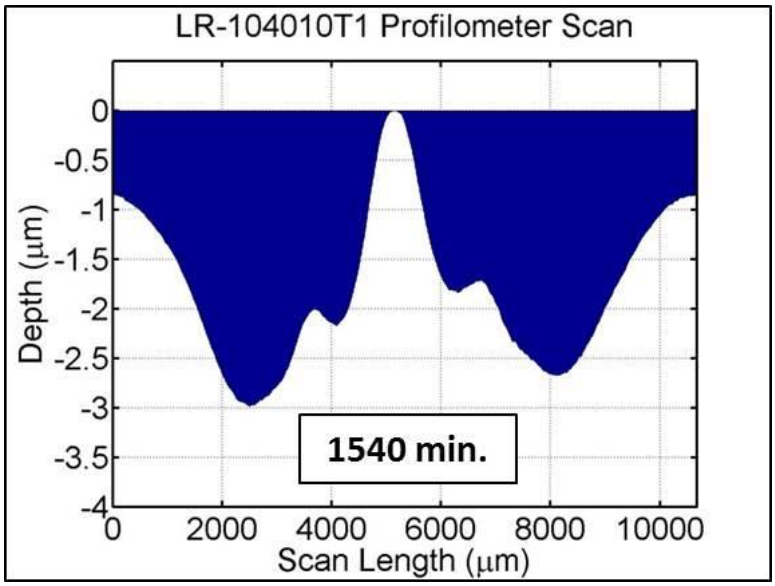

Figure 6-31 104010 Transient 1 Profile Scan

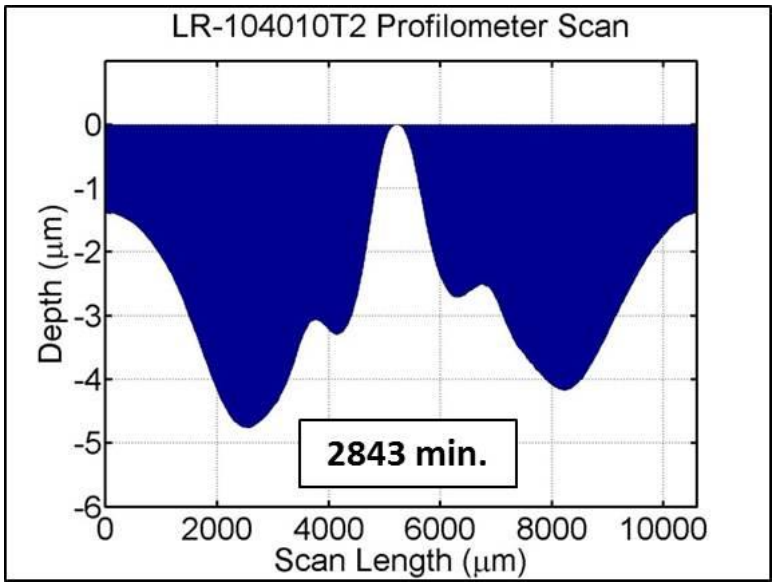

Figure 6-32 LR-104010 Transient 2 Profile Scan

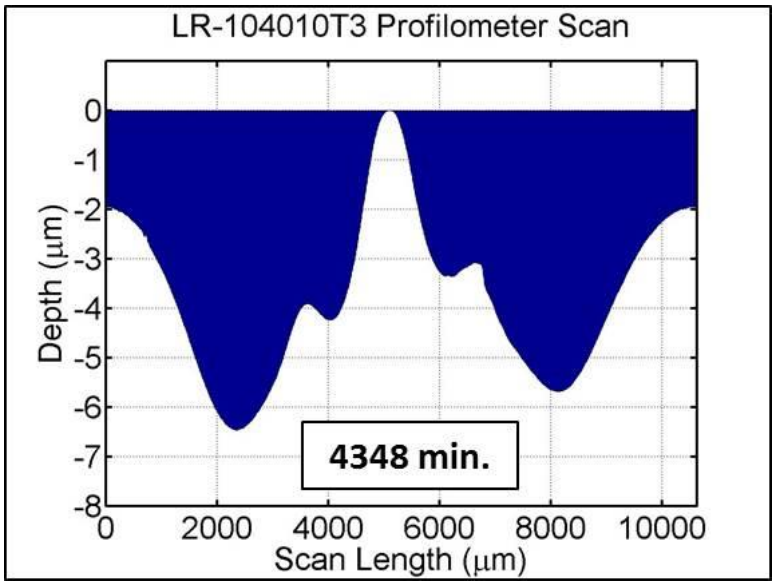

Figure 6-33 LR-104010 Transient 3 Profile Scan

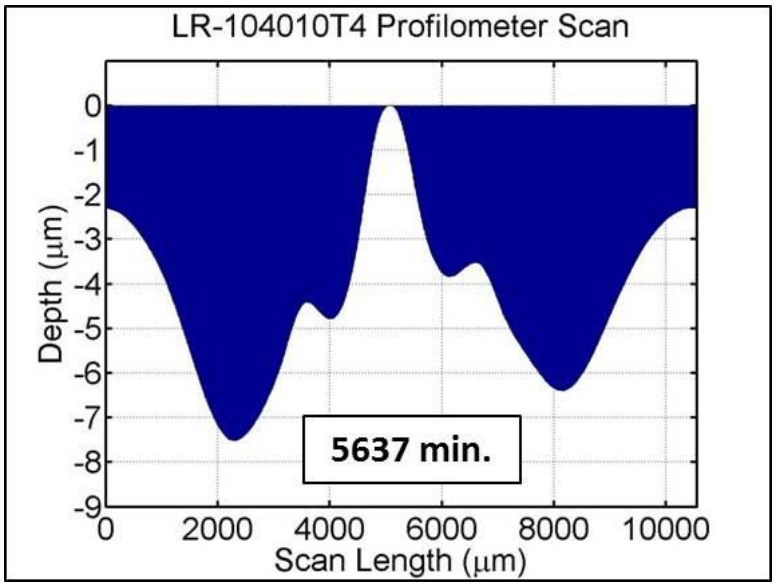

Figure 6-34 LR-104010 Transient 4 Profile Scan

Upon observation, the only distinguishable feature between each of the above profile scans is the y-axis scale. Each of the scans exhibit the same qualitative features and they all exhibit proportionally similar primary and secondary impact location depths.

The results of the mass loss rate experiments for the both the 30 m/s and 40 m/s test cases are shown in Figure 6-35.

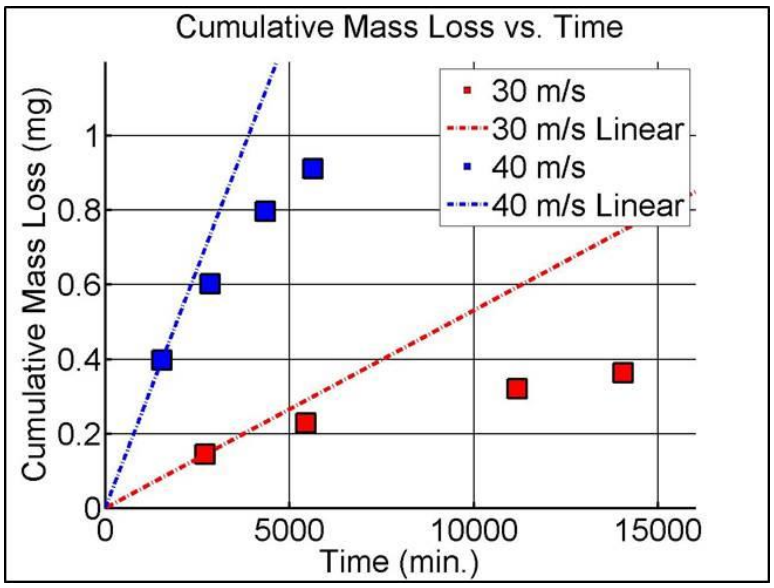

Figure 6-35 Cumulative Mass Loss vs. Time

Along the same logic of the concentration experiments, a linear relationship between mass removed and time should exist indicating a constant erosion rate. There have been many studies in literature which confirm that the amount of material removed has a linear relationship with the dose of impacting particles, in other words concentration or time [65] [125]. As such, it is thought that the major contributor to the non-linear relationship shown above is the fouling of particles on the surface of the test setup. Another contributor could be that the eroded surface changes the way particles interact with and impact the surface. However, given the similarities between each of the contours it can be assumed that the eroded surface does not change these impact properties significantly. If the erosion rates were orders of magnitude larger or the total depth was significantly greater, then this might become a concern.

Figure 6-36 shows the cumulative erosion rate as a function of time along with the expected linear erosion rate.

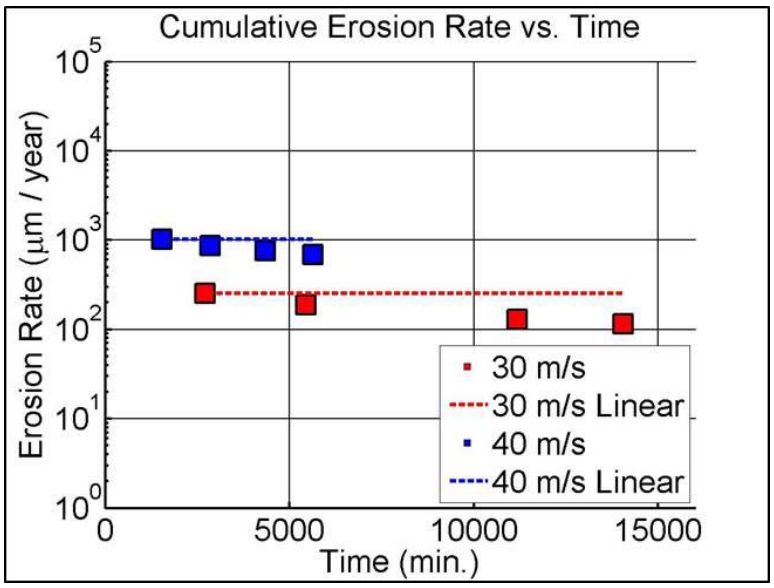

Figure 6-36 Cumulative Erosion Rate vs. Time

It can be seen that the cumulative erosion rate slightly decreases with time. Based on the experiments conducted in this study it is unknown whether or not the erosion rate will continue to decrease with time or if it will reach steady state eventually. In many respects this lies outside the scope of this study but can be suggested as an area for future work. However, for the purposes of this study and based on the findings that other factors such as velocity and particle size play a more critical role in erosion, it will be assumed that the particulate concentration remains constant with time.

6.5 SEM Observations of Ductile Erosion Modes

While the above section quantified the erosion metrics under different testing conditions, this section will comment on the various modes of erosion observed using a scanning electron microscope (SEM). All images presented in this section were

taken with an ultra-high resolution Hitachi SU-70 FEG SEM and the sample analyzed has the sample ID: 104010; 10μm particles, 40 m/s nominal jet velocity, 0.1% concentration in water.

Figure 6-37 shows an overview SEM image of the eroded surface taken near the region of maximum erosion. The first observation is that the surface features are significantly smaller than the particles creating them. While the average particle size is approximately 9μm, many of the features shown below have sizes on the order of 1μm. In addition, the direction of fluid flow can easily be recognized by the nearly uniform orientation of scratches on the surface.

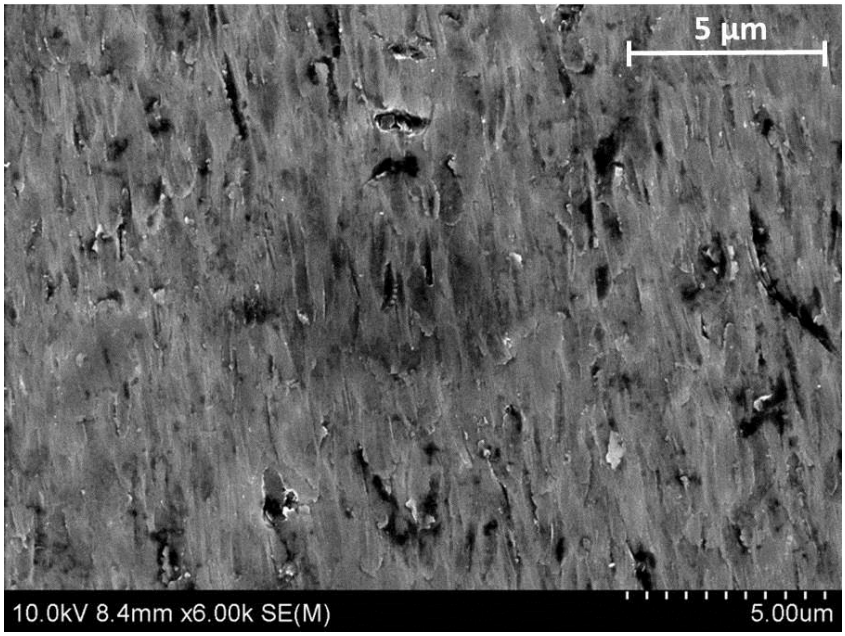

Figure 6-37 Overview of eroded surface

From this overview different modes of erosion can be identified, specifically scratching, indenting and flaking. A magnified image of this overview, shown in Figure 6-38, displays a small surface scratch on the order of 1μm in length.

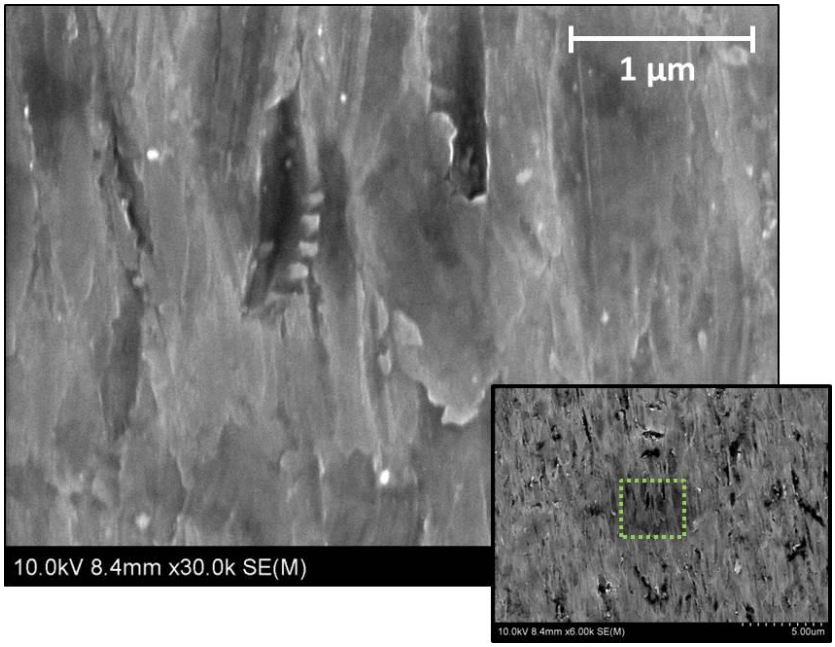

Figure 6-38 Magnified overview image showing small surface scratch

This type of surface asperity was likely caused by a sharp particle brushing lightly against the surface. However, it can also be seen in the above images that the geometries of scratches vary from thin and deep to broad and shallow. This suggests that the particulate shape plays a significant role in the type of wear observed. While sharper particles impacting the surface would cause thin and deep scratches, impacts by blunt or more rounded particles would yield wide and shallow abrasions taking on more of a ploughing mechanism.

Magnifying a different region of the overview image shows a particle indentation likely caused by a higher angle impact. Figure 6-39 shows two overlapping modes of erosion; an indentation with trapped debris and an overlaying shallower scratch.

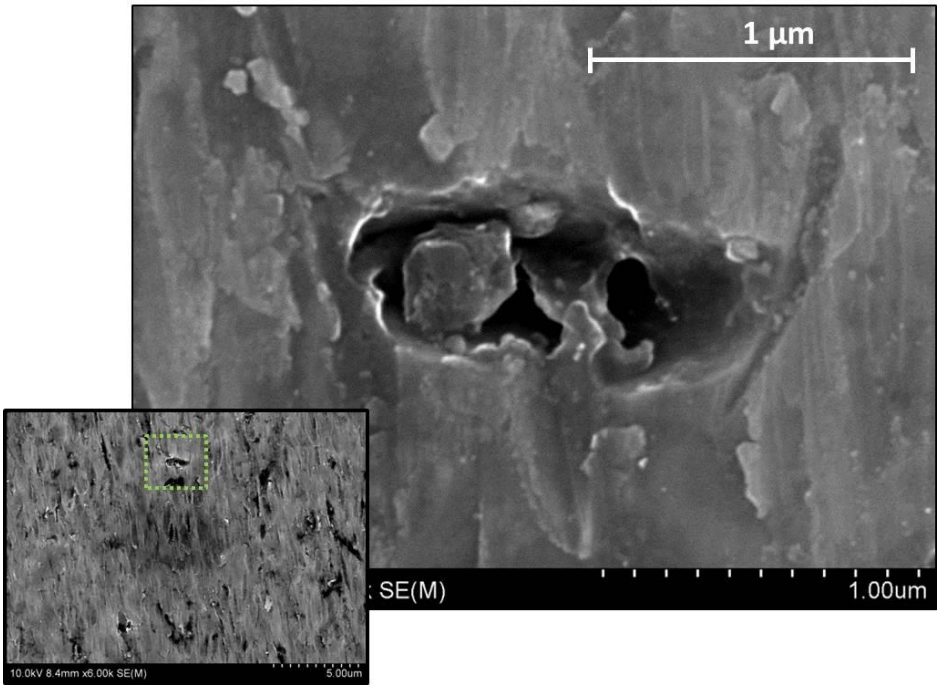

Figure 6-39 Magnified overview image showing particle indentation and shallow scratch

Although the CFD results suggest that the majority of impact angles are small, there may occasionally be an anomalously higher angle impact caused by local turbulent velocity fluctuations. This type of damage would fall in line with the quasi-static formulation of erosion which states that the particle's kinetic energy is transformed into plastic flow within the material. Unlike the quasi-static model however, the formation of median/radial and lateral crack systems cannot be seen and thus the observed indentations are thought to be primarily plastic in nature.

Although the terms 'plastic', 'plastic flow' and 'plastic deformation' are used throughout this section, the more appropriate term to be used would be 'pseudo-plastic'. As discussed in the literature review section, the differentiation between ductile and brittle wear can become hazy as the impact conditions largely dictate how the material responds. Along the quasi-static and dynamic models of brittle erosion, an impacting particle creates a region of plastic deformation followed by the creation

of various crack systems. With ductile erosion, impacting particles cause material displacement in the form of plastic deformation surrounding the impact site. With the type of wear observed in this study, it can be seen that the classical lateral and median/radial crack systems do not form thus rendering the quasi-static and dynamic model inapplicable. However, the mechanisms taking place at the crystallographic level cannot be observed using the techniques available in this study. In other words, it is unclear whether or not the 'plastic flow' is analogous to the movement of 'silly-putty', or if there exists small-scale microfracture and intracrystalline movement along slip bands. Most likely the observed mechanisms are a combination of both.

Flaking and platelet formation, as a result of shallow ploughing, can also be seen throughout the images. As described by Levy [126], ploughing can be described as the formation of a crater and the subsequent piling up of plastically deformed material around the impact zone. In the case of ductile materials like aluminum or copper, the displaced material may be removed due to additional particle impacts or flattened out to form platelets. In the case of silicon however, the piling up of material is not as pronounced but rather the formation of thin flakes originates from the shallow ploughing of relatively blunter particles. One such flake can be seen in Figure 6-40.

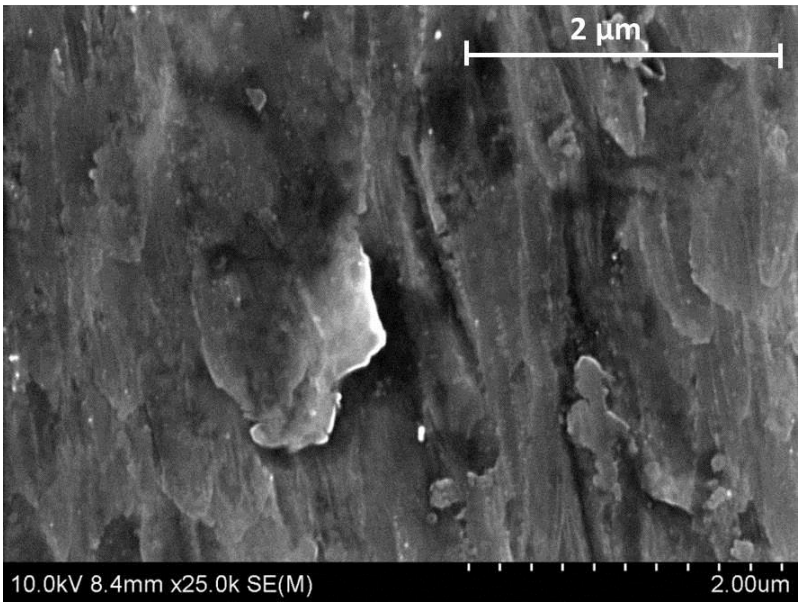

Figure 6-40 Flake formation as a result of shallow ploughing

It can be suggested that these flakes, having thicknesses on the order of approximately 50nm, break off from the bulk material as a unit. Levy [126] describes the platelet formation in nominally ductile materials arising from repeated particle impacts forging the material pile-up into flat segments. While it is unclear whether or not the observed platelet formation arises from a single impact or multiple, it is clear that predominately ductile material removal mechanisms are taking place.

Another potential explanation for these thin flakes is the somewhat bulk movement of material across a slip plane. Upon the shallow angle impact from a larger blunt particle, the induced shearing force may cause the crystallographic planes to slide over one another in a "deck-of-cards" type movement. While this may explain the formation of thin flakes, modeling this phenomenon at these size scales would be outside the scope of this work.

Another overview image, shown in Figure 6-41, reveals similar characteristics, such as the deeper scratches and ploughing but also indicates the presence of relatively discrete impacts causing mixed ductile/brittle modes of erosion.

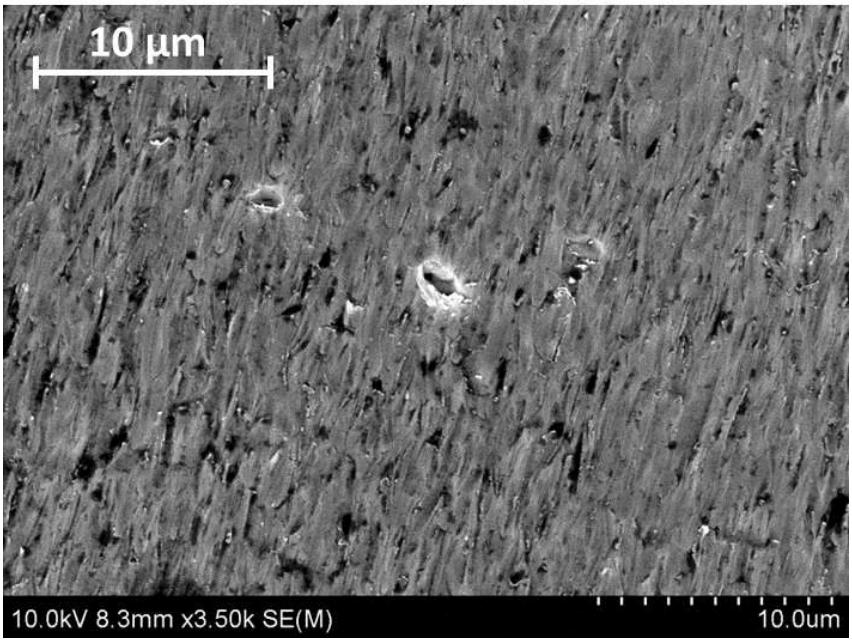

Figure 6-41 SEM overview showing discrete sites of ductile/brittle mixed erosion modes

For reference, the lighter parts of the image represent elevated regions while the darker parts represent depressed regions. As such, scratches can be seen as black gashes whereas the white locations represent elevated material and typically surround indentation sites. Figure 6-42 shows a magnified view of one of the discrete impact sites from the overview image.

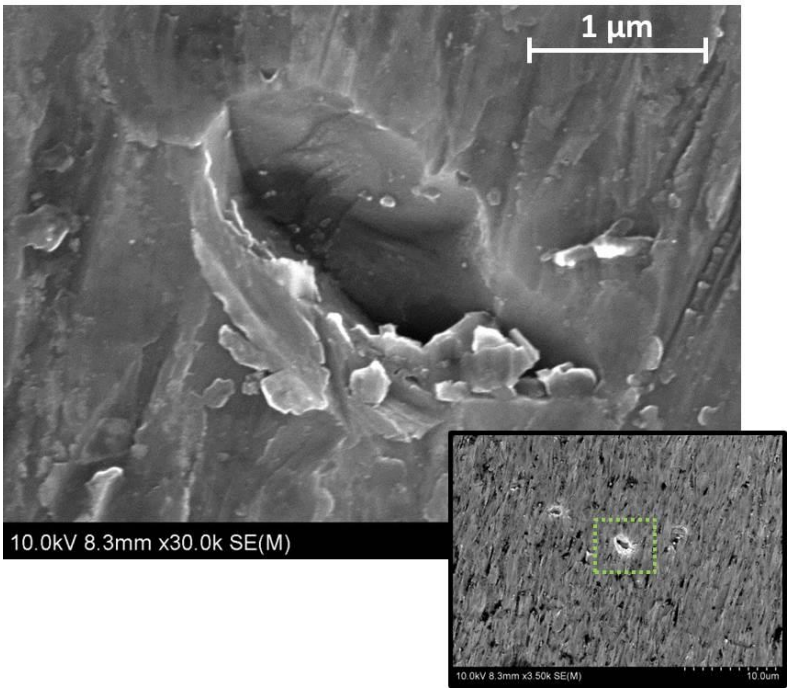

Figure 6-42 Magnified image of overview showing mixed ductile/brittle wear

It can be reasoned that the initial indentation was caused by a larger sharp particle with a significant amount of kinetic energy to cause the quasi-static indentation. However, the displaced material piling up on the sites appears to have fractured resulting in an array of micro-flakes surrounding the impact zone. Due to the fact that material was originally displaced in a plastic manner but ultimately removed due to the fracture and chipping away of the micro-flakes, it can be suggested that the mode of wear in this image is that of a combined ductile/brittle mode. The image also reveals fine-scale fracture along slip bands as indicated by the darker near-parallel bands within the indentation. Due to the fact that the radial crack systems cannot be observed, but material pile-up and microfracture can be, further suggests that the type of occurrence here is along the lines of a pseudo-plastic indentation.

Much like the flake formation previously discussed, the action of plastically deformed bulk material tends to facilitate the development of fine flake features near the surface. While the flake formation can be considered a nominally ductile mechanism, the susceptibility to flake formation would likely be higher in nominally brittle materials due to higher surface hardness properties. Increased surface hardness reduces the susceptibility to localized plastic deformation resulting in the formation of brittle flakes more easily. In this light the increased material hardness of silicon, as compared to other metals, inhibits the continuation of plastic flow causing the material to displace in other fashions, i.e. micro-scale chipping.

Another magnified image of a discrete impact site likely caused by a single larger particle is shown in Figure 6-43.

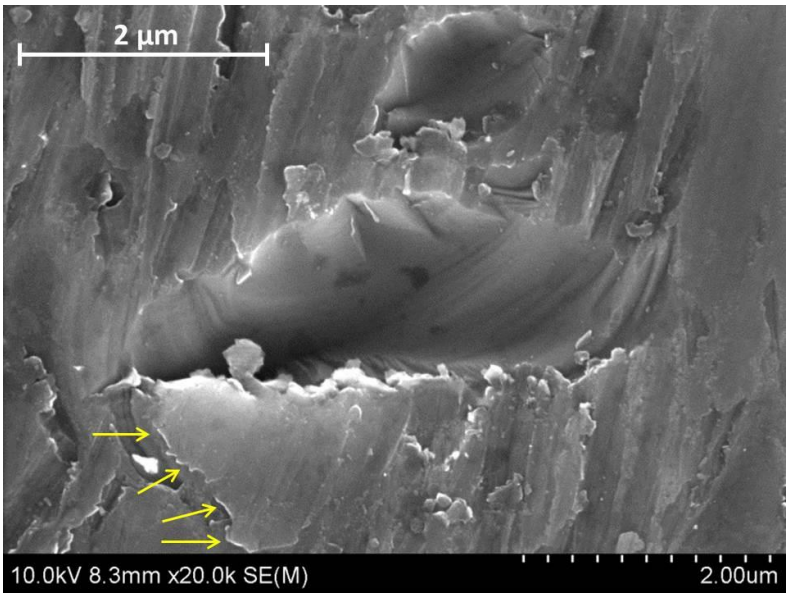

Figure 6-43 Magnified image of surface showing a discrete 'deep gouge'

In this image the material pile-up can clearly be seen surrounding, what can be referred to as, the 'deep gouge'. Additionally, the initiation of the micro-flaking mechanism within the plastically deformed pile-up is shown by the arrows. While the

initial material pileup is attributed to plastic flow, the subsequent material removal of the micro-flakes is likely brittle in nature. Due to the fact that the median/radial and lateral crack systems cannot be observed, the main mechanism of material removal here is plastic indentation coupled with the lateral motion of the particle. However, the initiation of flake formations can be observed towards the bottom of the impact site by the arrows. Unlike the Figure 6-42 which showed micro-fracture and small chip formations, the mechanism here suggests that a larger mass of material could be removed in a single flake. This indicates that the localized stresses in the plastically deformed region surpass a threshold value initiating the subsurface crack system. Much like the lateral crack system formed in quasi-static indentations, once the subsurface cracks reach the surface material can be removed in the form of a chipping mechanism.

Lastly, an image was taken near the edge region of the sample where the wet-abrasion mechanism is thought to dominate material removal. Shown in Figure 6-44, the presence of longer scratches and ploughing marks can be seen indicating that the majority of particle impacts are a result of low impact angle collisions where the particles are dragged along the surface under the influence of the squeeze film. The regions of the surface that appear to be “smeared” indicate that a localized plastic process is taking place.

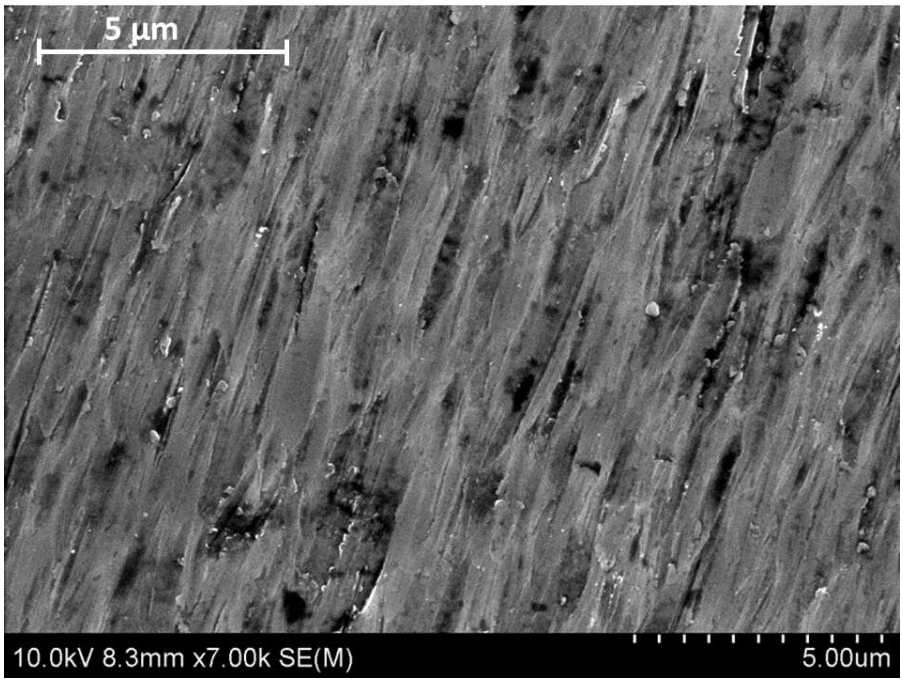

Figure 6-44 SEM image showing long scratches and ploughing marks

In addition the lack of deeper scratches, gouges and plastically deformed material leading to flaking suggests that the particles may be somewhat lubricated by the viscous sublayer of slower moving fluid directly above the surface. In reality, this may dampen the particle impact velocity resulting in less than predicted values compared to CFD. This dampening phenomenon will be discussed further in Chapter 7.

6.6 Conclusion

This chapter presented the testing methodologies and the experimental findings from the erosion experiments performed in this study. First, the design of experiments was presented that outlined 14 different test cases to investigate the effect of nominal jet velocity, particle size, particle concentration, fluid viscosity and time on erosion. Based on the information presented in the literature review chapter it was assumed

these were the most important factors contributing to erosion. Next, the measurement techniques were described which combine stylus profilometry and MATLAB to determine the total amount of material removed for each test sample. In addition the algorithm to factor in the initial warpage of each test sample was presented.

While there are a variety of different erosion metrics, this chapter presented both a mass loss rate in units of milligrams per year and a one-dimensional maximum erosion rate in units of micrometers per year. A sampling of raw erosion profile scans describing each of the different testing variables was included; however the complete array of raw data is included in Appendix A. It was found that the nominal jet velocity and average particle size each exhibit a power law relation with the mass loss rate and erosion rates, while concentration shows a linear relationship. This aligns well with previous erosion studies suggesting that particle size and velocity are the critical factors contributing to erosion. Viscosity showed a slight decreasing exponential relationship with erosion; however a more thorough investigation is needed to determine if this holds up over a wider range of viscosities. Lastly the mass loss rate and erosion rates were both expected to be constant with time; however experiments showed that the wear rates slightly decreased with time. One explanation is that the particulate concentration slightly decreases with time due to a fouling phenomenon where particle exist the bulk flow and deposit in the test setup. This can be shown in Figure 6-25, however quantifying this mechanism in depth lies outside the scope of this study.

SEM images were taken of the eroded surface and revealed valuable information regarding the types of erosion mechanisms taking place. For example, a

few overview images suggest the presence of deep scratches, gouges, flakes and ploughing marks. Upon further inspection, mixed modes of erosion were found where discrete particle impacts cause material to pile-up around the impact site under the action of plastic flow. Closer observation suggests that the piled-up material fractures and forms micro-flakes which are then subsequently removed by the fluid flow. From this information is can be deduced that the majority of wear occurs in a ductile manner due to low angle impacts. As such, a ductile erosion model would ideally be chosen to capture this specific type of wear.

The following chapter will use the experimental results from this chapter in order to redefine the primary erosion metric as a ratio, i.e. the mass of material removed to the mass of impacting particles. This will enable comparisons to be made from previous work but will also facilitate the development of a particle-based erosion model.

7 DEVELOPMENT OF A PARTICLE EROSION MODEL

7.1 Introduction

This chapter builds off the previous chapter and discusses the development, calibration and validation of a particle based erosion model. While Chapter 6 presented the erosion results as mass loss rates and one-dimensional erosion rates, this chapter will convert mass loss rates into non-dimension erosion ratios by utilizing particle impact data from the CFD simulations. The erosion ratio is a commonly used erosion metric and is defined as the mass of material removed to the mass of impacting particles. From a particle based perspective, this ratio describes the amount of mass removed from each individual particle impact. Given the nature of CFD simulations where hundreds of thousands, if not millions, of particle tracks can be simulated, implementing this type of erosion model yields an erosion flux, presented in units of kg/m^2-s. Dividing this value by the substrate's density alters the erosion metric to a one-dimensional erosion rate.

First, the experimental erosion results from the previous chapter will be presented in the newly transformed erosion metric. The method in which the total mass of impacting particles was calculated will be given followed by the erosion ratio graphs describing the effects of jet velocity, particle size, concentration, fluid viscosity and time. Next, the Huang et al. [127] phenomenological erosion model will be presented which serves as the framework for the new erosion model created. The calibration procedure will be described including the method used to determine the

velocity and particle size exponents and the material/system constant. This model will then be hooked into FLUENT for validation simulations where the one-dimensional erosion rates from the experimental efforts and the CFD simulations will be compared.

Although the validation simulations indicate a close comparison between CFD and experiments, the CFD results tend to over-predict the erosion rates in most test cases. To explain this small inconsistency an impact dampening coefficient, β, is proposed which suggests that the impact velocity from the CFD simulations is slightly larger than the real-life impact velocities. While individual particle impact velocities were not measured in this study, the inclusion of the proposed β factor significantly reduces the difference between the CFD simulations and the experiments.

7.2 Particle Based Erosion Results

This section will present the new form of the erosion data as the previously discussed erosion ratio.

7.2.1 Experimental Results as Erosion Ratios

Using the particle impact data from the CFD simulations and given that the erosion ratio is defined as the mass of material removed to the mass of impacting particles, the erosion results presented in Chapter 6 can be converted to erosion ratios. In the simplifying case of a single particle impact, the erosion ratio determines the amount of mass removed due to a single particle impact. Table 7-1 lists the raw data used to generate the erosion ratio graphs.

Table 7-1 Data used to calculate erosion ratios

Sample ID	Testing Time [min.]	Total Mass Loss [mg]	Particle Impacting Mass Rate [mg/sec]	Total Mass of Impacting Particles [mg]	Erosion Ratio [mg/mg]
24010	18714	0.0180	2.10E+02	2.36E+08	7.59514E-11
54010	8263	0.0909	2.22E+02	1.10E+08	8.24878E-10
104010C	7200	0.9739	2.72E+02	1.18E+08	8.28457E-09
103010	11650	0.2173	2.24E+02	1.57E+08	1.38547E-09
102010	15749	0.0336	1.32E+02	1.24E+08	2.70011E-10
104010D	6740	1.3090	2.72E+02	1.10E+08	1.18951E-08
103010C	11060	0.3892	2.24E+02	1.49E+08	2.61352E-09
102010B	21555	0.0463	1.32E+02	1.70E+08	2.71556E-10
102510	21297	0.1458	1.85E+02	2.37E+08	6.15363E-10
54010B	11137	0.2149	2.22E+02	1.48E+08	1.44734E-09
54010C	11253	0.0984	2.22E+02	1.50E+08	6.55705E-10
24010B	20390	0.0083	2.10E+02	2.58E+08	3.20387E-11
204010	1316	2.0725	2.82E+02	2.23E+07	9.302E-08
204010B	1346	2.5797	2.82E+02	2.28E+07	1.13204E-07
104005	5636	0.4993	1.36E+02	4.60E+07	1.08509E-08
104020	4033	1.6171	5.44E+02	1.32E+08	1.22791E-08
1040025	6936	0.1024	6.80E+01	2.83E+07	3.61516E-09
1040025B	9894	0.1535	6.80E+01	4.04E+07	3.80089E-09
104005B	5536	0.4006	1.36E+02	4.52E+07	8.86296E-09
TR40-1	1540	0.3967	2.72E+02	2.51E+07	1.57772E-08
TR40-2	2843	0.6031	2.72E+02	4.64E+07	1.29927E-08
TR40-3	4348	0.7978	2.72E+02	7.10E+07	1.12381E-08
TR40-4	5637	0.9124	2.72E+02	9.20E+07	9.91292E-09
TR30-1	2717	0.1445	2.24E+02	3.66E+07	3.94905E-09
TR30-2	5449	0.2287	2.24E+02	7.34E+07	3.11687E-09
TR30-3	11175	0.3203	2.24E+02	1.50E+08	2.12899E-09
TR30-4	14053	0.3629	2.24E+02	1.89E+08	1.91789E-09
PG10	5878	0.4576	3.92E+02	1.38E+08	3.31078E-09
PG25	5675	0.0583	4.27E+02	1.45E+08	4.009E-10

The erosion ratios for the nominal jet velocity and average particle size test cases are shown in Figure 7-1 and Figure 7-2 respectively.

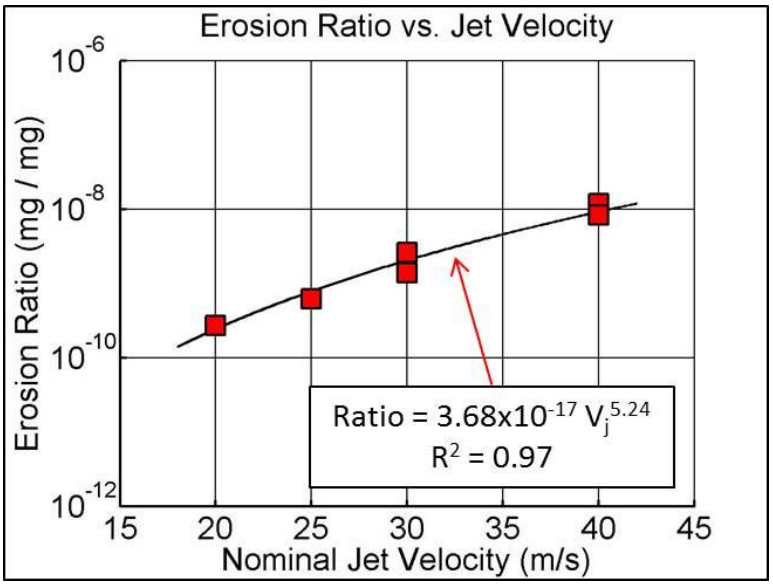

Figure 7-1 Erosion Ratio vs. Jet Velocity

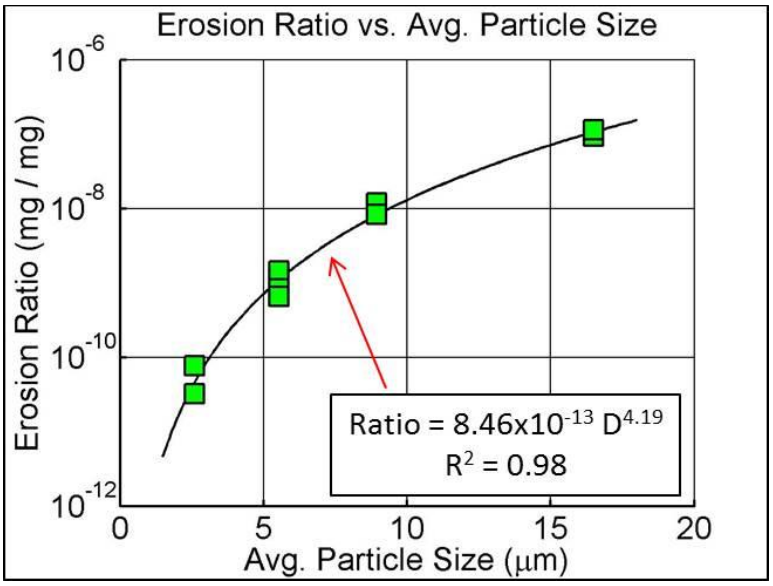

Figure 7-2 Erosion Ratio vs. Average Particle Size

Much like the mass loss and 1-D erosion rates in Chapter 6, jet velocity and particle size both exhibit power law relations with exponents of 5.24 and 4.19 respectively. The particle size results can directly be used in the development of a particle based erosion model due to the fact that the erosion ratio is directly

proportional to the particle size. Regarding jet velocity however, the erosion ratios described above need to be transformed into a form that considers individual particle impact velocities. Due to the fact that particle impact velocities are different than the nominal jet velocity and due to the wide ranges of impact velocities for a single jet velocity, further data processing will be necessary. This will be described in a later section of this chapter.

Figure 7-3 shows the relation between particulate concentration and erosion ratio. One of the assumptions in these experiments is that the particles are non-interacting due to the dilute nature of the slurries. As such, the concentration of particles should not have an effect on the erosion ratio. A single particle in a slurry with 0.1% concentration should yield the same amount of damage as a single particle in a slurry with a concentration of 0.2%.

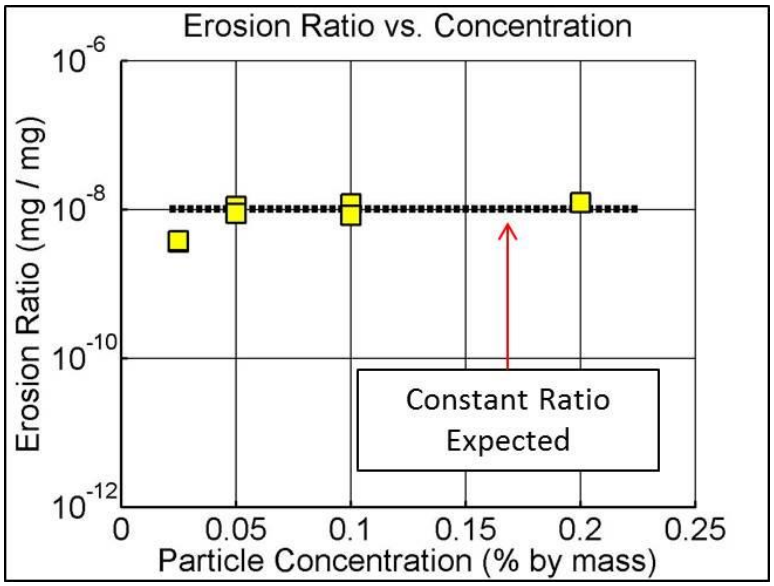

Figure 7-3 Erosion Ratio vs. Concentration

The graph above shows the data compared with the expected constant erosion ratio. While the data for the 0.05%, 0.1% and 0.2% cases align with this assumption,

the 0.025% case exhibits a slightly lower than expected erosion ratio. As discussed previously in Chapter 6, it is thought this inconsistency is due to a slight fouling phenomenon where particles settle out in the test setup.

Figure 7-4 shows the effect of viscosity on the erosion ratio. Similar to the mass loss and erosion rate results, viscosity shows an inverse relation with erosion ratio. While quantifying this trend would require a more thorough investigation, this information suggests that particles induce less damage as the viscosity increases for similar nominal jet velocities.

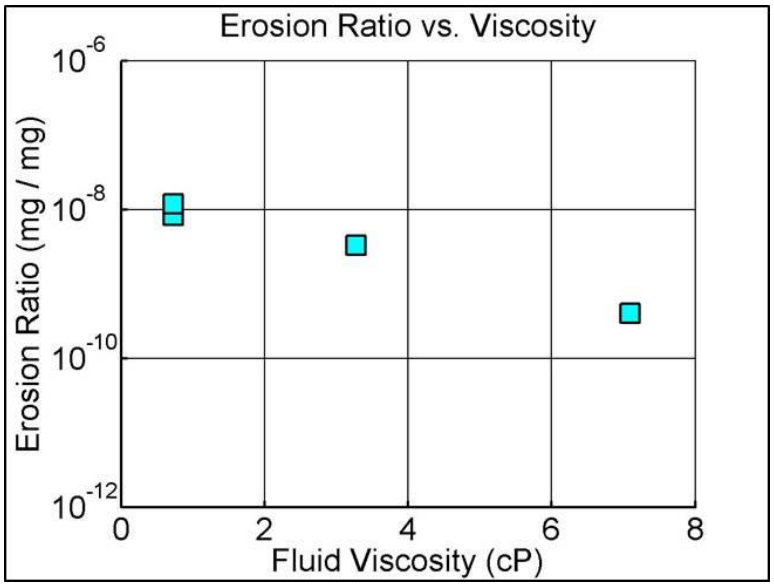

Figure 7-4 Erosion Ratio vs. Viscosity

This highlights the importance of understanding actual particle impact velocities rather than just fluid velocities. In the viscosity tests, the fluid acts to dampen the velocity of an approaching velocity. In addition, as particles are swept away in the tangential flow the more viscous fluid may act to lubricate the surface protecting it from particles trapped in the squeeze film. As such the rolling, bouncing

and scratching action of the particles would yield less damage compared to similar conditions in less viscous fluids.

Figure 7-5 shows the cumulative erosion ratio as a function of time for both the 30 m/s and 40 m/s transient tests. In addition, the assumed constant rates are shown on the graph where the value is equivalent to the erosion ratio calculated for the first data point.

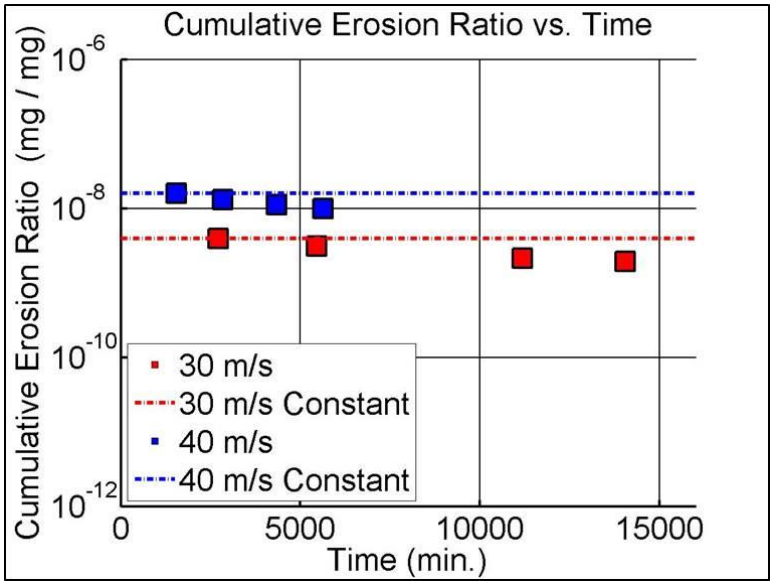

Figure 7-5 Erosion Ratio vs. Time, compared with constant ratio

It can be seen that the erosion ratio decreases slightly for both test cases and is thought to be caused by a decrease in particulate concentration with time. While it is assumed that the concentration of the solution stays constant with time, but in reality decreases, an apparent decrease in the erosion ratio would be observed.

7.2.2 Calculating Total Mass of Impacting Particles

Given that the mass of material removed was calculated in the Chapter 6 and that the erosion ratio is defined as the mass of material removed to the mass of impacting particles, the remaining unknown is the total mass of impacting particles.

While this cannot be directly measured from an experimental point of view, the CFD simulations provide a method through which this can be calculated.

In a steady state CFD simulation Lagrangian particle tracking is conducted such that the trajectories of particle streams, rather than individual particles, are determined. To begin, the mass flow rate of an individual particle stream must be calculated. First, the fluid flow rate is calculated:

$$Fluid\ Flow\ Rate = Nominal\ Jet\ Velocity * Nozzle\ Area \tag{7-1}$$

By considering the known particulate concentration defined as the ratio of the mass of particles to the mass of fluid, the total particle flow rate can be determined:

$$Total\ Particle\ FR = Fluid\ FR * Concentration \tag{7-2}$$

In Chapter 4, it was found that 320,000 particle streams must be simulated in order to achieve erosion independence with respect to the number of particle tracks. The individual particle stream flowrate is determined as:

$$Individual\ Particle\ Stream\ FR = \frac{Total\ Particle\ FR}{\#\ Particle\ Streams} \tag{7-3}$$

where the number of particle streams is approximately 320,000. Occasionally particle streams are deemed incomplete thus the real number of particle streams is often slightly less than then the defined 320,000.

To determine the total mass of impacting particles, the individual particle stream flow rate is multiplied by the total number of impacts determined from CFD.

$$Total\ Impacting\ Mass\ Rate = Particle\ Stream\ FR * Total\ \#\ Impacts * Time \tag{7-4}$$

The total number of impacts is taken across all ~320,000 particle streams and up to 10 impacts per stream. Given the steady state nature of the CFD simulations, a number of inherent assumptions exist in this calculation. First, the concentration is assumed to remain constant throughout the duration of the test. While the concentration was found to slightly decrease with time due to fouling, this assumption needs to be made and will be accounted for later in this Chapter. In addition, the number of impact locations is assumed to remain constant. The particle track independency study showed that a large number of streams are needed in order to make this assumption hold true. Lastly, the fluid flow rate is assumed to be constant. While direct flow measurement were not taken, as discussed in Chapter 5, continual observation and the initial calibration of the pump suggests that this can be a valid assumption.

7.3 Introduction to Huang et. al. Cutting Erosion Model

The Huang et al. cutting erosion model [127] is a phenomenologically developed erosion model that considers the major factors contributing to erosion such as particle size impingement angle, impingement velocity, particle shape and material properties. The term phenomenological is used as its derivation stems from an analytical formulation based on real-world phenomenon. The model captures two principle modes of erosion, namely deformation and cutting wear. Deformation wear originates from higher angle impacts resulting in plastic flow pile-up surrounding the impact crater while cutting wear originates from shallow angle impacts slicing into the surface. Analytically, the volume of material removed due to deformation wear is analyzed by factoring in the force and volume of indentation, the surface strain

induced from impact, the critical strain and the Coffin-Manson equation while the cutting wear is determined using an energy equation. Furthermore, this model has also been shown to be applicable in slurry jet-impingement erosion predictions [128] and slurry flow in a horizontal pipeline [129].

Although this model was calibrated for and assumes that the eroded material is ductile, the SEM images suggest that the major modes of erosion are ductile in nature despite the nominally brittle property of silicon. While the model considers two different modes of erosion, various simplifications and assumptions can be made such that the most prevalent modes of erosion are considered.

In the originally derived form, the total volume of material removed ΔQ from the Huang model is defined as follows where Table 7-2 lists the parameters:

$$\Delta Q = A\frac{M_p\rho_p^{\frac{1}{4b}}(Vsin\alpha)^{2+\frac{1}{2b}}}{\varepsilon_c^{\frac{1}{b}}P_n^{1+\frac{1}{4b}}} + B\frac{{M_p}^{1+\frac{3(1-s)}{4}}V^{2+\frac{3(1-s)}{2}}(cos\alpha)^2(sin\alpha)^{\frac{3(1-s)}{2}}}{D_p^{\frac{1-s}{4}}\varepsilon_o^i P_t P_n^{\frac{3(1-s)}{4}}} \quad (7\text{-}5)$$

Table 7-2 Parameters of the Huang et. al. cutting erosion model

A, B	Material coefficients
M_p	Particle mass
ρ_p	Particle density
b	Material exponent determined through experiments
V	Impact velocity
α	Impact angle
ε_c	Deformation damage removal, critical strain and Coffin-Manson
P_n	Constant pressure from particle impact
s	Particle shape exponent $0.5 < s < 1$
D_p	Particle diameter
ε_o^i	Material ductility, i exponent determined through experiments
P_t	Plastic flow pressure

The model can be broken up into two main parts, each representing a different erosion mechanism. The part of the formula with the A material coefficient represents

the volume of material removed due to deformation damage and the other part of the formula represents the volume of material removed due to cutting wear. Given that the CFD results and SEM images indicate primarily low-impact angle wear resulting in cutting and shallow ploughing, the first part of the equation can be assumed negligible. Additionally, the particle shape exponent was chosen to be 0.75. A value of 0.5 represents line cutting conditions while a value of 1 represent area cutting conditions. Typically line cutting occurs for extremely sharp particles where area cutting is a result of large impact surfaces and rounder particles. The SEM images suggested that a variety of different particle shapes induced the cutting damage and, in addition, the authors suggest that a value of 0.75 is a good approximation. Taking all these assumptions into consideration, conglomerating the material parameters into a single material/system constant, and converting the erosion units from volume loss to an erosion ratio, the Huang cutting model simplifies down to the following form:

$$ER = \frac{\Delta Q}{M_p \rho_{Si}} = K D^m V^n \cos^2 \alpha \sin^{0.375} \alpha \tag{7-6}$$

where *K* is the new material constant, and *m* and *n* are the particle size and velocity exponents respectively in need of new calibration. The reason these exponents need to be calibrated is because they were originally calibrated for ductile materials such as aluminum, copper and steel. Additionally, the experiments used to calibrate these values were conducted by Misra and Finnie [130] and assessed by Bitter [131] and thus the particle sizes and impact velocities are far outside the range used in the present experiments. Most of these experiments used 250μm particles with impact velocities greater than 100 m/s. As such, it becomes necessary to recalibrate these exponents within the particle size and velocity ranges of interest.

7.4 Model Calibration

This section describes the process through which the variables in the Huang cutting erosion model, namely the material constant, velocity and size exponents, were calibrated based on the erosion experiments described in Chapter 5.

7.4.1 Particle Size Exponent

The particle size exponent *m* is the most straightforward unknown to determine. Through the reformulation of erosion results into erosion ratios, it was shown that the erosion ratio is directly proportional to the average particle size raised to the power of 4.19.

$$ER \propto D^{4.19} \tag{7-7}$$

As such *m* can be taken as 4.19 where D represents the average particle size.

7.4.2 Velocity Exponent

In the previous section it was found that the erosion ratio is proportional to the jet velocity raised to the power of 5.24.

$$ER \propto V_j^{5.24} \tag{7-8}$$

However, the erosion ratio ultimately needs to be proportional to the particle impact velocity raised to a power; however the value of this power is unknown. Thus finding the exponent *n* requires a coupling between jet velocity and particle impact velocity. The CFD results shows that a single impact velocity could not be representative of the impacts caused at a specific jet velocity due to the wide spread

of values. In order to couple the jet velocity with particle impact velocity, it was deemed necessary to consider all impacts.

Based on the Huang model, a summation metric was proposed:

$$\sum V^n \sin^{0.375} \alpha \cos^2 \alpha \tag{7-9}$$

where the summation takes places across all impacts of each particle stream assuming a maximum of 10 impacts per stream. It was assumed that for each jet velocity case a proportional summation metric would exist. As such the following relation could be assumed:

$$V_j^{5.24} \propto \sum V^n \sin^{0.375} \alpha \cos^2 \alpha \tag{7-10}$$

To make this relation true, an appropriate *n* value needed to be found. This was conducted in a curve-fitting fashion where particle impact data from each CFD simulation was used to calculate the summation metric assuming different values of *n*. Figure 7-6 graphically displays the calibration procedure where *S* represents the summation metric.

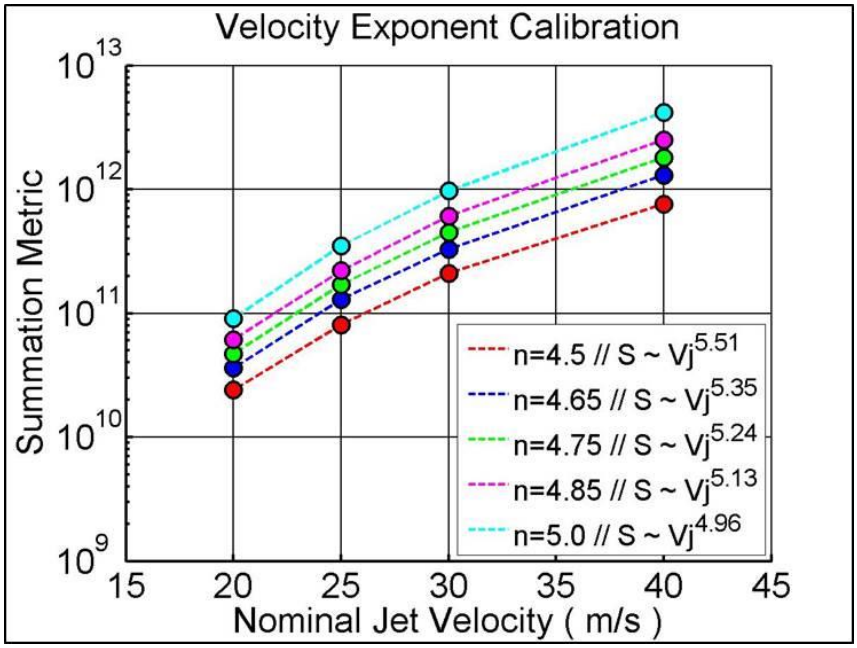

Figure 7-6 Velocity exponent calibration

For each of the jet velocity cases – 20, 25, 30 and 40 m/s – different values of *n* were assumed and the summation metric was calculated. Then for each *n*, a power law relation was found relating the summation metric to the jet velocity. Due to the fact that the summation metric is proportional to the jet velocity, which is in turn proportional to the erosion ratio, an appropriate *n* was found once the resulting jet velocity exponent was equivalent to the 5.24 determined previously. It was found that when *n* = 4.75, the following relation holds true:

$$ER \propto V_j^{5.24} \propto \sum V^{4.75} \sin^{0.375} \alpha \cos^2 \alpha \tag{7-11}$$

While the summation metric considers all particle impacts, the erosion ratio considers a single particle impact. In the simplifying case of a single particle impact the following relation can be made:

$$ER = KD^{4.19}\frac{\sum V^{4.75}\sin^{0.375}\alpha\cos^{2}\alpha}{Total\ \#\ Impacts} \tag{7-12}$$

The last stage of the calibration process was to find the material/system constant *K*. This was done simply by using algebra. Four different *K* values were found using the four different jet velocity test conditions and the average was taken to be the final system constant. *D* was taken to be 8.9μm as this was the average particle size for all the test cases. Given that multiple repeat tests existed for each test case, the average erosion ratio was used. The calibrated *K* value was calculated to be 4866920. The erosion model in its final calibrated form is as follows:

$$ER = 4866920\,D^{4.19}\,V^{4.75}\sin^{0.375}\alpha\cos^{2}\alpha \tag{7-13}$$

This represents the amount of material removed due to a single particle impact of known size, impact velocity and impact angle.

7.5 Model Validation

Given the number of assumptions made in developing and calibrating the erosion model, the validation procedure is imperative to assess accuracy. Due to the fact that the mass loss rate was ultimately used to calibrate the model, the one-dimensional erosion rate was chosen as the validating metric. The calibrated erosion model was hooked into FLUENT using an erosion UDF and simulations were conducted to identify the maximum one-dimensional erosion rate. In FLUENT the erosion rates are presented as erosion fluxes, in units kg/m^2-s. This can easily be converted into a one-dimensional erosion rate, or erosion velocity, by dividing by the substrate density.

The validation procedure involves performing CFD simulations that align with the experiments outlined in the DOE, described in Table 6-1. The simulation parameters are explicitly stated in Table 7-3.

Table 7-3 Parameters used in validation simulations

Jet Velocity [m/s]	Particle Size [μm]	Fluid	Concentration [% mass]	Particle Flow Rate [kg/s]
20	8.95	Water	0.1%	1.5303E-05
25	8.95	Water	0.1%	1.91288E-05
30	8.95	Water	0.1%	2.29545E-05
40	8.95	Water	0.1%	3.0606E-05
40	16.5	Water	0.1%	3.0606E-05
40	5.53	Water	0.1%	3.0606E-05
40	2.59	Water	0.1%	3.0606E-05
40	8.95	Water	0.2%	6.1212E-05
40	8.95	Water	0.05%	1.5303E-05
40	8.95	Water	0.025%	7.6515E-06
40	8.95	10% PG	0.1%	3.07015E-05
40	8.95	25% PG	0.1%	3.08446E-05

In order to hook the calibrated erosion model into FLUENT, an erosion UDF was created. This UDF calculates the mass loss rate at individual cell faces by summing up all the particle impacts that take place. The formula used in the erosion UDF is given as follows:

$$Erosion\ Ratio\ +=\ KD^m V^n \sin^{0.375}\alpha \cos^2\alpha * \frac{M_{dot}}{area} \qquad (7\text{-}14)$$

where M_{dot} refers to the particle stream mass flow rate and *area* is the area of the cell face. These terms are included to convert the unit less erosion ratio to an erosion flux. The '+=' enables multiple particle tracks to be included in the erosion results as this sums up the contributed erosion across all impacting particle tracks.

7.5.1 Effect of Velocity

This section presents the results of the validation simulations and compares them to the experimental results. As described earlier, the main erosion metric in this part of the study is the one-dimensional erosion rate in units of micrometers-per-year. Erosion contour maps resulting from the CFD simulations will also be shown, of which the maximum value will be compared to the maximum erosion rate from the samples in Chapter 6.

Figure 7-7 shows the CFD erosion contours comparing the 20 m/s and 40 m/s test cases. It can be seen that the characteristic 'W' shape is observed with the stagnation region in the center of the jet. This also helps validate the assumption that the height of the stagnation region can be taken as the reference plane due to the lack of particle impacts shown. However, one qualitative feature between the CFD and the experimental erosion contours is that the CFD simulations do not indicate the presence of the discrete locations for the first and second impacts. While this was most heavily observed in the experimental case of the 40 m/s jet, the CFD contours suggest a smoother erosion gradient rather than discrete impact sites. Further research will have to be conducted in this area, but one possible explanation could be due to the manner in which the particle tracking is performed within the near wall region. As has been stated previously, CFD treats each particle as a volume-less point and this fact may pose certain inconsistencies between experimental and simulation-based work. This discrepancy may also be more noticeable at smaller particle sizes especially in turbulent flow fields due to the complexity of modelling parcels of fluid comparably sized to the particles.

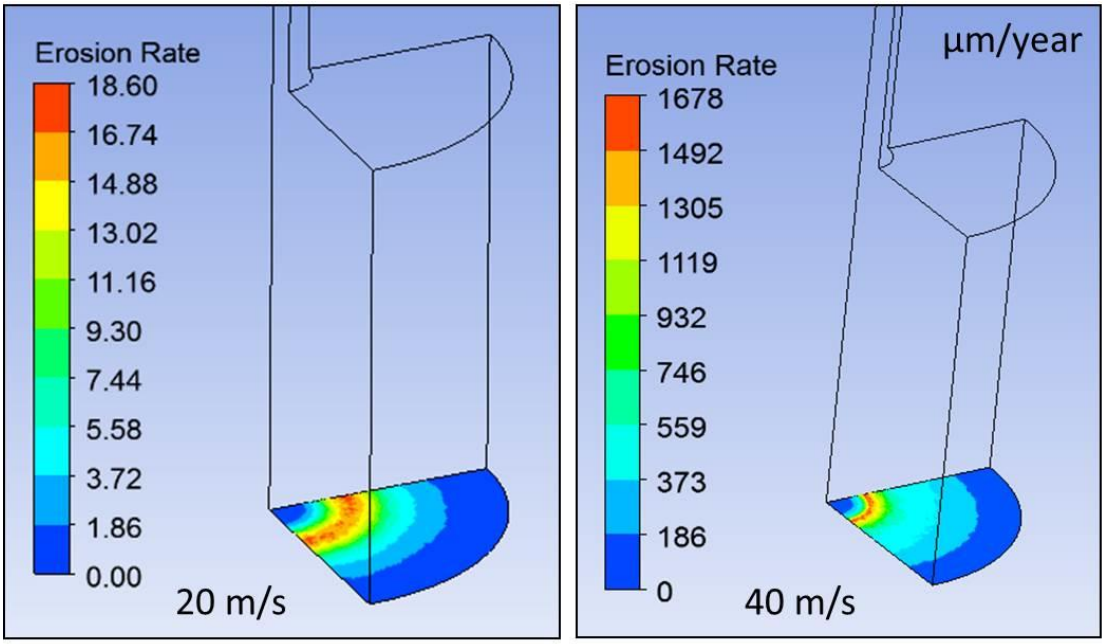

Figure 7-7 CFD erosion maps of velocity test cases, 20 m/s (left) and 40 m/s (right)

It can also be seen that the region of maximum erosion, shown by the red bands, is relatively thicker in the 20 m/s case and thinner in the 40 m/s case. This is likely due to the increased particle-fluid coupling that occurs at higher velocities whereas particles in the slower moving fluid may be more acted upon by turbulent fluctuations in the flow field.

Figure 7-8 shows the comparison between experimental and simulation-based erosion rate predictions for different nominal jet velocities.

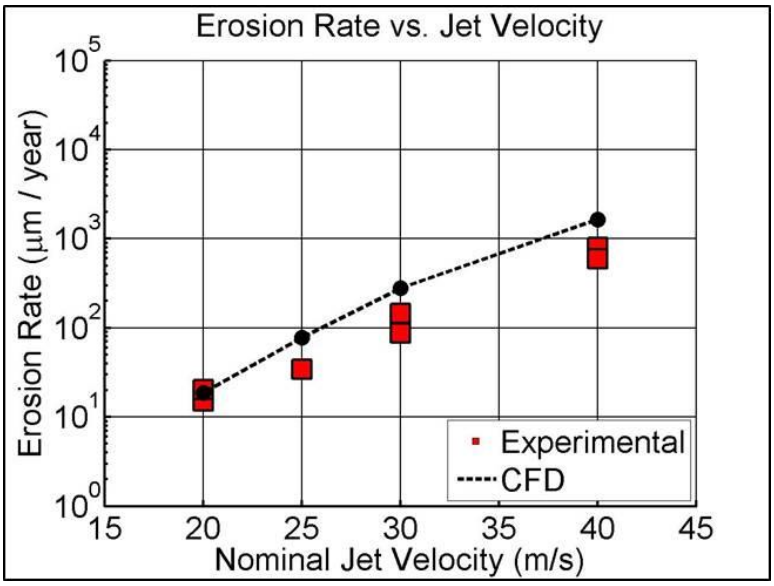

Figure 7-8 Comparison of experimental and simulation-based erosion rate prediction, nominal jet velocity

The graph shows that while the experimental data lines up fairly well with the CFD predictions, the predictions tend to overestimate the erosion rates across most test cases. While this will be discussed in a later section, this fact has also been observed by Chen [132], Mansouri [121], and Zhang [133] and is especially prevent in cases involving fine particles.

7.5.2 Effect of Particle Size

Figure 7-9 shows the CFD erosion contour maps comparing the 2.5μm and 20μm test cases. While the characteristic 'W' shape can be seen in the 2.5μm case, the 20μm test case indicates the presence of primary and secondary discrete impact zones. The experimental results showed that these discrete impact zones were not clearly visible in the 20μm test case but were more evident in the 10μm cases. While it is unclear precisely why this discrepancy exists, it is thought that the particle

tracking scheme, where particles are treated as point masses, may contribute to this observation.

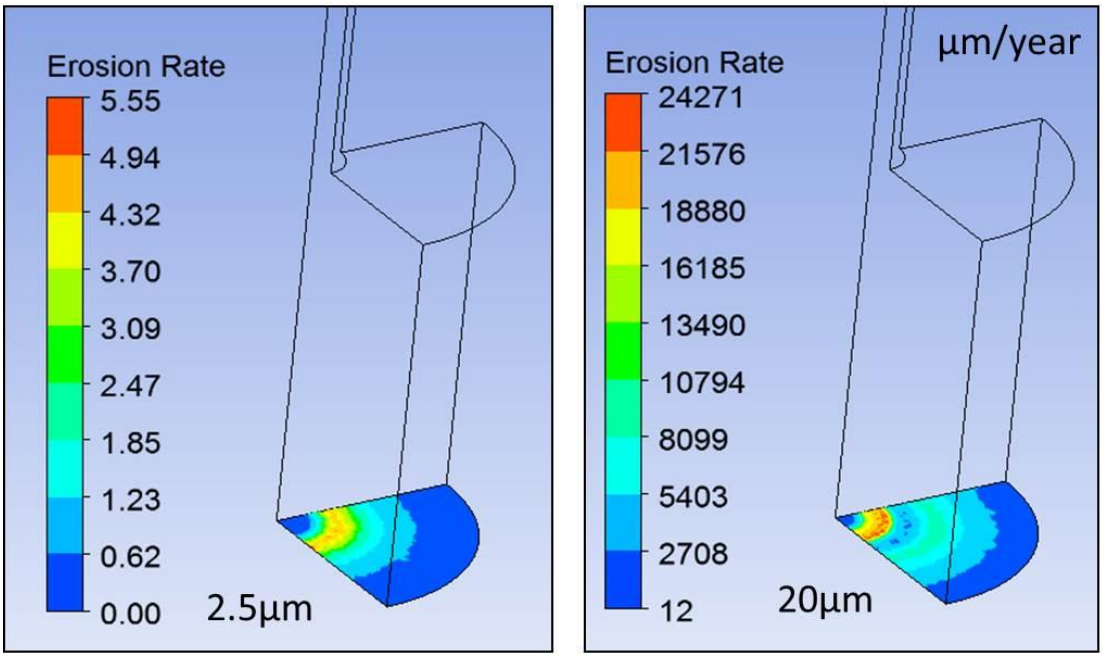

Figure 7-9 CFD erosion maps of particle size test cases, 2.5µm (left) and 20µm (right)

However, it can also be observed that the radial distance between the center of the stagnation region and the location of maximum erosion differs. In the smaller particle case, this location is further away from the center of the jet while it is closer to the stagnation region in the larger particle case. This aligns with the findings from Chapter 4 which showed that larger particles have much greater impact angles on the first impact compared to smaller particles.

Figure 7-10 shows the comparison between the CFD erosion predictions and the erosion experiments for the different average particle size test cases.

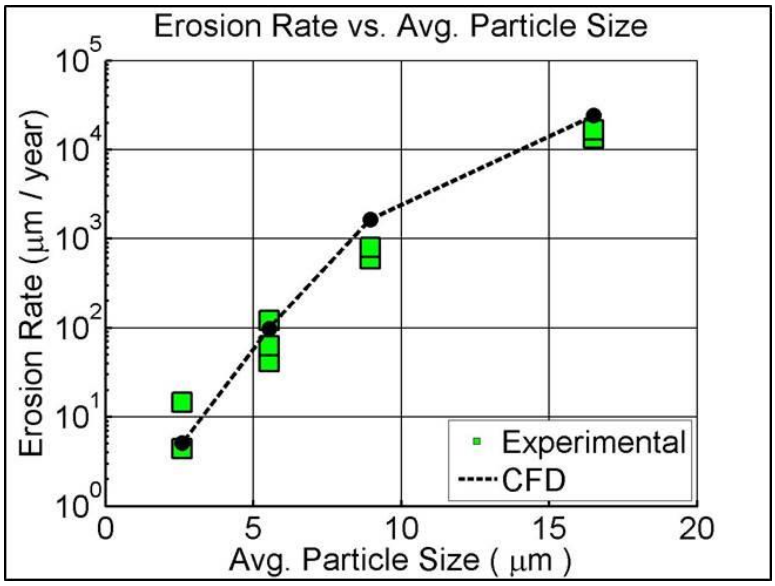

Figure 7-10 Comparison of experimental and simulation-based erosion rate prediction, average particle size

While the smaller particle test cases tend to align better with the erosion predictions, the larger particle test cases tend to result in a slight over-prediction by CFD. Overall, there exists good agreement between experimental and predicted erosion rates.

7.5.3 Effect of Concentration

Figure 7-11 shows the erosion contour maps comparing two concentration test cases. Qualitatively the graphs are identical with respect to the contour shape, but differ in the scale of erosion taking place. This aligns well the experimental erosion tests which showed that concentration does not significantly influence the shape of the erosion contour.

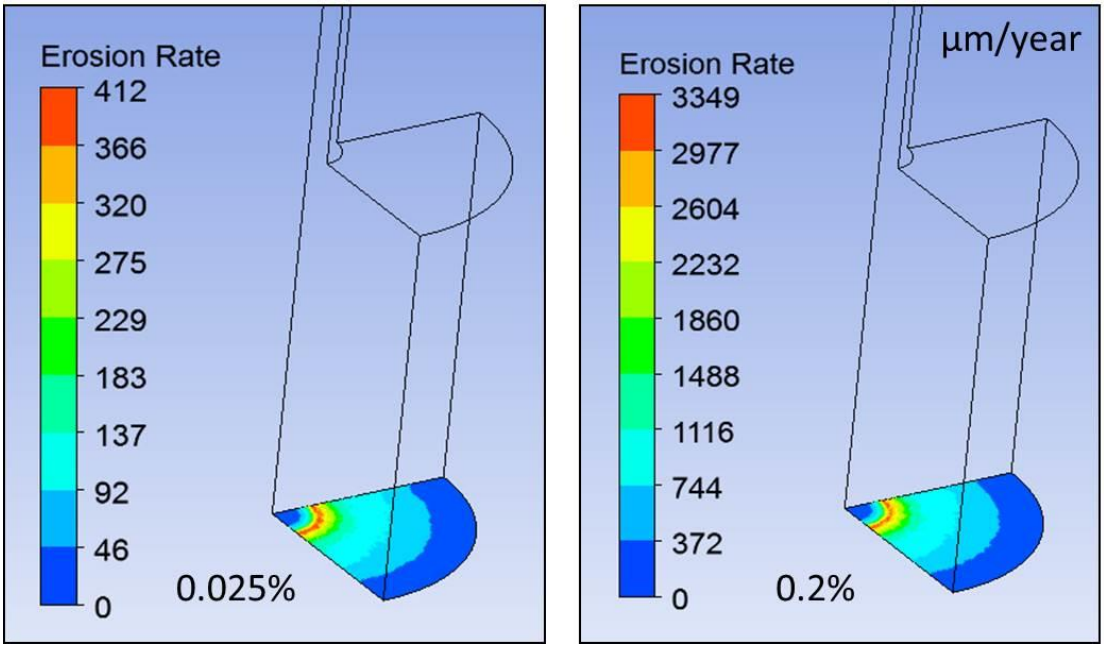

Figure 7-11 CFD erosion maps of concentration test cases, 0.025% (left) and 0.2% (right)

Both erosion maps exhibit similarly sized stagnation regions and the characteristic 'W' shape, however neither graph shows the discrete particle impact locations that were present in the corresponding experiments.

Figure 7-12 compares the erosion rate predictions from the CFD simulations and the experimental work. It should first be noted that the y-axis scale is linear compared to the previously shown graphs which have logarithmic scales. Nonetheless, the CFD predictions over-estimate the erosion in cases.

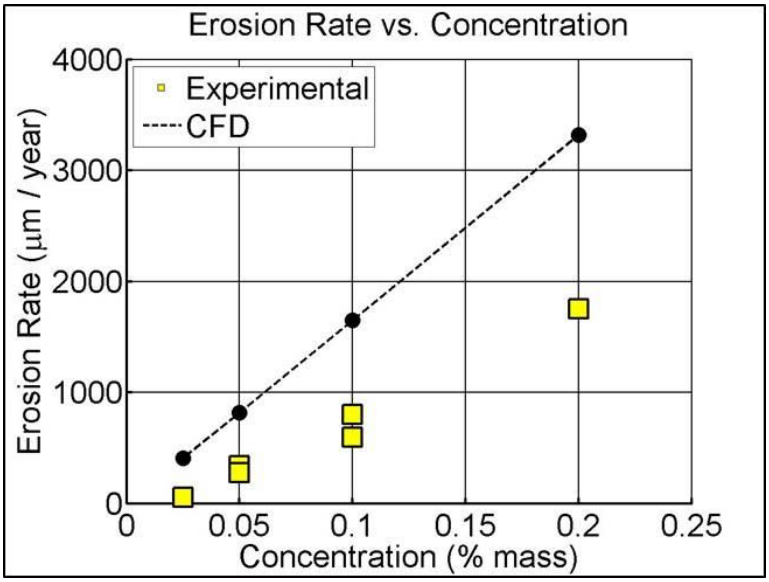

Figure 7-12 Comparison of experimental and simulation-based erosion rate prediction, concentration

According to the CFD erosion rate predictions, the curve appears to have a y-intercept value close to zero. This indicates that a threshold concentration is not predicted, as was suggested in the Chapter 6 analysis. It can also be seen that the difference between the predicted erosion rate and the experimental erosion rate increases as the concentration increases. As was described in Chapter 6, one explanation for this is that the concentration decreases with time as particles are deposited in the test setup due to a fouling phenomenon. It was also realized after performing the concentration experiments that they also indirectly measure the effects of the length of the test; the lower concentration test cases were run longer than the higher concentration test cases. Prior to this study it was assumed that the erosion rate would be constant with time and thus the test durations were not strictly chosen but rather recorded and factored into the erosion rate calculation.

In order to investigate this further, the results from the transient experiments (TR30 and TR40, Table 6-1) were used to approximate a fouling rate, or the rate at which the initial concentration decreases with time. Revisiting Figure 7-5 helps with this analysis, which compares the measured erosion ratios and the constant erosion ratio for the transient experiments. Looking at the 40 m/s transient test, as these operating conditions are identical to those in the concentration experiments, the difference between the measured erosion ratio and the assumed constant erosion ratio can be measured. This is depicted in Figure 7-13, adjusting the scale for better portrayal.

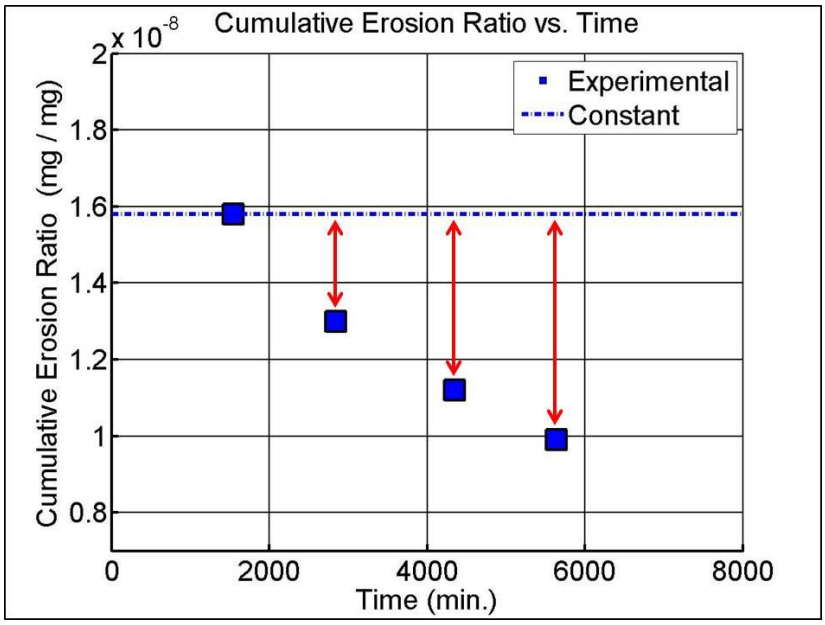

Figure 7-13 Calculating the difference between measured and constant erosion ratio for the 40 m/s transient test case.

For this analysis, it is assumed that negligible fouling occurs between the start of the test and the first data point. By calculating the difference between the assumed constant erosion ratio and the measured erosion ratio, the amount of mass that should

be impacting the substrate, but is not, can be calculated according to the equation below:

$$ER_{constant} - ER_{measured} = \frac{Mass\ Loss}{Mass\ that\ should\ be\ impacting} \quad (7\text{-}15)$$

In order to calculate a fouling rate, it is assumed that the amount of "missing" impacting mass is depositing in the test setup. As such, the change in concentration can be modeled as a function of time for both transient test cases, shown in Figure 7-14.

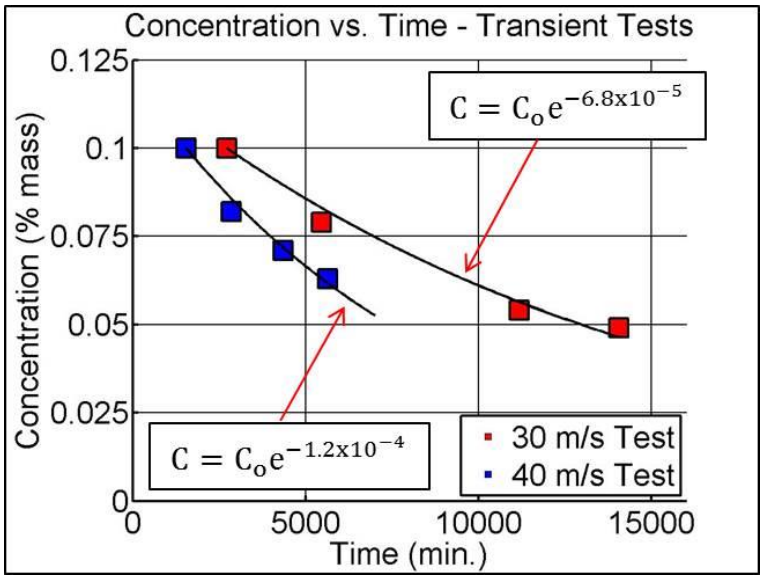

Figure 7-14 Change in concentration as a function of time for the transient test cases

It was found that a decreasing exponential function best fit the data within the range tested. To assess the accuracy of the change in concentration over time, the validation simulations were repeated with updated concentration values. Due to the fact that multiple samples were involved with each of the concentration test cases, the average testing time of the samples in each test case was used to calculate the time-adjusted concentration. The results of the time-adjusted concentration validation simulations are shown in Figure 7-15.

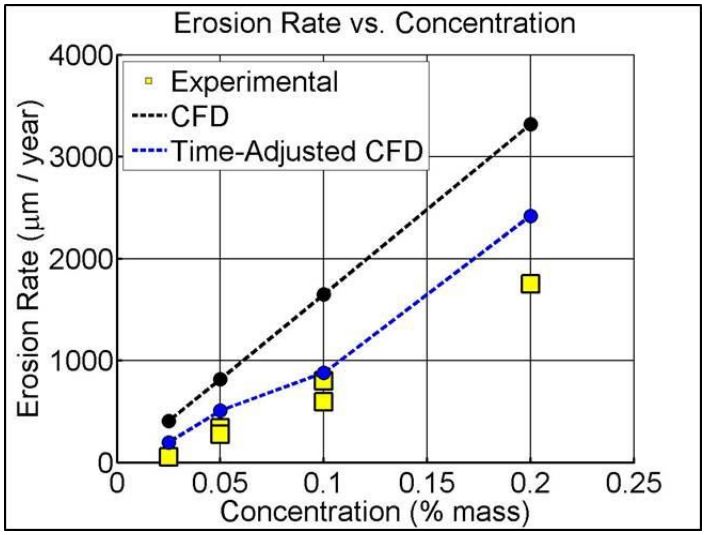

Figure 7-15 Comparison of experimental and CFD predicted erosion rates with time-adjustment

While it can clearly be seen that including the time-adjusted concentration greatly improves the CFD erosion predictions, the predictions slightly over-estimate the experiments. Furthermore, due to the fact that fouling is a complex process involving many factors, such as electrochemical properties, particle size, flow patterns, velocity and viscosity, determining a fouling rate for each experiment performed in this study would fall outside the basic objectives of this study. However, it can be stated that a change in concentration is significantly less influential than a change in particle size or jet velocity. As such, the final erosion model will account for a slight fouling rate inherently in the calibration process.

7.5.4 Effect of Viscosity

Figure 7-16 shows the CFD erosion maps comparing fluids of different viscosities. Both simulations use the same nominal jet velocity (40 m/s), same particulate concentration (0.1%) and same average particle size (10μm particles), however qualitatively and quantitatively there exists differences between the two.

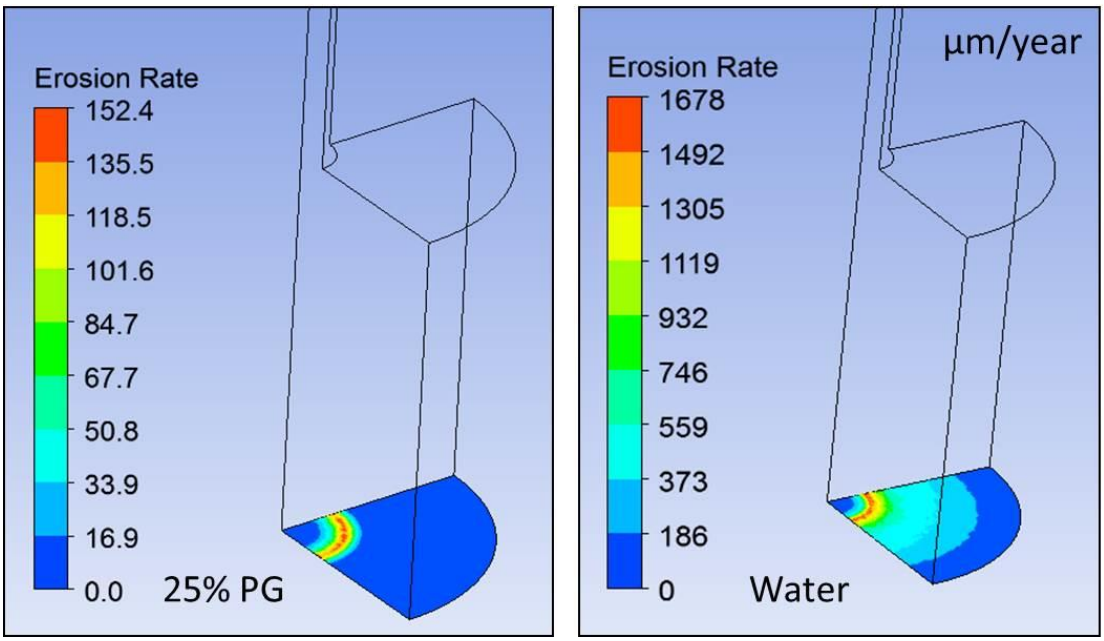

Figure 7-16 CFD erosion maps of viscosity test cases, 25% PG (left) and water (right)

In alignment with the experimental erosion profiles from Chapter 6, the more viscous fluid produces a thinner 'valley', or region, of maximum erosion. One explanation for this is that the higher particle Stokes number achieved in more viscous fluid decreases the ability for turbulent velocity fluctuations to alter particle trajectories. This would result in a lower spread of particle impact locations. In addition it can also be seen that the stagnation region covers a greater area in the more viscous fluid compared to that of water. Due to stronger particle-fluid coupling,

The comparison of the erosion rates between the CFD predictions and the experimental efforts are shown in Figure 7-17.

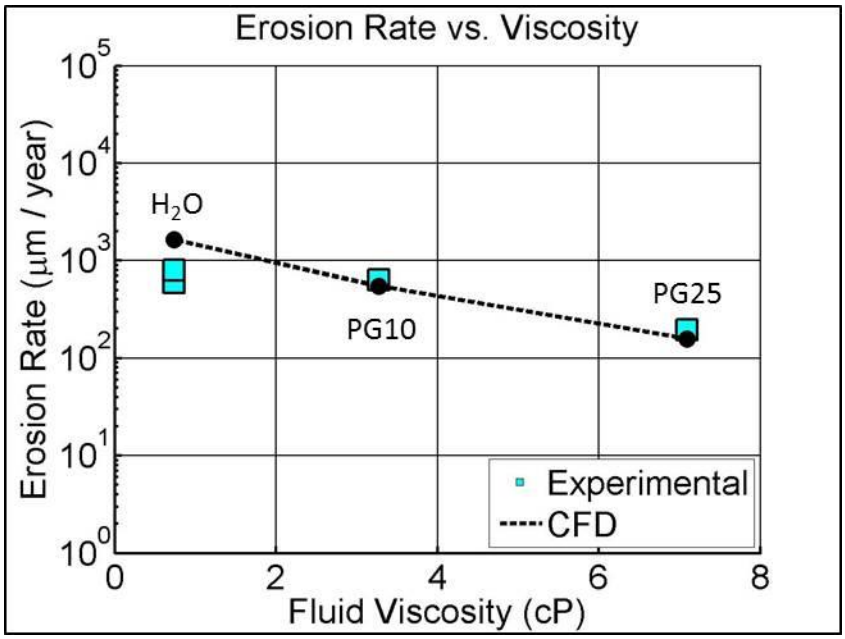

Figure 7-17 Comparison of experimental and simulation-based erosion rate prediction, viscosity

Interestingly, there exists good agreement between CFD prediction and experiment for the more viscous fluids. This suggests that viscosity may affect how particles interact with the surface in ways that may not be comprehensively modeled in FLUENT. This factor will be discussed more thoroughly in the next section.

7.6 Proposed Impact Dampening Coefficient

One characteristic prevalent throughout the validation simulations was that the CFD predictions tend to over predict the experimental erosion rates. As described earlier, this finding is not limited to this study but has been found throughout literature [132] [121] [133] suggesting that limitations exist in the particle tracking methodology employed by the CFD solver. This section proposes an impact dampening coefficient, β, which explains some of the discrepancies found in the original validation efforts.

One of the main limitations surrounding the Lagrangian particle tracking methodology is that it treats each particle as a point-mass. Although a drag-model is included in calculating the particle trajectory through the flow field, the empirical constants inherent in the model are generic and may not be appropriately calibrated for the system.

Looking at Figure 7-8, it can be seen that by shifting the CFD erosion curve down, the two curves would align better. Shifting this observation to a particle impact basis, this discrepancy indicates that that the CFD predicts more damage per particle impact than is occurring in the experiments. Assuming the calibration procedure and the impact velocity and angle capturing process were performed correctly, one explanation is that the particle impact velocity in the experiments is slightly lower than those in the CFD simulations.

The impact dampening coefficient β is defined as the ratio of the actual impact velocity in the experiments to the impact velocity found in simulations.

$$\beta = \frac{Experimental\ Impact\ Velocity}{Calculated\ CFD\ Impact\ Velocity} \tag{7-16}$$

Implementation in the final erosion model would appear as follows:

$$ER = K(\beta V)^n D^m \cos^2 \alpha \sin^{0.375} \alpha \tag{7-17}$$

Due to the fact that particles are treated as point-masses in FLUENT, certain surface-level effects cannot accurately be captured. For example, in the proposed impact dampening scenario adsorbed fluid surrounding the particle may act as a cushion dampening the impact velocity, shown in Figure 7-18. CFD would not be able to accurately predict this due to the size of the meshing elements involved in the

simulations. Furthermore, at these size scales the fundamental equations modeling fluid flow may break down due to other forces taking on more prevalent of a role, such as Van Der Waals attractive forces or electrochemical repulsion forces.

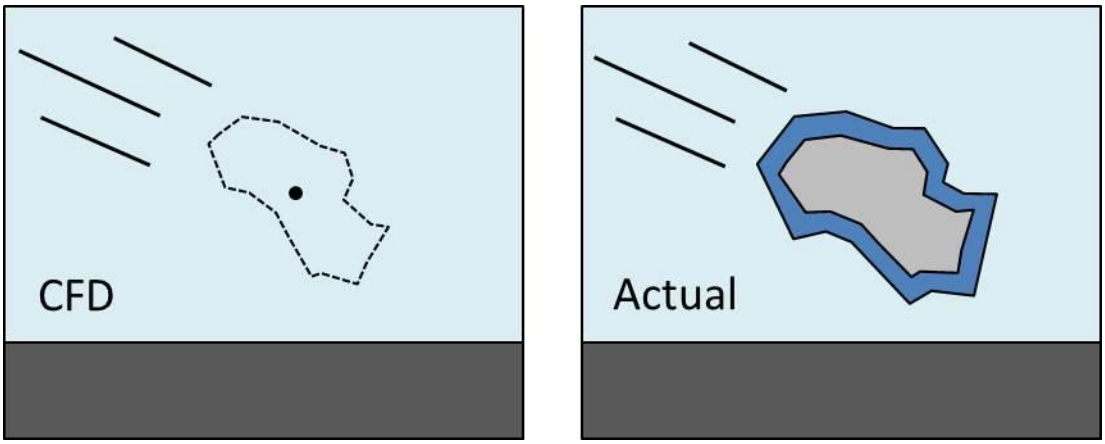

Figure 7-18 Difference between actual and CFD-based particle impact velocities

Like the effects of the squeeze film, the adsorbed fluid may alter the manner in which particles interact with the surface. While the effects of the squeeze film can be captured in CFD through the use of appropriate meshing techniques, the additional dampening caused by potentially adsorbed fluid cannot. Although the dampening coefficient is likely a complex function involving many variables such as free stream velocity, the drag model implement in FLUENT, particle size and shape, fluid viscosity, and particle-fluid adsorption characteristics, an empirical approach was used to determine an appropriate value. While assigning a more physical explanation to this dampening coefficient requires extensive further research, the final effect of reducing the CFD-determined impact velocity is the most important aspect in this work.

Through a trial-and-error process and using engineering judgement, it was found that a value of 0.92 better aligns the CFD predictions with the experimental

results. This suggests that the actual particle impact velocity is approximately 92% of the impact velocity found through CFD. In other words, the adsorbed fluid found in the experimental efforts results in an 8% decrease in impact velocity.

7.6.1 Model re-validation

In order to test this theory, the validation simulations were re-run implementing a β value of 0.92. Figure 7-19 and Figure 7-20 show comparisons of the experimental results, the initial CFD validation simulation results and the re-validated erosion rates for the nominal jet-velocity and particle size effects respectively.

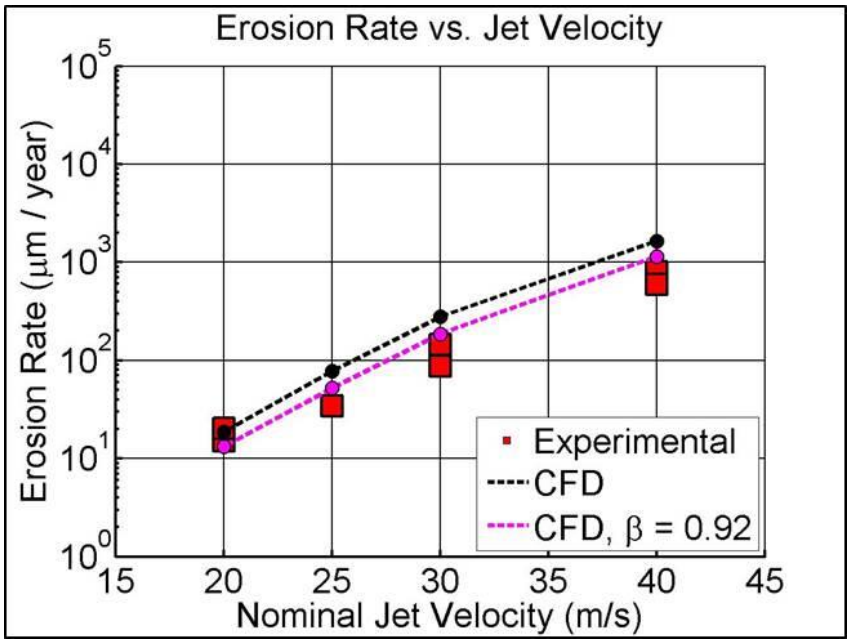

Figure 7-19 Comparison of experimental, validation and influence of β = 0.92, effect of nominal jet velocity

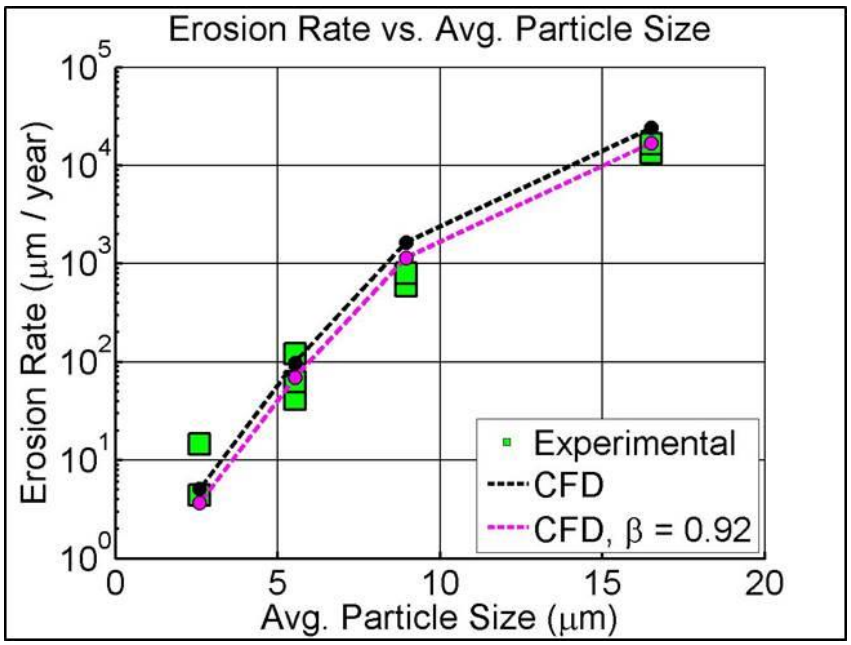

Figure 7-20 Comparison of experimental, validation and influence of β = 0.92, effect of average particle size

As expected, the inclusion of the impact dampening coefficient narrows the gap between the CFD and experimental erosion rates. For the 25, 30 and 40 m/s nominal jet velocity test cases, the re-validated results bring the CFD predictions closer to the experiments while for the 20 m/s test case the new results are still within the range of experimental error. With regards to the average particle size, the original CFD erosion rate predictions were fairly decent; however the inclusion of the dampening coefficient provides a slightly better fit. Although a smaller β-value, such as 0.88 or 0.85, would have provided an even better fit on the jet velocity curve, this would have degraded the fit on the average particle size curve specifically for the 2.5μm average particle size test case.

Figure 7-21 compares the experimental results, the initial CFD validation simulation results, the time-adjusted CFD results and the impact dampening coefficient erosion results as a function of particulate concentration.

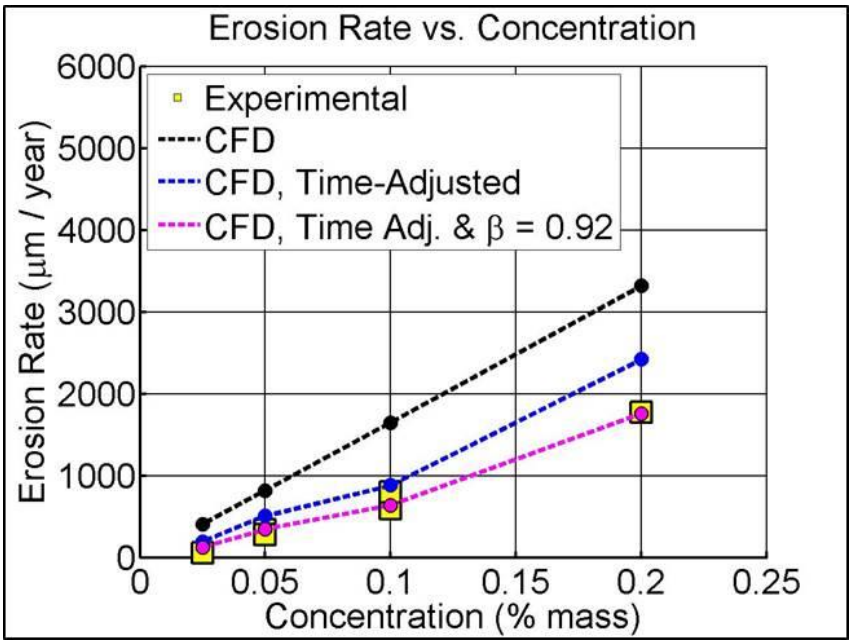

Figure 7-21 Comparison of experimental, validation and influence of β = 0.92, effect of concentration

It can be seen that the inclusion of the impact dampening coefficient significantly improved the fit between experimental and CFD predicted erosion rates. While the original CFD predictions showed were sub-par, the good fit brought about by the inclusion of the time adjusted concentration and the impact dampening coefficient indicate that the original mismatch can be accounted for by these two factors.

Figure 7-22 shows how the impact dampening coefficient influences the erosion rate as a function of fluid viscosity.

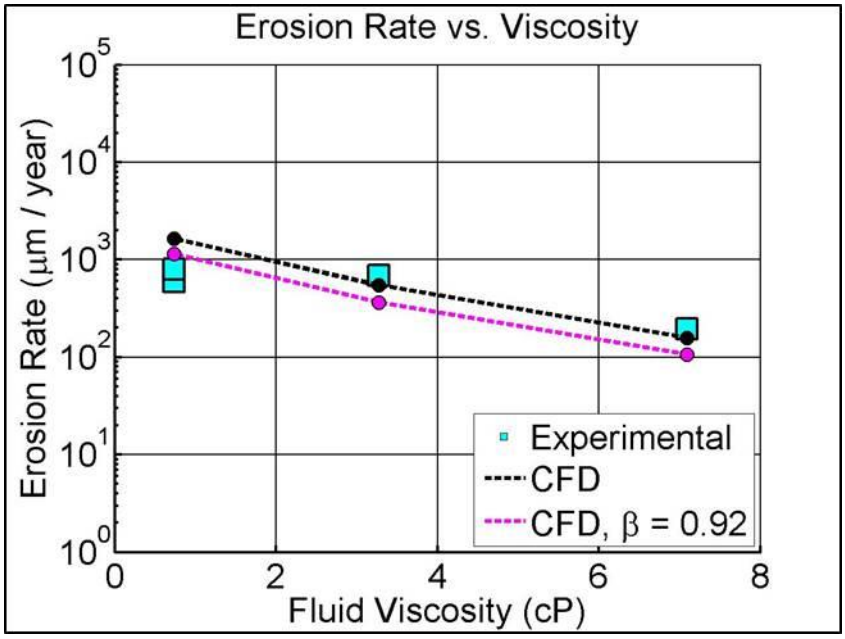

Figure 7-22 Comparison of experimental, validation and influence of β = 0.92, effect of viscosity

While it can be seen that for the lower viscosity fluid (water) the erosion rate prediction falls closer to the experimental results, the prediction for the higher viscosity fluid falls away from the experimental rates. This suggests that the β-value of 0.92 may not be appropriate for all fluids. In fact an impact dampening coefficient of approximately 1.00 would probably fit the data very well suggesting that the actual impact velocity and CFD predicted impact velocity are nearly the same. This goes back to the concept that the impact dampening coefficient is likely a complex function of many variables, of which a single value may not be appropriate for all situations.

In addition, the erosion model was calibrated in water and then applied to these simulations which implement higher viscosity fluids. This indicates that some of the lubrication and dampening effects caused by the higher viscosity fluids may not be accurately be captured in the CFD simulations. As discussed in Chapter 6, the

experiments conducted using the PG fluids indicated that the wet-abrasion mechanism was less pronounced than in water. Due to stronger fluid-particle coupling in the higher viscosity fluids, the particles would be less likely to impose abrasive damage onto the surface given their stronger ties to the fluid streamlines. This signifies the importance of the fluid used in the calibration procedure especially in the case of fine particles where surface effects become more pronounced. It would be interesting to observe how the erosion model would change if it was calibrated in a more viscous fluid.

7.7 Model Discussion

The final form of the erosion model developed in this research is shown below:

$$ER = KD^{4.19}(\beta V)^{4.75} \sin^{0.375}\alpha \cos^{2}\alpha \qquad (7\text{-}18)$$

In this model the velocity exponent is 4.75, the particle size exponent is 4.19 and the impact dampening coefficient β is 0.92. The material/system constant was found to be 4866920. Derived from the Huang model, the present model is based on the assumption that low-angle impacts dominate the overall wear as evident from the sine and cosine angle functions.

As discussed in the literature review section, brittle erosion is typically modeled using derivatives of the quasi-static or dynamic impact theory which both assume that the maximum erosive wear occurs at normal impact angles. This is typically found in literature by the inclusion of a $(V\sin\alpha)^n$ term first proposed by Hockey [61]. While the quasi-static and dynamic impact models were calibrated and validated using normal particle impact experiments, the inherent assumption in those

models is that the indenting or impacting element produces the greatest elastic/plastic damage if it impacts perpendicularly to the surface. This brittle erosion assumption is further justified from the early works of Sheldon and Finnie [39] [40] who found that the greatest elastic crack length is formed upon normal impact from a spherical particle.

In this research however, the shift in wear mechanisms from brittle to ductile suggests that a change in erosion model is also necessary to capture the physics of wear. Using fluid as the particle transfer medium also has direct influence on the type of model chosen as the fluid flow directly affects how the particles interact with the surface. In addition to showing that the squeeze fluid reduces the particle impact velocity, the concept of the impact dampening coefficients suggests that surface level forces may be acting to further dampen the impact.

To the best of the author's knowledge, this is the first time that a nominally ductile erosion model has been applied to predict the erosion of a nominally brittle material behaving in a ductile fashion. This suggests that the models are not necessarily material dependent, but rather mechanism dependent.

The exponents found through the calibration efforts may also have significant physical meaning. However, it becomes challenging to compare the data found in this research to the findings of others due to the great amount of differences in operating and test conditions. For example Routbort and Scattergood [65] [67] [69] studied the erosion of single crystal silicon, however the particle sizes and velocities used in their experiments were significantly higher than those performed in this study. In addition, they used sandblasting techniques. One thing they found in their research was that at

low particle impact angles (less than 20°) the amount of measurable erosion becomes anomalously low and deviates from the impact angle relation found at larger impact angles. This suggests that either a shift in mechanism or threshold effects begin to take place. Nonetheless, the velocity exponents found in their study were between 3.18 and 3.55 for 40μm particles across a velocity range of approximately 33 – 150 m/s. The velocity exponent found in this study was 4.75, slightly larger than the ones found by other authors.

In a study conducted by Wensink and Elwenspoek [100], they found two different velocity exponents corresponding to two different impact energy regimes. The high energy regime, characterized by kinetic impact energies above their determined threshold value of 21 nJ, exhibited an equivalent velocity exponent of 3.06 whereas the velocity exponent of the low impact energy regime was found to be 4.7. It was shown that this shift in regimes occurs when the primary wear mechanism shifts from brittle to ductile.

Validated by the SEM images, the primary wear mechanisms in the present research were shown to be primarily ductile in nature with pseudo-plastic and mixed-mode tendencies. Given the velocity exponent of 4.75, the findings here align quite well with the findings of Wensink. However the primary difference is that the study performed by Wensink utilized impact angles of 90° while the present study mainly contained impact angles less than 10°. One conclusion that can be made is that the velocity exponent is independent of impact angle as suggested by the similar velocity exponent found by this study.

The particle size exponent found in this study, 4.19, is significantly larger than those found in literature. The only comparable study were those conducted by Routbort and Scattergood who found particle size exponents between 0.6 – 1.8. The main difference between the present study and previous studies is the influence of water. The wet abrasion mechanism observed in this study acts by dragging particles across the surface inducing larger scratches and deep gouges. Due to the fact that air is the primary medium bringing particles to the surface, the wet-abrasion mechanism does not take place but rather a simple bouncing action occurs. It is thought the significantly increased particle size exponent originates from the shift in wear mechanism, but also from the scratching and gouging action. Given otherwise similar impact conditions, particles in water would remove more surface material due the added momentum induced by the fluid flow. This phenomenon can best be depicted in Figure 7-23.

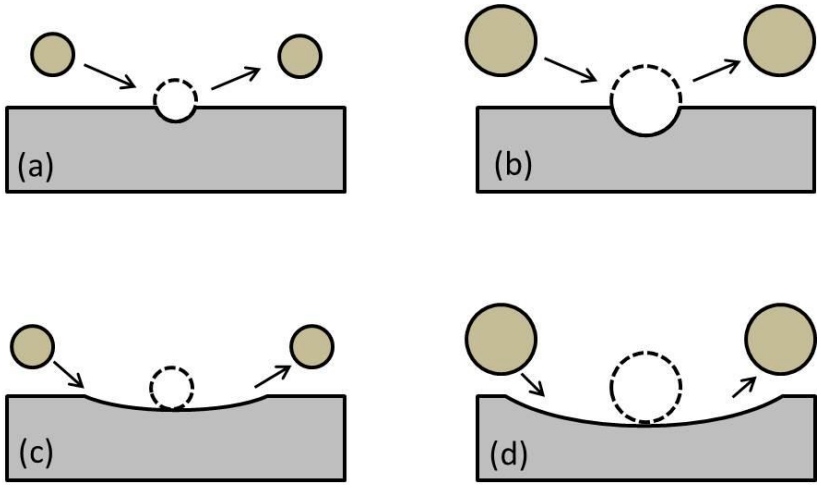

Figure 7-23 Effect of transport medium on particle size exponent. Small particles in air (a), large particles in air (b), small particles in fluid (c), large particles in fluid (d)

Figure 7-23a and Figure 7-23b show that a particle traversing through air rebounds from the surface leaving a localized region of material removal. The size of the particle most influences the affected area while the impact kinetic energy most influences the impact depth. However, Figure 7-23c and Figure 7-23d show how the particle interacts with the surface under fluid flow conditions. Since the particle's motion is coupled to the fluid flow and the fluid directly above the surface flows tangentially, there is a significant portion of the particle's momentum running parallel to the surface. This causes the particle to effectively carve out a larger volume of material under slurry flow conditions when compared to air conditions, even at low impact angles. As such, this may justify the significantly larger particle size exponent found in fluid flow conditions when compared to those found in sandblasting conditions

7.8 Notion of Threshold Conditions

An important aspect of erosion modeling efforts lies in the idea of identifying critical threshold conditions, under which erosion does not occur. This concept was briefly introduced in the literature review section by assuming the main mechanism of wear was the induction of crack systems followed by coalescence and ultimately mass loss. As such, the threshold conditions for those systems are identified as the impact conditions necessary to induce cracks. However, the findings of this study indicate that the primary mechanisms of wear shift away from brittle cracking and fracture to more pseudo-plastic scribing, gouging and ploughing. This also suggests a change in the conditions through which threshold conditions are defined.

Given this mechanism shift it can be assumed that threshold conditions may not exist in a physical sense, as scratching can still occur at low forces, but rather conditions can be identified under which erosion can be considered negligible. For example and specifically for the purposes of microchannel cooler reliability, predicted erosion rates in the single-digit nanometer-per-year range can be assumed negligible for all intents and purposes. To investigate the operating conditions producing both negligible and considerable erosion damage, a series of CFD erosion simulations were performed across a variety of jet-velocities and particle sizes. Implementing the model developed in this study and assuming an impact dampening coefficient of 0.92, these simulations were performed with water as the working fluid and a particulate concentration of 0.01% by mass. This concentration equates to 100 ppm of abrasive particles. The results of these simulations are shown in Figure 7-24.

The graph shows that as particle size decreases, the erosion rates fall to anomalously low levels. This can also be attributed to the fact that smaller particles, especially at lower jet velocities, have a lower propensity to reach the surface and are rather maintained in the bulk flow. As expected, decreasing the jet velocity also reduces the erosion rate. In order to adjust the curves for different concentrations, they can be shifted linearly as it was found that that doubling the concentration essentially doubles the erosion rates.

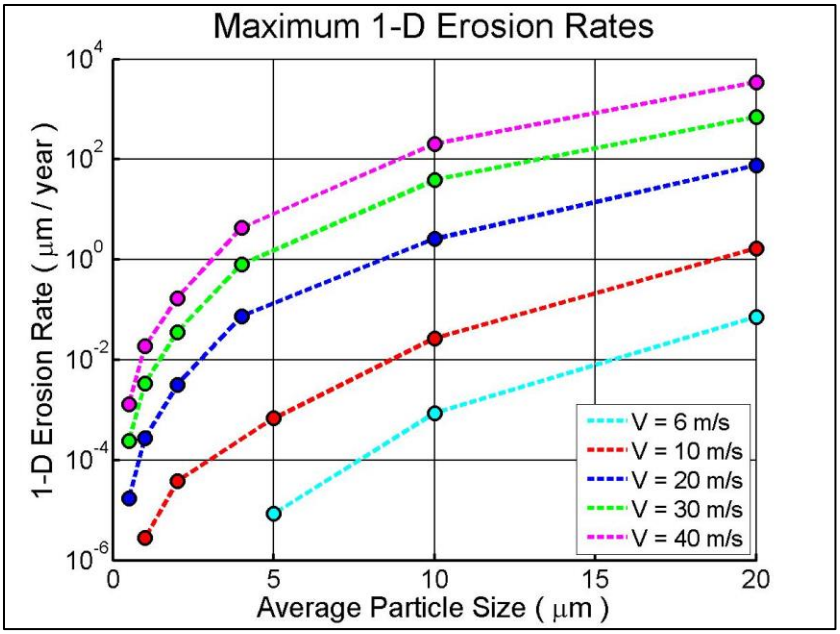

Figure 7-24 Maximum 1-D erosion rates for different jet velocities and particle sizes

With respect to identifying threshold conditions, this graph can provide valuable insight into the operating regions yielding negligible erosion rates. In microchannel cooling applications, specifically with respect to micro-impinging jets, the particle size – velocity conditions yielding erosion rates of less than 1 μm per year should be acceptable. Some examples of acceptable conditions could be any particle size at 6 m/s, particle sizes less than 18μm at 10 m/s, particle sizes less than 8μm at 20 m/s and particle sizes less than 3μm at 40 m/s. Another aspect that should be pointed out is that this graph represents worst case scenarios, i.e. a perpendicular impinging jet. These values would most likely be less in the cases of parallel channel flow or manifolded microchannel coolers. Nevertheless, this graph can be used as a sound framework for identifying reliable operating conditions in different types of geometries.

7.9 Limitations

This chapter describes the development of a particle erosion model that can be used to predict maximum one-dimensional erosion rates in microfluidic geometries. While this model has been validated and shows good agreement with experimental results, there exist some limitations when applying this model. First, the model has been calibrated specifically with the alumina particle and silicon substrate system. If this model were to be applied to another substrate material, the accuracy would be unknown without first conducting a couple validation experiments with the new material.

Secondly, the major wear mechanism taking place is assumed to be the deep cutting and gouging shown in Chapter 6. As described in the literature review chapter increasing the particle size or impact velocity could shift the wear mechanisms away from those plastic in nature to those behaving more in a brittle fashion. Since this model has been calibrated and validated within specific particle size and velocity ranges, it would be most accurate to apply this model in situations where the average particle size is less than 20μm and the average impact velocity is less than approximately 30 m/s (the CFD simulations indicated that 20μm particles in a 40 m/s jet impact the wall at approximately 30 m/s – see Chapter 4). A caveat to the above notion could occur in the case of smaller particles at larger velocities. While this would shift the conditions outside of the calibration/validation realm, it can be predicted that the fundamental wear mechanism would not change.

Another limitation is that this model was calibrated in water and, as shown by the validation simulations, may need to be re-calibrated if the working fluid is a more

viscous fluid such as 100% PG. This may also be necessary in less viscous fluids such as refrigerants or even two-phase flow. However, the validation simulations still showed good agreement between experimental and CFD predictions suggesting that this model could still serve as a sound prediction tool in a variety of working fluids.

As indicated by the concentration experiments, knowing the proper particulate concentration of the fluid is critical for ensuring accurate erosion predictions. However, this sometimes poses an issue as the concentration may change with time. Therefore when using this model to make an erosion prediction, it would be optimal to assume a maximum allowable concentration which would yield a worst case scenario prediction. Typically microfluidic or hydraulic systems have acceptable particulate contamination levels. When these levels are reached, an indicator would suggest that the fluid needs to be changed. While this approach would yield a worst case scenario erosion prediction, it can still be viewed as relatively accurate due to the fact that concentration has a linear relationship with erosion while particle size and impact velocity exhibit power law relations.

Furthermore, in developing this erosion model it was assumed that any surface changes caused by erosion would not influence future erosion. Essentially, the surface is always assumed to be flat while in reality the surface changes as erosion progresses. Due to the fact that the erosion depths achieved in these experiments were at most a few tens of micrometers and the particle sizes were of a similar order of magnitude, this effect was assumed negligible. However, future experiments may need to be conducted if the maximum expected erosion depth is on the order of a few hundred micrometers.

Lastly, an assumption inherent in the Huang model is that the wear is dominated by low angle particle impacts. In the section introducing this erosion model, two separate wear mechanisms are described: deformation wear and cutting wear. To simplify the model, deformation wear was assumed to be negligible compared to cutting wear due to the low angle impacts found via CFD simulations and the cutting mechanisms found in the SEM surface images. This assumption may not hold true in all operating conditions and scenarios, but for the velocity and particle size ranges of this study it was assumed to be true.

8 CONCLUSION AND SUMMARY

This chapter serves to summarize the contents of this dissertation, discuss the technical and academic contributions made throughout this research and outline a few pertinent areas for related future work.

Chapter 1 introduces the concept of embedded cooling by describing the paradigm shift away from conventional remote cooling techniques. Conventional power electronics cooling relies on conducting heat away from the source into an air or liquid cooled heat sink. While this established technique provides thermal management solutions for a variety of different applications, bringing cooling power virtually to the source enables significantly higher power levels to be reached while maintaining similar junction temperatures. Through various implementations such as manifolded microchannel coolers, arrays of impinging micro-jets and pin fin arrays, liquid cooling can be brought to within a few hundred micrometers of the source. However, as this cooling technique is relatively experimental and new there exist a number of potential reliability threats that have not thoroughly been explored, namely particle erosion, corrosion and clogging. This dissertation serves to investigate the particle erosion phenomenon.

Chapter 2 provides a detailed literature review focusing mainly on the subject of brittle erosion. Two main brittle erosion theories are discussed; the quasi-static model and the dynamic impact theory, both of which show good alignment with many other erosion studies. Characteristics of slurry erosion are also discussed which differs from typical particle erosion studies due to the effect that the fluid has on particle-surface interactions. One attribute of slurry erosion is the development of a

"squeeze-film" which is essentially a viscous sublayer forming directly above the surface. This slow moving fluid may act to trap smaller particles resulting in a wet abrasion mechanism as the particles are swept away by the tangentially moving flow. Additionally, the trapped particle bed may protect the surface from incoming particles. Studies involving abrasive slurry jet micromachining were discussed as they provide insight into the type of wear patterns thought to occur in the case of jet-impingement erosion. The characteristic 'W' shape arises mainly due to the stagnation region directly below the impinging jet where minimal particle impacts occur. Lastly, the concept of the brittle-to-ductile transition is discussed where nominally brittle materials behave in ductile fashions under specific wear conditions. When the kinetic energy of an impacting particle is low enough, either by a decreased particle size or low impact velocity, the elastic/plastic wear mechanism described by the quasi-static and dynamic impact theories are replaced by ductile wear mechanisms such as scratching and deep gouging. With regards to erosion modeling, this tends to increase the particle size and velocity exponents compared to those derived from strictly brittle erosion.

Chapter 3 briefly outlines the problem statement and summarizes the core objectives of this research. Given the need for high fidelity erosion predictions in embedded and microchannel cooling applications, a new particle erosion model needs to be developed. The literature review section indicated that existing erosion models would likely not suffice for the given applications due to the shift in wear mechanisms away from brittle cracking and fracture towards those ductile in nature. Ultimately, the main goal of this research is to develop a new particle erosion model

calibrated and validated within the typical operating conditions found in microchannel and embedded cooling systems. The steps taken to accomplish this can be broken down into six main objectives:

1) Develop a jet-impingement CFD model in ANSYS FLUENT to obtain localized particle impact characteristics.
2) Design and construct a jet-impingement slurry erosion test apparatus to perform slurry erosion experiments.
3) Formulate and execute a series of tests (DOE) to investigate the effects of jet velocity, particle size, concentration, fluid viscosity and time.
4) Gain insight into the wear mechanisms of single crystal silicon under microchannel cooler operating conditions. (Particle Sizes: < 20μm, Velocities: < 40 m/s)
5) Combine localized particle impact characteristics from CFD simulations with experimental erosion data to formulate a particle-based erosion model.
6) Perform validation simulations to identify how well the model predicts maximum 1-dimension erosion rates (μm/year).

Chapter 4 discusses the CFD simulations performed using ANSYS FLUENT in order to identify localized particle impact characteristics, specifically impact angle and impact velocity. Adjusting various operating conditions such as nominal jet velocity, average particle size and fluid viscosity resulted in significant changes in particle impact angle, impact velocity and percentage of entrained particles that actually impact the surface. The Stokes number can be used to justify the results from these simulations which describes how closely coupled the motion of a particle is to

the surrounding fluid. In addition, a series of user-defined functions were written and hooked into FLUENT in order to capture the necessary impact data.

Chapter 5 covers the design and construction of the slurry erosion jet-impingement test apparatus. The test setup is capable of handling nominal jet velocities of up to 60 m/s (through a 1.98 mm nozzle), a large spread of particle sizes due to abrasive slurry pump and is chemically compatible with a variety of working fluids including ethylene and propylene glycols solutions. A propeller-based stirring mechanism, powered by a motor, ensures that particle settling does not occur within the reservoir. Additionally, this chapter discusses topics such as cleaning the test setup in between uses, creating the testing slurry and the process used to manufacture the silicon samples for testing.

Chapter 6 outlines the experimental erosion testing performed in this study. A design of experiments outlining the 14 different test cases is presented enabling the most critical factors of erosion to be tested: nominal jet velocity, particle size, particulate concentration, fluid viscosity and time. A stylus profilometer was used to capture the erosion contour created by each of the different samples, and from this two principle erosion metrics could be evaluated: maximum one-dimensional erosion rate in units of micrometers per year and a mass loss rate in units of milligrams per year. The one-dimension erosion rate could be directly extracted from the erosion contour by factoring in the testing time. However, in order to convert the 2-D erosion contours to 3-D volumes (then convert to mass by dividing by density) an algorithm was developed in MATLAB. Based on a simple volume-of-revolutions type approach and assuming the contours were axisymmetric about the stagnation region, this

calculation was performed. To sum up the erosion results the following statements can be made where MLR and ER stand for the Mass Loss Rate and one-dimensional Erosion Rate respectively, and V and D stand for the nominal jet velocity and average particle size respectively:

$MLR \propto V^{6.29}$	$ER \propto V^{5.35}$
$MLR \propto D^{4.36}$	$ER \propto D^{4.11}$

Lastly, high-resolution SEM images were taken of the eroded surface in order to identify the types of wear mechanism taking place. Based on these images it was verified that ductile wear mechanisms dominated the erosion in the form of deep cutting, gouging, flaking.

Chapter 7 discusses the development and calibration of the particle-based erosion model. First, the total mass of impacting particles for each test case was determined using the CFD simulations in order to convert the mass loss rates from Chapter 5 into the conventional erosion ratios. The Huang cutting erosion model was also introduced which serves as the basis of the newly developed erosion model. Next the process through which the calibration efforts took place was described and validation simulations were performed to address how accurate the model was at predicting the maximum one-dimensional erosion rates. While good agreement was shown between experimental and simulation-based erosion predictions, the simulations tended to over-predict the experiments. As such an impact dampening coefficient was proposed, β, which is defined as the ratio of the actual impact velocity to the velocity determined through CFD predictions. It was found that a value of approximately 0.92 best fit the data, however future studies will have to be conducted

to further examine the physical nature of the dampening coefficient. The final erosion model produced in this study is shown below

$$ER = kD^m(\beta V)^n \sin^{0.375}\alpha \cos^2\alpha \quad (7\text{-}18)$$

ER	Erosion ratio [mg/mg]
k = 4866920	System constant
D	Average particle diameter [m]
m = 4.19	Particle size exponent
β ≈ 0.92	Impact dampening coefficient
V	Particle impact velocity [m/s]
n = 4.75	Particle impact velocity exponent
α	Impact angle

This model has the capability to be hooked into commercial CFD codes through user-defined functions in order to replace generic or built in erosion models. In addition to accurately performing erosion predictions in jet-impingement scenarios, this model can also be used to perform erosion predictions in a variety of microchannel-based environments, so long as the limitations discussed in Chapter 7 are considered.

8.1 Academic and Technical Contributions

From the results and methodologies proposed in this study, a number of academic and technical contributions have been made. First and foremost and to the best of the author's knowledge, this was the first slurry erosion study conducted on single crystal silicon. While a number of erosion studies on silicon have been performed using sandblasting techniques, the use of water as a transport medium has

contributed to the low angle impacts resulting in the ductile wear mechanisms not observed in previous studies.

Furthermore, erosion studies of brittle materials are typically conducted with impact velocities and particle sizes well outside the range of those tested in this research. This is often times necessary in order to produce measurable wear in a reasonable period of time. However, in this study the use of a slurry environment enabled longer testing times and therefore significantly lower velocities and particle sizes could be used. To the best of the author's knowledge this is the first slurry erosion study to be performed using particle sizes and velocities within the ranges present in microchannel coolers. Due to this factor, the erosion model developed here is optimally suited to make erosion predictions in these applications compared to other previously published models.

In addition, SEM images of the eroded surfaces revealed that the primary wear mechanisms were ductile in nature as was suggested by literature. These wear mechanisms were mainly in the form of deep and shallow scratches caused by sharp particles and shallow ploughing caused by blunter particles. Other less prevalent mechanisms were also observed such as a mixed-mode erosion mechanism where material was displaced in a ductile fashion to be subsequently followed by brittle flaking. While this wet-abrasion mechanism has been previously observed in slurry erosion studies of metals, to the best of the authors knowledge it has not been observed and quantified in brittle materials under jet-impingement conditions.

In conjunction with this finding, a ductile erosion model was used to capture the erosive wear of a nominally brittle material. As was shown in the literature review

section, typical brittle erosion models are derived from either the quasi-static or dynamic impact theory and assume that only the normal velocity component influences erosion. The model developed in this study rather assumes that the majority of wear comes from shallow angle impacts and thus considers ductile wear mechanisms. To the best of the author's knowledge this was the first time that a ductile erosion model has been shown to capture the erosive wear of a nominally brittle material.

From a modeling perspective, three primary contributions were made in this work. First, the particle size and velocity ranges of the Huang cutting erosion model were extended in order to consider the ranges within this study. This required the particle size and velocity exponents to be recalibrated through experimental efforts. Additionally, the application range of the Huang model was extended to include nominally brittle materials assuming that the fundamental wear mechanisms do not change. While the material/system constant and exponents were found for the silicon substrate, there would likely have to be a recalibration effort if different substrate materials were considered. Lastly, this was the first time that multiple particle impacts were factored into calibrating an erosion model. Sandblasting techniques essentially consider one impact per particle due to the fact that additional impact parameters cannot be found easily. Furthermore, a few studies have considered impact parameters found through CFD efforts in the model calibration process; however these studies only consider one impact per particle track. To the best of the authors' knowledge this is the first study to consider multiple impacts per particle track in the model calibration process. It should be mentioned that many studies perform CFD-

based erosion predictions that do consider multiple impacts per particle track, however the contribution referred to here is specifically with respect to the calibration procedure.

A new impact dampening coefficient was also proposed which implies that the actual impact velocity of a particle is less than the CFD predicted impact velocity. For this set of operating conditions, a value of 0.92 was found to fit the data well which suggests that the actual impact velocity is 92% of the CFD predicted impact velocity. From a physical perspective, the impact dampening coefficient may be an artifact of the method in which particle tracking is performed in CFD – that particles are treated as point-masses rather than having a definitive volume and surface area. This observation, where CFD-based erosion predictions tend to over predict experimental wear is a phenomenon prevalent throughout literature and is especially noticeable in applications involving micrometer-scale particles. While further research needs to be conducted in this area, it is thought that the particle tracking methodology loses accuracy at these small scales where other factors not accounted for in the CFD code may begin to take place.

From an engineering perspective, the methodology developed here can be extended to a variety of other materials that are likely to be found in microchannel coolers such as sapphire, titanium, tungsten and glass. Assuming the erosion mechanisms remain ductile and the impact angles are relatively low, a few additional experiments could be performed to recalibrate the constants from the final model to fit these new materials. Lastly, the final product of this research is a particle-based erosion model which can be hooked into commercial CFD codes and used to perform

erosion predictions in a variety of different microchannel and embedded cooling geometries. This enables more accurate erosion predictions to be made enabling system designers to determine the expected lifetime of coolers and necessary filtering requirements for different operating conditions.

8.2 Future Work

Based on the findings and results of this research, a number of areas involving potential future work can be identified. These potential future research areas will help enrich the findings of this study but will also provide relevant information in the fields of particle erosion modeling and microchannel/embedded cooler reliability.

First, the tests conducted in this study were performed using a jet-impingement style test setup mimicking one possible type of embedded cooling scheme. Although the particle erosion model developed here is considered geometry independent, it has not yet been validated for other types of embedded cooling styles such as pin fin arrays or manifolded microchannel coolers. One type of study could perform similar erosion experiments on etched silicon surfaces containing either pin fins or microchannels. It would be ideal to perform these experiments using a variety of different jet-impingement angles, which the test setup developed in this work is currently capable of doing. Typically in pin-fin array coolers, fluid is flowing parallel to the surface while in manifolded microchannel coolers fluid is flowing perpendicular to the surface as it enters the channels followed by an abrupt change in direction as it leaves. These different tests would enable a more real-world view of how the erosion phenomena affects different types of geometries in conjunction with the erosion predictions made using CFD.

Second, the results of the transient and concentration test cases indicated that a fouling mechanism took place within the setup. In addition to slightly skewing the calibration efforts, it can also be suggested that this phenomenon may be very prevalent in microchannel cooling systems. From a reliability perspective, this adds another layer of complexity with regards to modeling reliability and determining safe operating regimes for the coolers. The results of this study suggest that there exist certain operating conditions where particle erosion can be considered negligible; however these same regimes and conditions may lend themselves to a higher propensity for clogging and fouling. For example, erosion tends to be greatest at higher velocities and particle sizes, yet these conditions tend to reduce particle agglomeration and fouling. Due to the fact that particle fouling is the result of balancing various electrochemical attractive and repulsive forces, smaller particles have a greater tendency to become attracted to surfaces. This is magnified at lower velocities where particles are less tied to the fluid streamlines because they have less external momentum acting on them. As such it would be imperative to understand the physics behind the fouling phenomenon more in depth as it pertains to microchannel coolers. Once a more physical understanding of this phenomenon is known, it can then be assessed which degradation mechanism dominates under certain conditions.

Third, it would be interesting to perform the same type of experimental test cases on nominally ductile and corrosion resistant metals such as nickel-based alloys or titanium. While it was found that silicon erodes in a relatively ductile fashion under the conditions in this study, it would be useful to verify that the particle erosion model can be applied to various ductile materials rather than just brittle materials

behaving in a ductile manner. Corrosion resistance would be an important characteristic such that the dominant wear mechanism could be assumed physical in nature rather than chemical or a combination of the two.

Fourth, it should be pointed out that the final erosion model was calibrated using water with additional experiments performed in higher viscosity fluids. The idea behind this was to identify local particle impact characteristics in order to formulate the model. Once calibrated, the model could then be applied to predict wear rates in a variety of different geometries using a range of working fluids. It can be stated that particles in higher viscosity fluids typically exhibit lower impact velocities and the subsequent effects on erosion should inherently be accounted for in the calibration procedure. In order to validate this, it would be advantageous to perform the same calibration experiments using a higher viscosity fluid such as PG10 or PG25. After recalibrating the model, the particle size and velocity exponents could be compared in order to identify any effects that the working fluid has on the calibration procedure.

Finally, the impact dampening coefficient was found empirically using engineering judgement. Although a value of approximately 0.92 was shown to fit the data, further studies should focus on determining and quantifying the parameters that most affect this factor. It can be suggested that the variables likely influencing the impact dampening coefficient are free stream velocity, fluid viscosity, distance from surface, particle size, particle shape and fluid-particle adsorption properties. By examining this more in detail, further insight can be provided as to why CFD erosion predictions often over-estimate their experimental counterparts.

9 Appendices

Appendix A – Raw Erosion Profile Contours

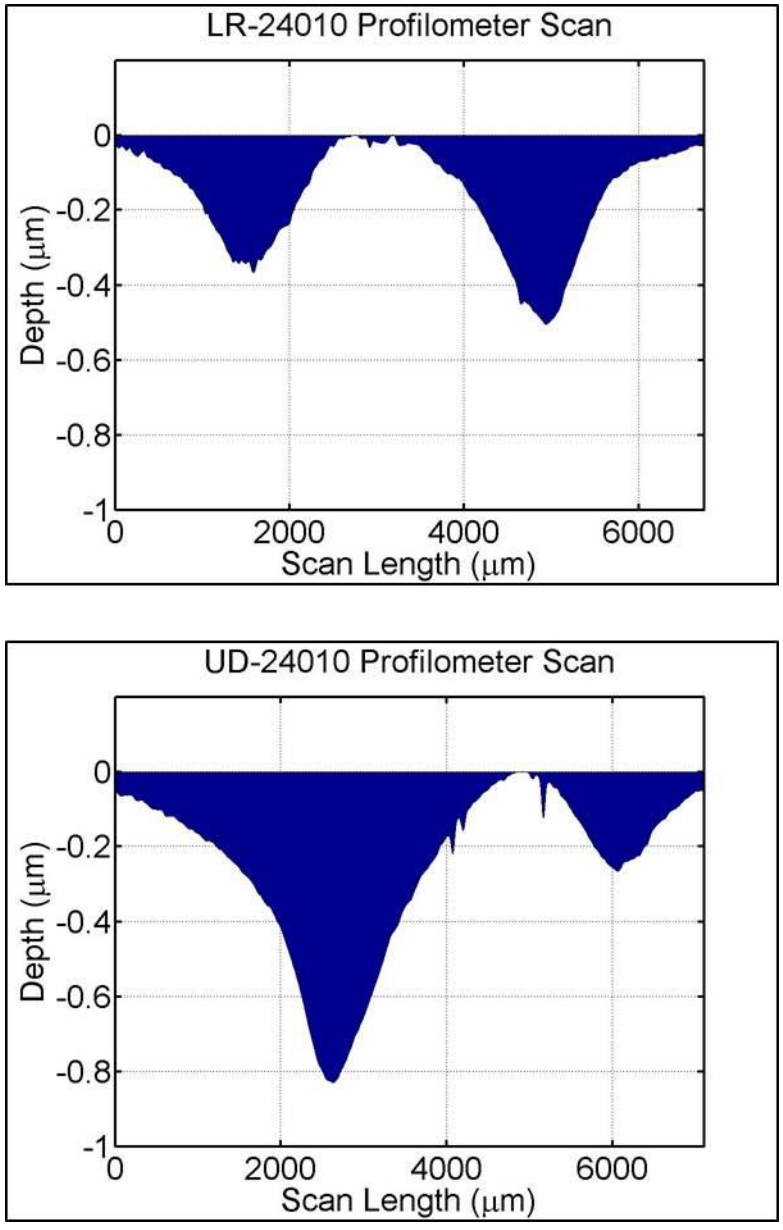

Figure 9-1 Erosion Profile for Test: 24010

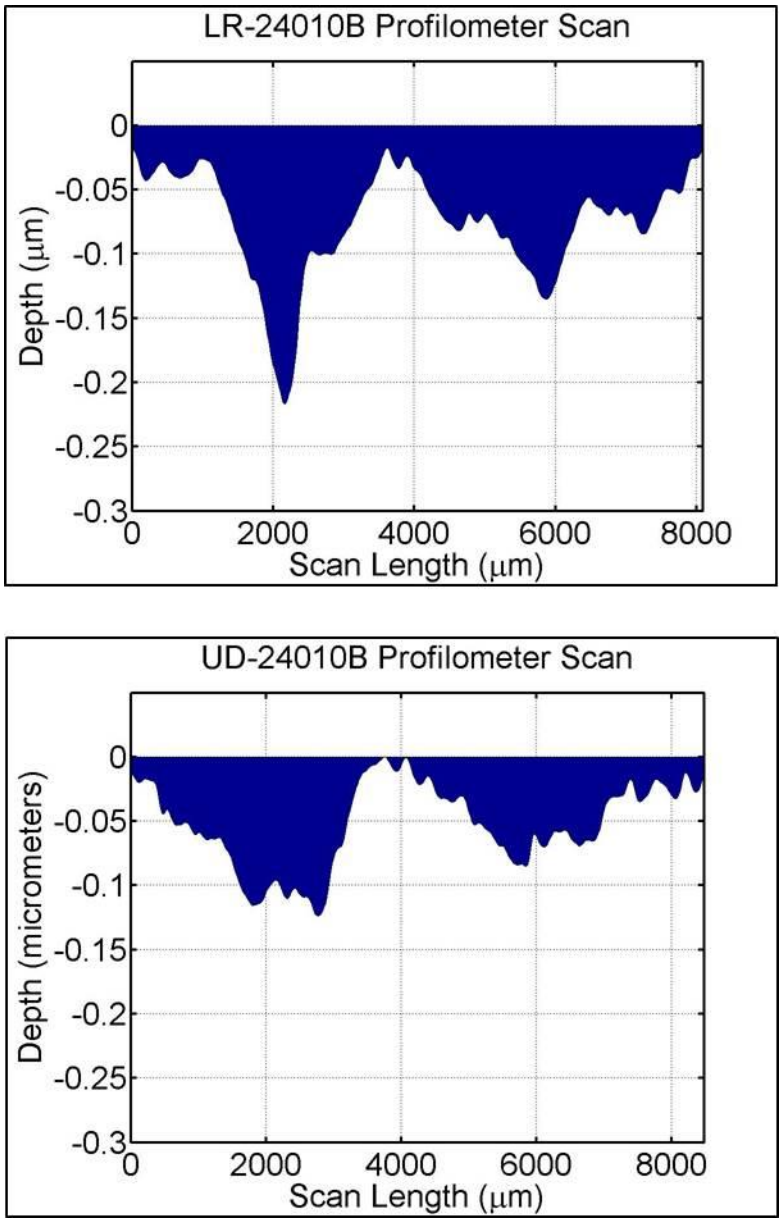

Figure 9-2 Erosion Profile for Test: 24010B

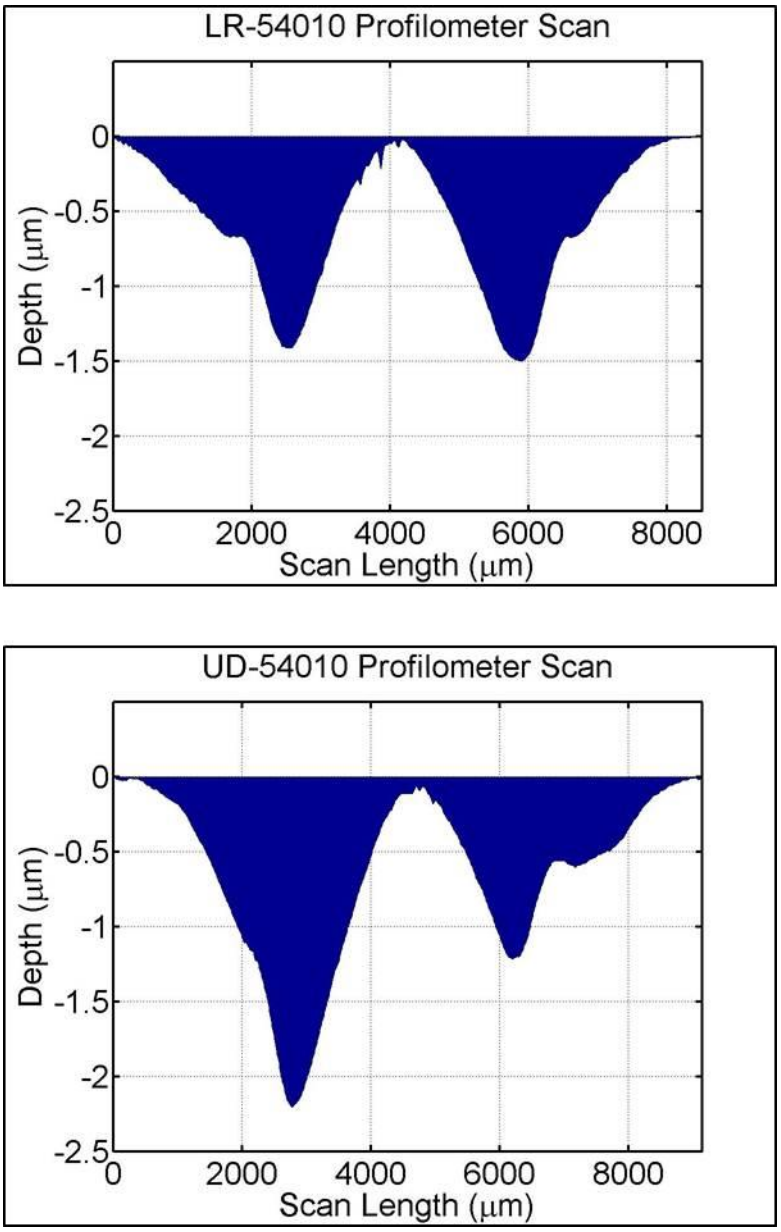

Figure 9-3 Erosion Profile for Test: 54010

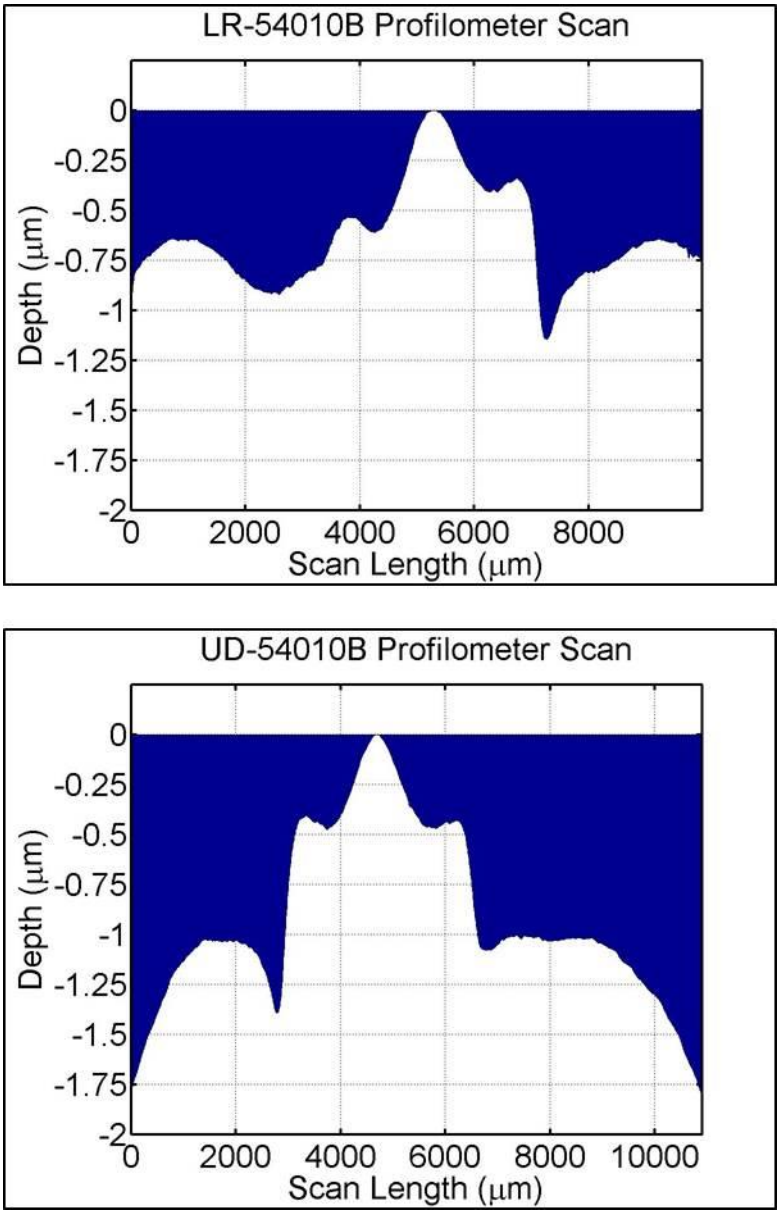

Figure 9-4 Erosion Profile for Test: 54010B

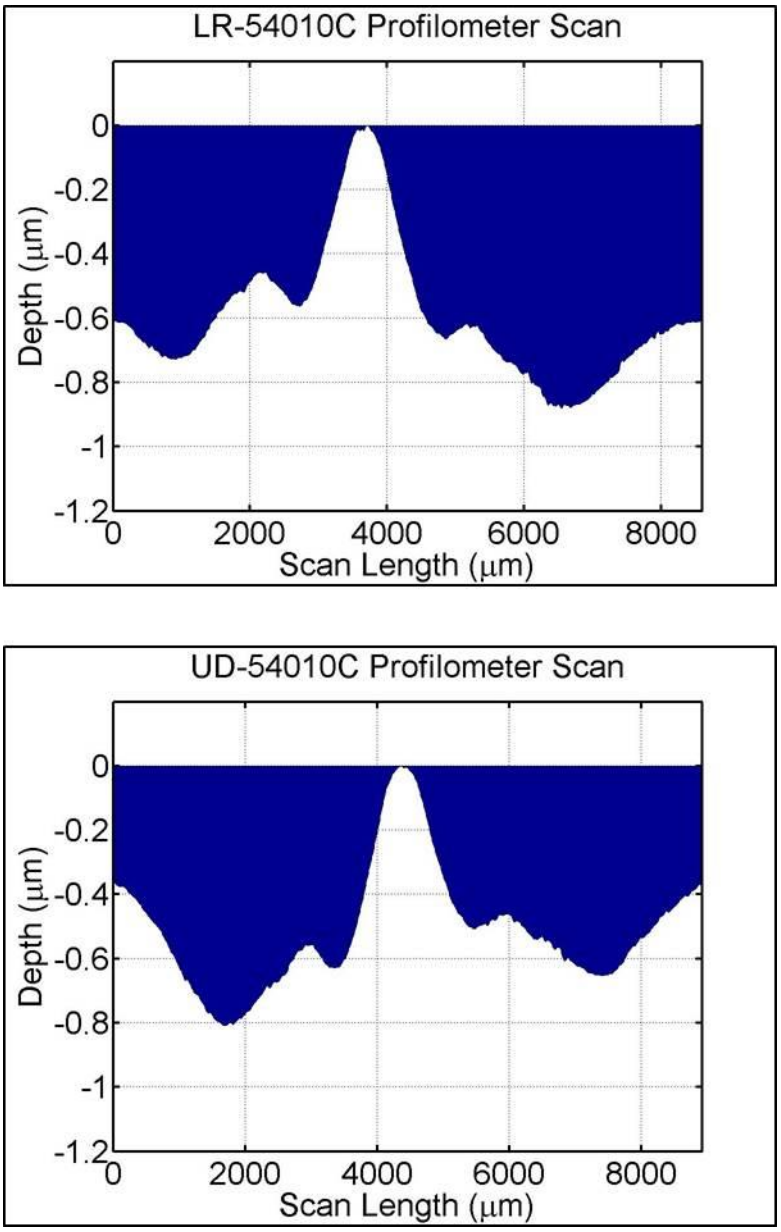

Figure 9-5 Erosion Profile for Test: 54010C

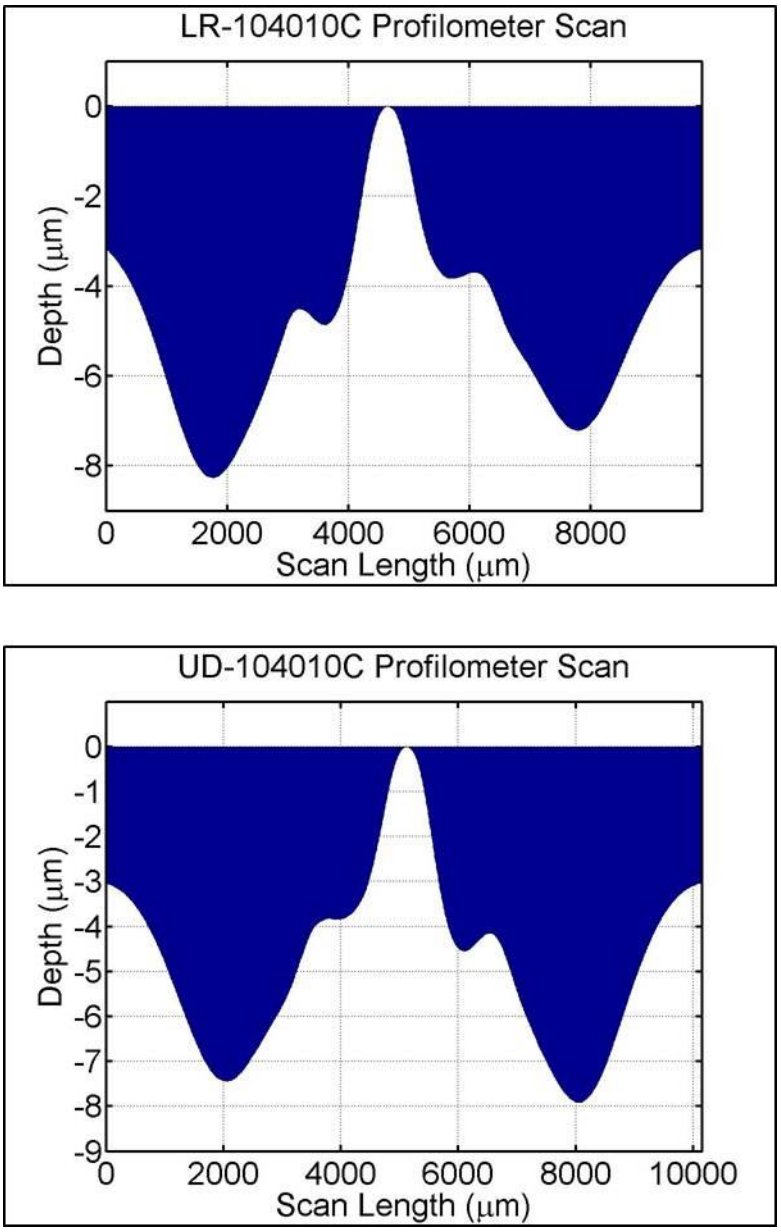

Figure 9-6 Erosion Profile for Test: 104010C

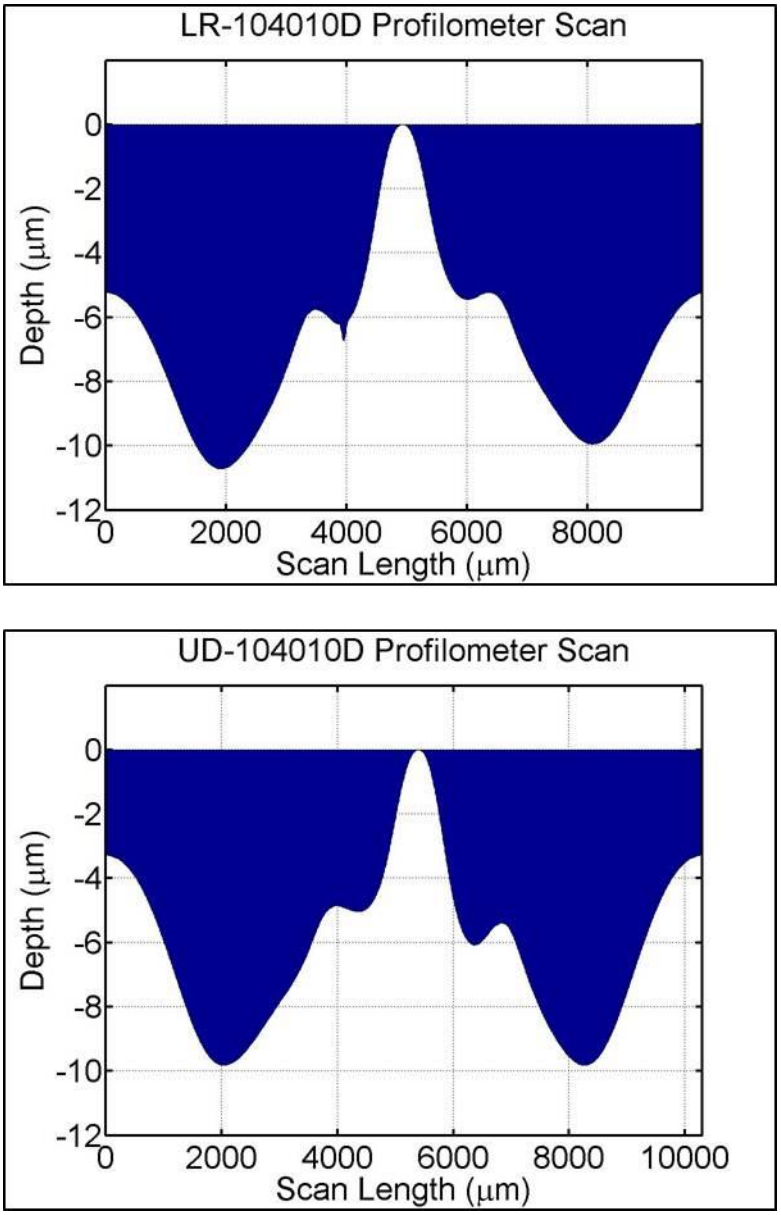

Figure 9-7 Erosion Profile for Test: 104010D

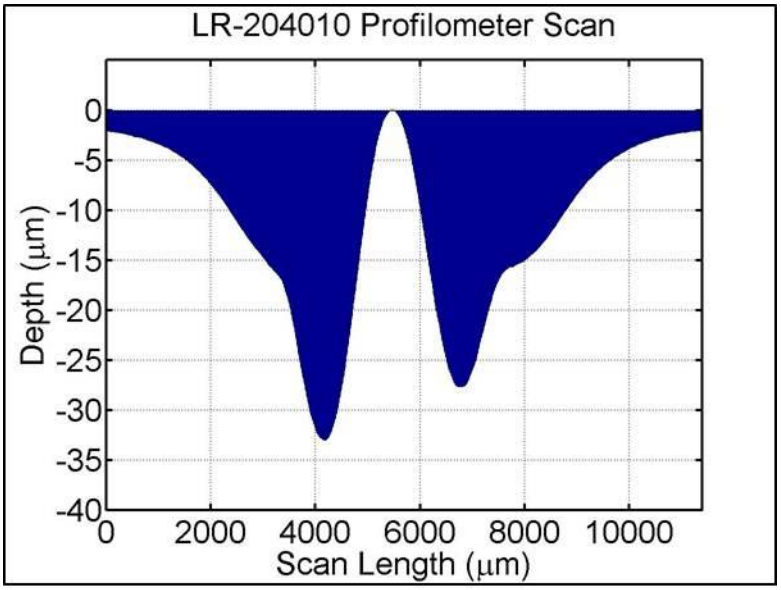

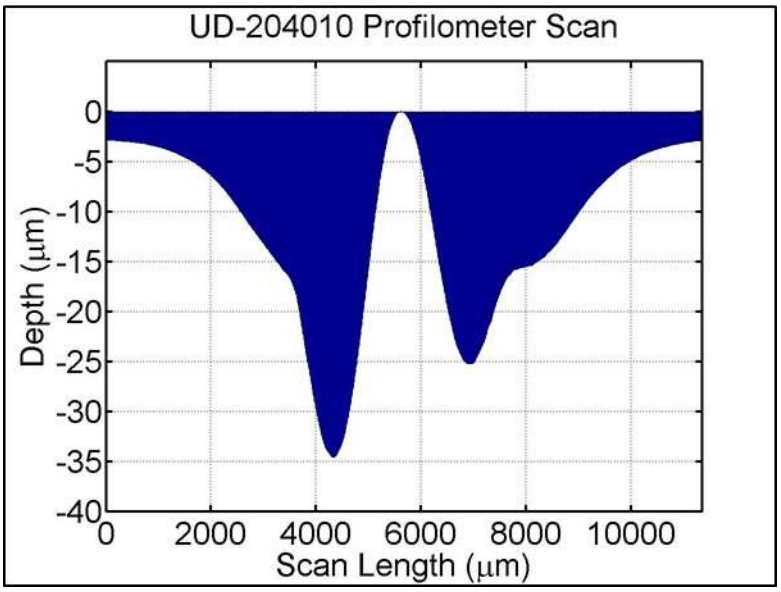

Figure 9-8 Erosion Profile for Test: 204010

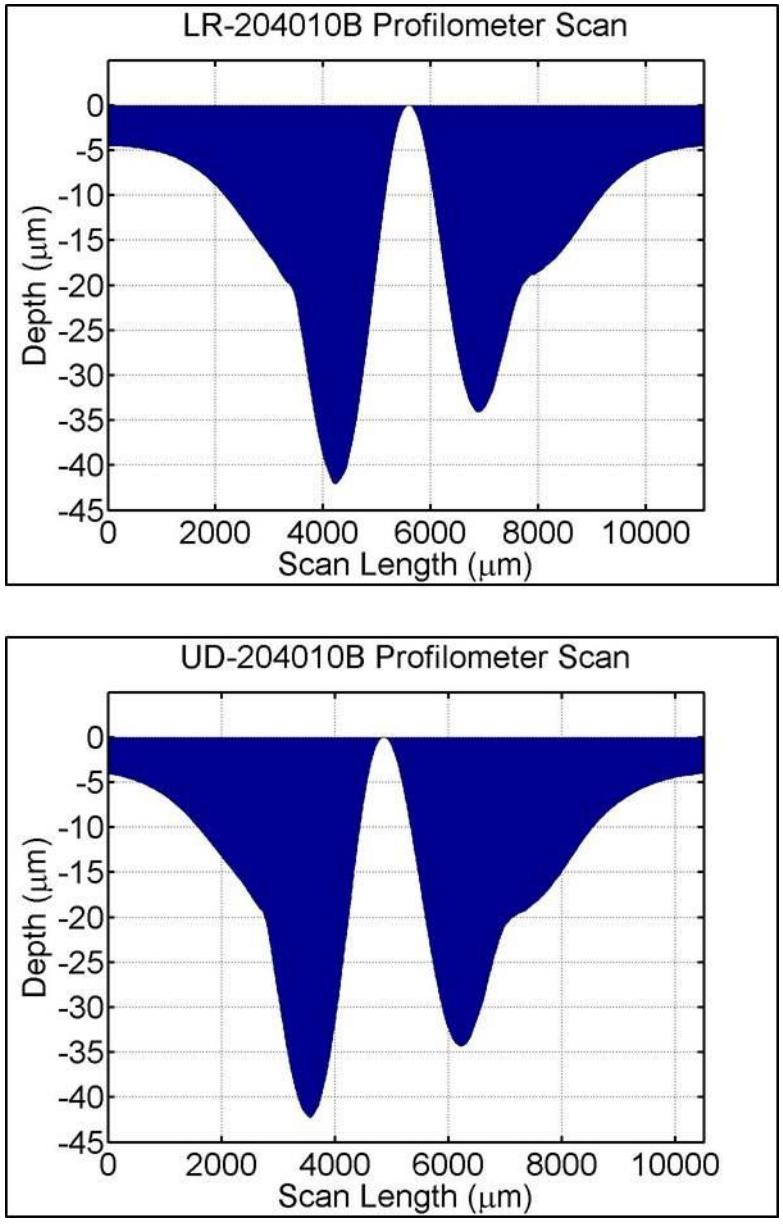

Figure 9-9 Erosion Profile for Test: 204010B

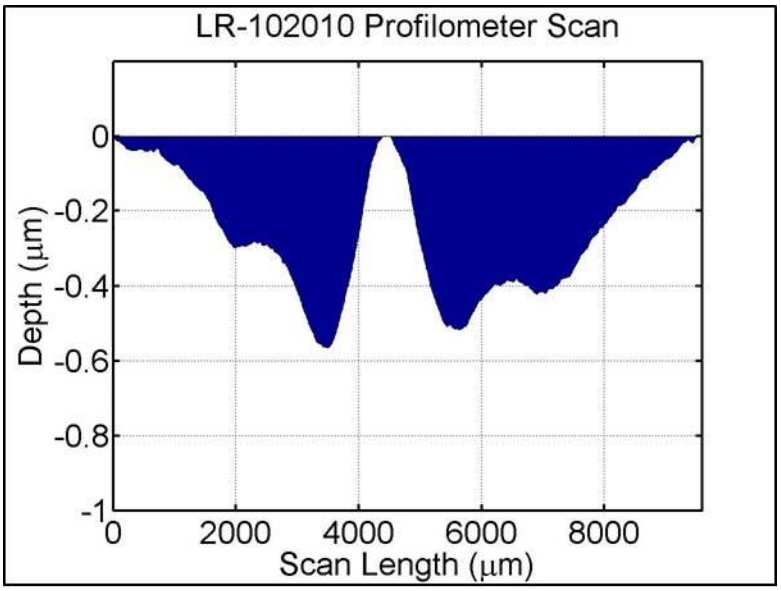

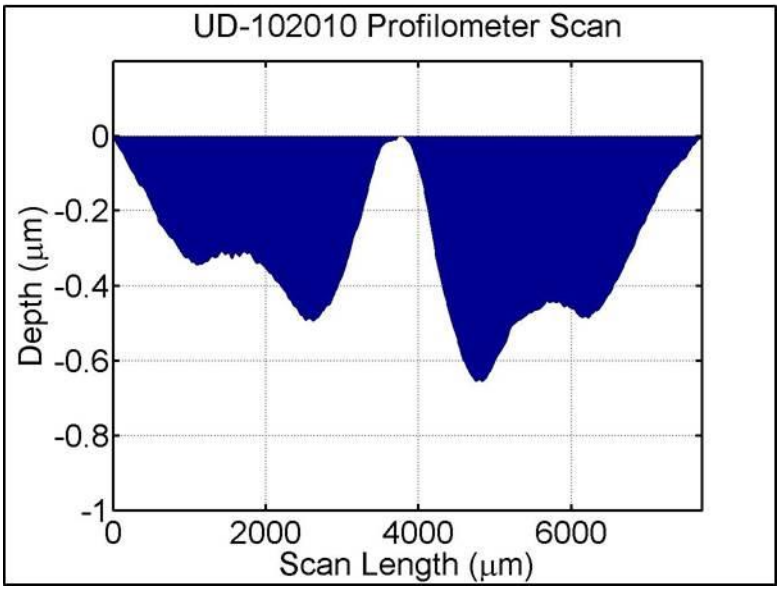

Figure 9-10 Erosion Profile for Test: 102010

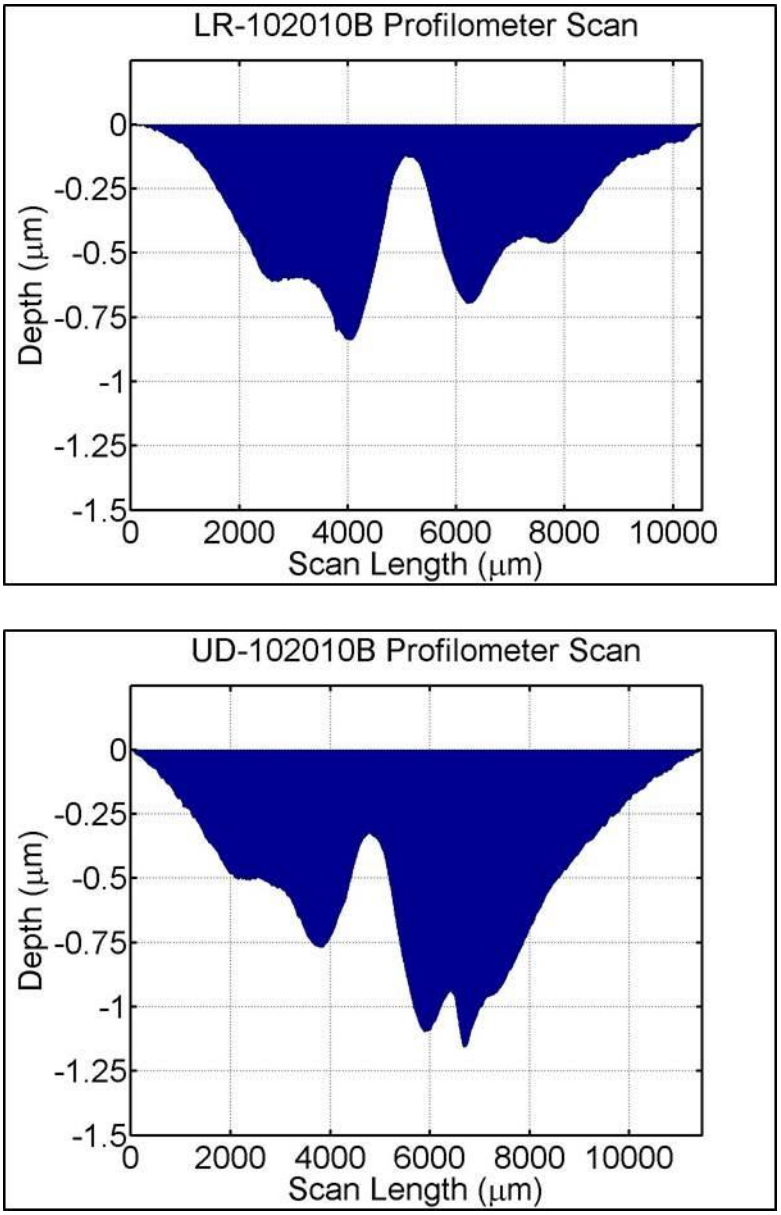

Figure 9-11 Erosion Profile for Test: 102010B

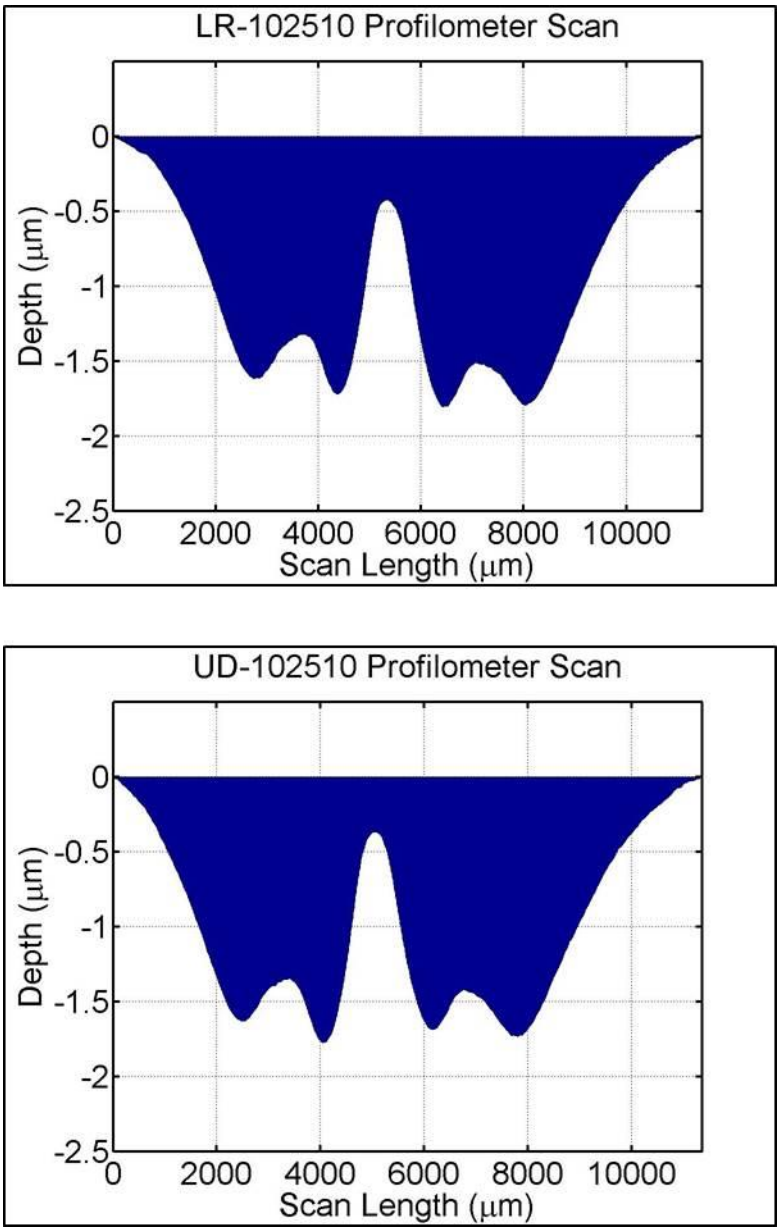

Figure 9-12 Erosion Profile for Test: 102510

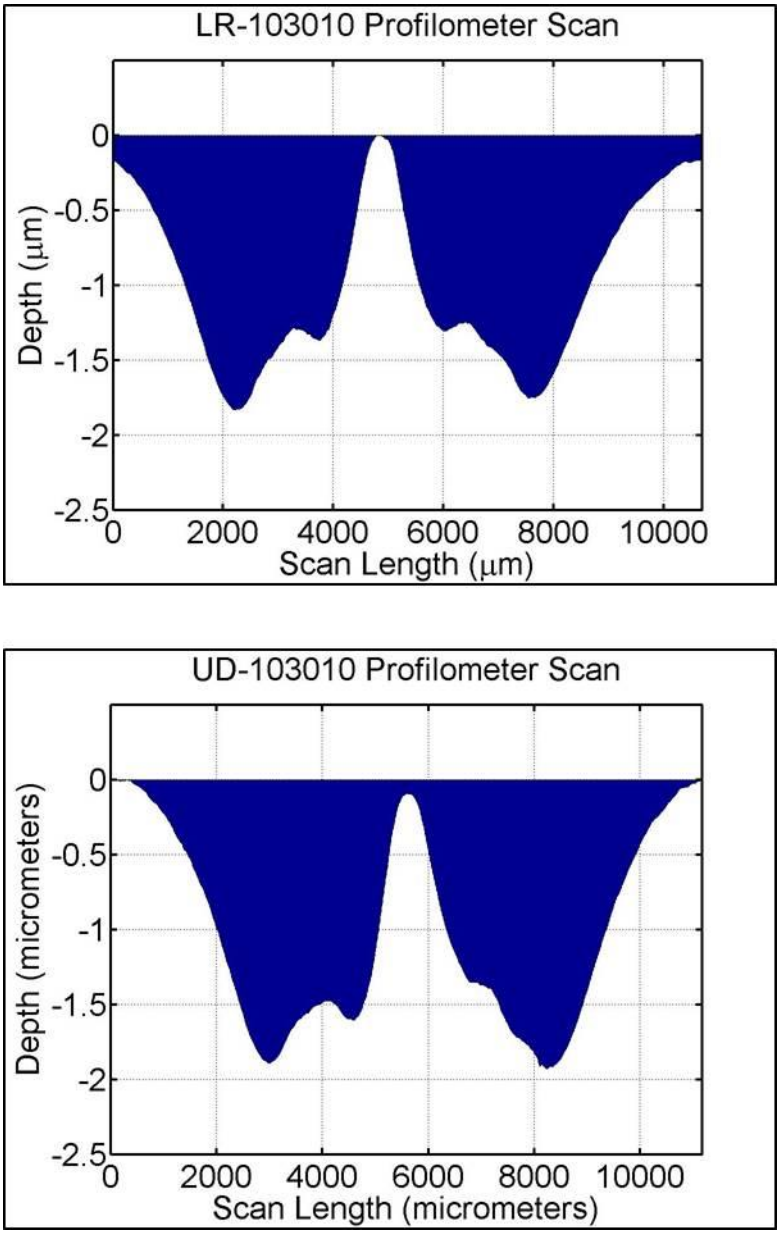

Figure 9-13 Erosion Profile for Test: 103010

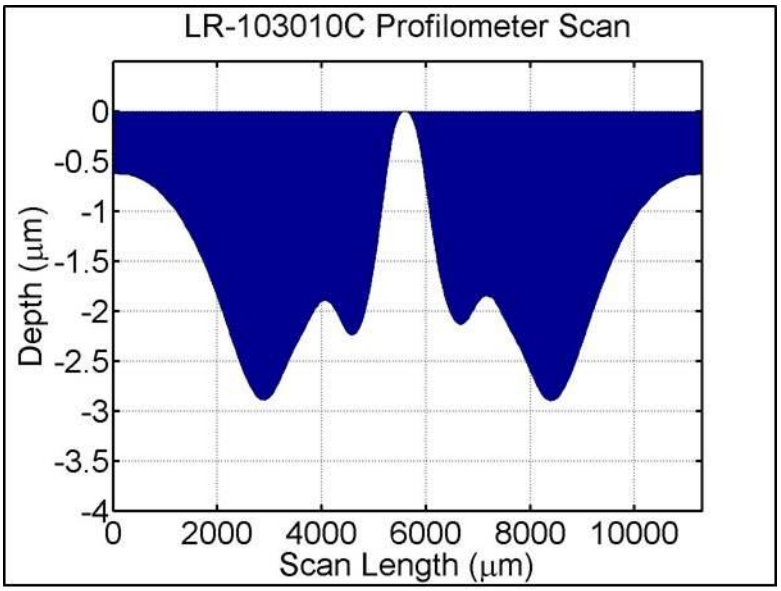

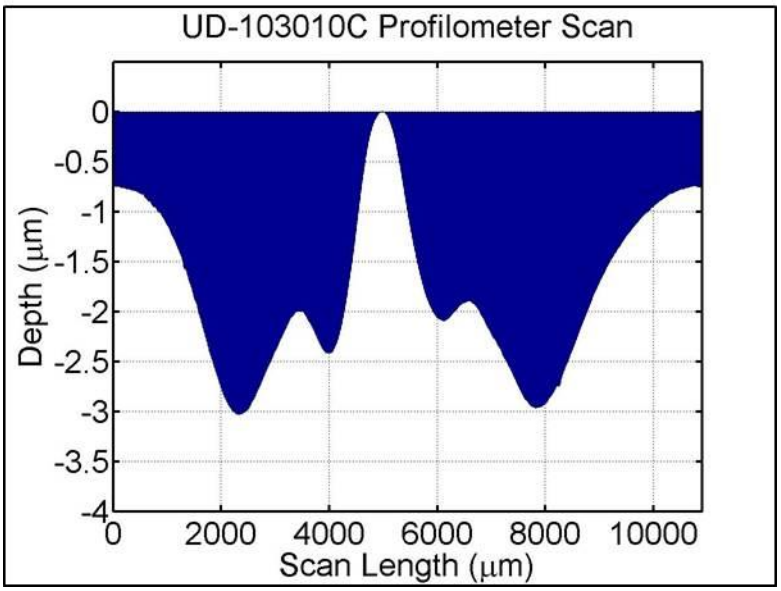

Figure 9-14 Erosion Profile for Test: 103010B

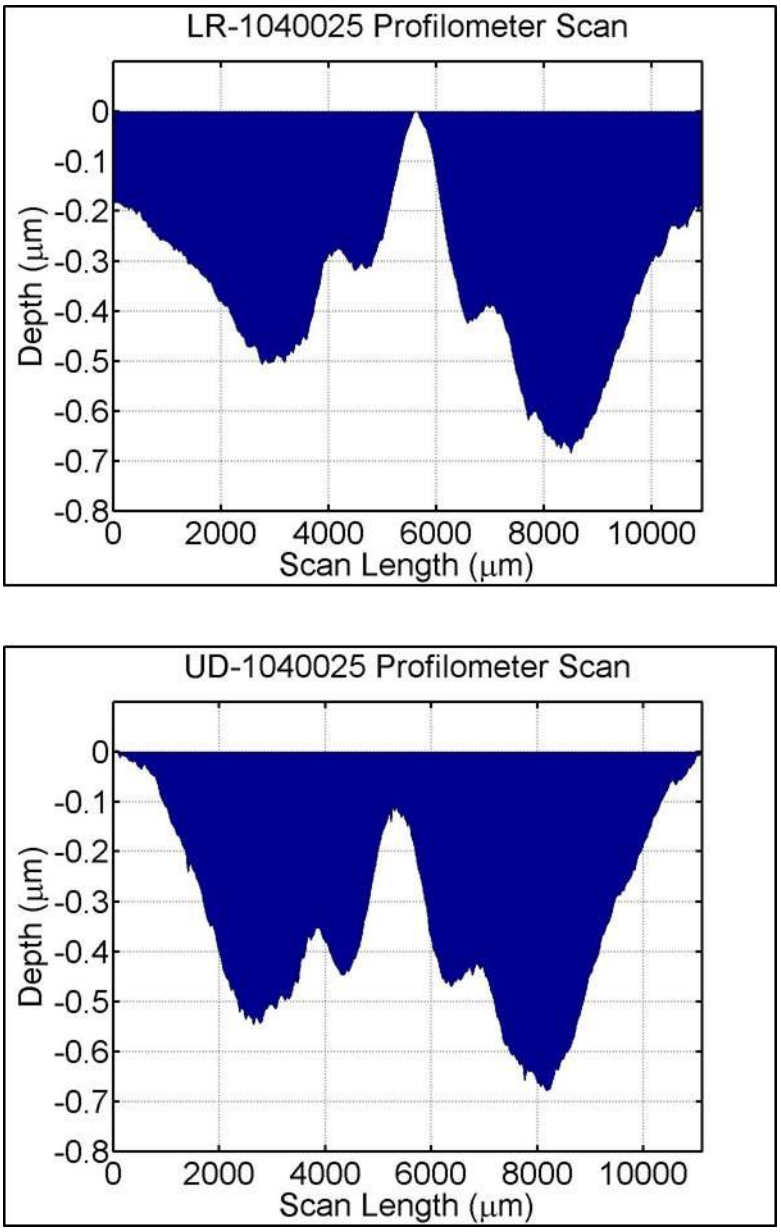

Figure 9-15 Erosion Profile for Test: 1040025

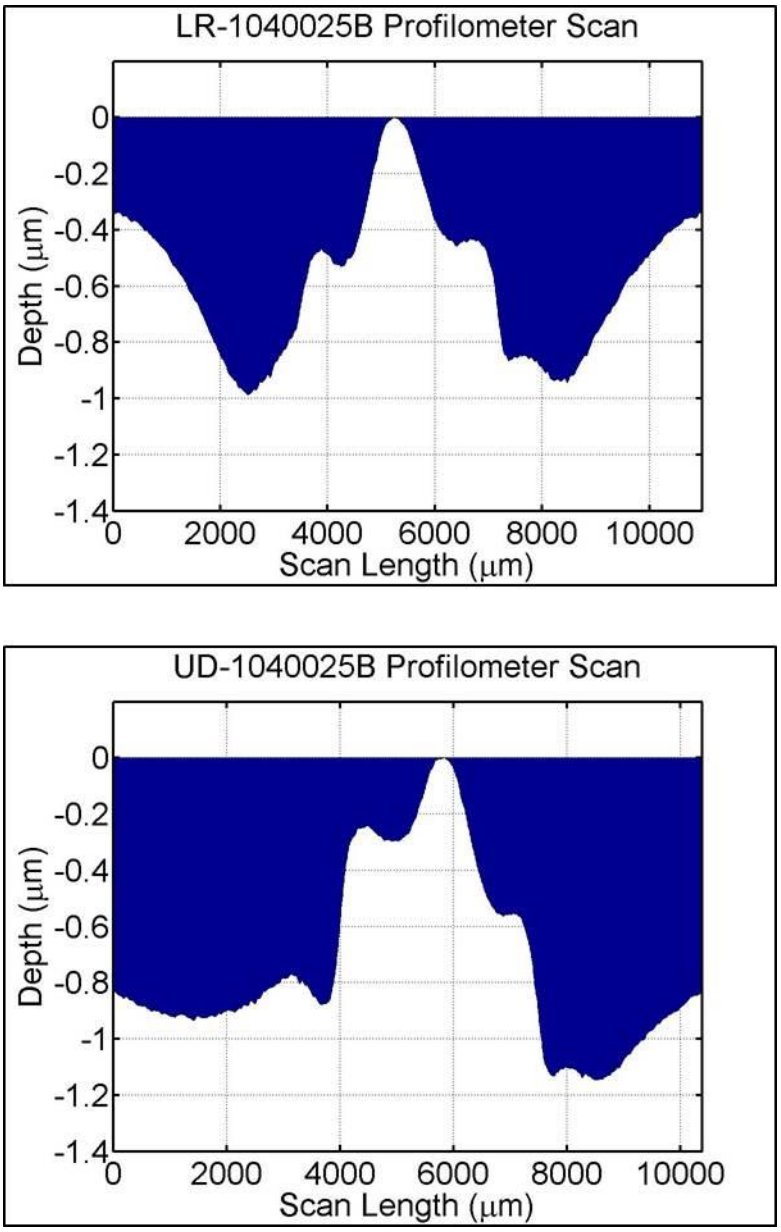

Figure 9-16 Erosion Profile for Test: 1040025B

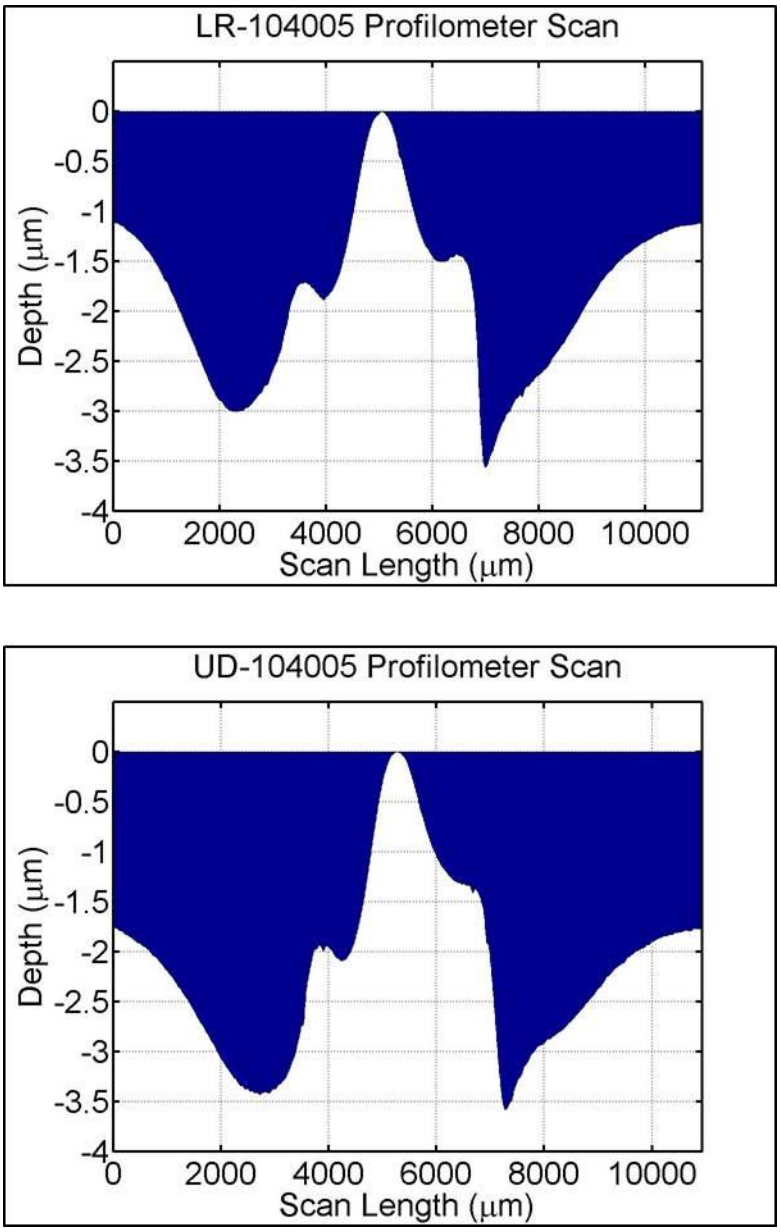

Figure 9-17 Erosion Profile for Test: 104005

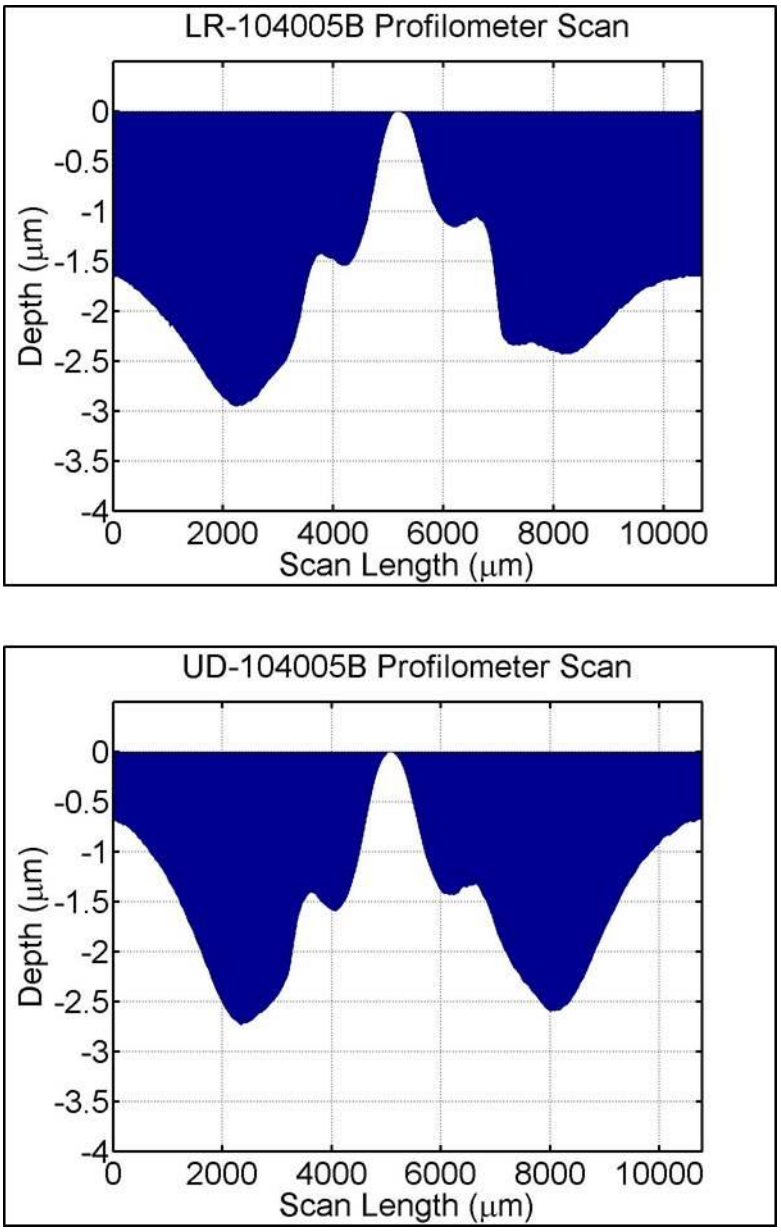

Figure 9-18 Erosion Profile for Test: 104005B

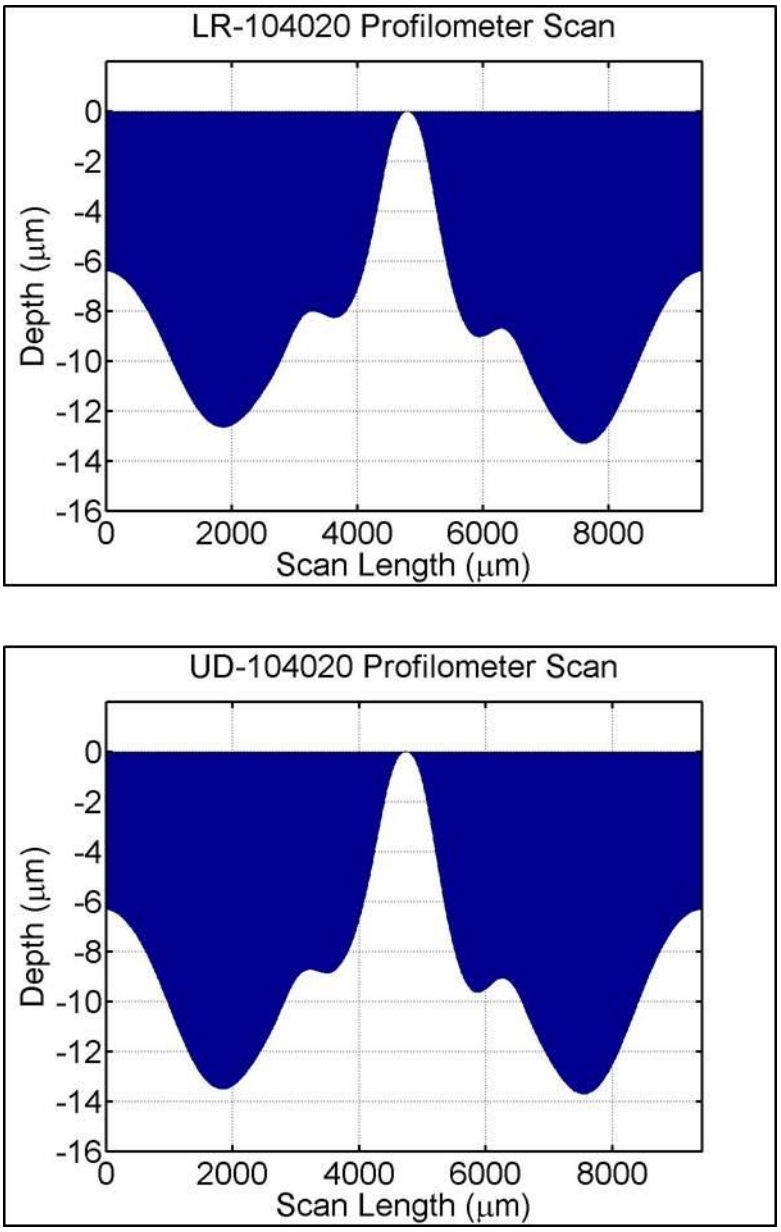

Figure 9-19 Erosion Profile for Test: 104020

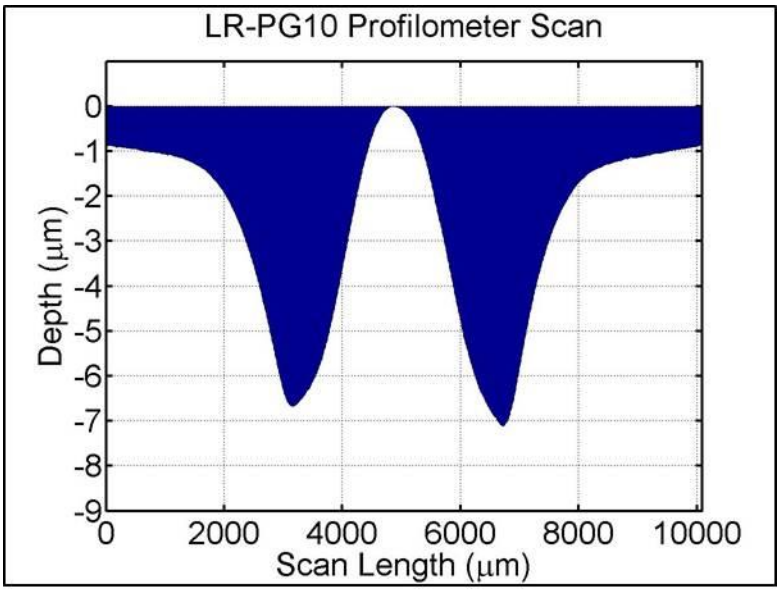

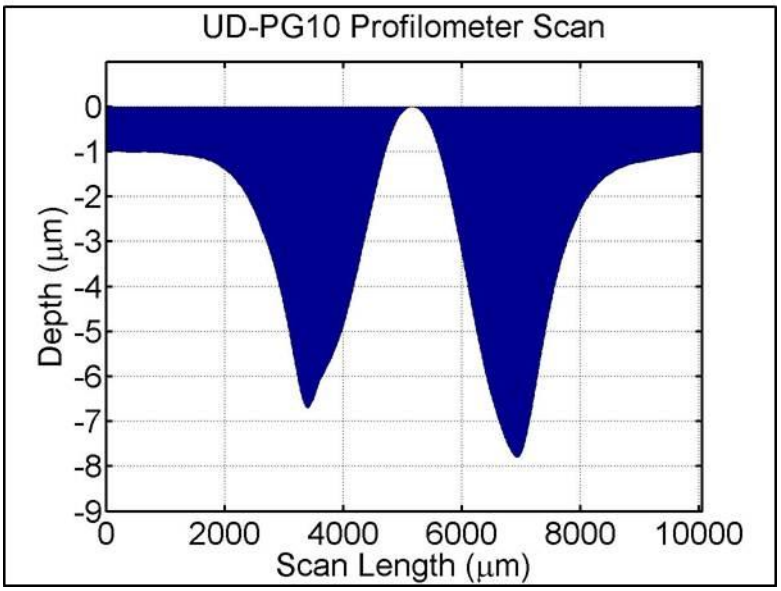

Figure 9-20 Erosion Profile for Test: PG10

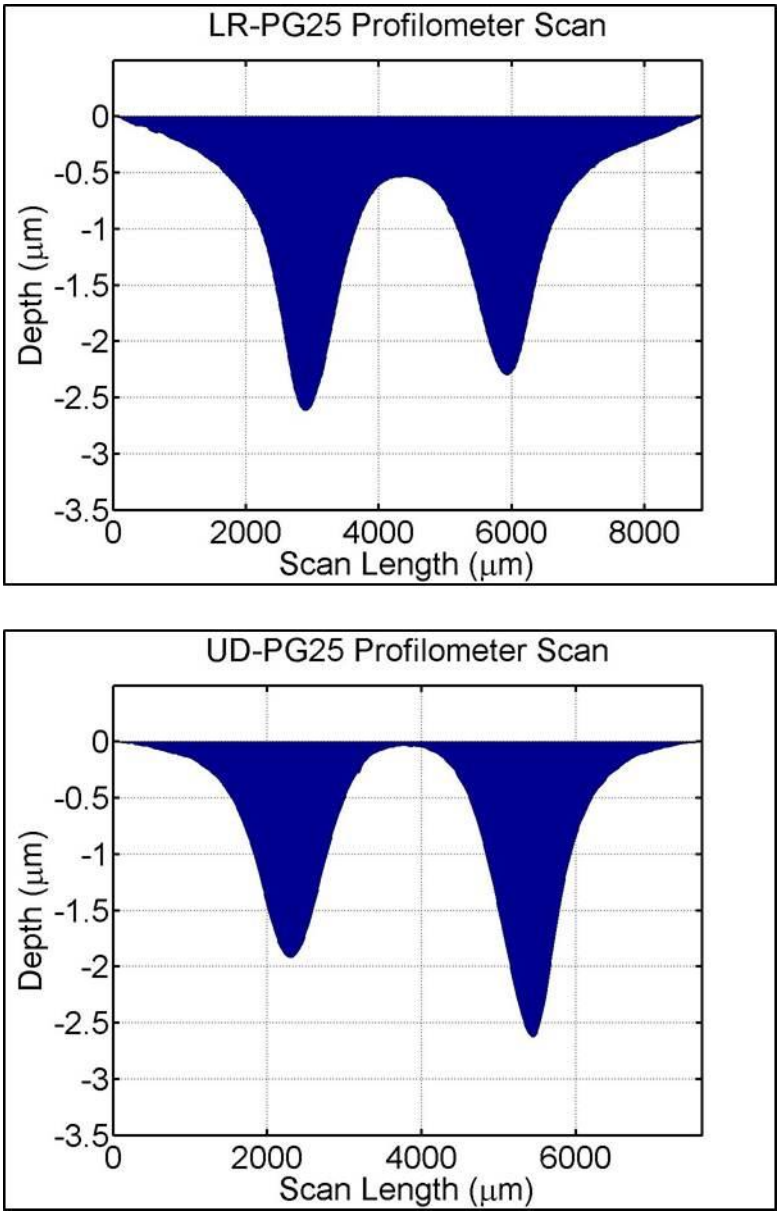

Figure 9-21 Erosion Profile for Test: PG25

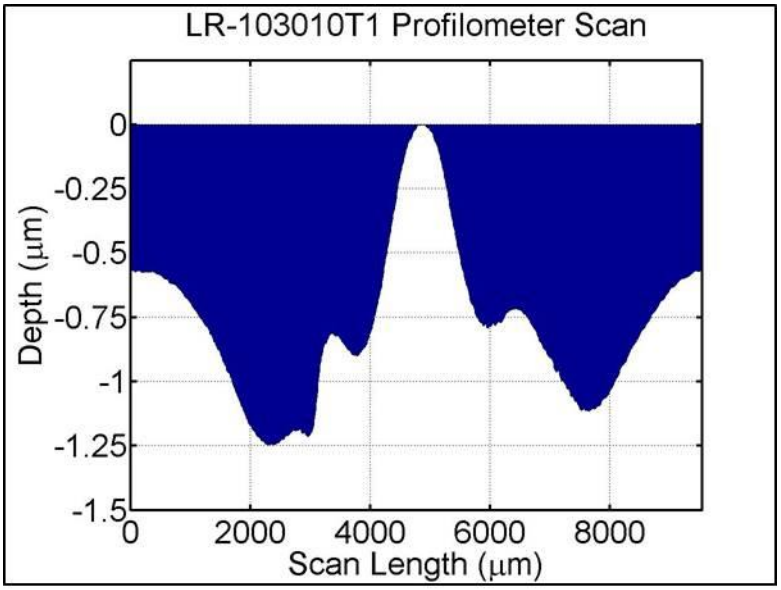

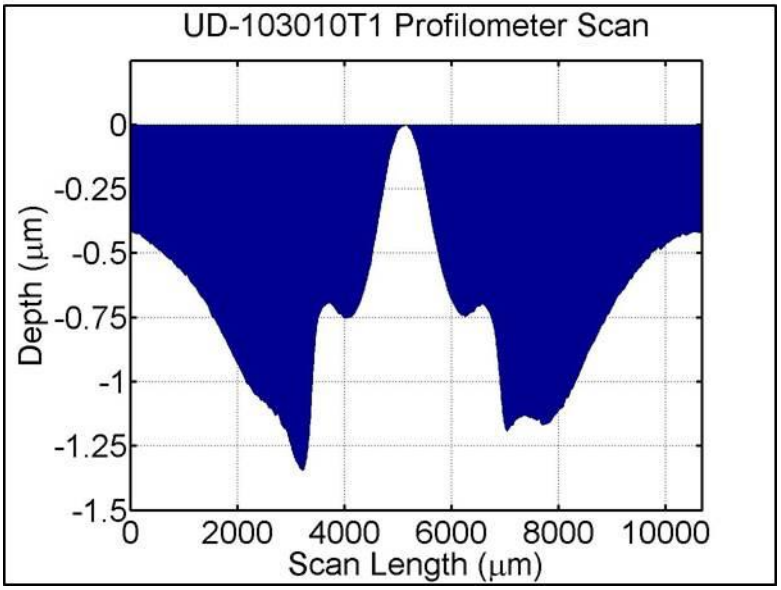

Figure 9-22 Erosion Profile for Test: 103010T1 – 2717 min.

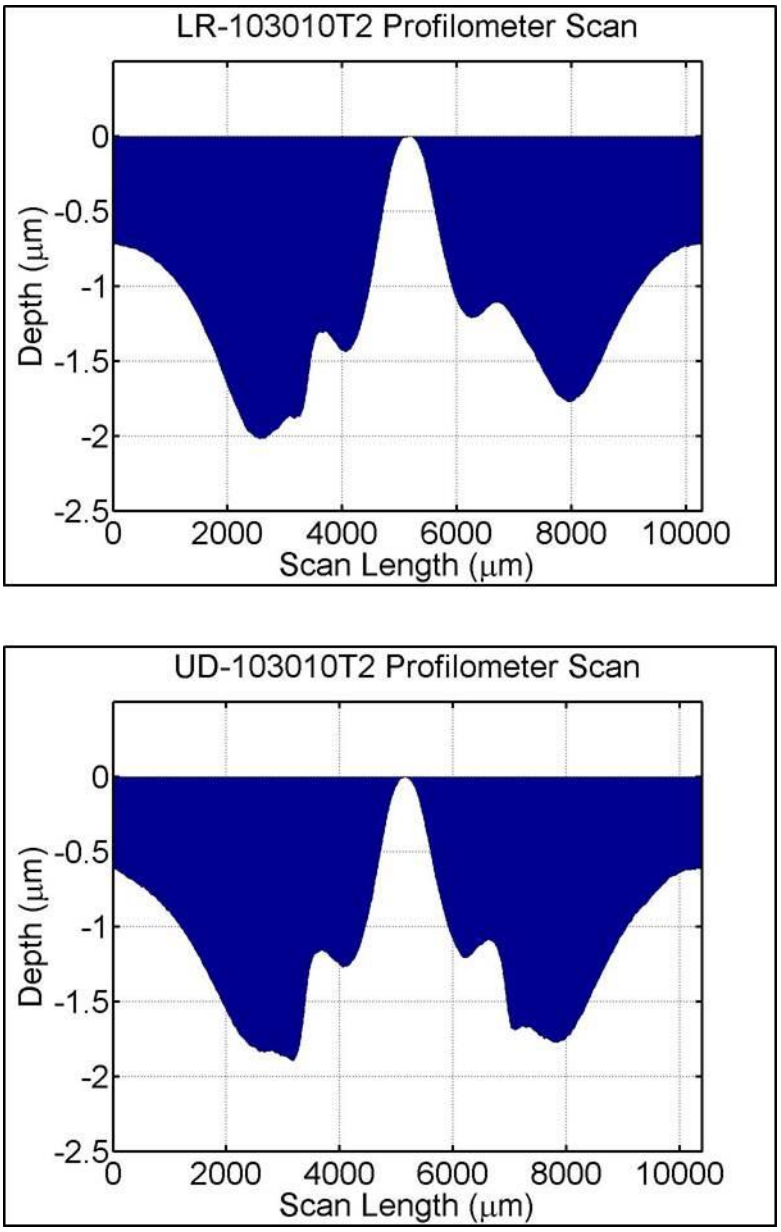

Figure 9-23 Erosion Profile for Test: 103010T2 – 5449 min.

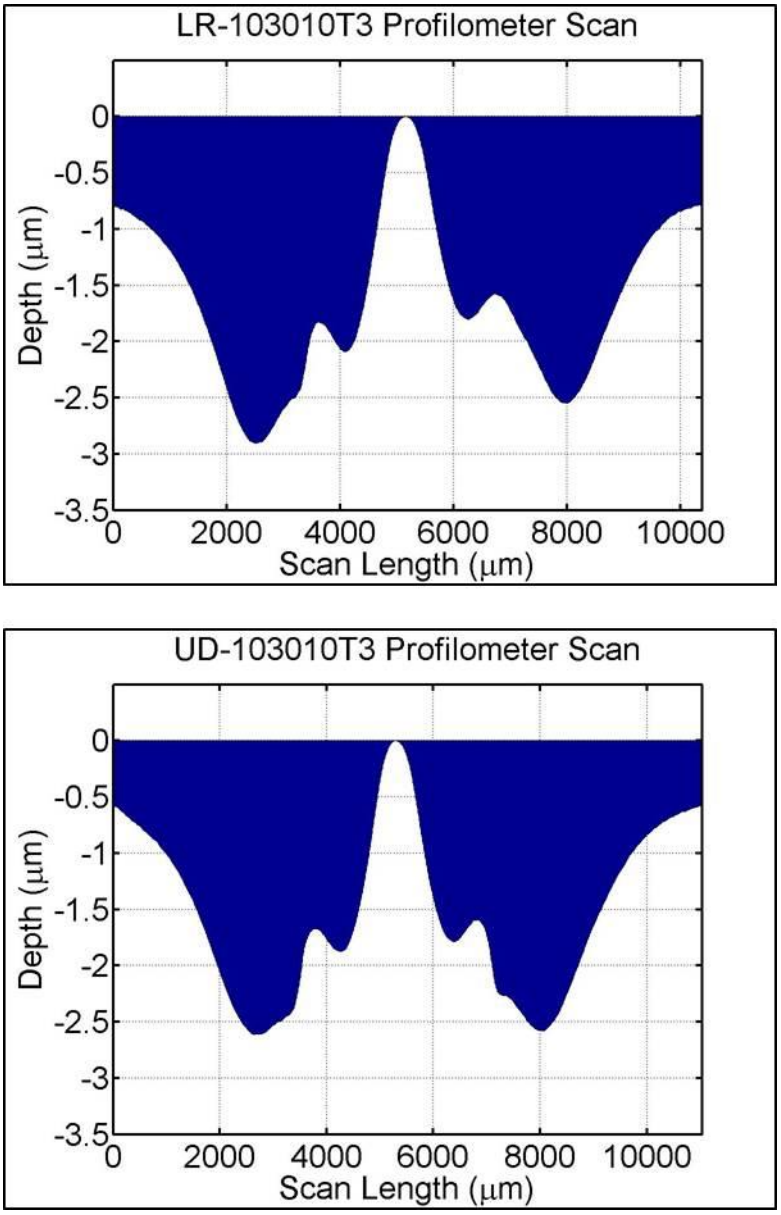

Figure 9-24 Erosion Profile for Test: 103010T3 – 11175 min.

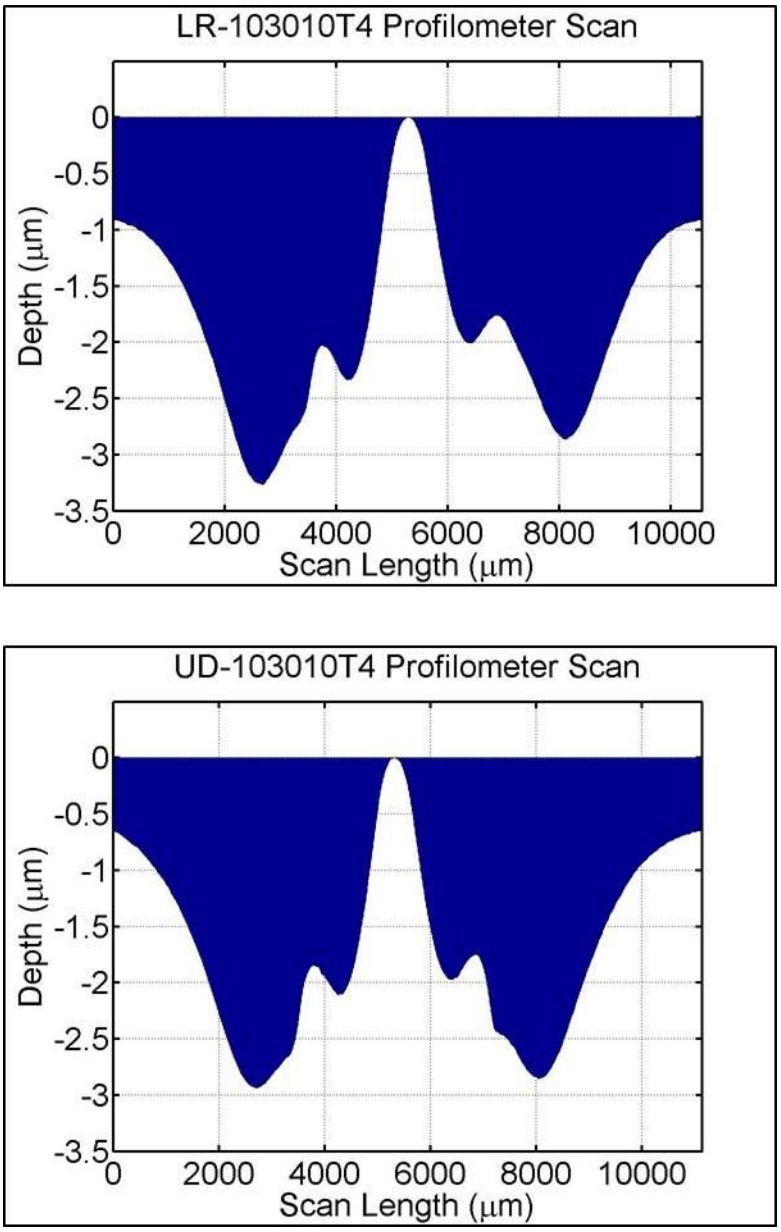

Figure 9-25 Erosion Profile for Test: 103010T4 – 14053 min.

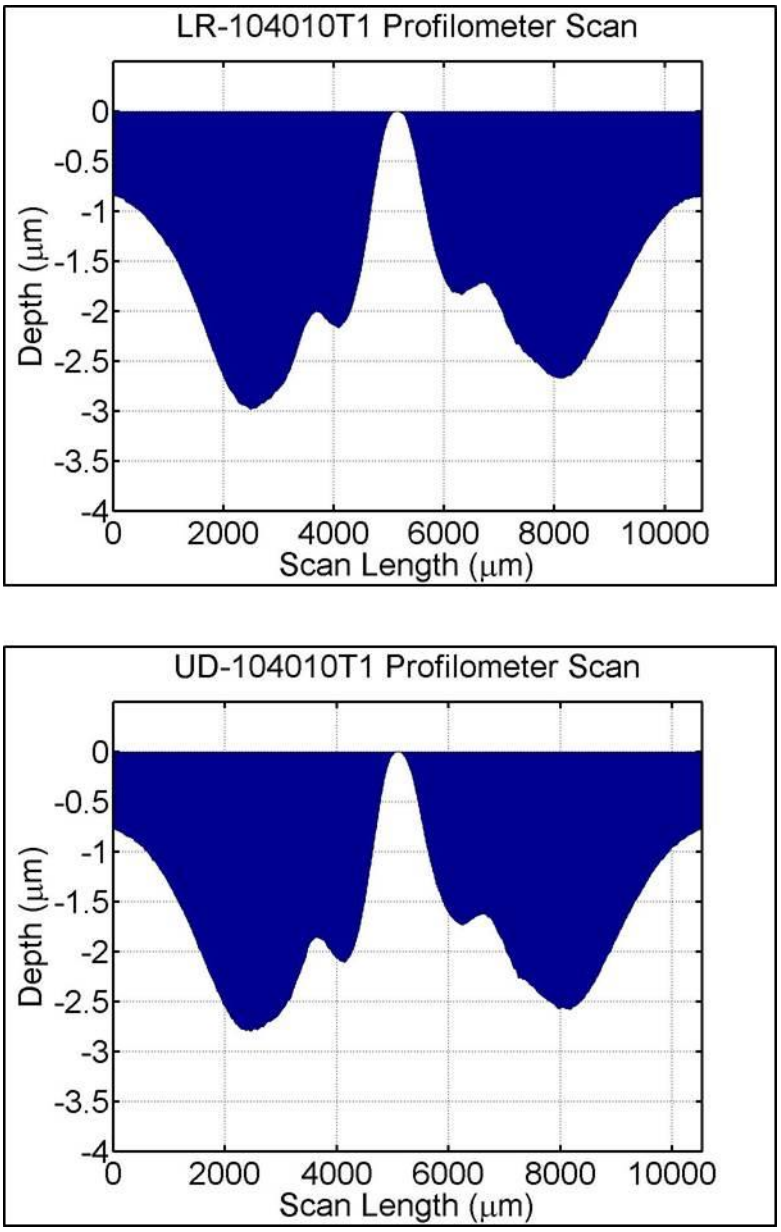

Figure 9-26 Erosion Profile for Test: 104010T1 – 1540 min.

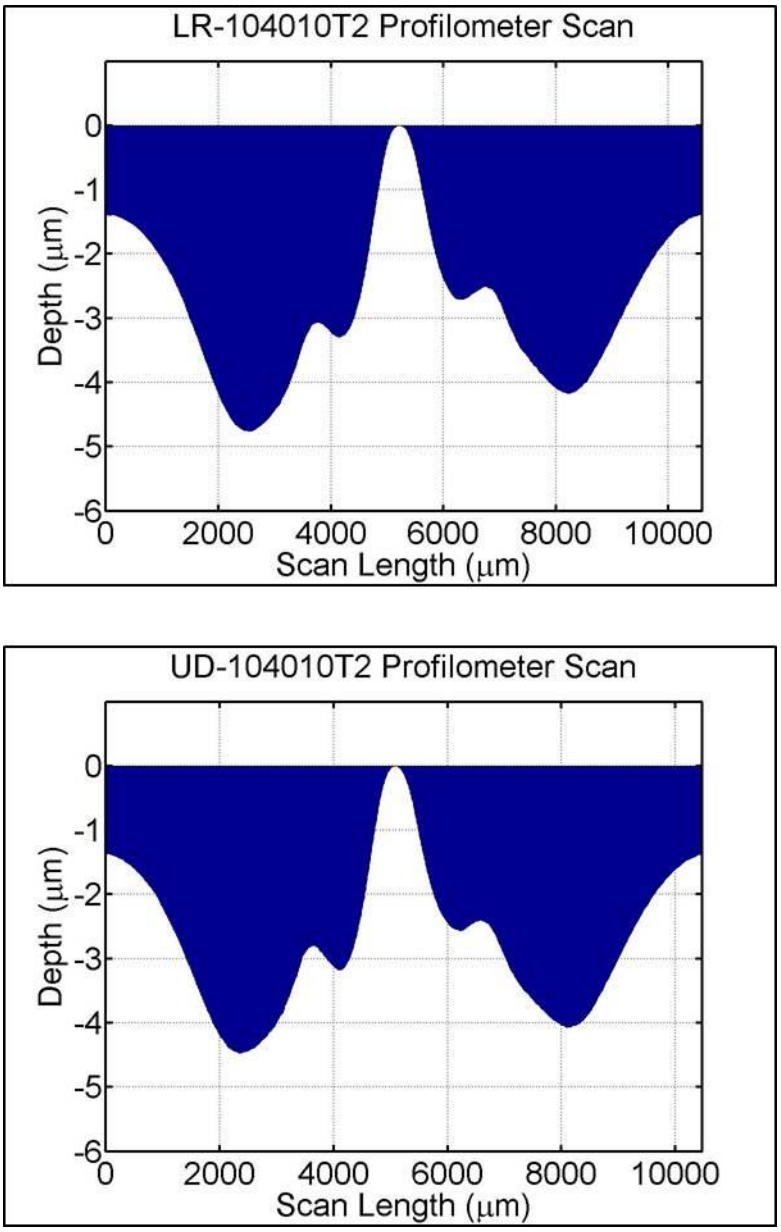

Figure 9-27 Erosion Profile for Test: 104010T2 – 2843 min.

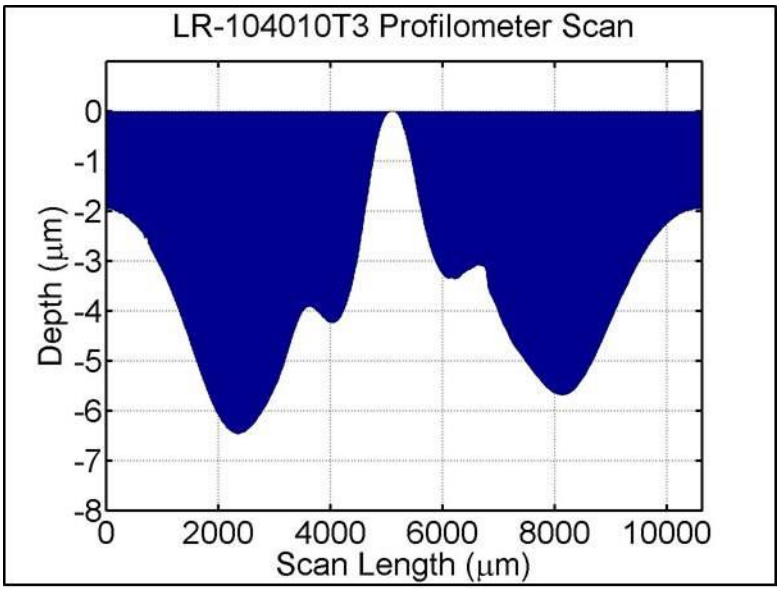

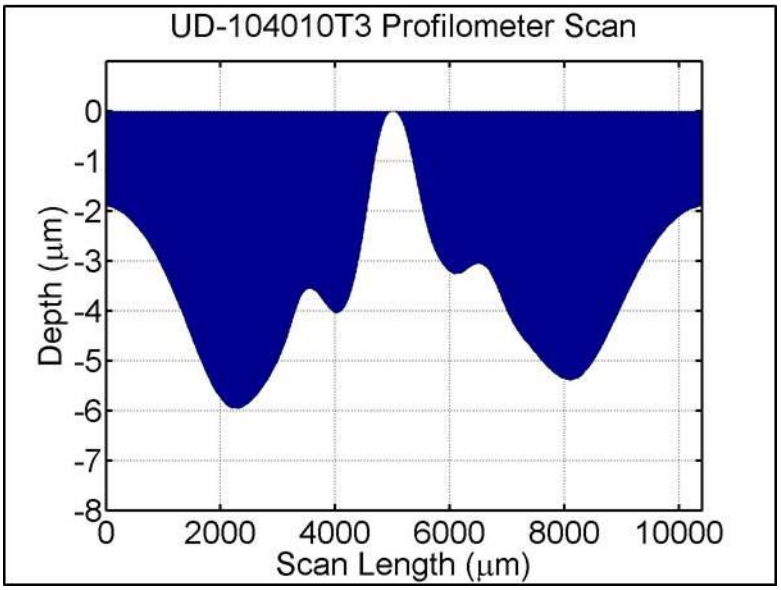

Figure 9-28 Erosion Profile for Test: 104010T3 – 4348 min.

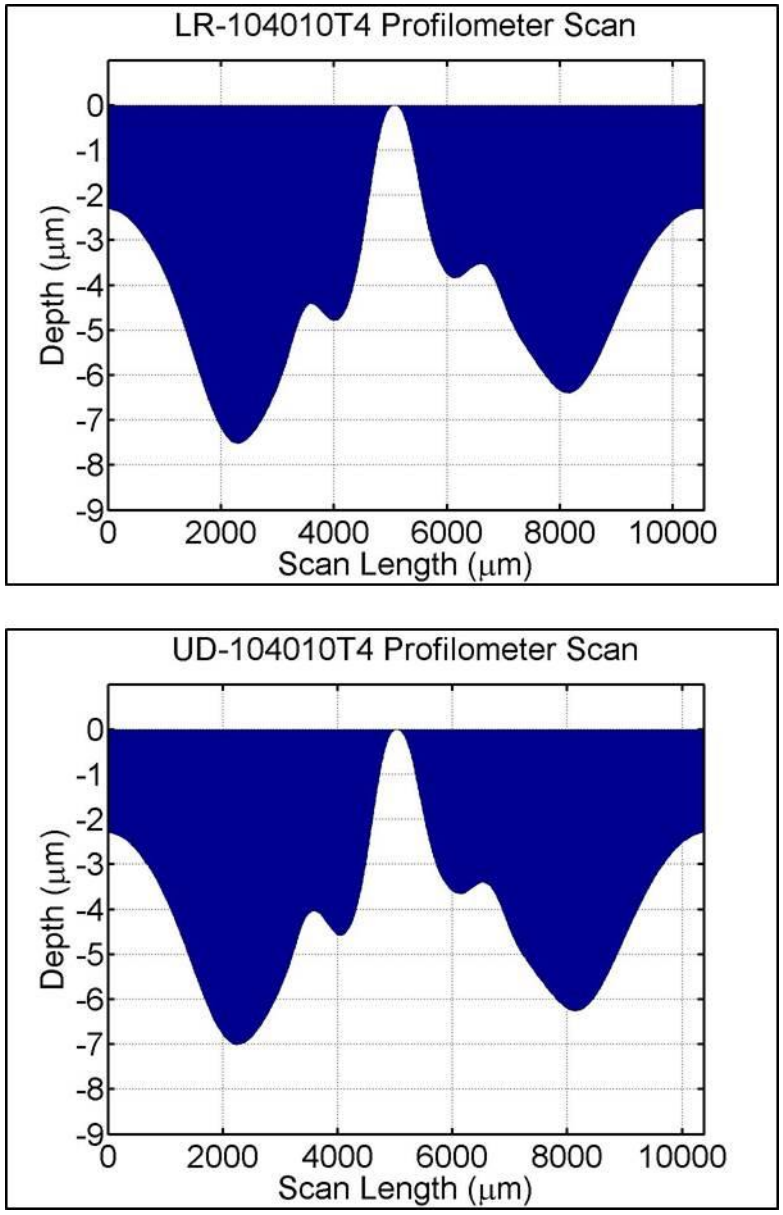

Figure 9-29 Erosion Profile for Test: 104010T4 – 5637 min.

Appendix B – Raw Particle Size Data

Sample ref.	: Sample A US 1.1
Sample Name	:
Sample type	:
Comments	:
Liquid	:
Dispersing agent	:
Operator	:
Company	:
Location	:
Date : 05/24/2016	Time : 10:18:41AM
Index meas.	: 829
Database name	: CilasDB1

Ultrasounds	: 60 s
Obscurations	: 8 / 0.11 %
Diameter at 10%	: 1.38 µm
Diameter at 50%	: 7.74 µm
Diameter at 90%	: 18.27 µm
Mean diameter	: 8.97 µm
Fraunhofer	
Density/Factor	---
Specific surface	---
Automatic dilution	: No / No
Meas./Rins.	: 60s/60s/4
SOP name	: Fraunhofer

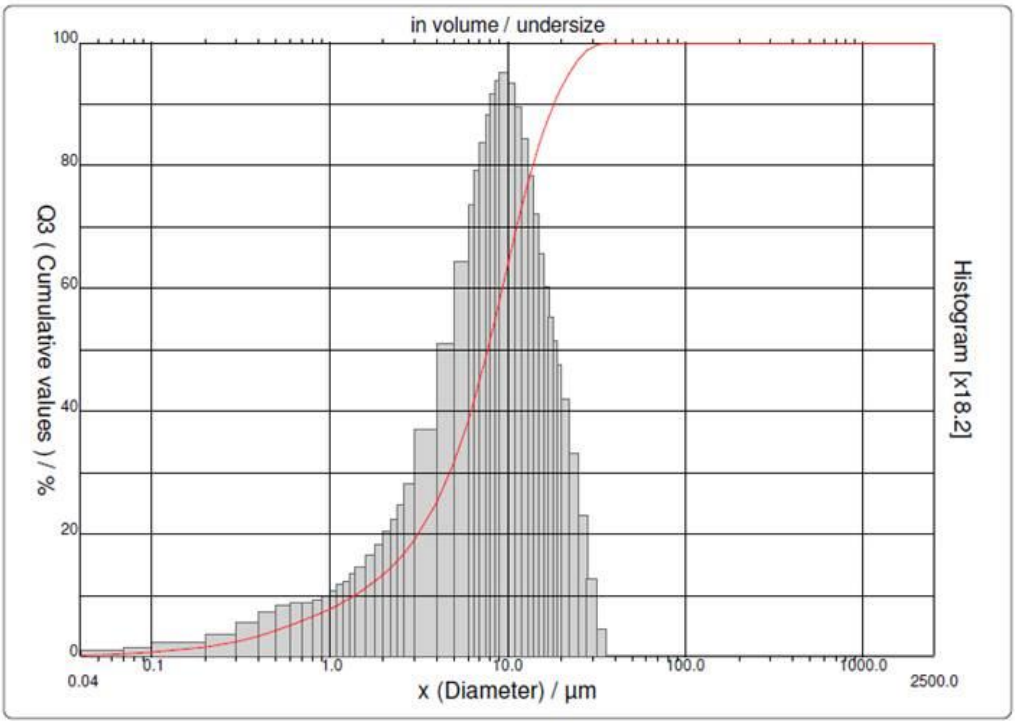

Figure 9-30 Raw Particle Size Data - 10µm, sample 1

Sample ref.	: Sample A US 1.2
Sample Name	:
Sample type	:
Comments	:
Liquid	:
Dispersing agent	:
Operator	:
Company	:
Location	:
Date : 05/24/2016	Time : 10:21:53AM
Index meas.	: 830
Database name	: CilasDB1

Ultrasounds	: 60	s
Obscuration	: 8 %	
Diameter at 10%	: 1.35	µm
Diameter at 50%	: 7.67	µm
Diameter at 90%	: 18.32	µm
Mean diameter	: 8.93	µm
Fraunhofer		
Density/Factor	---	
Specific surface	---	
Automatic dilution	: No / No	
Meas./Rins.	: 60s/60s/4	
SOP name	: Fraunhofer	

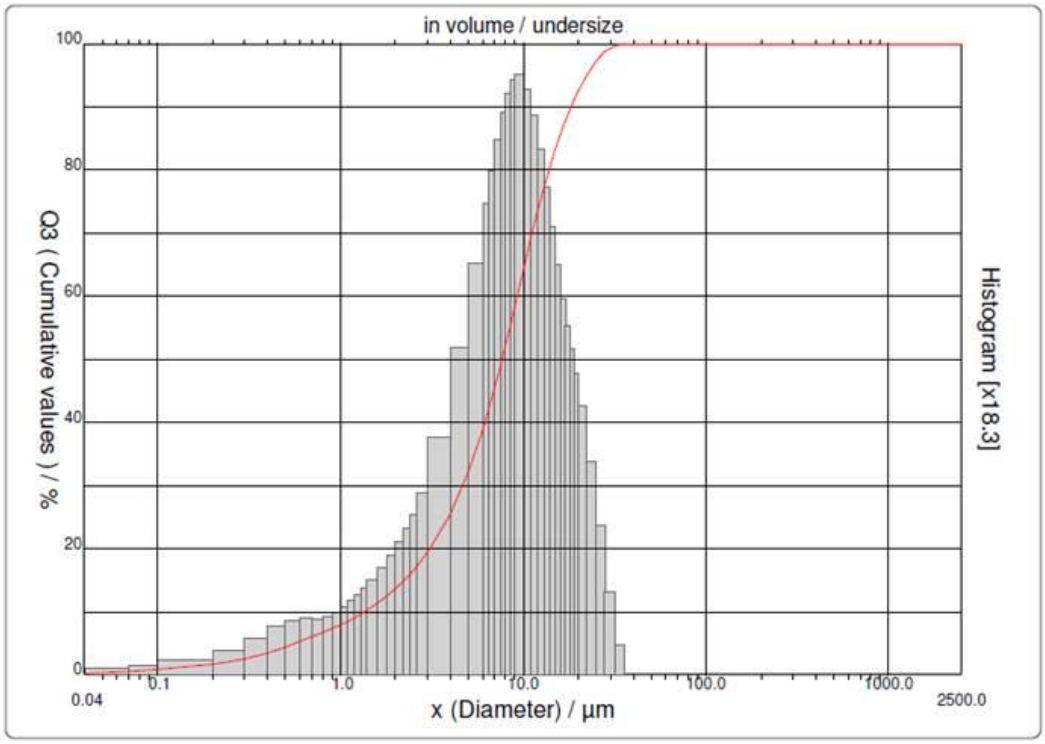

Figure 9-31 Raw Particle Size Data - 10µm, sample 2

Sample ref.	: Sample A US 1.3
Sample Name	:
Sample type	:
Comments	:
Liquid	:
Dispersing agent	:
Operator	:
Company	:
Location	:
Date : 05/24/2016	Time : 10:25:05AM
Index meas.	: 831
Database name	: CilasDB1

Ultrasounds	: 60 s
Obscurations	: 8 / 0.02 %
Diameter at 10%	: 1.42 µm
Diameter at 50%	: 7.69 µm
Diameter at 90%	: 18.32 µm
Mean diameter	: 8.96 µm
Fraunhofer	
Density/Factor	----------
Specific surface	----------
Automatic dilution	: No / No
Meas./Rins.	: 60s/60s/4
SOP name	: Fraunhofer

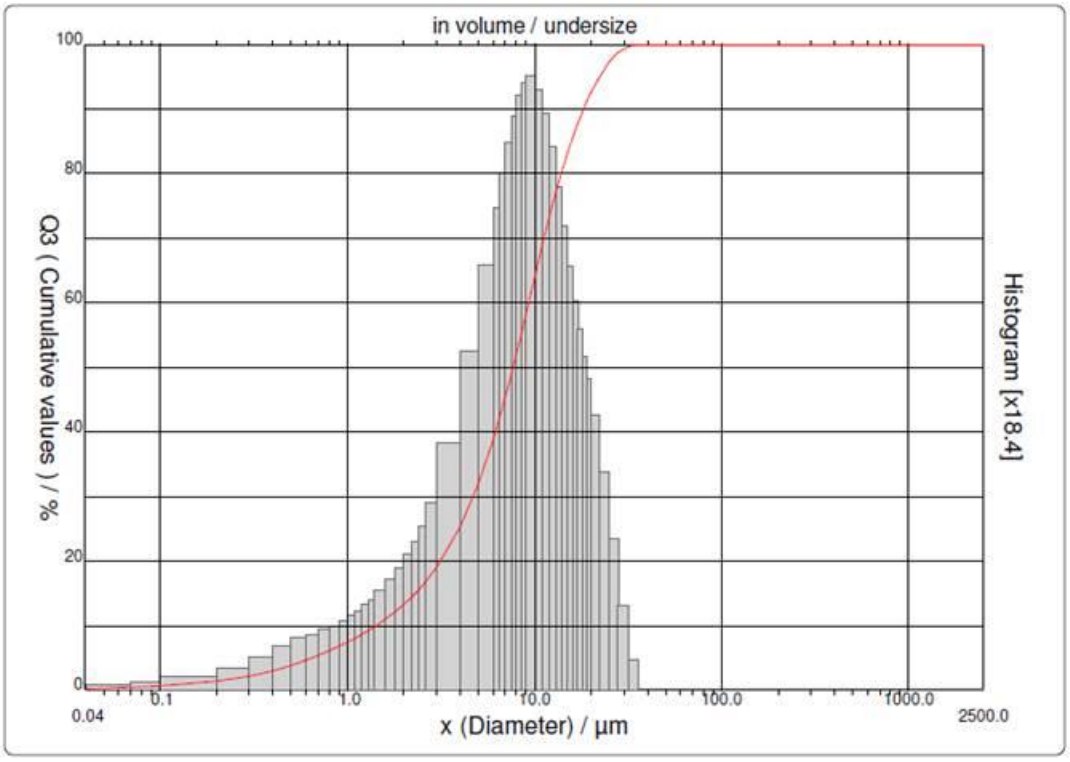

Figure 9-32 Raw Particle Size Data - 10µm, sample 3

Sample ref.	: Sample B US 1.1
Sample Name	:
Sample type	:
Comments	:
Liquid	:
Dispersing agent	:
Operator	:
Company	:
Location	:
Date : 05/24/2016	Time : 10:57:13AM
Index meas.	: 835
Database name	: CilasDB1

Ultrasounds	: 60 s
Obscurations	: 14 / 0.04 %
Diameter at 10%	: 0.67 µm
Diameter at 50%	: 4.41 µm
Diameter at 90%	: 10.95 µm
Mean diameter Fraunhofer	: 5.51 µm
Density/Factor	----------
Specific surface	----------
Automatic dilution	: No / No
Meas./Rins.	: 60s/60s/4
SOP name	: Fraunhofer

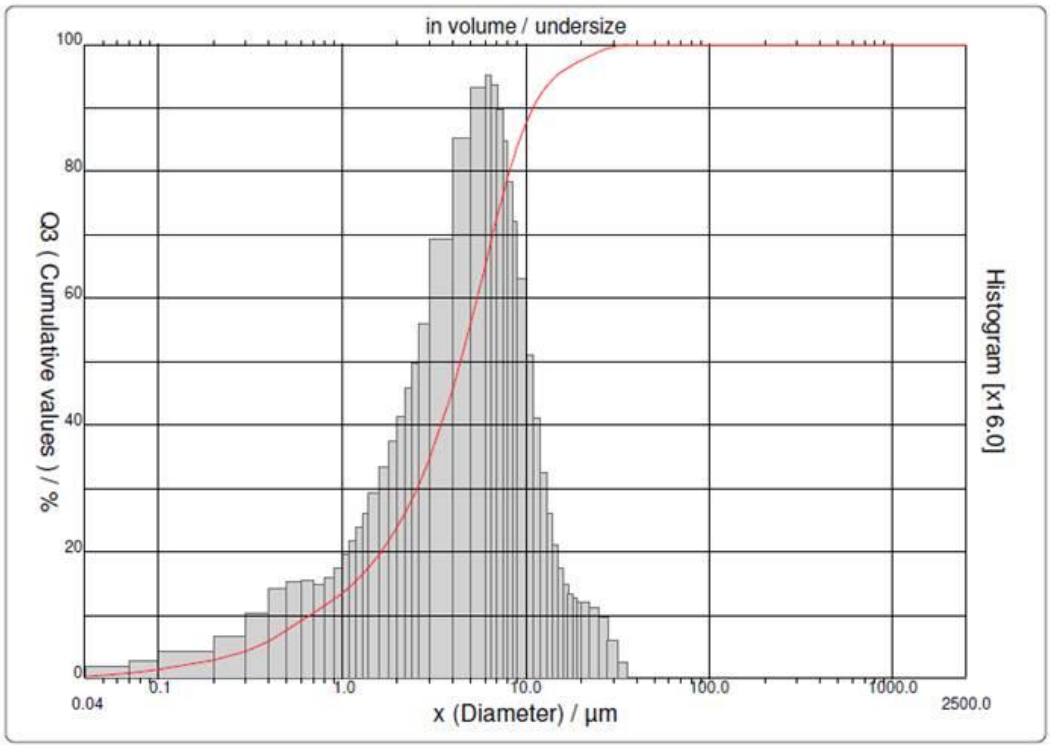

Figure 9-33 Raw Particle Size Data - 5µm, sample 1

Sample ref.	: Sample B US 1.2
Sample Name	:
Sample type	:
Comments	:
Liquid	:
Dispersing agent	:
Operator	:
Company	:
Location	:
Date : 05/24/2016	Time : 11:00:25AM
Index meas.	: 836
Database name	: CilasDB1

Ultrasounds	: 60 s
Obscurations	: 14 / 0.02 %
Diameter at 10%	: 0.78 µm
Diameter at 50%	: 4.43 µm
Diameter at 90%	: 10.97 µm
Mean diameter	: 5.53 µm
Fraunhofer	
Density/Factor	----------
Specific surface	----------
Automatic dilution	: No / No
Meas./Rins.	: 60s/60s/4
SOP name	: Fraunhofer

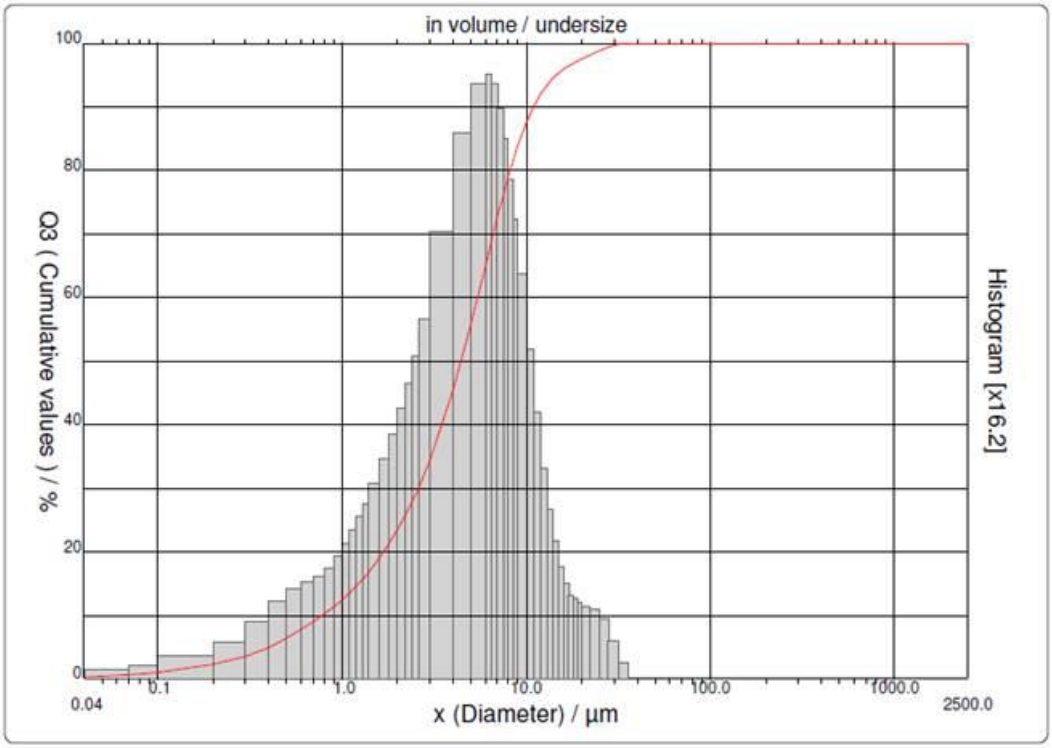

Figure 9-34 Raw Particle Size Data - 5µm, sample 2

Sample ref.	: Sample B US 1.3
Sample Name	:
Sample type	:
Comments	:
Liquid	:
Dispersing agent	:
Operator	:
Company	:
Location	:
Date : 05/24/2016	Time : 11:03:37AM
Index meas.	: 837
Database name	: CilasDB1

Ultrasounds	: 60 s
Obscurations	: 14 / 0.09 %
Diameter at 10%	: 0.77 µm
Diameter at 50%	: 4.41 µm
Diameter at 90%	: 10.97 µm
Mean diameter	: 5.56 µm
Fraunhofer	
Density/Factor	----------
Specific surface	----------
Automatic dilution	: No / No
Meas./Rins.	: 60s/60s/4
SOP name	: Fraunhofer

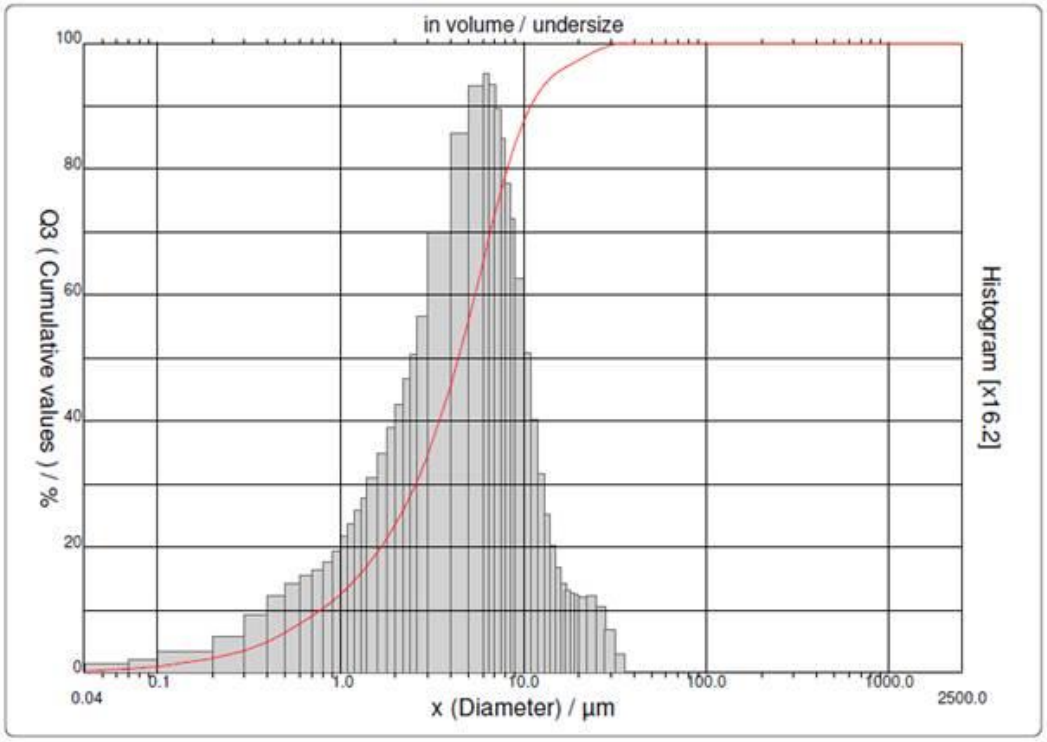

Figure 9-35 Raw Particle Size Data - 5µm, sample 3

Sample ref.	: Sample C US 1.1
Sample Name	:
Sample type	:
Comments	:
Liquid	: Water
Dispersing agent	:
Operator	:
Company	:
Location	:
Date : 05/24/2016	Time : 01:40:11PM
Index meas.	: 847 (841)
Database name	: CilasDB1

Ultrasounds	: 60 s
Obscurations	: 14 / 0.01 %
Diameter at 10%	: 1.21 µm
Diameter at 50%	: 2.36 µm
Diameter at 90%	: 4.38 µm
Mean diameter	: 2.61 µm
Fraunhofer	
Density/Factor	----------
Specific surface	----------
Automatic dilution	: No / No
Meas./Rins.	: 60s/60s/4
SOP name	: Fraunhofer

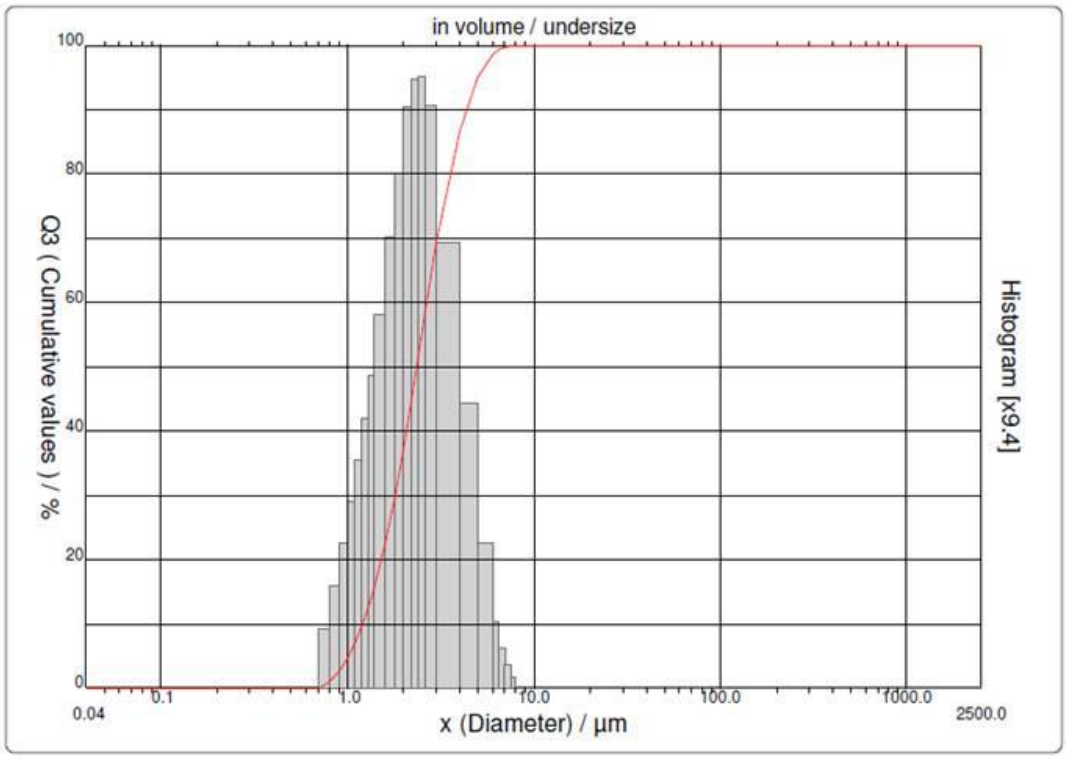

Figure 9-36 Raw Particle Size Data – 2.5µm, sample 1

Sample ref.	: Sample C US 1.2
Sample Name	:
Sample type	:
Comments	:
Liquid	: Water
Dispersing agent	:
Operator	:
Company	:
Location	:
Date : 05/24/2016	Time : 01:40:11PM
Index meas.	: 848 (842)
Database name	: CilasDB1

Ultrasounds	: 60 s
Obscurations	: 14 / 0.03 %
Diameter at 10%	: 1.18 µm
Diameter at 50%	: 2.33 µm
Diameter at 90%	: 4.37 µm
Mean diameter	: 2.59 µm
Fraunhofer	
Density/Factor	----------
Specific surface	----------
Automatic dilution	: No / No
Meas./Rins.	: 60s/60s/4
SOP name	: Fraunhofer

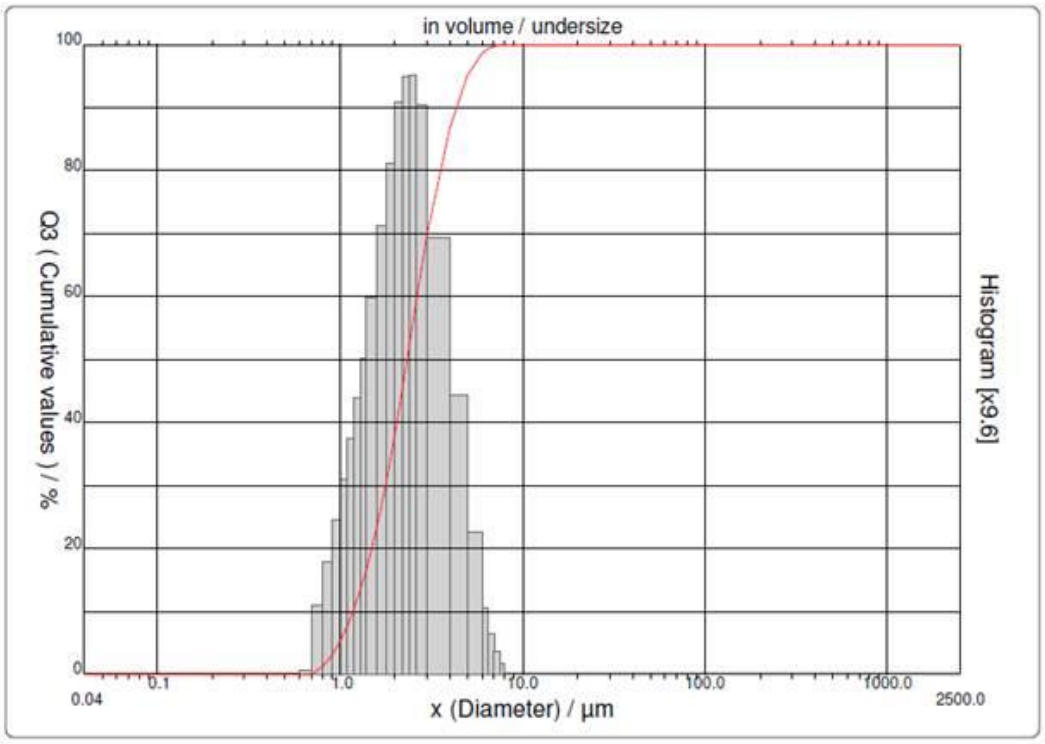

Figure 9-37 Raw Particle Size Data – 2.5µm, sample 2

Sample ref.	: Sample C US 1.3
Sample Name	:
Sample type	:
Comments	:
Liquid	: Water
Dispersing agent	:
Operator	:
Company	:
Location	:
Date : 05/24/2016	Time : 01:40:11PM
Index meas.	: 849 (843)
Database name	: CilasDB1

Ultrasounds	: 60 s
Obscurations	: 14 / 0.06 %
Diameter at 10%	: 1.18 µm
Diameter at 50%	: 2.33 µm
Diameter at 90%	: 4.36 µm
Mean diameter	: 2.58 µm
Fraunhofer	
Density/Factor	----------
Specific surface	----------
Automatic dilution	: No / No
Meas./Rins.	: 60s/60s/4
SOP name	: Fraunhofer

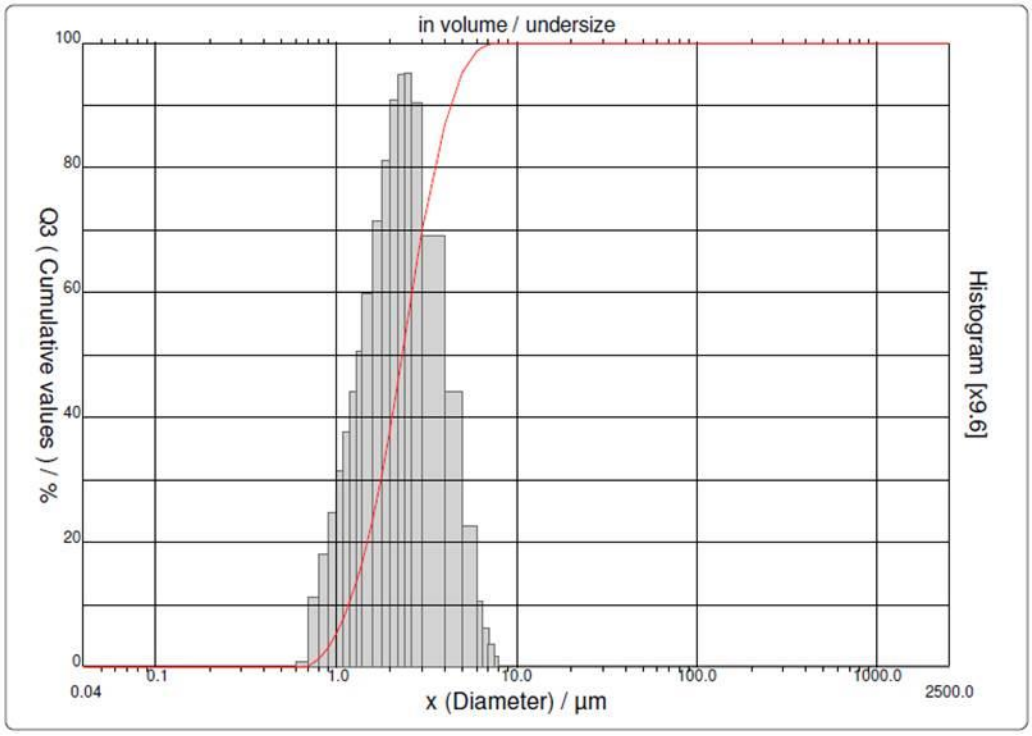

Figure 9-38 Raw Particle Size Data – 2.5µm, sample 3

Appendix C – FLUENT User Defined Function Codes

This code captures the impact velocity and impact angle of the particle tracks impinging on the surface. The DEFINE_DPM_BC function activates upon particle impact and stores the relevant data in the P_USER_REAL(p,x) variable where 'p' indicates the current particle and 'x' is a variable representing the index in the particle variable array. This UDF stores and tracks data for up to ten impacts, where the 11^{th} impact triggers the end of the particle and thus no more impact data is gathered for that particle. Following the impact, a new trajectory for the particle track is computed.

```
#include "udf.h"
DEFINE_DPM_BC(numhits2, p, t, f, f_normal, dim)
{

    /* increments particle impact counter */
    P_USER_REAL(p, 0) = P_USER_REAL(p, 0) + 1.;

   /* stops particle if too many hits occur */
    if (P_USER_REAL(p, 0) > 9)
      {
          return PATH_END;
      }

/* stores radial location of impact */

if (P_USER_REAL(p, 0) == 1)
     {
          P_USER_REAL(p, 21) = sqrt(pow(P_POS(p)[0],2) + pow(P_POS(p)[2],2));
     }

if (P_USER_REAL(p, 0) == 2)
     {
          P_USER_REAL(p, 22) = sqrt(pow(P_POS(p)[0],2) + pow(P_POS(p)[2],2));
     }

if (P_USER_REAL(p, 0) == 3)
     {
          P_USER_REAL(p, 23) = sqrt(pow(P_POS(p)[0],2) + pow(P_POS(p)[2],2));
     }

if (P_USER_REAL(p, 0) == 4)
     {
          P_USER_REAL(p, 24) = sqrt(pow(P_POS(p)[0],2) + pow(P_POS(p)[2],2));
     }
```

```
if (P_USER_REAL(p, 0) == 5)
    {
        P_USER_REAL(p, 25) = sqrt(pow(P_POS(p)[0],2) + pow(P_POS(p)[2],2));
    }

if (P_USER_REAL(p, 0) == 6)
    {
        P_USER_REAL(p, 26) = sqrt(pow(P_POS(p)[0],2) + pow(P_POS(p)[2],2));
    }

if (P_USER_REAL(p, 0) == 7)
    {
        P_USER_REAL(p, 27) = sqrt(pow(P_POS(p)[0],2) + pow(P_POS(p)[2],2));
    }

if (P_USER_REAL(p, 0) == 8)
    {
        P_USER_REAL(p, 28) = sqrt(pow(P_POS(p)[0],2) + pow(P_POS(p)[2],2));
    }

if (P_USER_REAL(p, 0) == 9)
    {
        P_USER_REAL(p, 29) = sqrt(pow(P_POS(p)[0],2) + pow(P_POS(p)[2],2));
    }

if (P_USER_REAL(p, 0) == 10)
    {
        P_USER_REAL(p, 30) = sqrt(pow(P_POS(p)[0],2) + pow(P_POS(p)[2],2));
    }


  /* stores impact velocity on first impact */
  if (P_USER_REAL(p, 0) == 1)
    {
        P_USER_REAL(p, 1) = NV_MAG(P_VEL(p));
    }

  /* stores impact velocity on second impact */
  if (P_USER_REAL(p, 0) == 2)
    {
        P_USER_REAL(p, 2) = NV_MAG(P_VEL(p));
    }

  /* stores impact velocity on third impact */
  if (P_USER_REAL(p, 0) == 3)
    {
```

```
      P_USER_REAL(p, 3) = NV_MAG(P_VEL(p));
  }

/* stores impact velocity on fourth impact */
if (P_USER_REAL(p, 0) == 4)
  {
      P_USER_REAL(p, 4) = NV_MAG(P_VEL(p));
  }

/* stores impact velocity on fifth impact */
if (P_USER_REAL(p, 0) == 5)
  {
      P_USER_REAL(p, 5) = NV_MAG(P_VEL(p));
  }

/* stores impact velocity on sixth impact */
if (P_USER_REAL(p, 0) == 6)
  {
      P_USER_REAL(p, 6) = NV_MAG(P_VEL(p));
  }

/* stores impact velocity on seventh impact */
if (P_USER_REAL(p, 0) == 7)
  {
      P_USER_REAL(p, 7) = NV_MAG(P_VEL(p));
  }

/* stores impact velocity on eight impact */
if (P_USER_REAL(p, 0) == 8)
  {
      P_USER_REAL(p, 8) = NV_MAG(P_VEL(p));
  }

/* stores impact velocity on ninth impact */
if (P_USER_REAL(p, 0) == 9)
  {
      P_USER_REAL(p, 9) = NV_MAG(P_VEL(p));
  }

/* stores impact velocity on tenth impact */
if (P_USER_REAL(p, 0) == 10)
  {
      P_USER_REAL(p, 10) = NV_MAG(P_VEL(p));
  }

real alpha; /* angle of particle path with face normal */
```

```
  real vn=0.;
  real nor_coeff = 1.0;
  real tan_coeff = 1.0;
  real normal[3];
  int i, idim = dim;
  real NV_VEC(x);

#if RP_2D
  /* dim is always 2 in 2D compilation. Need special treatment for 2d
    axisymmetric and swirl flows */
  if (rp_axi_swirl)
    {
      real R = sqrt(P_POS(p)[1]*P_POS(p)[1] +
          P_POS(p)[2]*P_POS(p)[2]);
      if (R > 1.e-20)
        {
          idim = 3;
          normal[0] = f_normal[0];
          normal[1] = (f_normal[1]*P_POS(p)[1])/R;
          normal[2] = (f_normal[1]*P_POS(p)[2])/R;
        }
      else
        {
          for (i=0; i<idim; i++)
            normal[i] = f_normal[i];
        }
    }
  else
#endif
  for (i=0; i<idim; i++)
    normal[i] = f_normal[i];

  if(p->type==DPM_TYPE_INERT)
    {

      alpha = (180/M_PI)*((M_PI/2) -
acos(NV_DOT(f_normal,P_VEL(p))/NV_MAG(P_VEL(p))));


  /* stores impact angle on first impact */
  if (P_USER_REAL(p, 0) == 1)
    {
        P_USER_REAL(p, 11) = alpha;
    }

  /* stores impact angle on second impact */
```

```
if (P_USER_REAL(p, 0) == 2)
  {
      P_USER_REAL(p, 12) = alpha;
  }

/* stores impact angle on third impact */
if (P_USER_REAL(p, 0) == 3)
  {
      P_USER_REAL(p, 13) = alpha;
  }

/* stores impact angle on fourth impact */
if (P_USER_REAL(p, 0) == 4)
  {
      P_USER_REAL(p, 14) = alpha;
  }

/* stores impact angle on fifth impact */
if (P_USER_REAL(p, 0) == 5)
  {
      P_USER_REAL(p, 15) = alpha;
  }

/* stores impact angle on sixth impact */
if (P_USER_REAL(p, 0) == 6)
  {
      P_USER_REAL(p, 16) = alpha;
  }

/* stores impact angle on seventh impact */
if (P_USER_REAL(p, 0) == 7)
  {
      P_USER_REAL(p, 17) = alpha;
  }

/* stores impact angle on eight impact */
if (P_USER_REAL(p, 0) == 8)
  {
      P_USER_REAL(p, 18) = alpha;
  }

/* stores impact angle on ninth impact */
if (P_USER_REAL(p, 0) == 9)
  {
      P_USER_REAL(p, 19) = alpha;
  }
```

```
  /* stores impact angle on tenth impact */
  if (P_USER_REAL(p, 0) == 10)
    {
        P_USER_REAL(p, 20) = alpha;
    }


      if ((NNULLP(t)) && (THREAD_TYPE(t) == THREAD_F_WALL))
          F_CENTROID(x,f,t);

      /* calculate the normal component, rescale its magnitude by
        the coefficient of restitution and subtract the change */

      /* Compute normal velocity. */
      for(i=0; i<idim; i++)
        vn += P_VEL(p)[i]*normal[i];

      /* Subtract off normal velocity. */
        for(i=0; i<idim; i++)
          P_VEL(p)[i] -= vn*normal[i];

      /* Apply tangential coefficient of restitution. */
        for(i=0; i<idim; i++)
          P_VEL(p)[i] *= tan_coeff;

      /* Add reflected normal velocity. */
        for(i=0; i<idim; i++)
          P_VEL(p)[i] -= nor_coeff*vn*normal[i];

      /* Store new velocity in P_VEL0 of particle */
      for(i=0; i<idim; i++)
        P_VEL0(p)[i] = P_VEL(p)[i];

      return PATH_ACTIVE;
    }
 return PATH_ABORT;
}
```

This code serves as a sampling tool to extract the particle impact data from the P_USER_REAL(p,x) variables. The code is activated using the Reports -> Discrete Phase -> Sample task in FLUENT where the boundary chosen to sample from is the outlet. This means that as the particles pass through the outlet boundary, all the P_USER_REAL(p,x) variables are read and stored in a data file for easy post-processing to take place in MATLAB.

```
#include "udf.h"
/************************************************************************/
/* UDF that samples discrete phase size and velocity distributions*/
/* within the domain.           */
/************************************************************************/
#define REMOVE_PARTICLES FALSE

DEFINE_DPM_OUTPUT(discrete_phase_sample,header,fp,p,t,plane)
{

  #if RP_2D
   real y;
   if(header)
   {
    par_fprintf_head(fp," #Time[s]  R [m]  X-velocity[m/s]");
    par_fprintf_head(fp," W-velocity[m/s] R-velocity[m/s] ");
    par_fprintf_head(fp,"Drop Diameter[m] Number of Drops  ");
    par_fprintf_head(fp,"Temperature [K] Initial Diam [m] ");
    par_fprintf_head(fp,"Injection Time [s] \n");
   }
   if(NULLP(p))
     return;
   if (rp_axi && (sg_swirl || rp_ke))
     y = MAX(sqrt(SQR(P_POS(p)[1]) + SQR(P_POS(p)[2])),DPM_SMALL);
   else
     y = P_POS(p)[1];
  par_fprintf(fp,"%d %" int64_fmt " %e %f %f %f %f %e %e %f %e %f \n",
 P_INJ_ID(P_INJECTION(p)),p->part_id, P_TIME(p),y,P_VEL(p)[0],
 P_VEL(p)[1],P_VEL(p)[2],P_DIAM(p),P_N(p),
 P_T(p), P_INIT_DIAM(p),p->time_of_birth);

  #else
   real r, x, y;
   if(header)
   {
     par_fprintf_head(fp," v1    v2    v3    v4    v5    v6    v7    v8    v9    v10    a1
a2    a3    a4    a5    a6    a7    a8    a9    a10    P1    P2    P3    P4    P5    P6
P7    P8    P9    P10    D\n");
```

```
    }
    if(NULLP(p))
      return;
    x = P_POS(p)[0];
    y = P_POS(p)[1];
    r = sqrt(SQR(x) + SQR(y));
    par_fprintf(fp,"%d %" int64_fmt " %6.3f %6.3f %6.3f %6.3f %6.3f %6.3f %6.3f
%6.3f %6.3f %6.3f %6.3f %6.3f %6.3f %6.3f %6.3f %6.3f %6.3f %6.3f %6.3f %6.3f
%6.6f %6.6f %6.6f %6.6f %6.6f %6.6f %6.6f %6.6f %6.6f %6.8f\n",
   P_INJ_ID(P_INJECTION(p)),p-
>part_id,P_USER_REAL(p,1),P_USER_REAL(p,2),P_USER_REAL(p,3),P_USER_
REAL(p,4),P_USER_REAL(p,5),P_USER_REAL(p,6),P_USER_REAL(p,7),P_USE
R_REAL(p,8),P_USER_REAL(p,9),P_USER_REAL(p,10),P_USER_REAL(p,11),P
_USER_REAL(p,12),P_USER_REAL(p,13),P_USER_REAL(p,14),P_USER_REAL
(p,15),P_USER_REAL(p,16),P_USER_REAL(p,17),P_USER_REAL(p,18),P_USER
_REAL(p,19),P_USER_REAL(p,20),P_USER_REAL(p,21),P_USER_REAL(p,22),
P_USER_REAL(p,23),P_USER_REAL(p,24),P_USER_REAL(p,25),P_USER_REA
L(p,26),P_USER_REAL(p,27),P_USER_REAL(p,28),P_USER_REAL(p,29),P_USE
R_REAL(p,30),P_DIAM(p));

   #endif

   #if REMOVE_PARTICLES
     MARK_PARTICLE(p, P_FL_REMOVED);
   #endif
 }
```

This UDF contains the final code of the erosion model developed.

```
#include "udf.h"
#include "dpm.h"

DEFINE_DPM_EROSION(Scattergood, p, t, f, normal, alpha, Vmag, Mdot)
{
        real A[ND_ND], area;

        double k = 4866920;

        double n = 4.75;

        double m = 4.186;

        //k is A in the delta w equation

        F_AREA(A,f,t);
        area = NV_MAG(A);

      F_STORAGE_R(f,t,SV_DPMS_EROSION) +=
k*pow(P_DIAM(p),m)*pow(1.00*Vmag,n)*pow(sin(alpha),0.375)*pow(cos(alpha),2
)*Mdot/area;

}
```

Appendix D – MATLAB Post-Processing Codes

This code was used to formulate the erosion profile graphs and to calculate the total amount of material removed. Once generated, the graphs were then used to identify the maximum eroded depth. This code was used in the test case: 104010D.

```
% Obtain middle peak of Edited Data image
LR_LengthPeak = 5415.4;
UD_LengthPeak = 4781.1;
LR_HeightPeak = 5.2226; % offset above y = 0
UD_HeightPeak = 9.8226; % offset above y = 0

% Obtain resolution from raw Data
ScanLength = 11600; % microns
delimiterIn = ' ';
headerlinesIn = 4;
LR_RawData =
importdata('LR_104010D_raw.txt',delimiterIn,headerlinesIn);
UD_RawData =
importdata('UD_104010D_raw.txt',delimiterIn,headerlinesIn);
LR_ptDist = ScanLength / length(LR_RawData.data(:,1));
UD_ptDist = ScanLength / length(UD_RawData.data(:,1));

% Code for edited LR Scan
f1 = figure();
A = importdata('LR_104010D_edited.txt',delimiterIn,headerlinesIn);
LR_HeightEdited = A.data(:,4)/10000 - LR_HeightPeak;
LR_LengthEdited =
transpose([0:LR_ptDist:LR_ptDist*length(A.data(:,1))-LR_ptDist]);
area(LR_LengthEdited, LR_HeightEdited, 0)
xlabel('Scan Length (\mum)', 'fontsize', 24);
ylabel('Depth (\mum)', 'fontsize', 24);
title('LR-104010D Profilometer Scan', 'fontsize', 24')
axis([0, LR_LengthEdited(length(LR_LengthEdited)), -12, 2])
set(gca,'ytick',[-12:2:0], 'fontsize', 24);
set(gca, 'LineWidth', 2);
grid on
%grid minor

% Calculating the volume over 180 degrees of rotation
LR_discrVolArray = [];
for i=1:1:size(LR_LengthEdited)-1
    LR_discrVolArray(i) =
0.5*abs(pi()*LR_HeightEdited(i)*abs((abs(LR_LengthPeak-
LR_LengthEdited(i)-LR_ptDist/2))^2 - (abs(LR_LengthPeak-
LR_LengthEdited(i)+LR_ptDist/2))^2));
end


% Code for edited UD Scan
B = importdata('UD_104010D_edited.txt',delimiterIn,headerlinesIn);
UD_HeightEdited = B.data(:,1)/10000 - UD_HeightPeak;
```

```
UD_LengthEdited =
transpose([0:UD_ptDist:UD_ptDist*length(B.data(:,1))-UD_ptDist]);
f2 = figure();
area(UD_LengthEdited, UD_HeightEdited, 0)
title('UD-104010D Profilometer Scan', 'fontsize', 24)
xlabel('Scan Length (\mum)', 'fontsize', 24);
ylabel('Depth (\mum)', 'fontsize', 24);
axis([0, UD_LengthEdited(length(UD_LengthEdited)), -12, 2])
set(gca,'ytick',[-12:2:0], 'fontsize', 24);
set(gca, 'LineWidth', 2);
grid on
%grid minor

% Calculating the volume over 180 degrees of rotation
UD_discrVolArray = [];
for i=1:1:size(UD_LengthEdited)-1
    UD_discrVolArray(i) =
0.5*abs(pi()*UD_HeightEdited(i)*abs((abs(UD_LengthPeak-
UD_LengthEdited(i)-UD_ptDist/2))^2 - (abs(UD_LengthPeak-
UD_LengthEdited(i)+UD_ptDist/2))^2));
end

saveas(f1,'LR-104010D Profilometer Scan.jpg')
saveas(f2,'UD-104010D Profilometer Scan.jpg')
DensitySi = 2329; % kg/m^3
UD_TotalErodedVolumeMicrons3 = sum(UD_discrVolArray)
UD_TotalErodedVolumeMeter3 = UD_TotalErodedVolumeMicrons3*10^-18;
UD_MassLoss = UD_TotalErodedVolumeMeter3*DensitySi*10^6
LR_TotalErodedVolumeMicrons3 = sum(LR_discrVolArray)
LR_TotalErodedVolumeMeter3 = LR_TotalErodedVolumeMicrons3*10^-18;
LR_MassLoss = LR_TotalErodedVolumeMeter3*DensitySi*10^6
```

This code contains the post-processing script used to analyze the particle impact data. A number of metrics and values were calculated in this code including the average impact velocity and average impact angle for each of the ten impacts, percentage of entrained particles that impact the surface, the total impacting mass flow rate, and the summation metric used in the model calibration. Additionally, if the radial impact location was larger than the experimental graph boundaries, the impact was not included in the analysis.

```
%% Particle Post-Processing

% considers first 10 impacts for each particle v1-10, a1-10
fileIn = importdata('34C_320K_40ms_10mic_Water.dat',' ',1);
rawData = fileIn.data;
aveImpact = mean(rawData);

numImpactsConsidered = 10;
% splits rawData into three matrices
rawVel = abs(rawData(:,1:numImpactsConsidered));
rawAng = abs(rawData(:,11:(10+numImpactsConsidered)));
rawPos = abs(rawData(:,21:(20+numImpactsConsidered)));

avgPerc = [];
avgVel = [];
avgAng = [];
avgPos = [];

for i=1:numImpactsConsidered
    avgPerc(i) = nnz(rawVel(:,i))/length(rawData);
    avgVel(i) = sum(rawVel(:,i))/nnz(rawVel(:,i));
    avgAng(i) = sum(rawAng(:,i))/nnz(rawAng(:,i));
    avgPos(i) = sum(rawPos(:,i))/nnz(rawPos(:,i));
end

% moves all velocity and angle data into single columns
velCol = rawVel(:);
angCol = rawAng(:);
posCol = rawPos(:);

%takes out impacts past a radial position
maxPos = 5012.5e-6;
newVelCol = [];
newAngCol = [];

for i=1:length(posCol)
    if(posCol(i) < maxPos)
        newVelCol(i,1) = velCol(i);
        newAngCol(i,1) = angCol(i);
    else
        newVelCol(i,1) = 0;
        newAngCol(i,1) = 0;
    end
end
```

```
masterArray = zeros(length(velCol), 3);

% Nandakumar erosion models
% col-1 = combined, col-2 = line, col-3 = area
masterArray(:,1) = cosd(angCol).^2;

exp = [4:0.1:6.6];
combined = zeros(length(masterArray),length(exp));

% raises each impact velocity to a fitted pwoer
for i= 1:length(exp)
        combined(:,i) = newVelCol.^exp(i).*masterArray(:,1);
        %line(:,i) = velCol(:,1).^exp(i).*masterArray(:,2);
        %area(:,i) = velCol(:,1).^exp(i).*masterArray(:,3);
end

% calculates sum metric for erosion model
sumCombined = sum(combined);

QSYMpartMassFR = 3.0606e-05; % [kg/s] Particle mass flowrate, from
FLUENT injection for WATER
trackFR = QSYMpartMassFR / length(rawVel); % mass FR per particle
track
numImpacts = nnz(newVelCol);  % total number of impacts
impMassFR = 4*numImpacts*trackFR
```

Bibliography

[1] *DARPA-BAA-1250. Intrachip/Interchip Enhanced Cooling Fundamentals (ICECool Fundamentals). Microsystems Technology Office,* June 7, 2012.

[2] *DARPA-BAA-13-21. ICECool Applications (ICECool Apps). Microsystems Technology Office,* February 6, 2013.

[3] G. Jiang, L. Diao and K. Kuang, *Properties of WCu, MoCu, and Cu/MoCu/Cu High-performance Heat Sink Materials and Manufacturing Technologies,* In Advanced Thermal Management Materials (pp. 73-87). Springer New York., 2013.

[4] M. Faqir, T. Batten, T. Mrotzek, S. Knippscheer, M. Massiot, M. Buchta and M. Kuball, *Improved thermal management for GaN power electronics: Silver diamond composite packages,* Microelectronics Reliability, 52(12), 3022-3025, 2012.

[5] S. Narumanchi, M. Mihalic, K. Kelly and G. Eesley, *Thermal interface materials for power electronics applications,* Thermal and Thermomechanical Phenomena in Electronic Systems, ITHERM 2008. 11th Intersociety Conference, 2008.

[6] C. Creamer, K. Chu, P. Chao, B. Schmanski, T. Yurovchak, S. Sweetland and P. McCluskey, *S2-T6: Microchannel cooled, high power GaN-on-Diamond MMIC,* Lester Eastman Conference on High Performance Devices, 2014.

[7] C. J, R. Myers, F. Wood and S. Binari, *Simulations of direct-die-attached microchannel coolers for the thermal management of GaN-on-SiC microwave amplifiers,* Components and Packaging Technologies, IEEE Transactions on, 28(4), 79, 2005.

[8] P. McCluskey, T. Podlesak and R. Grzybowski, *High temperature electronics,* CRC press, 1996.

[9] D. Squiller, H. Greve, E. Mengotti and P. McCluskey, *Physics-of-failure assessment methodology for power electronic systems,* Microelectronics Reliability, 54(9), 1680-1685.

[10] G. Beheim, P. Neudeck, D. Spry, M. Scardelletti, G. Ponchak, R. Meredith and G. Hunter, *High Temperature SiC Electronics: Update and Outlook,* Propulsion Controls and Diagnostics Workshop Cleveland (pp. 28-29), 2012.

[11] A. Kashyap, C. Chen, R. Ghandi, A. Patil, E. Andarawis, L. Yin and W. Johnson, *Silicon carbide integrated circuits for extreme environments,* Wide Bandgap Power Devices and Applications (WiPDA), 2013 IEEE Workshop, 2013.

[12] B. Ozpineci and L. Tolbert, *Comparison of wide-bandgap semiconductors for power electronics applications,* United States. Department of Energy, 2004.

[13] Wolfspeed, [Online]. Available: http://www.wolfspeed.com/Power/Products/MOSFETs/TO247/C2M1000170D. [Accessed December 2015].

[14] J. Felbinger, M. Chandra, Y. Sun, L. Eastman, J. Wasserbauer, F. Fali and F. Ejeckam, *Comparison of GaN HEMTs on diamond and SiC substrates,* Electron Device Letters, IEEE, 28(11), 948-950, 2007.

[15] R. Pengelly, S. Wood, J. Milligan, S. Sheppard and W. Pribble, *A review of GaN on SiC high electron-mobility power transistors and MMICs,* Microwave Theory and Techniques, IEEE Transactions on, 60(6), 1764-1783.

[16] J. Chung, K. Ryu, B. Lu and T. Palacios, *GaN-on-Si technology, a new approach for advanced devices in energy and communications,* Solid-State Device Research Conference (ESSDERC) (pp. 52-56), 2010.

[17] D. Tuckerman and R. Pease, *High-performance heat sinking for VLSI,* Electron Device Letters, IEEE, 2(5), 126-129, 1981.

[18] F. Laermer and A. Urban, *Challenges, developments and applications of silicon deep reactive ion etching,* Microelectronic Engineering, 67, 349-355, 2003.

[19] G. Harpole and J. Eninger, *Micro-channel heat exchanger optimization,* Semiconductor Thermal Measurement and Management Symposium, 1991. SEMI-THERM VII (pp. 59-63), 1991.

[20] L. Boteler, *Microfabrication and analysis of manifold microchannel coolers for power electronics (Doctoral Dissertation),* UNIVERSITY OF MARYLAND, COLLEGE PARK, 2001.

[21] L. Boteler, N. Jankowski, P. McCluskey and B. Morgan, *Numerical investigation and sensitivity analysis of manifold microchannel coolers,* International Journal of Heat and Mass Transfer, 55(25), 7698-7708, 2012.

[22] M. Ohadi, K. Choo, S. Dessiatoun and E. Cetegen, *Next Generation Microchannel Heat Exchangers,* Springer, 2013.

[23] E. Colgan, B. Furman, M. Gaynes, W. Graham, N. LaBianca, J. Magerlein and R. Schmidt, *A practical implementation of silicon microchannel coolers for high power chips,* Components and Packaging Technologies, IEEE Transactions, 2007.

[24] K. Moores, Y. Joshi and G. Schiroky, *Thermal characterization of a liquid cooled AlSiC base plate with integral pin fins*, Components and Packaging Technologies, IEEE Transactions on, 24(2), 213-219, 2001.

[25] A. Kosar and Y. Peles, *Boiling heat transfer in a hydrofoil-based micro pin fin heat sink*, International Journal of Heat and Mass Transfer, 50(5), 1018-1034, 2007.

[26] J. Ditri, M. McNulty and S. Igoe, *S3-P10: Embedded microfluidic cooling of high heat flux electronic components,* Lester Eastman Conference on High Performance Devices (pp. 1-4)., 2014.

[27] Y. Han, B. Lau, H. Zhang and X. Zhang, *Package-level Si-based micro-jet impingement cooling solution with multiple drainage micro-trenches,* Electronics Packaging Technology Conference (pp. 330-334), 2014.

[28] A. Bhunia, A. Brackley, C. Nguyen and B. Brar, *Device scale heat removal for high power density GaN devices,* Compound Semiconductor Integrated Circuit Symposium (pp. 1-4), 2012.

[29] S. Narumanchi, V. Hassani and D. Bharathan, *Modeling single-phase and boiling liquid jet impingement cooling in power electronics*, National Renewable Energy Laboratory, 2005.

[30] K. Kapur and M. Pecht, *Reliability Engineering*, John Wiley & Sons, 2014.

[31] M. Pecht and D. A, *Physics-of-failure: an approach to reliable product development*, Journal of the IES, 38(5), 30-34, 1995.

[32] C. Glassbrenner and G. Slack, *Thermal conductivity of silicon and germanium from 3 K to the melting point,* Physical Review, 134(4A), A1058, 1964.

[33] R. Powell, C. Ho and P. Liley, *Thermal Conductivity of Selected Materials,* National Standard Reference Data Series - National Bureau of Standards, 1996.

[34] V. Souza and A. Neville, *Corrosion and synergy in a WC Co Cr HVOF thermal spray coating—understanding their role in erosion–corrosion degradation,* Wear, 259(1), 171-180, 2005.

[35] M. Stack and G. Abdulrahman, *Mapping erosion-corrosion of carbon steel in oil exploration conditions: Some new approaches to characterizing mechanisms and synergies,* Tribology International, 43(7), 1268-1277, 2010.

[36] R. Wood, *Tribo-corrosion of coatings: a review,* Journal of Physics D: Applied Physics, 40(18), 5502, 2007.

[37] C. Henry, J. Minier and G. Lefevre, *Towards a description of particulate fouling: From single particle deposition to clogging,* Advances in colloid and interface science, 185, 34-76, 2012.

[38] I. Finnie, *Erosion of surfaces by solid particles,* Wear, 3(2), 87-103., 1960.

[39] G. Sheldon and I. Finnie, *The mechanism of material removal in the erosive cutting of brittle materials,* Journal of Manufacturing Science and Engineering, 88(4), 393-399, 1966.

[40] G. Sheldon and I. Finnie, *On the ductile behavior of nominally brittle materials during erosive cutting,* Journal of Manufacturing Science and Engineering, 88(4), 387-392, 1966.

[41] A. Smekal and W. Klemm, *Mechanische Messung chemischer Bindefestigkeiten,* Monatshefte für Chemie/Chemical Monthly, 82(3), 411-421, 1951.

[42] A. Smekal, *Uber die Abmessungen ideates Kristallgittes,* Acta Physica Austriaca, 7, 324., 1953.

[43] W. Klemm and A. Smekal, *über den Grundvorgang des Polierens von Gläsern,* Naturwissenschaften, 29(45), 688-690., 1941.

[44] B. Hockey, *Plastic deformation of aluminum oxide by indentation and abrasion,* Journal of the American Ceramic Society 54.5 (1971): 223-231.

[45] B. Lawn and R. Wilshaw, *Indentation fracture: principles and applications,* Journal of Materials Science, 10(6), 1049-1081, 1975.

[46] B. Lawn, M. Swain and K. Philips, *On the mode of chipping fracture in brittle solids,* Journal of Materials Science 10.7 (1975): 1236-1239, 1975.

[47] S. Srinivasan and R. Scattergood, *On lateral cracks in glass,* Journal of materials science, 22(10), 3463-3469, 1987.

[48] B. Hockey and B. Lawn, *Electron microscopy of microcracking about indentations in aluminium oxide and silicon carbide,* Journal of Materials Science, 10(8), 1275-1284, 1975.

[49] A. Evans and T. Wilshaw, *Quasi-static solid particle damage in brittle solids—I. Observations analysis and implications,* Acta Metallurgica, 24(10), 939-956, 1976.

[50] A. Evans and T. Wilshaw, *Dynamic solid particle damage in brittle materials: an appraisal,* Journal of Materials Science, 12(1), 97-116, 1977.

[51] M. Swain and B. Lawn, *Indentation fracture in brittle rocks and glasses,* International Journal of Rock Mechanics and Mining Sciences & Geomechanics Abstracts. Vol. 13. No. 11. Pergamon, 1976.

[52] B. Lawn and A. Evans, *A model for crack initiation in elastic/plastic indentation fields,* Journal of Materials Science, 12(11), 2195-2199, 1977.

[53] C. Perrott, *Elastic-plastic indentation: Hardness and fracture,* Wear, 45(3), 293-309, 1977.

[54] J. Lankford and D. Davidson, *The crack-initiation threshold in ceramic materials subject to elastic/plastic indentation,* Journal of Materials Science, 14(7), 1662-1668, 1979.

[55] B. Lawn and D. Marshall, *Hardness, Toughmess, and Brittleness: An Indentation Analysis,* J. Am. Ceram. Soc., 62(7), 347, 1979.

[56] B. Lawn, A. Evans and D. Marshall, *Elastic/plastic indentation damage in ceramics: the median/radial crack system,* Journal of the American Ceramic Society, 63(9-10), 574-581, 1980.

[57] D. Marshall, B. Lawn and A. Evans, *Elastic/plastic indentation damage in ceramics: the lateral crack system,* Journal of the American Ceramic Society, 65(11), 561-566, 1982.

[58] D. Tabor, *Hardness of Metals,* Clarendon Press, Oxford, 1951.

[59] S. Wiederhorn and B. Lawn, *Strength degradation of glass impacted with sharp particles: I, Annealed surfaces,* Journal of the American Ceramic Society, 62(1-2), 66-70, 1979.

[60] A. Ruff and S. Wiederhorn, *Erosion by solid particle impact (No. NBSIR-78-1575),* National Bureau of Standards, National Measurement Lab. Gaithersburg, MD., 1979.

[61] B. Hockey, S. Wiederhorn and H. Johnson, *Erosion of brittle materials by solid particle impact (pp. 379-402),* Springer US, 1978.

[62] A. Evans, M. Gulden and M. Rosenblatt, *Impact damage in brittle materials in the elastic-plastic response regime,* Proceedings of the Royal Society of London A: Mathematical, Physical and Engineering Sciences (Vol. 361, No. 1706, pp. 343-365), 1978.

[63] S. Wiederhorn and B. Hockey, *Effect of material parameters on the erosion resistance of brittle materials,* Journal of Materials Science, 18(3), 766-780, 1983.

[64] D. Tabor, *A simple theory of static and dynamic hardness,* Proceedings of the Royal Society of London A: Mathematical, Physical and Engineering Sciences (Vol. 192, No. 1029, pp. 247-274), 1948.

[65] J. Routbort, R. Scattergood and E. Kay, *Erosion of silicon single crystals,* Journal of the American Ceramic Society, 63(11-12), 635-640, 1980.

[66] J. Routbort, R. Scattergood and A. Turner, *The erosion of reaction-bonded SiC,* Wear, 59(2), 363-375, 1980.

[67] R. Scattergood and J. Routbort, *Velocity and size dependences of the erosion rate in silicon,* Wear, 67(2), 227-232, 1981.

[68] J. Routbort and R. Scattergood, *Anomalous Solid-Particle Erosion Rate of Hot-Pressed Silicon Carbide,* Journal of the American Ceramic Society, 63(9-10), 593-595, 1980.

[69] R. Scattergood and J. Routbort, *Velocity Exponent in Solid-Particle Erosion of Silicon,* Journal of the American Ceramic Society, 66(10), c184-c186, 1983.

[70] C. Yust and R. Crouse, *Melting at particle impact sites during erosion of ceramics,* Wear, 51(1), 193-196, 1978.

[71] P. Shewmon, *Particle size threshold in the erosion of metals,* Wear, 68(2), 253-258, 1981.

[72] R. Telling and J. Field, *The erosion of diamond, sapphire and zinc sulphide by quartz particles,* Wear, 233, 666-673, 1999.

[73] F. Auerbach, *Measurement of hardness,* Ann. Phys. Chem, 43, 61, 1891.

[74] R. Mouginot and D. Maugis, *Fracture indentation beneath flat and spherical punches,* Journal of Materials Science, 20(12), 4354-4376, 1985.

[75] R. Jaccodine, *Surface energy of germanium and silicon,* Journal of The Electrochemical Society, 110(6), 524-527, 1963.

[76] J. Humphrey, *Fundamentals of fluid motion in erosion by solid particle impact,* International Journal of Heat and Fluid Flow, 11(3), 170-195, 1990.

[77] H. Clark, *On the impact rate and impact energy of particles in a slurry pot erosion tester,* Wear, 147(1), 165-183, 1991.

[78] H. Clark, *The influence of the flow field in slurry erosion,* Wear, 152(2), 223-240, 1992.

[79] H. Clark, *The influence of the squeeze film in slurry erosion,* Wear, 256(9), 918-926, 2004.

[80] H. Clark and L. Burmeister, *The influence of the squeeze film on particle impact velocities in erosion,* International journal of impact engineering, 12(3), 415-426, 1992.

[81] H. Clark and R. Hartwich, *A re-examination of the 'particle size effect' in slurry erosion,* Wear, 248(1), 147-161, 2001.

[82] A. Gadhikar, A. Aniruddha, A. Sharma, D. Goel and C. Sharma, *Fabrication and testing of slurry pot erosion tester,* Transactions of the Indian Institute of Metals, 64(4-5), 493-500, 2011.

[83] S. Rajahram, T. Harvey and R. Wood, *Electrochemical investigation of erosion–corrosion using a slurry pot erosion tester,* Tribology International, 44(3), 232-240, 2011.

[84] G. Desale, B. Gandhi and S. Jain, *Improvement in the design of a pot tester to simulate erosion wear due to solid–liquid mixture,* Wear, 259(1), 196-202, 2005.

[85] S. Lathabai and D. Pender, *Microstructural influence in slurry erosion of ceramics,* Wear, 189(1), 122-135, 1995.

[86] R. Lynn, K. Wong and H. Clark, *On the particle size effect in slurry erosion,* Wear, 149(1), 55-71, 1991.

[87] B. Ghandi and S. Borse, *Nominal particle size of multi-sized particulate slurries for evaluation of erosion wear and effect of fine particles,* Wear, 257(1), 73-79, 2004.

[88] Q. Fang, H. Xu, P. Sidky and M. Hocking, *Erosion of ceramic materials by a sand/water slurry jet,* Wear, 224(2), 183-193, 1999.

[89] Y. Zhang, Y. Cheng and S. Lathabai, *Erosion of alumina ceramics by air-and water-suspended garnet particles,* Wear, 240(1), 40-51, 2000.

[90] J. Zhou and S. Bahadur, *Erosion characteristics of alumina ceramics at high temperatures,* Wear, 181, 178-188, 1995.

[91] O. Ajayi and K. Ludema, *The effect of microstructure on wear modes of ceramic materials,* Wear, 154(2), 371-385.

[92] J. Wang, T. Nguyen and K. Pang, *Mechanisms of microhole formation on glasses by an abrasive slurry jet,* Journal of Applied Physics, 105(4), 044906, 2009.

[93] J. Wang, *Abrasive Waterjet Machining of Engineering Materials,* Trans Tech Publications Ltd, Zurich, Switzerland, 2003.

[94] A. Momber and R. Kovacevic, *Principles of abrasive water jet machining,* Springer Science & Business Media, 1998 and 2012.

[95] K. Dadkhahipour, T. Nguyen and J. Wang, *Mechanisms of channel formation on glasses by abrasive waterjet milling,* Wear, 292, 1-10, 2012.

[96] K. Pang, T. Nguyen, J. Fan and J. Wang, *A study of micro-channeling on glasses using an abrasive slurry jet,* Machining Science and Technology, 16(4), 547-563, 2012.

[97] H. Nouraei, A. Wodoslawsky, M. Papini and J. Spelt, *Characteristics of abrasive slurry jet micro-machining: a comparison with abrasive air jet micro-machining,* Journal of Materials Processing Technology, 213(10), 1711-1724, 2013.

[98] A. Ghobeity, T. Krajac, T. Burzynski, M. Papini and J. Spelt, *Surface evolution models in abrasive jet micromachining,* Wear, 264(3), 185-198, 2008.

[99] A. Ghobeity, D. Ciampini and M. Papini, *An analytical model of the effect of particle size distribution on the surface profile evolution in abrasive jet micromachining,* Journal of Materials Processing Technology, 209(20), 6067-6077, 2009.

[100] H. Wensink and M. Elwenspoek, *A closer look at the ductile–brittle transition in solid particle erosion,* Wear, 253(9), 1035-1043, 2002.

[101] A. Ghobeity, H. Getu, M. Papini and J. Spelt, *Surface evolution models for abrasive jet micromachining of holes in glass and polymethylmethacrylate (PMMA),* Journal of Micromechanics and Microengineering, 17(11), 2175, 2007.

[102] H. Li, Z. Wang and J. Fan, *Analysis and modelling of particle velocities in micro-abrasive air jet,* International Journal of Machine Tools and Manufacture, 49(11), 850-858, 2009.

[103] D. Dehnadfar, J. Friedman and M. Papini, *Laser shadowgraphy measurements of abrasive particle spatial, size and velocity distributions through micro-masks used in abrasive jet micro-machining,* Journal of Materials Processing Technology, 212(1), 137-149, 2012.

[104] K. Pang, T. Nguyen, J. Fan and J. Wang, *Modelling of the micro-channelling process on glasses using an abrasive slurry jet,* International Journal of Machine Tools and Manufacture, 53(1), 118-126, 2011.

[105] R. Jafar, H. Nouraei, M. Emamifar, M. Papini and J. Spelt, *Erosion modeling in abrasive slurry jet micro-machining of brittle materials,* Journal of Manufacturing Processes, 17, 127-140, 2015.

[106] P. Slikkerveer, P. Bouten, F. In't Veld and H. Scholten , *Erosion and damage by sharp particles,* Wear, 217(2), 237-250, 1998.

[107] R. Jafar, J. Spelt and M. Papini, *Surface roughness and erosion rate of abrasive jet micro-machined channels: experiments and analytical model,* Wear, 303(1), 138-145, 2013.

[108] J. Routbort, D. Singh, E. Tomofeeva, E. Yu and R. Smith, *Erosion of Radiator Materials by Nanofluids,* Vehicle Technologies Annual Review. Argonne National Lab, 2001.

[109] D. Singh and J. Routbort, *Effects of nanofluids on heavy vehicle systems,* Argonne National Laboratory (ANL) Report, US Department of Energy, 2008.

[110] D. Singh, J. Routbort, T. Sofu and R. Smith, *Erosion of Radiator Materials by Nanofluids,* Vehicle Technologies Annual Review. Argonne National Labs, 2009.

[111] C. Nguyen, G. Laplante, M. Cury and G. Simon, *Experimental investigation of impinging jet heat transfer and erosion effect using Al2O3-water nanofluid,* Proceedings of the 6th IASME/WSEAS International Conference on Fluid Mechanics and Aerodynamics, 2008.

[112] G. Molina, F. Aktaruzzaman, W. Stregles, V. Soloiu and M. Rahman, *Jet-impingement effects of alumina-nanofluid on aluminum and copper,* Advances in Tribology, 2014.

[113] A. Sparks and I. Hutchings, *Transitions in the erosive wear behaviour of a glass ceramic,* Wear 149.1 (1991): 99-110, 1991.

[114] I. Hutchings, *Ductile-brittle transitions and wear maps for the erosion and abrasion of brittle materials,* Journal of Physics D: Applied Physics 25.1A (1992): A212.

[115] S. Wiederhorn and B. Lawn, *Strength degradation of glass resulting from impact with spheres,* Journal of the American Ceramic Society, 60(9), 451-58, 1977.

[116] I. Hutchings, *Strain rate effects in microparticle impact,* Journal of Physics D: Applied Physics, 10(14), L179, 1977.

[117] I. Finnie, *Some reflections on the past and future of erosion,* Wear, 186, 1-10, 1995.

[118] ANSYS v16.0 Documentation.

[119] N. Chougule, G. Parishwad, P. Gore, S. Pagnis and S. Sapali, *CFD analysis of Multi-jet air Impingement on flat plate,* Proceeding of the World Congress on Engineering, London, UK (Vol. 3), 2011.

[120] A. D. Gosman and E. Ioannides, *Aspects of computer simulation of liquid-fuelled combustors,* J. Energy 7(6). 482–490, 1983.

[121] A. Mansouri, H. Arabnejad, S. Karimi, S. Shirazi and B. McLaury, *Improved CFD modeling and validation of erosion damage due to fine sand particles,* Wear, 338, pp.339-350, 2015.

[122] Wanner Engineering, Hydracell D10 Series Pump Specifications Documentation, September 2014.

[123] http://www.waterblast.com/Products/Nozzles/Nozzle_Inserts_(Tips)/HHTC_Nozzles/HHTC0_Nozzle_Tips/.

[124] K. Anand, S. Hovis, H. Conrad and R. Scattergood, *Flux Effects in Solid Particle Erosion,* Wear, 118(2), 243-257, 1987.

[125] A. Mansouri, M. Mahdavi, S. Shirazi and B. McLaury, *Investigating the Effect of Sand Concentration on Erosion Rate in Slurry Flows,* CORROSION 2015. NACE International, 2015.

[126] A. Levy, *Solid particle erosion and erosion-corrosion of materials,* Asm International, 1995.

[127] C. Huang, S. Chiovello, P. Minev, Luo, J and K. Nandakumar, *A comprehensive phenomenological model for erosion of materials in jet flow,* Powder Technology 187.3 (2008): 273-279, 2008.

[128] M. Wang, C. Huang, K. Nandakumar, P. Minev, J. Luo and S. Chiovelli, *Computational fluid dynamics modelling and experimental study of erosion in slurry jet flows,* International Journal of Computational Fluid Dynamics, 23(2), 155-172, 2009.

[129] C. Huang, P. Minev, J. Luo and K. Nandakumar, *A phenomenological model for erosion of material in a horizontal slurry pipeline flow,* Wear, 269(3), 190-196., 2010.

[130] A. Misra and I. Finnie, *On the size effect in abrasive and erosive wear,* Wear, 65(3), 359-373., 1981.

[131] J. Bitter, *A study of erosion phenomena: Part II,* Wear, 6(3), 169-190., 1963.

[132] X. Chen, B. McLaury and S. Shirazi, *Application and experimental validation of a*

computational fluid dynamics (CFD)-based erosion prediction model in elbows and plugged tees., Computers & Fluids, 33(10), 1251-1272, 2004.

[133] Y. Zhang, B. McLaury and S. Shirazi, *Improvements of particle near-wall velocity and erosion predictions using a commercial CFD code,* Journal of Fluids Engineering, 131(3), 031303., 2009.

[134] D. Singh and J. Routbort, *Effects of nanofluids on heavy vehicle systems,* Argonne National Laboratory (ANL) Report, US Department of Energy, 2006.

[135] A. Levy, *Solid particle erosion and erosion-corrosion of materials,* ASM International, 1995.